APPLICATION OF PEA TECHNIQUE TO SPACE CHARGE MEASUREMENT IN CYLINDRICAL GEOMETRY HV CABLE SYSTEMS

Thesis submitted for the degree of

Doctor of Philosophy

at the University of Leicester

by

Hualong ZHENG, MSc, BSc

Department of Engineering

University of Leicester

2015

APPLICATION OF PEA TECHNIQUE TO SPACE CHARGE MEASUREMENT IN CYLINDRICAL GEOMETRY HV CABLE SYSTEMS

by

Hualong ZHENG

Abstract

Space charge, as one of the major concerns for the reliability of polymeric High Voltage Direct Current (HVDC) cables, has drawn wide attention in both academia and industry. Accordingly, measurement techniques along with accurate data interpretation have been required to study space charge behaviour in insulation materials and to provide solid bases for simulation activities. In this work, a high temperature space charge measurement system for mini-cables has been developed based on the Pulsed Electro-Acoustic (PEA) method. In parallel, simulation tools for space charge accumulation, based on non-linear unipolar charge transport models, the acoustic signal formation, transmission of acoustic waves, and their detection, have been developed for PEA measurement on mini-cables to provide an alternative way for interpreting the raw experimental data rather than the traditional approaches of reconstructing space charge information by signal processing and calibration. The simulation uses 2-D simulation tools and includes the clamping unit of the PEA cell to provide, for the first time, a detailed comparison of the two commonly used shapes, flat and curved, of the base electrode. Benefiting from the ability of applying isothermal experimental conditions of 20 – 70 °C, the transient of 'intrinsic' space charge accumulation due to the field and temperature dependent conductivity has been studied by means of a novel experimental data analysis method proposed in this work. In addition, the analysis provides a way to assess conductivity models by matching the simulation results with the experimental space charge results. By applying the simulation tools, the effect of the possible cable defects of non-concentricity and a mismatch between the insulation and semicon layers could be assessed. Furthermore, the origin of the bulk space charge signal experimentally observed in a mini-cable was found to be consistent with a radius dependent conductivity which may be a consequence of incomplete degassing.

Acknowledgements

First of all, I would like to express my gratitude to my supervisor Dr Stephen Dodd for his excellent guidance and support on my project. Despite his enormous workload, he has been always patient in helping me get through my difficulties and problems.

I would also like to thank Professor John Fothergill who offered me the opportunity to study for this PhD in the first place; he guided me through the first year, showed me how to work as a researcher and gave me a lot of support even after he was promoted to City University London.

My gratitude also goes to Professor Len Dissado for his spontaneous guidance and encouragement in this work and life in general. I truly admire his spirit of hard work and dedication to science and research.

I am thankful to Professor Stéphane Holé for his kindly guidance and training especially on the simulation which laid the solid foundation for the simulation work achieved in this project.

I feel indebted to many people in our group and the Engineering Department. My particular thanks go to Dr Nikola Chalashkanov and Andy Willby. Nik has given me a lot of help in life and work and has been a good friend to me. Andy assisted me with the practical work and experiments. I also appreciate the support from the work shop in developing the equipment hardware.

I would like to acknowledge the fact that this research would not have been possible without the financial support of the Nexans Research Center, Lyon, France. Not only did I obtain financial support, but I also benefited from the fruitful discussion with the researchers in NRC, especially Dr Arnaud ALLAIS and Dr Lazhar KEBBABI.

I am sincerely grateful to my current boss Professor Simon Rowland for his patience and tolerance regarding my later submission of this thesis.

I would also like to express my appreciation to Dr Mingli Fu and Dr Antonios TZIMAS.

Last but not least, I thank my parents and my beautiful wife Jie LIAN. They are the reason that I have never given up.

Contents

1 INTRODUCTION

1.1 Background

This thesis sets out research work that has been carried out to develop a methodology for the robust interpretation of pulsed electroacoustic measurements when applied to the understanding of space charge development in cable insulating materials. The work is of particular interest to the manufacturers of HVDC power cables as the accumulation of space charge within the cable primary insulation material can lead to electrical breakdown. This is also a particular concern to end users such as the electrical power transmission companies as electrical breakdown can lead to power outages, concerns regarding the health & safety of workers, expensive repairs and reduced reliability of the power system. In this chapter, the background of the work is summarised leading to a statement of the aims and objectives of the work. A brief overview of the structure of the thesis and the approach taken in this work will then be given.

1.1.1 HVDC Transmission

Recent developments in power electronic semiconductors have led to a renewed interest in direct current (DC) transmission. Compared with traditional alternating current (AC) transmission, the DC transmission system has the following advantages [1]:

- It contributes to the stability of the whole network by virtue of the asynchronous interconnection and rapid control of power flow.
- The lengths of the DC transmission line are not restricted by charging the alternating current and reactive power compensation is no longer required. Consequently, the HVDC system may be the only feasible solution for long submarine connections.
- DC transmission lines are more economical, because conductors are free of skin effect and proximity effect, as well as the insulation and conductor saving for the same power rating with respect to AC insulation.

These advantages, in addition to the continuous development in high voltage direct current (HVDC) technologies, indicate a wider scope of opportunity for DC transmission to expand significantly in the near future. In the meantime, the trend to DC would raise requirements for the development of insulating materials with improved endurance and properties to address the detrimental electrical properties of current polymeric based materials.

In an electrical power system, energy delivery is achieved through either overhead transmission lines or underground power cables. Overhead transmission lines take a dominating role in the power transmission system. However, the usage of underground cables has dramatically increased in recent decades, for reasons such as: the visual impact of overhead lines and safety considerations in urban areas; increasingly mature techniques for cable manufacture as well as reducing costs, and additional demands for offshore power transmission. Due to the general fact that the energy generation points are normally far from the load, investment in power transmission lines is considerable. Therefore, methods to reducing the costs of cable manufacture without compromising on reliability have always been of interest to the industry.

1.1.2 DC cable insulation and space charge

Insulating materials take a large percentage of the entire cost of cables and, to a certain extent, determine the voltage rating of cables. A variety of materials have been utilized as cable insulations, for example natural and synthetic rubber compounds, mass impregnated paper, polyvinyl chloride, polyethylene (PE) and its cross-linked products (XLPE) [2]. Since the 1990s, extruded XLPE polymeric cable has almost entirely substituted paper-oil in both high voltage (HV) and extra high voltage (EHV) AC systems due to their advantages of reduced costs, ease of processing, increased reliability, low maintenance and environmental impact with respect to oil-paper cable [3]. However their usage as HVDC cables seems not so successful considering premature breakdown problems which are widely believed to be related to the presence of space charge [1, 4, 5].

Dielectric materials possess macroscopic charge neutrality in normal conditions, where negative and positive charges (for example, electrons, protons or ions) achieve equilibrium where the net space charge density is zero. However, this equilibrium can be broken under applied electrical stress. Under application of an electrical field, material polarization will occur, and regions of charge in the insulation may accumulate as a result of either injected charges (holes or electrons) from electrode/insulator interfaces or of the drift of ionised impurities within the bulk of the dielectric [6]. The risks associated with DC electrical stresses are fundamentally different to that under AC stresses. Under AC stress (50 Hz or 60 Hz) the applied voltage is reversed many times per second leaving little time for space charge to accumulate within the cable insulation. However, cables for HVDC applications will have unipolar voltages applied for considerable lengths of time. For this reason, the electric field distribution in AC cables will be determined by the permittivity of the polymer which is less insensitive to temperature. On the contrary, the steady-state electric field under DC stress is determined by the electrical conductivity of the material which in general is highly sensitive to temperature. The adoption of XLPE technology requires the long-term processes, under which space charge accumulation occurs, to be fully understood. Charge accumulation may also result from the non-linear electrical conductivity dependence with electric field in XLPE based cable insulation [7] or by a temperature gradient inside the cable insulation owing to the heat dissipated by the central conductor of the cable [8]. Charge transport within the bulk is also governed by trapping (at chemical and physical defects). In addition, the enhanced electric field and the presence of space charge may also accelerate the polymeric electro-thermal ageing process during service [9] leading to long term changes in the electrical conductivity of the polymer. As long as the processes of charge generation are not equal to the charge removal, charges would accumulate or decay within the dielectric forming regions of space charge. The presence of space charge would distort the electrical field inside the insulating material and at the electrode/insulator interfaces. More seriously, the distorted field may reach critical values within certain regions of the cable insulation, causing electrical breakdown of the insulation. Manufacturers and end users of HVDC cables are therefore interested in developing reliable techniques for space charge measurement and characterisation for quality control of commercial cables, particularly as the cables are expected to have a lifetime of 40 years.

1.2 Space charge measurement techniques

Considerable effort has been put into developing measurement techniques for the detection of space charge distributions in insulating materials in order to understand the mechanism of the space charge phenomena.

Currently, the measurement techniques can be generally separated into two categories:

- Destructive methods like TSC (Thermally Stimulated Current), TSSP (Thermally stimulated Surface Potential) and TL (Thermoluminescence).
- Non-destructive methods like TSP (thermal step pulse) method, LIPP (Laser-Induced Pressure Wave Propagation) and PEA (Pulsed electro-acoustic) methods.

Compared with destructive methods, non-destructive methods have the substantial advantage of preventing the space charge distribution from being affected by sample preparation [10].

Among these non-destructive methods, the pulsed electroacoustic (PEA) method (also known as electrically stimulated acoustic wave (ESAW) method) has gained in popularity due to the apparatus simplicity and low-cost. For the last three decades, the PEA method has been applied to measure the accumulation of space charge in thin film samples, thick plate samples and recently the technique has been applied to coaxial cable samples. [11-15]

1.3 Gap in knowledge when applying PEA measurements on cables

The PEA technique is based on inducing a change in mechanical force on charges within the insulating material by the application of a pulsed electric field. The change in force induced on the charges gives rise to the generation of acoustic waves which propagate as longitudinal pressure waves that pass through an earthed metal electrode to a piezo-electric sensor. The electrical signal from the sensor contains the information of net charge density within the insulator and from this the space charge distribution is recreated using signal processing techniques [11, 16-18]. For measuring thin film samples, that have a parallel plane geometry, in which the applied electric field is uniform, the PEA method is sufficiently mature such that few controversial assumptions exist for interpreting the system output. However, adapting the technique to cylindrical geometry cable insulation involves a thorough understanding of the PEA technique and a reassessment of the basic assumptions that underpin the interpretation of the output signal. These are explored in more detail below.

1.3.1 Generation of pressure waves

The forces that are exerted on space charge depend on the magnitude of the pulsed field applied. However, this will be a function of radius within the cable owing to the cylindrical electrode geometry. In thin film PEA systems, the only source term for the formation of the pressure waves is the net space charge. However, in the case of the cylindrical cable geometry, additional components of pressure waves generated include those generated due to the induced bulk polarisation charge and electrostriction. The effect of these additional pressure wave source terms need to be taken into account. To date, this has not been addressed in the literature except in a number of theoretical articles where these additional pressure wave sources have been proposed from the underlying physics [19, 20].

1.3.2 Propagation of the acoustic pressure waves

Unlike the plane wavefront longitudinal waves generated and propagated in plane-plane samples, the cylindrical wave-front acoustic waves propagating in the radial direction in cylindrical cable insulation spread out in space. Consequently, a correction needs to be made for the reduction in their amplitudes during the propagation.

When applying the PEA method to thick plate and cylindrical samples, the pressure waves would encounter acoustic attenuation and dispersion within the insulation material. Although signal processing methods to reconstructing the original acoustic wave have been proposed [18], it is difficult in practice to determine the acoustic attenuation and dispersion coefficients from the PEA output data. The technique relies on comparing the PEA output peaks from the two electrode-insulator interfaces in the frequency domain to establish a transfer function that is then used to correct the data. However, the technique is prone to high frequency instability and assumes that the PEA signal was derived from a sample in which no space charge is present and that the signal is not distorted for other reasons, such as imperfections in the real cable that may not be purely cylindrical. Rather than incurring potential numerical errors by compromised acoustic compensation methods like [17, 21], some authors [15, 18, 22, 23] made the compromise of assuming the acoustic dispersion is negligible when the sample thickness is not great.

1.3.3 Geometry of PEA base electrode

Applying the PEA method to coaxial cables not only increases the complexity of the signal processing on the basis of the difficulties with thick samples, but also requires the modification of the system hardware. Two basic approaches have been adopted in the literature. These employ either a flat base electrode to couple the acoustic pressure waves into the PEA apparatus or a cylindrically cut surface that matches the outer dimension of the cable. The idea behind using a flat electrode is to produce a 'line' contact between the cylindrical cable surface and the base electrode of the PEA apparatus. As the acoustic wave reflects back from the surrounding cable-air boundaries, only the line contact between the cable and the electrode allows the acoustic signal to pass through and onward to the piezoelectric sensor. The PEA output signal therefore represents the space charge information on the slice of the insulation that is in the radial direction and perpendicular to the flat electrode surface. This approach has the advantage in that it is not necessary to machine a special base electrode that matches the outer dimension of the cable.

However, there is no work in literature comparing the two techniques or querying the applicability of the assumption of a line contact and the feasibility of using a flat electrode. To achieve a good acoustic contact between the cable and the electrode, a reasonably high clamping force would normally be required. Under the clamping force, the cable will deform against the flat electrode especially at high temperatures. The deformation will disturb the cylindrical geometry of the insulation and consequently affect the electric field distribution. Moreover, the increased contact area of a deformed cable may not satisfy the primary assumption of a line contact.

1.3.4 PEA calibration and cable charging

In order to calibrate the PEA instrument, it is usual to take preliminary measurements under low applied voltages to avoid the accumulation of space charge. However, due to the employment of a cylindrical geometry, space charge may accumulate (called 'cable charging' in this work) owing to the non-linear dependence of electrical conductivity with electric field [2, 24-26]. For a typical cable geometry, the electric field will be higher by a factor of approximately 2 near the inner conductor-insulator interface compared with the field at the outer conductor-insulator interface. The local electrical conductivity of the insulation will therefore take on a non-uniform radial distribution and this will give rise to space charge accumulation. The effect of this accumulation is to reduce the gradient of electric field in the radial direction and will change the ratio of the PEA output peaks from the conductor-insulator interfaces from that expected when no space charge is present. In the literature, this effect is either ignored [15, 18, 22, 23] where the calibration assumes no accumulation of space charge or the steady-state cable charging of the cable has occurred [27]. In the latter case, an empirical formula is employed assuming that there is a power law dependence of the electrical conductivity with electric field. Very little work has appeared in the literature regarding the existence or otherwise of cable charging and how it impacts on the calibration of the PEA instrument.

1.4 Objectives of the work

The usual approach to the interpretation of PEA signals for the reconstruction of the space charge profiles in cable geometry systems is to work backwards from the PEA raw data. The usual steps are to perform deconvolution to remove instrumental imperfections, radial correction for cylindrical longitudinal pressure wave propagation in the cable followed by attenuation/dispersion correction and finally calibration. These techniques are not without their problems as discussed above. In this thesis an alternative approach to the interpretation of PEA data is proposed by reversing the processes above. This will involve:

- Development of a simulation model for charge transport and accumulation in cable insulation.
- Development of a simulation model for pressure wave generation by space charge based on the current understanding of the underlying physics of forces on charges in dielectrics.
- Development of a simulation model for acoustic pressure wave propagation in the cable and the coupling of the waves to the PEA instrument. To include the two different PEA base electrode geometries and the possibility of acoustic attenuation.
- Development of a simulation model for the piezo-electric sensor and subsequent amplification.

- Bringing the above simulations together to form an integrated simulation model that encompasses all the processes from charge accumulation, the measurement technique and detection so that simulation outputs can be compared with experimentally derived raw data.
- Verifying the above simulations and providing raw PEA output data for interpretation. The system should be able to perform reliable and reproducible space charge measurement on mini-cables at a temperature range of 25 °C – 70 °C and should be manufactured to have interchangeable base plates (flat and curved) and adjustable cable clamping force for comparison with experiments.

1.5 Thesis overview

Chapter 2 covers the background knowledge and literature reviews for HVDC cable, space charge formation, the principle of PEA measurement and features on measuring cable geometry samples.

The PEA apparatus for mini-cables designed and constructed for this project featuring the ability of high temperature test, cable clamping unit, changeable base electrode and interchangeable buffer amplifiers is introduced in Chapter 3. In addition to the hardware, as an equally essential part, the signal processing and calibration approaches are reviewed.

To pursue an alternative way for the interpretation of PEA outputs subjected to cable geometry samples, simulation tools are developed in Chapter 4. The one-dimensional models which together represent the whole process from charge formation to PEA system output consist of the unipolar charge transport model, PEA acoustic model for signal formation and propagation and a Pspice based sensor model. Moreover, the PEA acoustic model is further upgraded to two-dimensional with an additional COMSOL based mechanical model to study the effect of cable deformation with a flat base electrode on PEA output.

Chapter 5 compares the performance of two types of electrode, flat and curved, proposed for cable PEA measurements in both the simulation and experiments.

Chapter 6 describes cable charging phenomena with a novel method based on monitoring the electrode charge peak ratio as proposed in this work for monitoring the charging transient. Two empirical transport models and one hopping theory based conductivity model are studied by matching the experimental results under different field and temperature conditions.

In Chapter 7, the applications of the simulation tools and the bespoke mini-cable PEA system are demonstrated. Specifically, the effect of the cable defects of non-concentricity and an acoustic mismatch between the insulation and semicon layers are analysed. In Section 7.3, space charging measurements are performed on a mini-cable which was found to have a morphological contrast difference as observed visually on cut cross-sections of the cable and probably due to incomplete degassing of the cable insulation. Simulation models are used to mimic the experimental results with the hypothesis of nonlinear conductivity.

Chapter 8 gives the overall discussion of the work.

Chapter 9 contains the conclusions of the thesis with suggested further work.

2 BACKGROUND AND LITERATURE REVIEW

In this chapter, background information will be given on high voltage DC cables, their construction, usage and the current state of knowledge regarding the investigation of cable reliability through space charge measurements. The materials employed and the processes that lead to electrical conduction and space charge accumulation will also be introduced.

2.1 HVDC cable technology

2.1.1 Different types of HVDC cables

All manufactured HVDC cables have a similar structure with the main difference being the insulation materials. The basic structure of HVDC cables is illustrated in Figure 2-1. The conductor is metallic strands made of copper (or aluminium for reducing weight). A layer of semicon compound called the conductor screen or often referred to as the inner semicon layer, which is usually made of the same base compound of insulation but loaded with carbon particles, surrounds the inner conductor to produce a uniform electric interface between the conductor and the primary insulation. The relatively high electrical conductivity of the semicon material ensures a homogeneous electrical contact and avoids any air-gaps that may otherwise exist between the central conductor and insulator. The primary insulation protects the cable from electrical breakdown. A second semicon layer often referred to as the outer semicon layer surrounds the primary insulation layer and acts as an insulation screen to produce a homogeneous electrical contact between the insulation and the metallic sheath. Again this prevents air gaps being formed at the electrical contact between the insulation material and the outer sheath. The semicon layers therefore suppress the possibility of electrical discharges occurring in air gaps which would eventually cause electrical failure of the insulating material. The semicon layers are therefore fundamental to the reliability of electrical cables and protect the insulation layer. Consequently, the semicon layers enable the insulation layer to withstand the rated voltage of the cable. Additional components like reinforcement of steel tapes, bedding, and armour of steel wires may be included subject to the application of cable, for example submarine cables. [28-31]

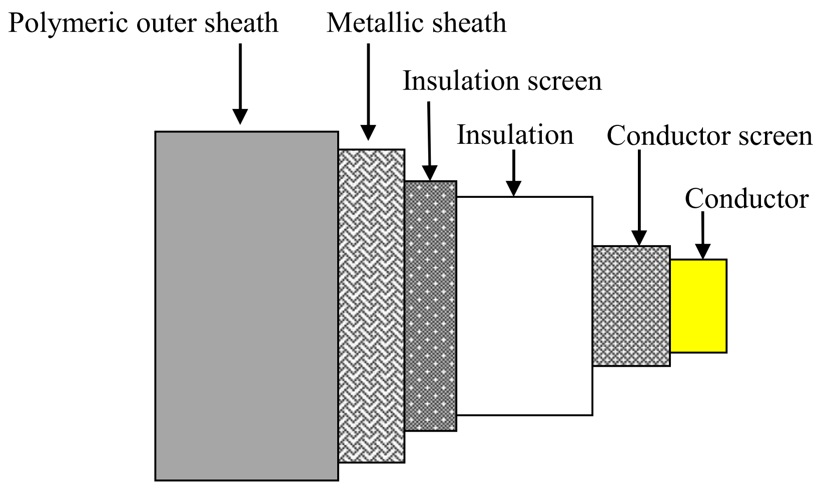

Figure 2-1. Schematic drawing of the common design of high voltage cables.

So far, the most widely used types of HVDC cable technology for existing underground and undersea cable transmission systems have been paper-oil insulated cables which include [28]:

- Mass impregnated Nondraining (MIND)
- Self-contained oil filled (SCOF)
- High-pressure oil filled (HPOF)

Although the oil-paper insulated cables are of more established experience, they are not without problems [32]: normally the operating temperature and thus the power capacity are limited by the maximum allowable temperature of paper-oil insulation; the installation lengths of SCOF, HPOF and oil-paper insulated cables are limited by the requirement on oil/gas pressure which also increases the complexity and cost of installation and maintenance; moreover, the potential environmental impact associated with oil leaks is also a major consideration.

Due to the above disadvantages of paper-oil insulated cables, considerable attention has been paid to developing highly reliable polymer based extruded HVDC cables. Compared to the oil-paper insulation cables, the extruded HVDC cables have the following advantages: Higher conductor temperatures and thus a more compact design (for the same power rating); no limitation on the length; lighter weight due to the lighter moisture barriers; easier cable joining; no environmental hazards. [33]

2.1.2 PE based insulation

The insulation materials for extruded cables are highly pure polymeric materials, mainly polyethylene (PE) based polymers. Additional additives such as antioxidants and cross linking agents are used for improving their thermal or electrical properties. PE is a polymer of ethylene whose molecular structure is shown in Figure 2-2.

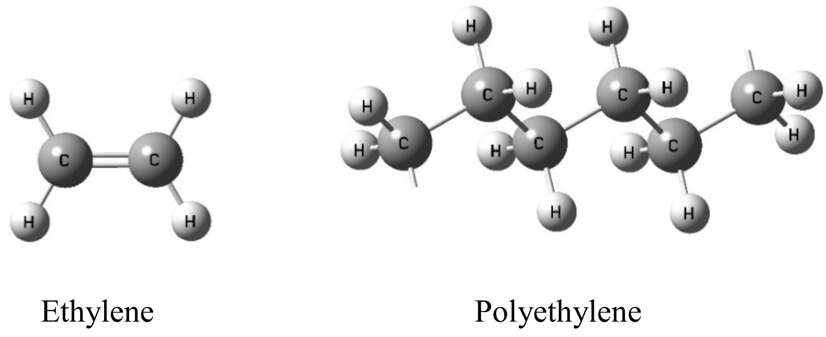

Figure 2-2. Molecular structures of ethylene and polyethylene

Depending on the pressure and temperature applied during the polymerisation of ethylene, the structure of PE is distinct [34]. At low pressure of a few atmospheres and about 100 °C, the produced PE molecules have long linear polymer chains with few side branches enabling them to fold on themselves and form crystals. A material with high crystallinity of 70-80% and a density of 0.94-0.98 g/cm^3 is produced and therefore named as high density PE (HDPE). On the contrary, at high pressure of about 150-300 atmospheres and around 200 °C, the product named as low density PE (LDPE) has linear chains with short chain side branches. The side branches prevent crystallisation (folding of the polymer chains) and thus a low crystallinity of 45-55% results. The density of LDPE is normally around 0.91-0.923 g/cm^3.

The crystallinity affects both the mechanical and electrical characteristics [35] of the PE based insulation. In particular, the space charge behaviour is found to differ between the LDPE and HDPE [36-39]. The amorphous phase is more electrically conductive than the crystalline part, and has the potential to generate and trap charge carriers [40].

The amorphous polymeric material between the crystalline regions of PEs (LDPE and HDPE) will melt at increased temperatures and consequently degrade the insulation properties. Therefore the maximum operating temperature of PE is normally restricted to below 70 °C for LDPE and 80 °C for HDPE. [41]

To improve the thermal properties of thermoplastic PEs and therefore increase the maximum operating temperature, the polymer is cross-linked to produce cross-linked PE (XLPE). XLPE insulating materials have been developed since the 1950s [41]. The crosslinking is firstly achieved chemically by using peroxide as the cross-linking agent under a high temperature and pressure. The XLPE possesses the raised continuous working temperature of 90 °C and the higher short circuit temperature of 250 °C compared to 150 °C for LDPE [29].

As indicated by the name, extruded HV cables are made via the extrusion process. Currently the widespread extrusion technique employed for the reliable manufacture of XLPE cables is the triple extrusion process where the inner semi-conductive layer (conductor screen), insulation and the outer semi-conductive layer (insulation screen) are formed in a single operation [42-44].

2.2 Space charge formation

Owing to the success of the triple extrusion process to form homogeneous electrical interfaces between the cable conductors and the insulating material, cable faults due to electrical discharges in air gaps at the central conductor and the at the outer sheath have largely been eliminated. The application of extruded cables for reliable HVDC transmission is mainly restricted by the formation and accumulation of space charge, overall or locally, within the cable insulation during service [4, 45]. Space charge has been implicated as a major factor in failure mechanisms either directly (space charge accumulation induced electric field magnification) or indirectly (space charge controlled failure mechanisms) [46] . The premature failure of cables for HVDC can occur during service and especially during polarity reversal as a consequence of space charge formation [4, 33, 47].

As mentioned before (Chapter 1), the presence of space charge can be explained as an unbalance of charge injection and extraction in a localized domain within the cable insulation. Non-homogeneous properties which result from either the semi-crystalline properties induced during the extrusion process or service conditions of the cable, for example a temperature gradient, would also contribute to this unbalance [48]. In a perfect insulator, intrinsic free charges are rare; it is therefore necessary to identify the origin of charges [25].

2.2.1 Energy band theory for polymers

The energy band theory for semiconductors has been expounded in order to understand the electronic properties of the covalently-bonded crystal materials. It may also be able to describe the electron energies found in polymers. Based on the conventional energy band theory, a large band gap is assumed to exist for an insulator (at least the crystalline part of a polymer) which alone is less likely to provide enough free electrons or holes for the conduction by thermal excitation of valence electrons across the band gap. However, polymer DC insulation materials have complex structures. For example, the simplest form of PE, LDPE, contains a crystalline part surrounded by an amorphous phase, additives and residual by-products of the cross-linking reactions. The structural disorder of polymer chains and chemical inhomogeneity (induced by the additives and residuals) change the band gap (spatially and temporally) and bring in localised states instead of an extended conduction band which are also called trap centres. With respect to the origin of the traps, they can be further classified into two categories: 1) physical traps which are shallow trapping centres due to chain bends and entanglements and 2) chemical traps which are formed due to the presence of impurity atoms or molecules which have deeper energy levels. The presence of traps for electrons and holes and the thermally activated hopping and tunnelling of charge carriers between traps provide the transport mechanisms for electrons and holes, in amorphous polymeric materials.[25]

2.2.2 Charge generation

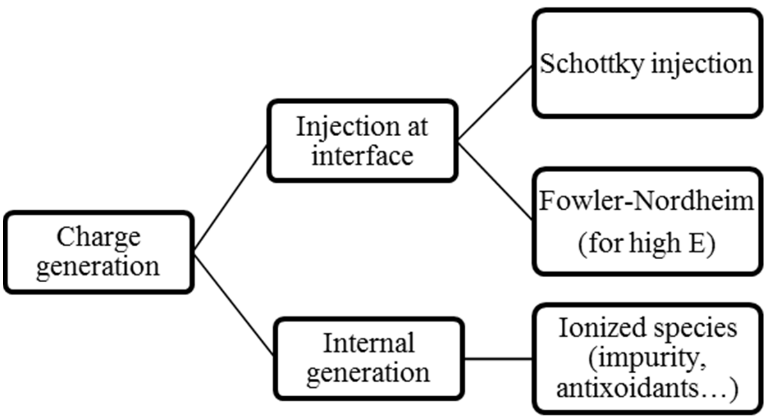

Figure 2-3. Charge generation mechanisms.

Generally, the source of space charge can be separated into two categories as illustrated in Figure 2-3: injected charges from electrodes and internally generated charges due to the field assisted drift of ionised impurities [49].

Schottky injection theory [50] can be used to describe the charge injection process at the metal/dielectric interface where electrons of sufficient thermal energy enter the conduction band of the insulation by overcoming a field-reduced potential barrier. At very high electric fields, above 100 kV/mm, Fowler-Nordheim injection due to the tunnelling through the narrow potential barrier should be adopted. [25]

However, at low applied electric fields, the exchange of charges across the electrode/insulator interface is usually considered Ohmic [51, 52] as contact charge is usually exchanged at interfaces between different materials.

2.2.3 Bulk charge transport

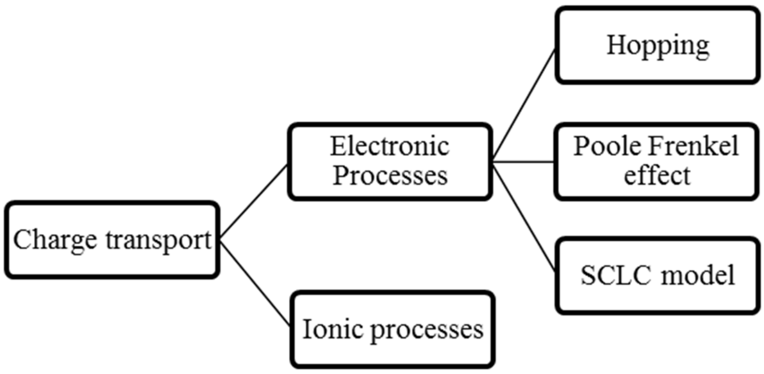

Figure 2-4. Charge transport mechanisms.

Charge transport mechanisms can be separated into electronic processes and ionic processes as summarised in Figure 2-4. Furthermore, electronic processes can be interpreted by: Hopping, Poole Frenkel effect and space charge limited current (SCLC) models [25, 53-55].

The hopping process describes electrons that move from one trapping site to adjacent trap sites by overcoming a potential barrier due to thermal energy or tunnelling through it if the applied electrical field is sufficiently high [56]; The Poole-Frenkel effect which involves hopping transport [57] can be treated as a bulk-version of Schottky injection.

The SCLC model relates the mobility of carriers to the density of available trap states. As for ionic processes, ionic conduction is due to the drift of ions in an applied electric field and will have a mobility that depends on the molecular mass (size, shape) of the molecular ion and the nature of the polymeric host material [58].

2.2.4 Heterocharge and homocharge

The two words, 'homocharge' and 'heterocharge', have been frequently used when describing space charge accumulation adjacent to the electrode/insulator interfaces. The homocharge / heterocharge represents the accumulated space charge having the same / opposite polarity with the adjacent electrode. Apart from the convenience, the necessities for emphasizing the polarity of accumulated charges with respect to the neighbouring electrode may be:

- Firstly, the polarities of the accumulated charge relate to either the reduction or enhancement of the interfacial electrical field. To be more specific, the formation of homocharge reduces the electrical field across the interface while heterocharge does the opposite.
- Secondly, the formation of homocharge or heterocharge may suggest different dominating mechanisms. The net charge distribution is the result of the competition between all the charge related processes including the charge generating and transport mechanisms. For example, the formation of the homocharge may be caused by charge injection from the electrode into the insulator dominating over charge transport in the bulk material. Heterocharge accumulation, on the other hand, may be caused by charge transport within the bulk of the insulator dominating over charge injection at the electrodes. Moreover, experimental work [59, 60] has demonstrated that homocharge is normally observed in cross-linked polymers, probably as a result of injected charges being trapped by carbonyl groups, whereas residual cross-linking by-products (such as acetophenone) contribute to the formation of heterocharge.

2.3 Electrical field in HVDC cables

Unlike the well-known capacitive electric field distribution that is set up in an HVAC cable insulation, the distribution of the electrical field in the HVDC cable insulation is more complicated as the DC electric field is both time and temperature dependent, which is, in turn, due to the field and temperature dependent electrical conductivity of the polymeric insulation. [61-63]

To be more specific, the AC electric field is determined by the electrical permittivity which is less insensitive to temperature and electric field change. If the permittivity of a homogeneous insulation is a constant and has negligible change over the operating temperature of the HV cable, then the electric field distribution, $E_{AC}(r)$, as a function of radius, r, inside the cable insulation under the applied voltage U_0 (phase to ground) can be expressed as [34]:

$$E_{AC}(r) = \frac{U_0}{r \ln \frac{b}{a}} \tag{2.1}$$

where a and b are the inner and outer radius of the insulation layer.

The DC electric field is however governed by the distribution of electrical conductivity of the insulation material. Unlike the permittivity that has an almost constant value, the conductivity of commonly used DC insulation materials is strongly related to the temperature (primary) and electric field (secondary) [2, 24, 25, 61, 64].

Under loading conditions, the inner conductor of the HVDC cable will normally be of a higher temperature due to Joule heating. This may result in a temperature gradient along the radius of the insulation as the outer temperature of the cable will be determined by a usually lower ambient temperature. The presence of a temperature gradient will modify the conductivity distribution inside the cable insulation and may in some circumstance lead to a ‘field inversion’ [8] where the electrical stress at the outer radius becomes higher than that at the inner radius. Even under isothermal conditions, the conductivity may still be non-uniform across the thickness of the cable insulation as the electric field is divergent owing to the cylindrical geometry and if the electrical conductivity is field dependent.

The dependence of the insulation conductivity on the temperature and electric field can therefore result in the formation of space charge which in turn modifies the electric field within the insulation. It is therefore essential when studying space charge accumulation to have representative electro-thermal models for electrical conduction in the cable insulation.

2.4 Electrical conductivity models

Electrical conduction in polymers is in general non-ohmic, which means the conductivity is not a linear function of the electric field. A number of functional relationships between the electrical conductivity as a function of electric field and temperature have been proposed in the literature. The DC electrical field within cable insulation is normally derived from the functional relationships of the conductivity, $\sigma(E,T)$, which is both temperature, T, and electric field, E, dependent. Therefore the knowledge of DC conductivity and its dependence on temperature and field are fundamental to the HVDC cable design as they take into account the space charge accumulation. Three of the most common models describing the conductivity of DC insulating polymers are given below. Two of the models are empirical in origin whilst the third model is based on a hopping model for electrical conduction.

- Model 1 – Empirical power law field relationship [2, 26]:

In this model, the electrical conductivity takes an empirical power law form for the electric field and the exponential temperature dependence.

$$\sigma(E,T) = \sigma_0 e^{\alpha(T-T_0)} (\frac{E}{E_0})^{C_m} \qquad (2.2)$$

where σ_0 is the reference conductivity at the temperature T_0 and applied electrical field E_0; α is the temperature coefficient and C_m is the power law index for the electric field dependence. Here T has units of Celsius and hence the first term does not represent a thermal activated process unless temperature in Kelvin are employed and T_0 is absolute zero temperature.

- Model 2 – Empirical exponential field relationship [2]:

$$\sigma(E,T) = \sigma_0 e^{\alpha T+\beta E} \tag{2.3}$$

In this model, the conductivity is given by an empirical function which possesses not only an exponential field but also exponential temperature dependence. The parameter, α, is the temperature coefficient and the parameter β is called the stress coefficient. The parameter σ_0 represents the conductivity at a standard voltage and temperature. The possibility of using the above relationship to describe the conductivity of extruded polymeric insulation was studied in [61]. For XLPE, a consistent temperature coefficient of 0.11 /℃ for α was obtained. In order to use this model to describe a thermal activated process with an activation energy related to the value of α, then temperature in Kelvin should be used. The temperature term $e^{(\alpha T)}$ appears to be an approximation adopted for computational convenience in the early days of DC cable design [24].The stress coefficient β was however found to be unpredictable as it varies with temperature. For XLPE extruded cable insulation with carbon loaded screens, the value of 0.24-0.55 mm/kV for β may be reasonable [61].

- Model 3 – Hyperbolic sine field relationship [24, 25]:

$$\sigma(E,T) = Ae^{-\frac{\varphi\cdot q}{k_B T}} \frac{sinh(B|E|)}{|E|} \tag{2.4}$$

where A and B are constants; φ is the thermal activation energy in eV; T is temperature in Kelvin, k_B is Boltzmann’s constant and q is the charge on an electron. This model is based on a hopping model for charges in traps of a fixed energy depth. Therefore it has been regarded as a well-established theoretical model and not an empirical model in the literature.

Model 1 is similar to Model 2 with the field dependence changed to follow a power law. Model 1 yields analytical equations for the steady state electric field distribution in a cylindrical geometry appropriate for HVDC cables under a DC applied voltage of U [65, 66]:

$$E(r) = \frac{kr^{k-1}U}{b^k - a^k} \tag{2.5}$$

where

$$k = \frac{C_m + C_T}{C_m + 1} \tag{2.6}$$

where C_m and C_r are material and temperature associated dimensionless constants. C_m is approximately 2.1-2.4 for PE, and C_T is 0 when the cable is under isothermal conditions.

The conductivity describes the overall behaviour of charge transport processes. Considering the complexity of accessing the macroscopic transport phenomena of various charge carriers, these conductivity models may provide an easy way to model the space charge formation.

2.5 Mini-cables

Space charge measurement on commercial HVDC cables may be beyond the ability of laboratory-based experiments due to the high cost of equipment and the considerable amount of laboratory space required for the required voltage rating. Instead, the common test samples used in the laboratory are either plane-plane samples (usually laboratory-made using a heated press) or mini-cables (cables usually provided by the manufacturer and made using the extrusion process).

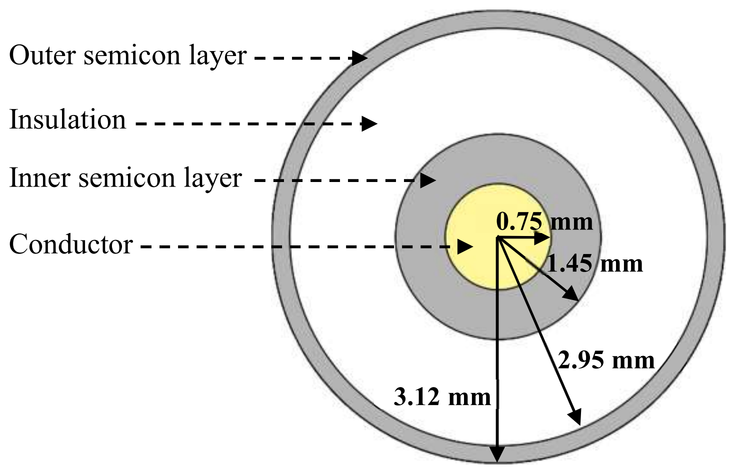

Figure 2-5. Structure of a mini-cable; Dimensions are for the mini-cables used in this project.

The so called mini-cables are small-size models of the normal power cables. Like the full size cable, mini-cables are composed of a solid copper or aluminium conductor (with a diameter of 1-2 mm), extruded XLPE insulation (with thickness of 1-2 mm), and inner and outer semicon layers as shown in Figure 2-5 . The dimensions shown are consistent with those provided in this work. Mini-cables have proved to be convenient models for the study of space charge phenomena on real-size DC cables [67] in a laboratory environment and they have advantages over film (or plane) samples due to the following aspects:

1. Mini-cables are more representative of commercial full-size cables than plane film samples in terms of their morphological characteristics, because they benefit from a similar extrusion process employed in their manufacture. The underlying crystalline morphology of films manufactured by hot pressing or injection moulding may be distinct from that of cable insulation.
2. Normally, film samples are manufactured without the semicon layers. However the semicon/insulator interfaces are critical for power cables as they affect charge injection and therefore affect the resultant space charge phenomena.
3. Film samples are unable to simulate the non-uniform electrical field in cylindrical insulators.
4. Crosslink by-products and impurities have significant effects on the dielectric characteristics of XLPE. Film samples are less likely to represent the concentration and distribution of by-products and impurities that result from the extrusion process.

2.6 The PEA space charge measurement technique

The general idea of the PEA method is to detect the acoustic waves generated by the displacements of space charge when the space charge is subjected to an applied pulsed electric field. From the magnitude and time delay of the generated acoustic waves as they propagate through the system, the magnitude and location of the net charge in the insulator material can be inferred. [68]

2.6.1 Principle of the PEA method

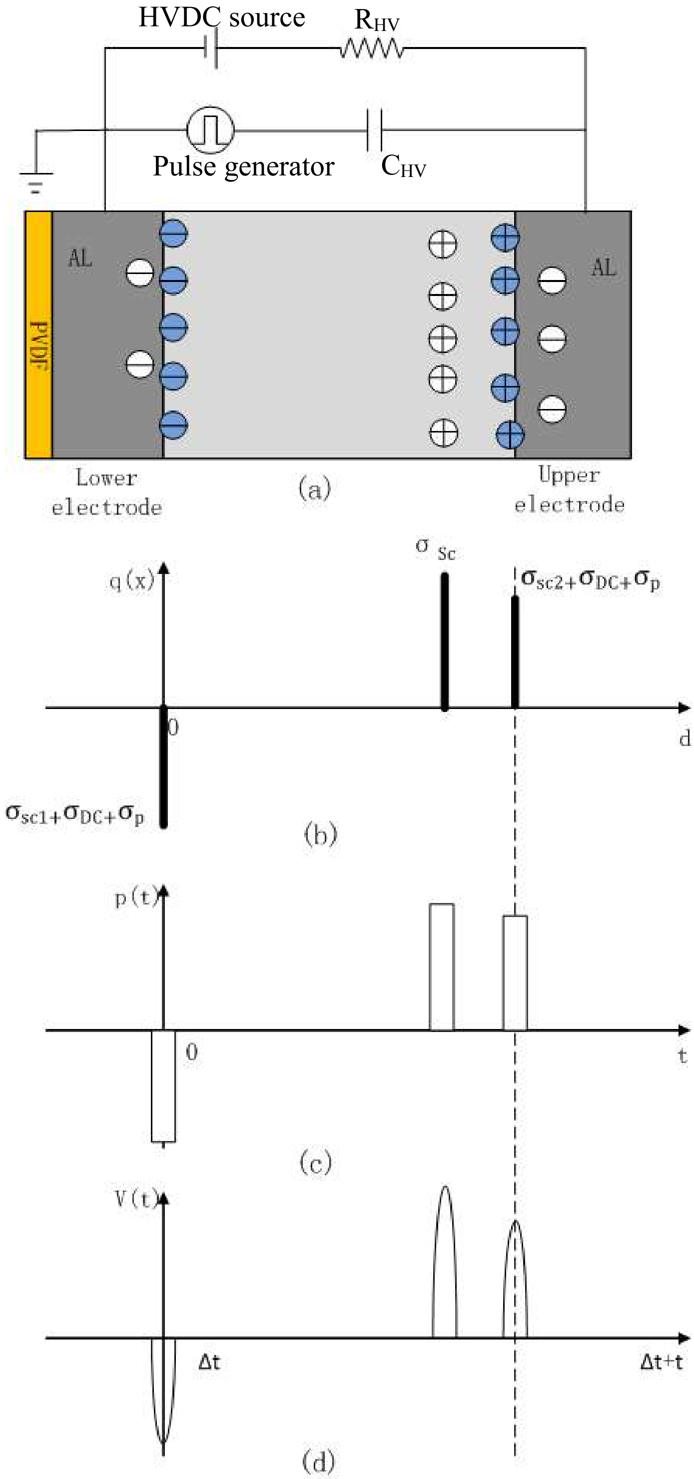

Figure 2-6. Principle of the PEA method (adapted from [68]). (a) Schematic representation of the PEA space charge measurement system for film samples; (b) Charge distribution: σ_{sc1} and σ_{sc2} are the internal space charges σ_{sc} induced charge density on cathode and anode interfaces respectively, σ_{DC} and σ_p are surface charges induced by DC voltage and pulsed voltage respectively; (c) Acoustic pressure waves whose polarity indicates a rarefaction or compression wave; (d) Voltage induced across PVDF acoustic sensor, Δt indicates the time of the acoustic wave travelling through the lower electrode.

A classic setup of the PEA method is shown in Figure 2-6 (a). A flat or thin film sample is sandwiched between two aluminium electrodes. A high voltage is applied across the sample to set up an electric field inside the material. A pulse generator having amplitude of around one-tenth of the applied DC voltage is used to induce a pulsed electric field that is superimposed on the applied DC field. The HVDC source and pulse generator are coupled to the electrode via a high value resistor R_{HV} (to prevent loading of voltage pulse by the DC source) and a capacitor C_{HV} (for isolating the pulse generator from the HVDC).

Under the high applied DC bias voltage, capacitive charges are formed immediately on both electrodes due to the capacitive nature of the sample. The surface charges on each interface are labelled as σ_{DC}. Under a suitably high DC voltage, the internal field will be sufficiently high to cause space charges to accumulate in the sample bulk as in the example of the space charge σ_{sc} shown in Figure 2-6 (b). In the meantime, the formation of the space charge would induce surface charges σ_{sc1} and σ_{sc2} on the two interfaces. The sum of σ_{sc1} and σ_{sc2} should be equal to the σ_{sc}.

When a voltage pulse is applied, a transient electric field is formed in the insulator material. As the transient field is normally much smaller than (< 10%) of the DC field, the pulse induced surface charges σ_p are normally negligible. Under Coulomb force, $F = q \times E$ [69], the charges experience transient displacements and correspondingly produce acoustic waves, as shown in Figure 2-6 (c), which are assumed to have the same shape as the charge distribution in Figure 2-6 (b). In fact, the perturbation of the charge would generate two kinds of stress waves, the rarefaction and compression wave, which then propagate in opposite directions [49]. Only the wave propagating towards the bottom electrode (where the piezoelectric sensor is attached) is detected to produce the charge profile. For acoustic waves travelling towards the top electrode, part of them would reflect back from the free surface and the reflected wave travels towards the PVDF sensor. However, these reflected waves will be separated by the time delay caused by the additional acoustic path length. Whether the un-reflected waves travelling towards the lower electrode are rarefaction waves or compression waves depends on the polarity of the charge and the pulsed voltage. After travelling through the sample and the lower electrode, the acoustic waves finally reach the piezoelectric transducer. The piezoelectric sensor transforms the pressure signal into a voltage signal. The output signal, as a function of time, is then amplified and recorded by the oscilloscope as shown in Figure 2-6 (d). The magnitude of the voltage signal represents the net charge quantity and the time delay indicates the position of charge inside the insulator material. By analysing the voltage signal, the space charge profile can then be obtained.

2.6.2 Forces in the electrostatic field

As described above, the source of the PEA signal is the electric stimulated variation of the electrostatic force induced on charges in the material by the application of an applied pulsed electric field. The transient increment of the force density acts on the material and results in the generation of elastic waves, which after propagating through the insulator material and the PEA base plate (acting here as a waveguide for the acoustic waves), are converted to voltage signals by a piezoelectric sensor.

The force per unit volume that acts on a dielectric body is [70-72]:

$$\vec{f} = \rho \cdot \vec{E} - \frac{\varepsilon_0}{2} \cdot E^2 \cdot \nabla\varepsilon_r - \frac{\varepsilon_0}{2} \cdot \nabla(E^2 \cdot a) \tag{2.7}$$

where the arrows placed above certain parameters (*f* and E) indicate that these are vector quantities. ρ is the space charge density, ε_0 and ε_r are the vacuum permittivity and relative permittivity of the dielectric respectively, *a* is the electrostriction coefficient. The first term represents the Columbic force due to the applied electric field E. The second term exists whenever there is an inhomogeneous dielectric (regions of differing relative permittivity) in the insulator. The third term is the force due to electrostriction, which is due to a dimensional change of the dielectric when an electric field is present in the dielectric. [20]

As the PEA method was original proposed for measuring thin film samples, two assumptions are normally made in that the sample is homogenous and the applied electrical field is uniform across the plane-plane sample. Consequently only Columbic force is usually considered when interpreting the PEA signal [16, 18, 68, 73] and thus leads to the widely accepted conclusion that the raw PEA output is in proportion to the space charge density. However, when the PEA method is applied to cable geometry samples, the divergent field within the cable enhances the last two terms because they contain either spatial derivatives of the electric field or the square of the electric field as shown in Equation (2.7). Therefore systematic errors may be incurred if the last two terms are ignored when a highly divergent electric field is present as in the case of an HV cable.

2.6.3 PEA acoustic signal

In the brief description of the PEA principle (Section 2.6.1), a perfectly elastic loss-less sample was assumed. Then the acoustic pressure wave would maintain the same amplitude and shape as it propagates through the insulation. Although the pressure waves may be generated at different locations within the sample and therefore have different acoustic path lengths in the sample, the amplitude and shape of the waves will be preserved. Based on this assumption, the area of the detected acoustic signal can be regarded as proportional to the electrostatic force generated inside the sample. This is also the case for the pressure waves generated by the charges at the material/electrode interface if the Columbic force is the only source of pressure waves. However, if the acoustic waves propagate through a non-ideal material, as is likely in most polymeric materials used for DC insulation [27], the propagating pressure waves are subject to absorption and dispersion, leading to signal broadening and attenuation. The degree of attenuation and broadening of the pressure waves will depend on the acoustic path length in the material. Accordingly, the detected PEA output signal will also change as a function of the transmission length. For the quantitative study of space charge, the effect of the acoustic attenuation and dispersion therefore needs to be considered. The influence of the acoustic attenuation and dispersion on the PEA measurement will be briefly illustrated below.

Since the PEA technique is a 1D measurement, the wave equation for a time-harmonic plane wave in a lossy homogeneous media can be expressed as [18]:

$$p(t,z) = Pe^{-\alpha z}e^{j(\omega t-\beta z)} \tag{2.8}$$

where P is the amplitude of the pressure wave p(t) at the generation point, z=0, and where α and β are the frequency dependent attenuation and dispersion coefficients respectively. With the assumed coefficients (attenuation dominated) as shown in Figure 2-7, an example of the pressure wave propagation is shown in Figure 2-8. This example simulated a Gaussian wave travelling through a 1.5 mm polymeric plate. The graph of the normalised pressure wave (Figure 2-8 (b)), where the pressure wave is time shifted to centralise all the peaks at the centre of the graph, clearly shows the broadening and attenuation of the acoustic wave at different positions during its propagation.

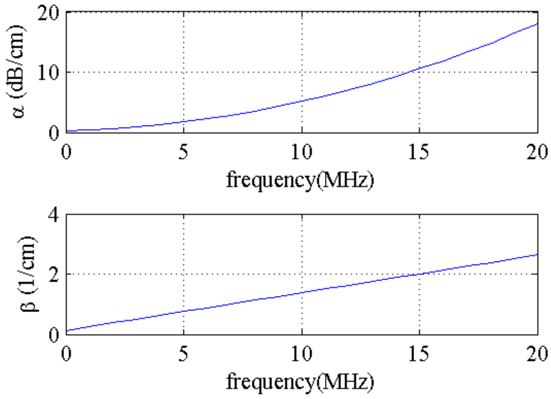

Figure 2-7. Assumed attenuation and dispersion spectrums for the demonstration of wave propagation.

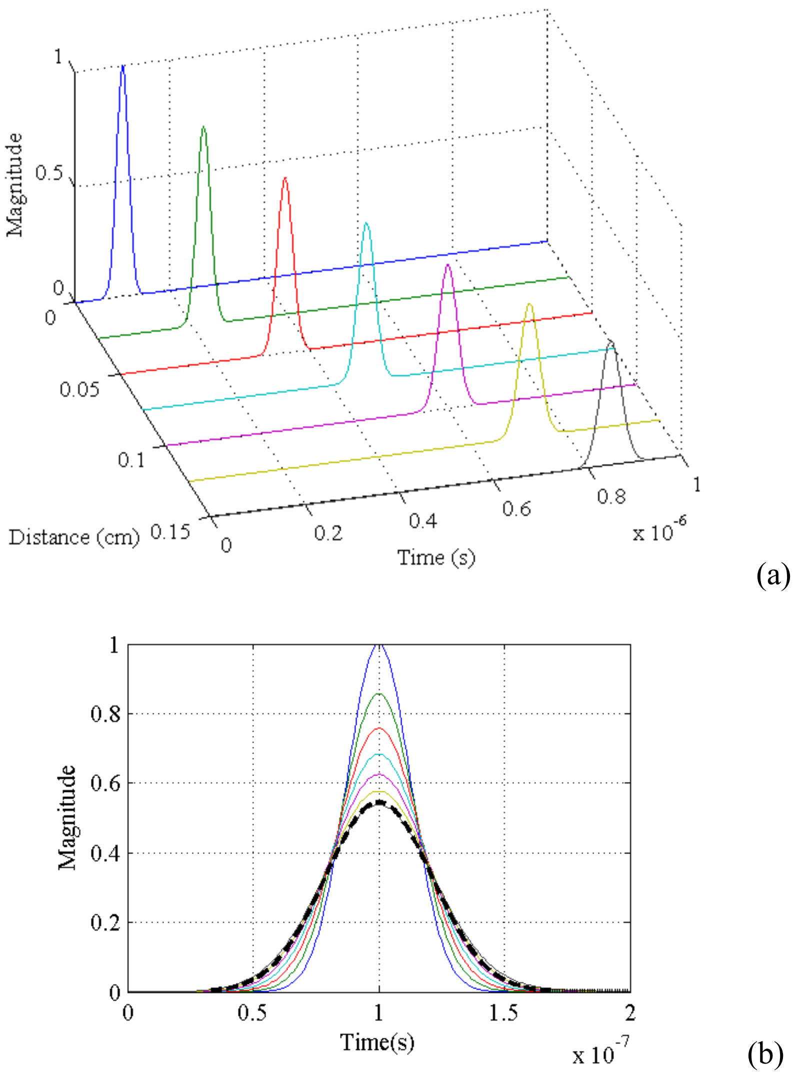

Figure 2-8. (a) Propagation of acoustic wave in an acoustically lossy medium. (b) Normalised (centralise to the peaks) waves of various positions.

A typical initial measurement of a 1.5 mm thick flat sample made from an acoustically attenuating and dispersive insulator in which no space charge is present is shown in Figure 2-9. The two peaks represent the electrode charges at two interfaces where the charge density should be identical due to a uniform electrical field in the plane-plane geometry. However, the acoustic signal generated at the upper interface will travel through the thickness of the sample and therefore be attenuated and dispersed compared to the signal generated at the sample – electrode (lower interface) as shown in the figure.

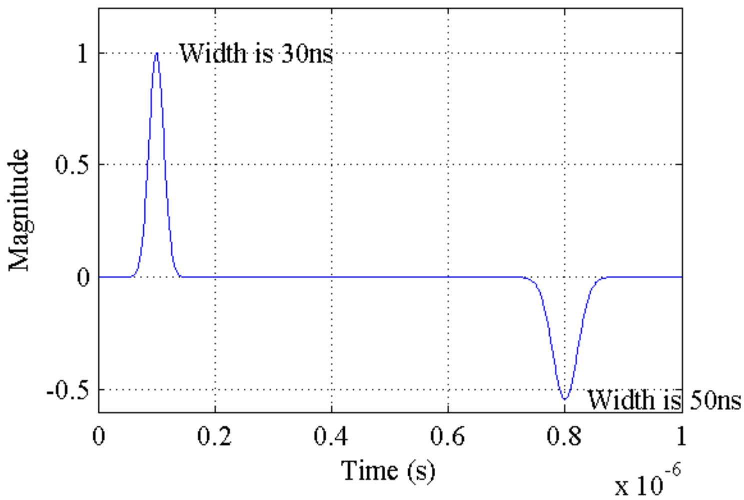

Figure 2-9. Example of the PEA output for a 1.5 mm plant (polymeric) sample. The second peak is attenuated during propagation. Width is the full width at half maximum.

As it is the peak area that represents the space charge density, the maximum signal reduction is about 5% for the wave propagating through the entire 1.5 mm thick sample as shown in the example in Figure 2-10. Consequently even for materials exhibiting moderate attenuation and dispersion, this needs to be taken into account when being applied to cable geometry systems. This applies particularly to the interpretation of PEA signals from full size commercial cables where the insulation may be approximately 10 times the thickness of a typical mini-cable [1].

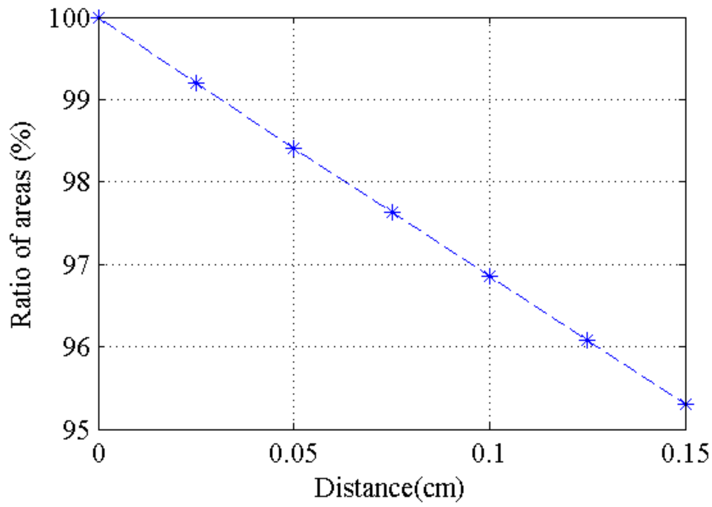

Figure 2-10. Peak area change during propagation.

Although the signal processing method used to reconstruct the original acoustic wave has been proposed in [18], it is difficult to determine the acoustic attenuation and dispersion coefficients [21]. The reconstruction technique is based on establishing a transfer function describing the attenuation and dispersion. However, identifying the values of the transfer function from the experimental PEA output assuming zero bulk space charge is difficult as the procedure can lead to numerical instability and oscillations in the recovered signal. Rather than incurring potential numerical errors by compromised acoustic compensation methods like [17, 21], some authors [15, 18, 22, 23] reached a compromise in assuming that the acoustic dispersion is negligible when the sample thickness is not great.

2.6.4 PEA method for cable geometry

The PEA method is an excepted technique that has been widely and successfully used in measuring the space charge distribution in both thick and thin plate samples [74, 75]. To apply the technique to cable geometry samples, it is necessary to take into account a number of factors that are usually not considered when the technique is applied to flat specimens. The question of 'whether the PEA method is capable for measuring space charge in cable insulation' leads to the question of 'what is different when measuring a flat sample and cable insulation'. Obviously one difference is that the cable insulation has a cylindrical geometry, which consequently results in a non-uniform applied electrical field [69]. Both the HVDC field and the applied pulse field decrease with increasing radius. This results in a non-uniform (radially dependent) force density as the source of the acoustic waves. In addition, the propagation of waves with a cylindrical wave-front causes the intensity of the pressure waves to decrease as they spread out in space during their propagation along the radial direction of the cable [76]. More specifically, the alterations of the PEA method for the cable are:

1. The DC electrical field applied to cylindrical geometry systems is non-uniform across the insulation and is a function of the radial position. (Section 2.3)
2. The divergent field may initialise the formation of space charge formation (as cable charging) due to the impact of a non-Ohmic electrical conductivity [77].
3. The magnitude of the applied pulsed electrical field is also non-uniform. It is a function of time and radial position in the cable insulation. The amplitude of the pressure wave for unit charge density (the Columbic force) will therefore be a function of radial position [27].
4. Columbic force may not be the only source of pressure waves in the insulating material due to a change in the electrostatic field. Electrostriction force may need to be considered in the divergent field [19].
5. The amplitude of the cylindrical pressure waves reduce during the propagation through the insulating material [76].

Although the space charge measurements on cable samples seem more complex than that on plane – plane samples, they offer unparalleled benefits for analysing the reliability of polymeric HVDC cables. The benefits of adapting the PEA space charge measurement technique to cable geometry samples are that space charge measurements can be taken without disturbing the electrical stress applied; the technique is non-destructive and allows the development of space charge accumulation to be investigated without disturbance or dissecting the cable and the impact of non-uniform field distribution can be experimentally assessed.

2.6.5 Acoustic radiation from cylinders

In order to study the impact of applying the PEA system to cylindrical cable geometry samples, it is necessary to understand the physics of acoustic wave propagation within a cylindrical geometry. In this work it is assumed that the media has elastic properties similar to a dielectric fluid. This follows the work of Holé [71] where it was pointed out that transverse pressure waves have velocities of propagation that are much less than for longitudinal pressure waves. Hence within the PEA apparatus, by employing a suitable length waveguide for the base electrode it is only necessary to consider the propagation of longitudinal waves. The coordinate independent wave equation for the propagation of longitudinal pressure waves in a homogeneous loss-less elastic media is:

$$\frac{1}{c^2}\frac{\partial^2 p}{\partial t^2} - \rho\nabla \cdot (\frac{1}{\rho}\nabla p) = 0 \tag{2.9}$$

where p is the pressure, ρ is the density and c is the speed of sound. If the density is a constant, then it can be expressed as:

$$\frac{1}{c^2}\frac{\partial^2 p}{\partial t^2} - \nabla^2 p = 0 \tag{2.10}$$

In cylindrical coordinates (where r is symbolizes radius), the solution to the above equation is [78]:

$$p = AH_0^{(1)}(kr) + BH_0^{(2)}(kr) \tag{2.11}$$

where the two Hankel functions represent the inward and outward propagating waves respectively having a propagation coefficient k. In Appendix A, it has been verified that the magnitude reduction of outgoing cylindrical waves fit with the approximation of the Hankel function for far field that follows the behaviour of $1/\sqrt{r}$ (which was used in [76]).

2.6.6 Cable PEA systems – state of art

The PEA measurement on the cylindrical cable was firstly attempted by Fukunaga [79] using a curved electrode matching the outer surface of the cable, a curved piezoelectric film and curved acoustic absorber. This design maintains the propagation of cylindrical acoustic waves, but in the meantime the application of a system (the PEA cell) is limited to cables of a specific dimension. Moreover, in practice, good acoustic contacts may be difficult to achieve between the outer surface of the cable, the electrode, the piezoelectric sensor and the backing acoustic absorber. To overcome these drawbacks, it was proposed to substitute the flat electrode and associated flat sensor and absorber for these curved parts as the works in [80, 81].

PEA systems, with the curved electrode, have been used commercially for measuring full-size HVDC XLPE cables as the works presented in [15, 82, 83] with the pulse coupling method for long cables proposed by [13]. However, due to the large space demand and high investment of experimental HV equipment, most laboratory based experiments (for example with the system in [84, 85]) are using model cables instead. For convenience, these PEA systems developed for measuring model cables are quoted as mini-cable PEA systems hereafter in the work. Compared with the work using a PEA system for plane-plane samples, the application of cable PEA systems makes up a smaller proportion. Some examples of the application of the cable PEA systems are briefly introduced below.

By using a Digital Signal Averager (the same approach in [86]), fast measurements on mini-cables are achieved in [87, 88] to observe the charge packets under DC stress. A few works [67, 89, 90] focus on the interface which may be present in the cable associates with considering the effect of temperature. However, in these works less information is given about the specific measurement system and the signal calibration process. To the author's knowledge, so far there has not been a universal protocol for the PEA system design specification and the signal processing methods. In fact, the PEA raw output obtained from measuring cables/mini-cables could largely depend on the features and characteristics of the measurement system and the therefore the signal calibration process may be different.

Currently in the literature, there are few mini-cable systems that perform in isothermal conditions. Some systems [84, 85] use induced current to heat the conductor and leave the outer surface to the ambient temperature to apply the temperature gradient. However, the temperature gradient may be very difficult to be accurately controlled in practice.

Moreover, to the author's knowledge, neither the effect of the clamping pressure on the PEA output response has been investigated nor a detailed comparison of the PEA base electrode, curved or flat, on PEA system performance has been reported in the literature.

3 DESIGN OF PEA SYSTEM FOR MINI-CABLES

3.1 Introduction

To measure the space charge behaviour in model polymeric DC cables (mini-cables), a measurement system based on the PEA method was developed and features the ability of high temperature measurements, adjustable cable clamping pressure and two base electrode configurations, flat and cylindrical. The main components of the system developed in this work will be introduced in detail in the following sections of this chapter with respect to the design requirements as discussed at the beginning (Section 3.2). At the end of this chapter, the traditional method of signal processing to reconstruct the space charge distribution from measured data and calibration of the PEA system are reviewed and demonstrated step by step using experimental data.

3.2 Design requirements of PEA system

Subject to the dimension of the model cables (mini-cables) provided for this project (as given in Chapter 2.5), the design requirements of the PEA method based space charge measurement system for model cables (quoted as mini-cable PEA system thereafter in this work) are listed in Table 3-1. The detailed descriptions of each requirement are given in the following subsections.

Table 3-1. Design requirements for the mini-cable PEA system.

E(kV/mm)	Temperature (°C)	Spatial resolution	Sensitivity (C/m^3)	Features
0 – ±30	20 – 70	5%×1.5 mm	0.1-0.5	Controllable Clamping force; Different shapes of base electrode.

3.2.1 Electrical stress

For the purpose of investigating the reliability of commercial HVDC polymeric cables, it is necessary that the experimental electric stresses are comparable to the real working conditions (10 kV/mm – 30 kV/mm). This is due to the fact that at different field/voltage levels the dominating mechanisms for space charge formation may vary, for example the charge injection models at the cable – electrode (semicon) interfaces are different as discussed in Chapter 2.2.2. As a consequence, the interested range of electrical field applied to the cable insulation is relatively low (up to ±30 kV/mm) in this work.

Experiments on the mini-cables under low electrical stresses not only allow the processes of space charge accumulation to be examined at the service stresses of commercial cables, but also make it possible to observe the cable charging phenomena as will be described in detail in Chapter 6.

3.2.2 Isothermal condition

As discussed in Chapter 2.4, temperature is an important concern for the reliability of polymeric HVDC cables as the conductivity of polymeric insulation is believed to be temperature dependent. Therefore, the mini-cable PEA system is required to be able to monitor the space charge formation in a temperature range from 20 °C to 70 °C.

In addition, a well-controlled temperature is critical for the reproducibility of the PEA measurements as the location of charge is calculated by the time delay of the PEA output signal and the temperature dependent wave velocity in the insulation material. The variation of temperature would therefore affect the spatial information of the space charge profiles.

3.2.3 Spatial resolution

Spatial resolution is a significant parameter for a space charge measurement system. For the PEA apparatus, a high resolution is particularly valid for detecting charges adjacent to the interfaces. The spatial resolution of a PEA system is affected by various factors which include the pulse width of the pulse generator, pulse coupling method (which may alter the pulse width), thickness of acoustic sensor which may be compromised for increasing the Signal to Noise Ratio (SNR), bandwidth of amplifiers (and analogue optical link circuit if applied), and numerical signal processing (especially for recovering the acoustic attenuation and dispersion).

In this project, the requested spatial resolution is 75 μm, e.g. 5% of the 1.5 mm insulation.

3.2.4 Sensitivity

The sensitivity of the PEA systems varies and can be as low as 10^{-1} C/m^3 [32]. The high sensitivity normally requires a large number of signal averaging iterations to reduce the white noise of the system for an acceptable signal to noise ratio. However it may not be necessary to pursue the lowest possible sensitivity with the expense of longer measurement time (thus lower measurement rate) and a compromise is often made. For this project, the sensitivity of 0.1-0.5 C/m^3 is the aim but which may vary dependent on the different types of mini-cables and experimental conditions.

3.2.5 Cable clamping unit

In order to investigate the reproducibility of measurements, it is required to mechanically load the mini-cable in the PEA cell under the controllable force conditions. In addition, for the purpose of examining the influence of cable deformation upon the PEA measurements, a robust clamping unit is required to be able to apply sufficient clamping force to cause considerable deformation on the mini-cable.

3.2.6 Different base electrode

Although using a flat electrode for cable PEA system have been proposed and used [81], little attention has previously been paid on carefully examining the influence of cable deformation against the flat electrode under a constant temperature and during a successive temperature cycling of the cable. To experimentally compare the two types of base electrode, flat VS curved, the design of the PEA cell should facilitate the easy replacement of the electrode with less interruption on the remaining parts of the PEA system.

3.3 Overview of the high temperature mini-cable PEA system

The system designed responding to the above requirements is shown in Figure 3-1.

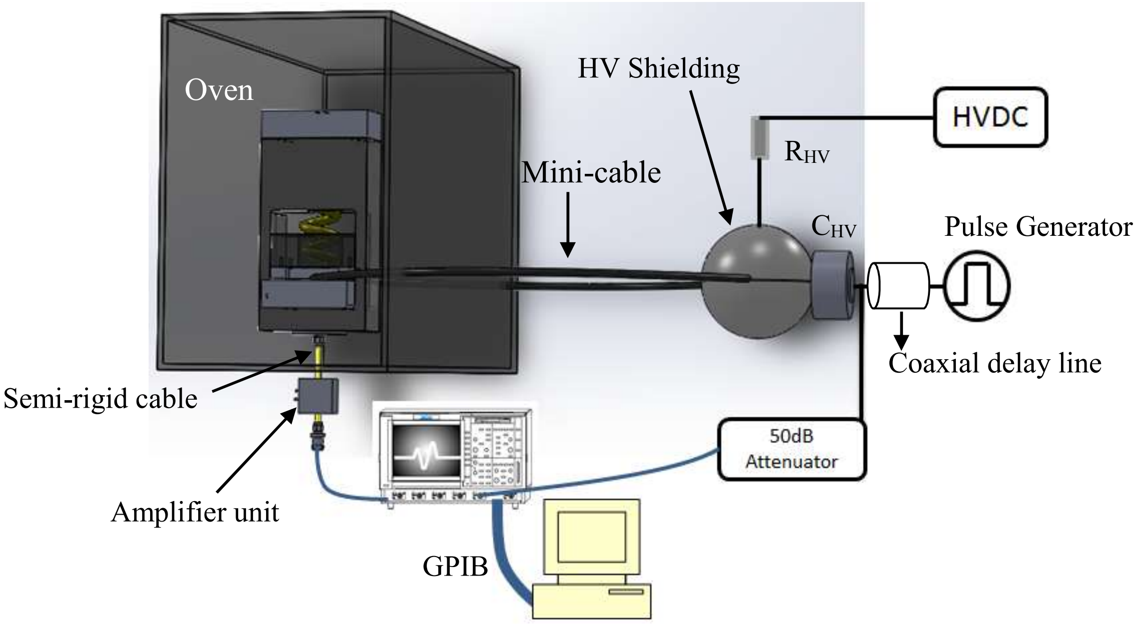

Figure 3-1. Schematic diagram of the high temperature mini-cable PEA system.

A purpose-made pulse generator provides 200 Hz, 20 ns, 0.8 – 8 kV voltage pulses which are then coupled to the mini-cable conductor via a coaxial delay line and an HVDC blocking capacitor C_{HV}. The HVDC source unit is connected to the mini-cable conductor via a high resistance resistor, R_{HV}, which prevents loading of the voltage pulses by the low output impedance of the HVDC source. At the connection point, a metallic shield was used to smooth the electric field and therefore to prevent the corona discharge. A purpose-made Π (pi) type 50 dB attenuator provides a matched 50 Ω termination for the pulse generator and simultaneously sends trigger signals to the oscilloscope. The PEA cell that is composed of a spring loaded cable clamp, bottom electrode, and piezoelectric sensor is placed inside an oven to achieve the accurately controlled isothermal conditions. The piezo-electric voltage generated by the pressure wave sensor is connected to an amplifier unit via a short semi-rigid cable. The amplifier unit contains two amplifiers, a purpose-made transimpedance amplifier (buffer) for improving the electrical impedance and a 50 Ω input impedance Low Noise Amplifier (LNA) of gain 49 dB. The amplifiers are necessary to boost the small piezo-voltage signal. The amplified PEA output signals are sent to an oscilloscope which communicates with a computer for data recording and further processing. Moreover, the system has the ability of automatic measurements with computer controlled pulse generator and HVDC source.

3.4 HVDC source

The HVDC source provides the electrical stress, for example for poling and polarity reversal, on the mini-cables. The required voltage rating of the HVDC source is determined by the thickness of the cable insulation and the required maximum electric field in the cable insulation. In this work, the insulation thickness of the mini-cable is 1.5 mm and the maximum field is ± 30 kV/mm (in the insulation adjacent to the inner conductor). Consequently the corresponding HVDC sources are required to provide at least ± 30kV DC.

Normally, the commercial HVDC sources are of single polarity, but are supplied with a replaceable voltage multiplication unit to produce voltages of opposite polarity. For convenience of changing polarity, two GLASSMAN high voltage DC supplies, -100 to 0 kV and 0 to +100 kV, were used and could be interchanged quickly. These were combined with the same earthing point and utilized in the PEA system.

3.5 Pulse generator

The width of the voltage pulses determines the maximum possible spatial resolution of a PEA system.

The schematic drawing of the pulse generator circuit is shown in Figure 3-2. The core component of the pulse generator is a fast HV MOSFET switch (BEHLKE Power Electronics GmhH) which features the maximum switching voltage of 8 kV, maximum pulse peak current of 200 A and on-time of 20 ns. The switching is controlled by a 200 Hz TTL signal. When the switch is off, the energy storage capacitor, C_{store}, is charged by a DC power supply in series with a current limiting resistor R_{HV}. When the switch is triggered by a 2 V – 10 V voltage pulse (high level of the TTL signal), the switch is closed for about 20 ns to form a voltage pulse. The voltage pulse then propagates to the sample and the 50 Ω impedance matching unit (which is the attenuator in the system) through the 50 Ω delay line made from coaxial cable (RG 213/U). Details concerning the pulse coupling will be given in Section 3.6.

The simulation of the pulse generator is given in Appendix B.

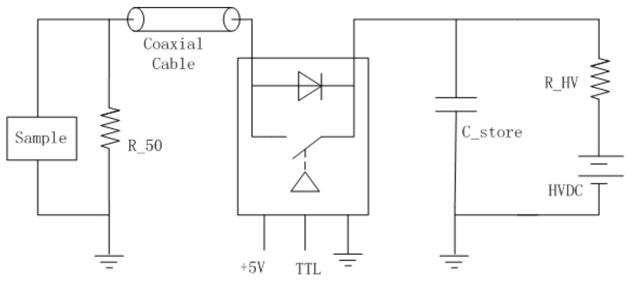

Figure 3-2. Schematic diagram of the pulse generator circuit.

3.6 Pulse delay line

An RG 213/U coaxial cable (50 Ω) is used to transmit the pulses from the output of the pulse generator to the mini-cable conductor. As the cable is effectively equivalent to a capacitor, in order to match the impedance of the coaxial cable, an attenuator of 50 Ω input impedance is connected to the output terminal of the coaxial cable as a matched load. However, the capacitance of the mini-cable is connected in parallel with the attenuator and thus makes it practically difficult to match the impedance to 50 Ω at high frequencies. Therefore a certain amount of pulse energy would inevitably reflect back to the pulse generator. At the pulse generator side, due to the low switching frequency of 200 Hz, the switch would remain open for 5 ms after sending out each pulse. Therefore the pulse generator is an open circuit for the reflected pulses. Consequently the reflected pulse oscillates forwards and backwards along the coaxial cable until being damped-out as indicated by the schematic diagram of pulse and reflections in Figure 3-3.

In addition, it has been experimentally observed that the high frequency noise signals produced by the pulse reflections would be induced in the PEA voltage output. This interference signal may superimpose on the space charge measurement window (the time window which contains the space charge information of the mini-cable insulation). A sufficiently long coaxial cable is therefore necessary to ensure that the reflected pulses do not occur at the same time as the PEA output signal is recorded.

As demonstrated in Figure 3-3, when a voltage pulse reaches the sample after a pulse propagation time t_1 in the coaxial cable, space charge inside the sample would respond to the voltage perturbation and generate the acoustic waves which would result in the PEA signal (P_{1st}) after travelling through the aluminium electrode to a piezoelectric sensor. The acoustic wave generated at the lower surface would directly travel through the PEA base electrode after a time delay of t_3, while the acoustic wave generated at the upper surface of the sample would spend an extra time of t_2 to travel through the sample itself. Then the window of space charge measurement is from t_1+t_3 to $t_1+t_3+t_2$ as shown in Figure 3-3. The first reflected pulse, V_{1st}, from the pulse generator would act on the sample after the time delay $2\times t_1$ and generate another space charge profile (P_{2nd}) likewise.

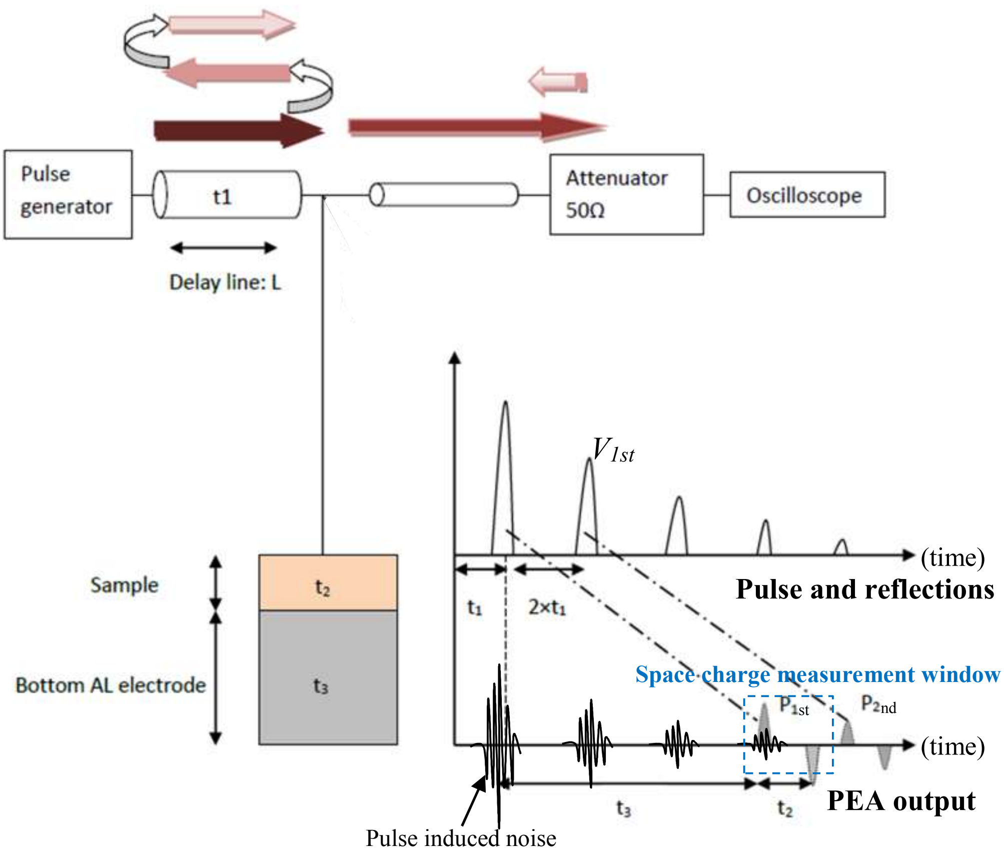

Figure 3-3. Schematic diagram of the pulse reflections in PEA system and the PEA output corresponding to the time delay of pulse and reflections with considering the pulse induced noises.

To avoid the problem of the reflected pulse disturbing the space charge signal, the following two conditions have to be satisfied:

1. (a) Reflected pulse generated signal P_{2nd} does not overlap the space charge measurement output signal P_{1st} or (b) P_{2nd} is much smaller than P_1.
2. Pulse induced noise does not present itself in the space charge measurement window.

Condition 1

For condition 1(a), it requires that the time delay of the reflected pulse $2\times t_1$ is larger than the length of space charge window t_2, i.e. $2\times t_1 > t_2$. If assuming the sound velocity in the coaxial cable and insulation sample are a constant of 1.98×10^8 m/s and 2000 – 1500 m/s at 20 – 70 °C respectively and the thickness of the sample is 1.5 mm, then the length of coaxial cable should be longer than 75 m at 20 °C and 100m at 70 °C.

Condition 1(b) is equivalent to that the first reflected pulse should be much smaller in amplitude than the main pulse, as the first reflected pulse, V_{1st}, will be the biggest among the reflected pulses. Assuming 50 % (conservative value for the worst circumstances) of the pulse is reflected back from the sample side to the pulse generator and the attenuation in RG 213 coaxial cable for 20 ns pulses is 5 dB / 100 m (assumed to be less than that in manufactory's datasheet), the normalised magnitude of the first reflected pulse with various lengths of the coaxial cable is plotted in Figure 3-4. It can be seen that the reflected pulse is less than 10 % of the pulse that generates the PEA signal when the length of the coaxial cable is longer than about 140 m.

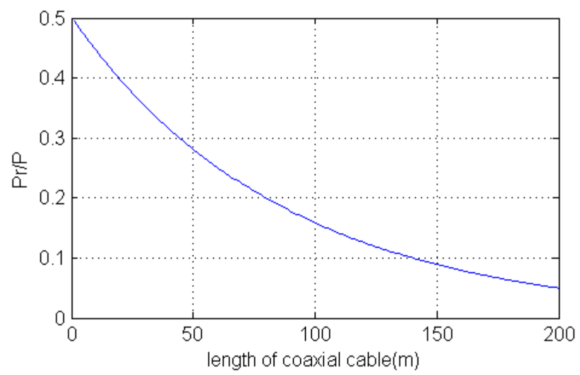

Figure 3-4. Normalised magnitude of the first reflected pulse Pr with different length of coaxial cable with the assumption that 50 % of the pulse would reflect back from the sample side and the coaxial cable has an attenuation factor of 5 dB / 100 m.

Condition 2

Figure 3-5 shows an example of the pulse induced noise in a PEA raw voltage signal with a 70 m RG 213/U coaxial cable. The theoretical locations of the reflected pulses have a time interval of $2\times t_1$ and are indicated using dash lines. It can be seen that the calculated locations match the experimental results. Moreover, low frequency noise oscillations (due to earth loops) were found occurring after the high frequency direct coupled noise with a longer time period. The presence of the low frequency noise near the space charge measurement window would disturb the baseline.

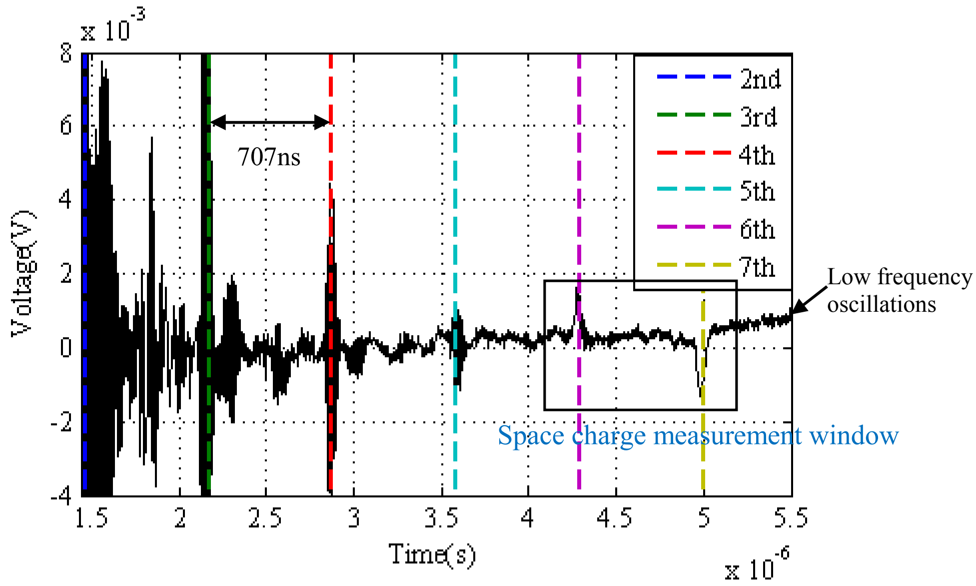

Figure 3-5. Example of a PEA raw voltage output (1000 sweeps averaged) when using a 70 m RG 213/U coaxial delay line and the calculated time of reflected pulses, from the 2nd to the 7th, acting on the sample.

The locations of the reflected pulses in time with different lengths of delay line are plotted in Figure 3-6. To satisfy condition 2, the length of the coaxial delay line needs to be longer than 175 m. However, as indicated in Figure 3-4, the pulse induced noise may become negligible even when the delay line is short than 175 m.

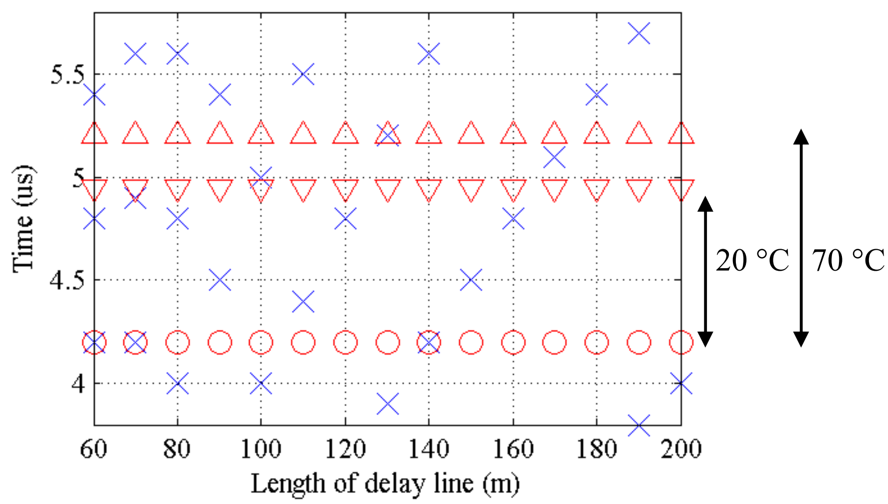

Figure 3-6. Locations (blue cross) of the coupled reflected pulse in the PEA output. The estimated (from experimental results) window of PEA signal is from 4.2 µs to 4.95 µs at 20 °C and 4.2 µs to 5.2 µs at 70 °C. Circles represent the position of the first interface charge peak and the triangles represent the position of the second interfacial charge peak at the two temperatures 20 °C and 70 °C.

Combining the above two conditions, the optimised length of the coaxial delay line should be around 170 m in order that the location of the reflected pulses occur outside the PEA measurement window. To verify this conclusion, the performance of the PEA system with different lengths of coaxial cables is evaluated experimentally using three lengths of delay lines, 0.7 m, 70 m and 170 m. The raw PEA outputs are shown in Figure 3-7.

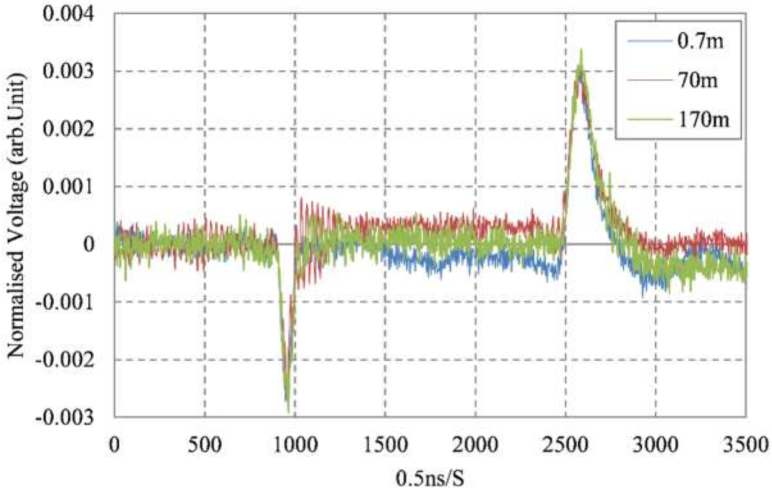

Figure 3-7. Normalised PEA raw outputs (1000 sweeps averaging with 3.2 kΩ buffer at 30 °C) with different lengths of coaxial delay line. DC bias voltage is 8 kV.

With a 0.7 m delay line, low frequency noise was found in the measured PEA raw output and disturbed the base line. With a 70 m delay line, the high frequency pulse noise appeared near the first PEA peak as estimated in Figure 3-6. With a 170 m delay line, neither the low nor high frequency noise was present in the PEA raw output. Although the pulse magnitude is attenuated by the long delay line, the S/N ratio (after 1000 sweeps averaging) of the PEA raw signal is comparable to that with a 0.7 m delay line. Therefore a 170 m coaxial delay line was used in the system.

In addition, the pulse shapes with the three lengths of delay lines are simulated using the simulation circuit introduced in Appendix B with typical propagation parameters for RG 213/U cable. The simulation results, shown in Figure 3-8, demonstrate that longer delay lines would result in a longer pulse propagation time and more attenuation on the pulse magnitude and slightly broadening of the pulse width.

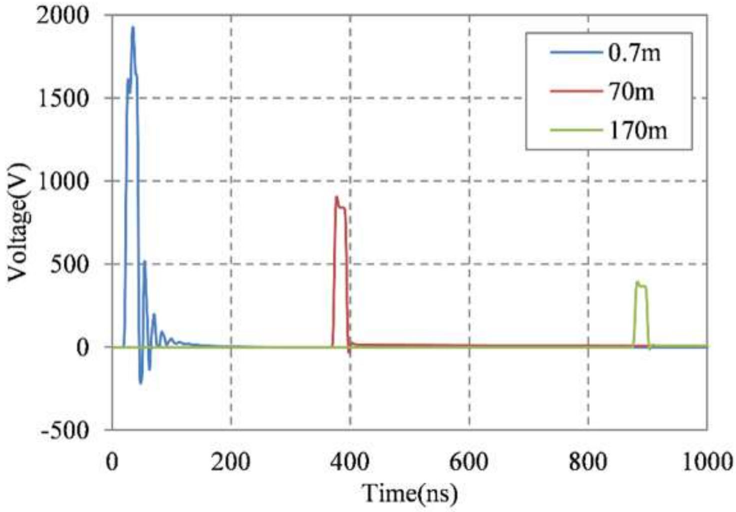

Figure 3-8. Simulated pulse shapes at the output of 0.7 m, 70 m and 170 m coaxial delay lines.

3.7 Solutions for high temperatures

The requirement of high experimental temperatures (up to 70 °C) is one of the main challenges for the system design. Most conventional PEA systems are designed for room temperature measurements in which case, the PEA unit is able to have a compact design combining the upper electrode, pulse coupling circuit, lower electrode, piezoelectric sensor and amplifier. More specifically, the piezoelectric sensor is normally shielded together with the amplifier to improve the noise immunity. With such a design, to realise isothermal conditions in the sample, it would inevitably be required that the temperature for the whole PEA cell should be the same. However some components may not survive at high temperatures or may have temperature dependent characteristics and therefore affect the measurement during the temperature change. These components are discussed below:

1. Piezoelectric sensor:
   The piezoelectric sensor is attached to the lower surface of the bottom Al electrode. PVDF film has been widely used in the past as the piezoelectric senor in PEA space charge measurement systems. It is stable under room temperature, however it becomes ineffective as a piezo-electric sensor at high temperatures [91, 92].

2. Amplifier:

   For a conventional film PEA system, the common approach is to place the amplifier in an electrically shielded box together with the piezoelectric sensor to avoid external noise signals. For example this method is employed in the PEA systems described in [93, 94]. The amplifier will therefore have to experience the high temperatures. However, the maximum operating temperature of commercial amplifiers are normally rated less than 70 °C or 85 °C. And, more importantly, their characteristics may change with temperature.

3. HV coupling capacitor:

   The role of a coupling capacitor, which connects the output of the pulse delay line to the mini-cable conductor, is to isolate the pulse generator from HVDC applied on the mini-cable conductor. It is desirable for the capacitor to be directly coupled to the conductor of mini-cable to minimise the inductance of connection, and hence it would be necessary for the capacitor to be positioned in the oven along with the PEA system and the mini-cable. However the capacitor may not be able to survive at the high temperature, and even it can, its capacitance would significantly vary with the temperature and thus affect the pulse magnitude as the HV coupling capacitor forms a potential divider with the cable capacitance. For example the capacitance of a TDK UHV ceramic capacitor would decrease by 33 % when the temperature rises from 25 °C to 85 °C [95].

The solutions adopted for the above issues were:

1. For the piezoelectric sensor, a co-polymer of PVDF, poly[(vinylidenefluoride-co-trifluoroethylene] [P(VDF-TrFE)], which has a maximum operating temperature of 110 °C (according to the datasheet provide by Precision Acoustics Ltd) is utilized instead of PVDF film. Moreover, the temperature stability of the PVDF-TrFE film was tested experimentally in Section 5.5.4.

2. To maintain a relative constant operating temperature for the amplifier, the amplifier unit is separated from the shielded box of the piezo-electric sensor in

the PEA cell and placed outside the oven with a short semi-rigid coaxial cable connection as shown in Figure 3-1.

3. The HV capacitor is placed outside the oven along with the ends of the mini-cable. This would incur a temperature gradient through the length of mini-cable at elevated oven temperatures. However the space charge measurement region of the cable would not be unduly affected as demonstrated by the analysis shown in Appendix C.

3.8 Design of PEA cell

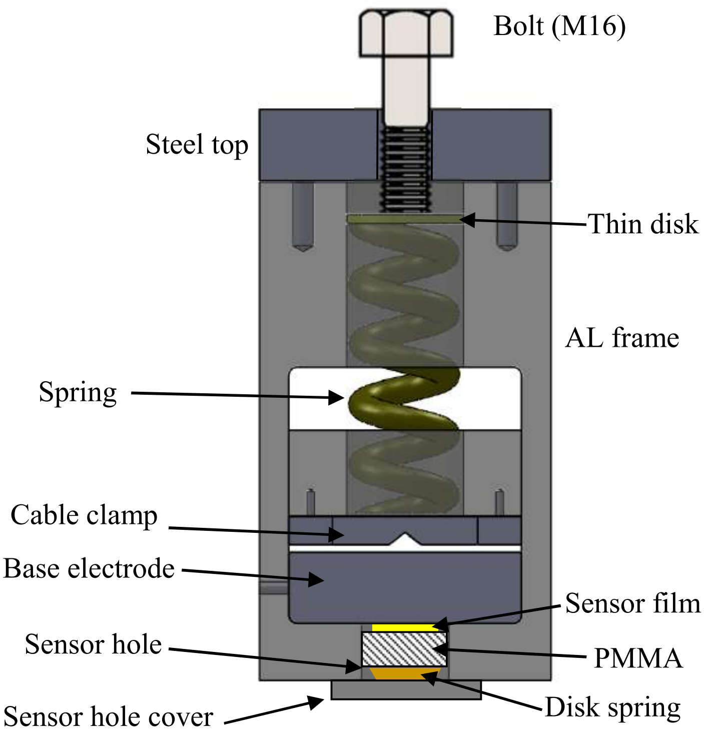

Figure 3-9. Schematic drawing of the PEA cell structure.

Responding to the demands of the clamping unit and changeable base electrode, the PEA cell designed for this project is shown in Figure 3-9. The main aluminium (AL) frame provides a robust structure for the spring loaded cable clamp to apply the high clamping force (up to 2200 N limited by the spring) onto the mini-cable. Additionally, the main aluminium frame and base electrode acts as a thermal mass to damp the effect of temperature fluctuation inside the oven on the mini-cable. There are two cable clamps with a ‘V’ shaped cut-out to centralise the cable along the axis of the PEA system and provided with different lengths, 30 mm and 50 mm, in contact with the mini-cable. The short 30 mm clamp was purposely used to maximise the deformation of the mini-cable with a flat base electrode for examining the effect of cable clamping pressure on the PEA raw output. The 50 mm clamp is of the same length as the base electrode and is used for normal tests. The steel top with a tapped hole in the centre provides a solid base for the M16 Hex bolt and is assembled to the main frame with 4 × M8 (socket cap) bolts. The M16 bolt is to adjust the cable clamping pressure. The detached top also facilitates assembling the spring (assembly without removing the base electrode or increasing the overall height of the PEA cell). The base electrode is fixed to the bottom plate of the frame with 4 × M4 (socket cap) bolts. Accordingly the sensor hole is in the centre of the bottom plate and contains the PVDF copolymer sensor film, PMMA acoustic absorber and a disk spring. With this design, it is easy to change the bottom electrode without interrupting the sensor connection as well as the other parts of the PEA cell.

3.9 Design of PEA base electrode

3.9.1 Flat electrode

Historically, when the PEA method was first adapted to measure cable samples, a curved bottom electrode (and piezoelectric sensor) was utilized to match the outer surface of cables and maintain the cylindrical propagation of the acoustic waves [11]. However, practical difficulties arise when using a curved electrode. Firstly, a good homogeneous acoustic coupling is hard to obtain if the cable has a non-perfect curvature. Secondly, the curved electrode can only be used for cables of one size. To overcome these difficulties, cable PEA systems with a flat earth electrode were then developed [80]. In this case, acoustic waves are coupled to the flat aluminium electrode along the ‘line’ of contact which acts as a secondary source of cylindrical acoustic wavefronts in the base electrode. The flat electrode PEA technique features flexibility in that the dimension (radius) of cable samples is no longer critical. However, the flat electrode is not without problems.

The substantial assumption of using a flat electrode is that the mini-cable has a line contact with the base electrode. In another words, it is assumed that the mini-cable does not deform under the clamping force. In practice, a reasonable high clamping force is critical to keep a good acoustic coupling between the mini-cable and the base electrode for the transmission of acoustic signals and some deformation of the cable is inevitable. This assumption may hold to some extent at room temperature when the insulation material is relatively hard. However at high temperatures, as the insulating material softens, mini-cables are likely to have noticeable deformation which leads to an increased contact area with the electrode. Detailed analysis of using a flat electrode at various clamping force and temperatures will be given in Chapter 5.

3.9.2 Half-curved electrode

With the raised concerns about employing a flat electrode for cable PEA system particularly at elevated temperatures, a curved electrode which fits the outer surface of tested mini-cables was manufactured for comparison with the flat base electrode.

In principle, a curved electrode as shown in Figure 3-10 is ideal for the PEA system measuring the space charge in cylindrical coaxial samples. The matched contact maintains the cylindrical wavefront of waves generated within the mini-cable insulation and the increased contact area minimises the deformation of mini-cables under clamping force. However in practice it is not easy to mount the sensor (PVDF-TrFE) film on the rear of a curved electrode. Moreover it is relatively inconvenient to produce a mirror finish on the curved surfaces.

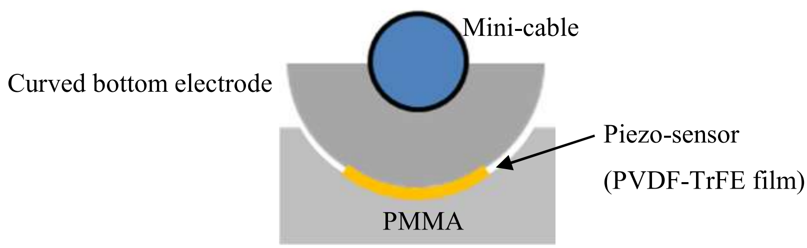

Figure 3-10. Schematic drawing of a curved electrode PEA cell.

Limited by practical difficulties, a compromised design was manufactured to be used as shown in Figure 3-11, where a cylindrical groove of the same diameter as the outer diameter of the mini-cables was machined in the surface of a flat bottom electrode. In this way, the deformation of the mini-cable can be restricted and a low surface roughness can be preserved on the flat rear surface where the sensor film attached.

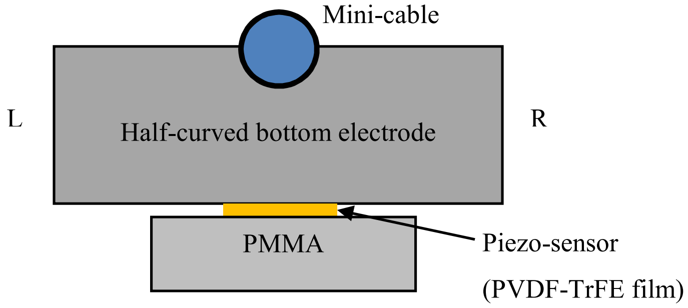

Figure 3-11. Schematic drawing of the half-curved electrode.

For the sake of convenience, the half-curved electrode will be called the 'curved electrode' instead in the following content.

3.9.3 Design requirements of base electrode

3.9.3.1 Thickness

The bottom electrode acts as a waveguide to delay the transverse pressure waves (having a lower propagation velocity) from longitudinal ones, so only longitudinal waves are transferred to form PEA output signal by the piezoelectric transducer during the measurement time window [71]. Then the length of waveguide, i.e. the thickness of electrode, has to verify:

$$T_{electrode} > t_{sc} \frac{v_T \, v_L}{v_L - v_T} \tag{3.1}$$

where t_{sc} is the duration of the space charge profile, v_T and v_L are the speed of transverse and longitudinal waves in the waveguide respectively.

In addition, the bottom electrode needs to provide enough acoustic delay to separate the acoustic wave reflections within the electrode from the measurement time window. To separate reflected waves at front and bottom aluminium/air interface, the thickness of the bottom electrode has to verify:

$$T_{electrode} > \frac{t_{sc}\, v_L}{2} \tag{3.2}$$

In practice, a much thicker electrode may be preferred to keep the measurement window away from the pulse generator induced noise at the trigger point (when the main voltage pulse acts on the cable). Moreover, a longer propagation distance is also beneficial in reducing the mismatch between the cylindrical wavefront and the flat transducer. Consequently, with satisfying above requirements, the electrodes used in the system are: 25 mm thick flat electrode and 30 mm thick curved electrode with 3 mm depth groove.

3.9.3.2 Width

Reflections also occur at sides of the electrode (boundaries L and R in Figure 3-11). So the electrode also requires enough width, $W_{electrode}$, to avoid detection of these reflected waves in the measurement time window. The minimum width of the bottom electrode has to satisfy the following equation (as details in Appendix D):

$$W_{electrode} > V_{AL} t_{sc} \sqrt{1 + \frac{2 \cdot T_{electrode}}{V_{AL} t_{sc}}} \tag{3.3}$$

With an electrode thickness of 25 mm and a measurement window of 700 ns, the minimum width of the bottom electrode is about 16 mm. In practice, a conservative design of 80 mm width is used for both flat and curved electrodes.

3.10 Piezoelectric sensor

3.10.1 Thickness

The thickness of the sensor film affects the spatial resolution of the PEA system and should be matched to the duration of the applied voltage pulse. The resolution is primarily determined by the width of the voltage pulses. Normally all the acoustic signals generated by charges under the application of the pulsed electric field are assumed to have the same width. This is the case if acoustic dispersion does not occur in the sample, base electrode wave guide and the sensor. Matching the sensor thickness to the wavelength of the pressure pulses is required to maintain the pulse determined resolution. In principle, this requires the wave propagation time inside the sensor film to be much less than the pulse width. However the thickness of PVDF-TrFE film is limited by availability in the market where the common thicknesses available are 9 µm, 28 µm, 52 µm and 110 µm. An empirical choice for the thickness is that the wave propagation time is about the same with the acoustic pulse width. In this project, the pulse width is about 20 ns. Then the thickness of the PVDF-TrFE film should be approximately 40 µm when assuming the sound velocity in PVDF-TrFE is 2000 m/s.

To investigate more thoroughly the effect of the sensor thickness and acoustic coupling with the backing material (acoustic absorber), a simulation model has been utilised and will be presented in Section 4.5.

3.10.2 Area

Specific to the geometry of the bottom electrode, the surface area of the sensor film is limited in a cable PEA apparatus. For the PEA cells designed for plane samples, the sensor film can be relatively large as acoustic waves generated in the sample are plane waves. However as the acoustic waves originated from the cable samples are of cylindrical wavefront, the shape mismatch between acoustic waves and the sensor film may cause signal distortion and reduce the spatial resolution. As illustrated in Figure 3-12, assuming the cable has a line contact (point contact in cross-section view) with the flat base electrode (which is equivalent to a curved electrode where the centre of cable is at the contact point of flat electrode), then the line of contact acts as a secondary wave source. The range of time delay, Δt, of the acoustic wave reaching the sensor film varies in accordance with:

$$\Delta t = \frac{\sqrt{D^2 + (\frac{W}{2})^2} - D}{V_{AL}} \tag{3.4}$$

where D is the thickness of the bottom aluminium electrode, W is the width of the piezo-electric film, V_{AL} is the sound velocity in aluminium.

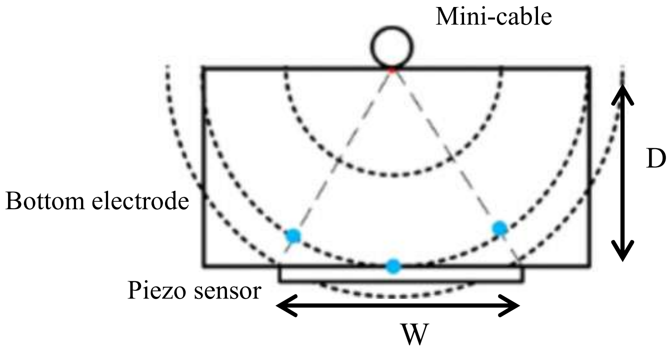

Figure 3-12. Schematic drawing of the cross-section of PEA cell illustrating the time delay of the cylindrical wave arriving at the flat piezo sensor.

Figure 3-13 shows the variation of time delay with different film width (up to 10 mm) when a 25 mm aluminium electrode is utilized. Therefore, for detecting cylindrical waves, the width of the flat sensor film would limit the maximum possible spatial resolution which is primarily determined by the sensor thickness. For example, a 5 mm wide and infinity thin senor film would reduce the spatial resolution by half when the duration of acoustic waves is 20 ns. Nevertheless, the effect of the time delay on spatial resolution would reduce with the increase of the sensor thickness.

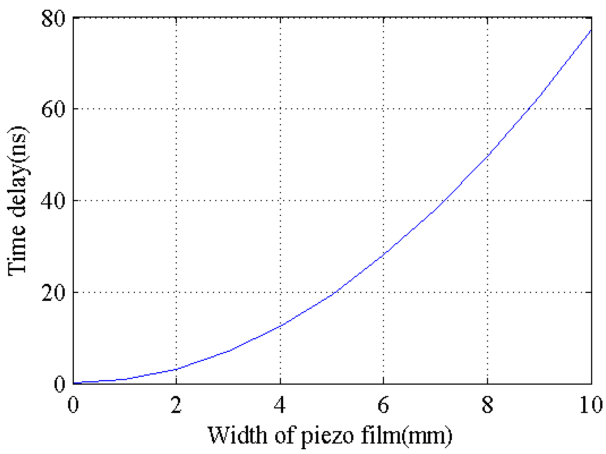

Figure 3-13. Time delay of a cylindrical wave reaching a flat piezo film when the thickness of bottom electrode is 25 mm and assuming the sound velocity in aluminium is 6400 m/s.

Although the length of the sensor film is only limited by the physical size of the PEA cell, it should be as short as possible in practice to avoid any possible deviation in the axial direction of the mini-cable. Consequently, the sensor film used for a cable PEA system with a flat bottom electrode has a very restricted acting area.

The effect of the sensor area with respect to a 52 μm PVDF-TrFE film will be further studied by the 2D simulation tools in Section 4.7.7.

3.11 Transimpedance preamplifier (buffer)

A low noise amplifier (LNA) is generally required in a PEA system to amplify the low output voltage of the piezoelectric sensor. However the input impedance of the commercially available LNAs are normally low (50 Ω or 75 Ω) compared to the high and frequency dependent capacitive impedance of a piezoelectric film. Thus a frequency dependent impedance mismatch exists that result in signal distortion equivalent to that caused by the high pass filter and the PEA apparatus incurs signal overshoots in the amplified raw output data [10]. To solve this problem, a transimpedance amplifier (buffer) has been developed.

3.11.1 RC circuit

The PVDF-TrFE sensor film utilized in the system has a relative permittivity of $\varepsilon_r = 10$ [96], thickness d of 52 μm and area A = 20 mm × 5 mm (restrict to the size of the sensor hole in Figure 3-9). The equivalent capacitance of the sensor is given by the following relation:

$$C = \frac{\varepsilon_0 . \varepsilon_r}{d} A = 170\ pF \tag{3.5}$$

With a 50 Ω LNA, the time constant of the RC circuit is therefore only 8.5 ns which is much less than the minimum signal width (20 ns). The RC circuit is acting as a high pass filter which therefore works as a differentiator on the piezo-electric signal. The resultant effect on the amplifier output is shown in Figure 3-14. The distortion of the amplifier output signal is normally regarded as signal overshoots in PEA raw signals [10]. Integration seems to be a possible way to numerically restore the signal from the RC differentiator circuit. However it may not be practical due to the instrumental noise as discussed in Appendix E. Consequently, it is preferred to find a solution from the hardware side (rather than through numerical signal processing).

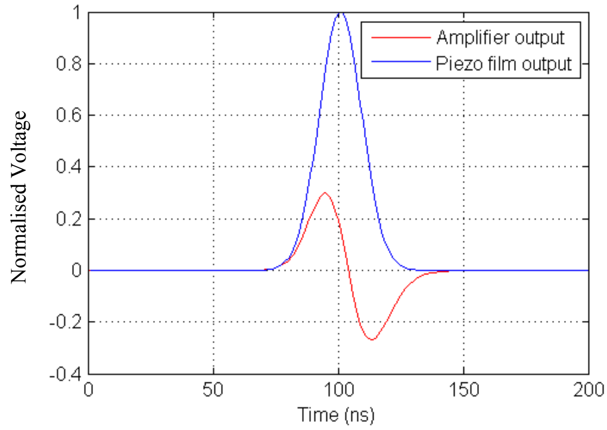

Figure 3-14. Time domain response of the sensor – amplifier system with the input of a 20 ns pulse signal (taken the capacitance of sensor film as 170 pF and input impedance of amplifier as 50 Ω).

To solve this distortion, it is necessary to increase the time constant by either increasing the capacitance of the piezo film or the input resistance of the amplifier. The capacitance of piezo film is proportional to its area and inversely proportional to its thickness. The area of piezo film is limited as discussed in section 3.10.2 and its thickness depends on the availability of films for the manufacturer (9 μm is the thinnest available in the market). On the other hand, most LNA features low input impedance (50 Ω or 75 Ω). Since it is difficult to change either of these two components, the solution lies in adding a transimpedance circuit (buffer) in-between to increase the amplifier input impedance from 50 Ω to a much larger value.

3.11.2 Input impedance of the buffer amplifier

The space charge signal covers a wide frequency bandwidth. The highest possible frequency component is defined by the pulse width. Therefore the upper-limit of the PEA signal spectrum would be 50 MHz if 20 ns pulses were applied. The lower limit is set by the time window of the PEA response and will be approximately 1 MHz consistent with the propagation time of the acoustic waves through the mini-cable insulation of approximately 1 μs. The input impedance of the buffer amplifier should be as high as possible to record these low frequency components. However, on the other hand, high impedance would incur high noise level. Consequently, with respect to the estimated piezo-sensor capacitance of 170 pF, two buffer amplifiers with 3.2 kΩ and 75 kΩ input impedances were developed with the circuits and simulation detailed in Appendix F.

3.11.3 Performance of the buffer amplifiers

The performance of the buffer circuits of two different input impedances (3.2 kΩ and 75 kΩ) have also been assessed experimentally. Under a very low DC bias voltage of 8 kV (which generates the maximum electrical field of 7.7 kV/mm in the 1.5 mm thick insulation), raw buffered and amplified data was obtained. In the data acquiring system, synchronous averaging of 1000 sweeps was performed (as default for all PEA measurements) by the oscilloscope before sending to the computer. The raw output for the same sample using the two buffer amplifiers are shown in Figure 3-15.

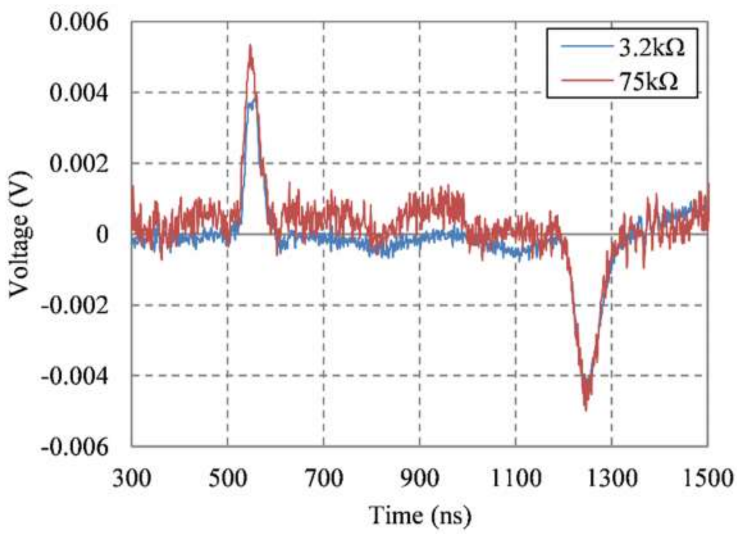

Figure 3-15. Raw PEA outputs (1000 sweeps averaging as default) with 3.2 kΩ and 75 kΩ input impedance buffer circuits at room temperature (18 – 20 °C) with +8 kV DC bias voltage.

The raw PEA output with 3.2 kΩ buffer was found to have a good signal to noise ratio. When using the 75 kΩ buffer, the SNR of the PEA raw output is much worse but could be improved by more averaging or employing a numerical noise filter on the PEA output data.

The noise reduced PEA outputs using the numerical filter (80 MHz Gaussian high pass filter implemented using MATLAB) and 4000 sweeps averaging are shown in Figure

3-16. The main difference between the two buffers appears on the low frequency signals while the two interfacial peak signals (high frequency) are about the same.

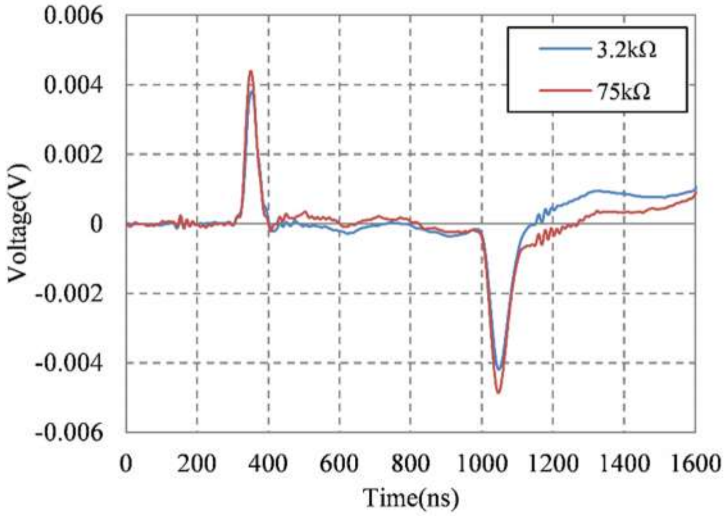

Figure 3-16. Noise reduced PEA outputs using an 80 MHz Gaussian high pass filter and 4000 sweeps averaging.

In summary, although the 75 kΩ buffer provides sufficient bandwidth and hence a voltage output with less distortion than the 3.2 kΩ buffer, abundant signal averaging to achieve a reasonable signal to noise ratio (SNR) is required. The two buffer amplifiers could therefore be used interchangeably. When the SNR using the 75 kΩ buffer is too low, the 3.2 kΩ buffer could be used instead. However, in this case the effect of impedance mismatch must then be numerically recovered using signal processing (see Section 3.12.4).

3.12 Traditional approach to signal processing and calibration of the PEA

The PEA method is a non-direct measurement technique with output being the voltage signal representing the space charge density distribution convoluted with the instrument response function (IRF) of the PEA apparatus. Consequently, signal processing of the raw PEA voltage signal and calibration is required to reconstruct the original space charge distribution.

This section starts with illustrating the relationship between the space charge density distribution and the PEA raw output based on the assumptions made for each stage. These assumptions are also the foundation for PEA signal interpretation as well as signal processing and calibration. Based on these relationships, the system transfer functions subjected to the cylindrical geometry sample are introduced individually. Then the conventional calibration method is reviewed. A step by step example of the signal processing will be then demonstrated using experimental raw data obtained from the PEA apparatus followed with a detailed discussion on the geometry effect and acoustic loss during propagation.

3.12.1 Relationship between space charge and PEA output

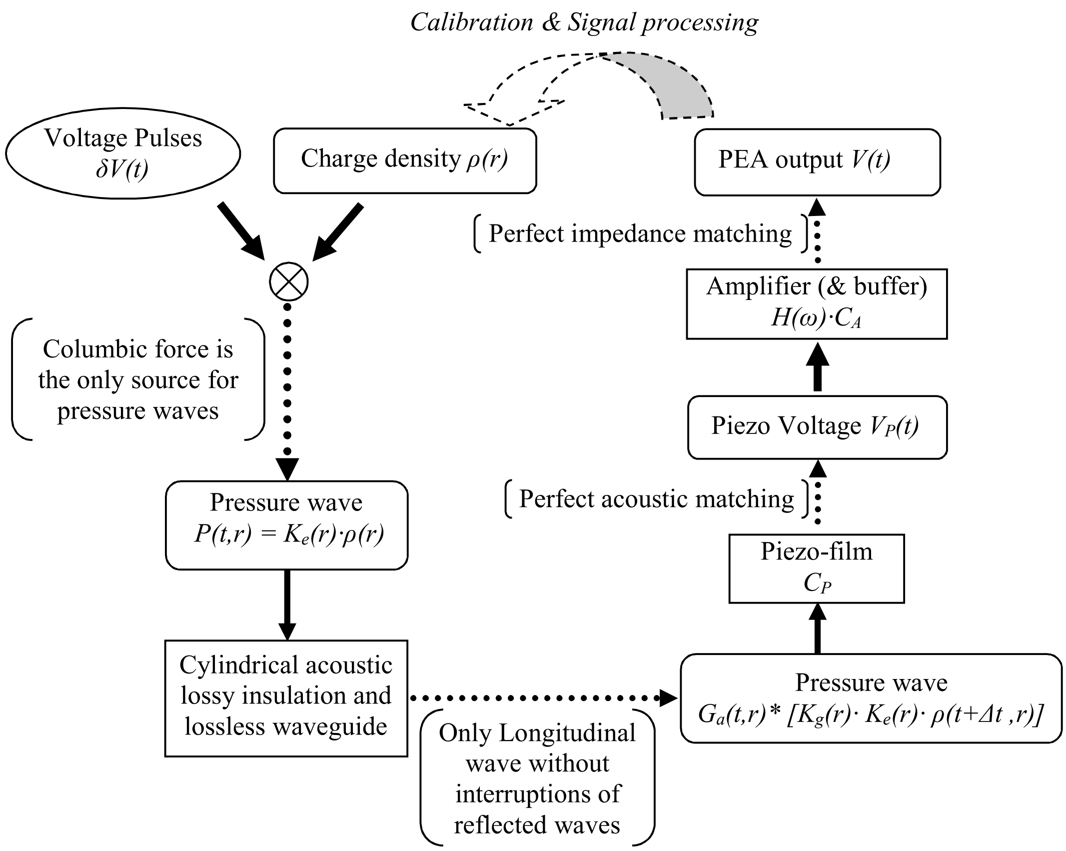

Figure 3-17. From charge density to PEA output and vice versa.

Figure 3-17 demonstrates the processes of producing a PEA output signal from the charge density with the assumptions for each stage.

To start with, the fundamental assumption of the PEA method is that the Columbic force is the only source of electrostatic force, so that the generated acoustic signal P(t,r) can be possibly related to an image of the net charge. Whilst it needs to be pointed out that for cable geometry samples, there are other potential force terms as discussed in Section 2.6.2 and the pulsed field is divergent which results in a radius dependent enhancement $K_e(r)$ on the resultant pressure wave P(t,r).

The generated pressure wave then propagates through the cable insulation and the thin outer semicon layer, to the base electrode waveguide and finally arrives at the piezoelectric sensor after a time delay Δt. Subjected to cylindrical geometry, the magnitude of the pressure wave reduces during propagation through the cable insulation with a geometry factor $K_g(r)$. Moreover, during propagation inside an acoustic lossy media, the pressure wave would suffer from acoustic attenuation and dispersion with a transfer function $G_a(t,r)$. An underlying assumption for the wave propagation stage through the aluminium base electrode is that the acoustic wave guide successfully separates the acoustic shear waves from the measured longitudinal waves and any reflected acoustic signal.

The transfer function, C_P, represents the conversion of the pressure waves to an electrical signal. If it is assumed that the PVDF-TrFE sensor has a wide uniform bandwidth and with a matched acoustic absorber, then the transfer function would be regarded as a constant.

Afterwards the PEA raw output would be directly proportional to the sensor output with a voltage gain of C_A if no impedance mismatch existed for the buffer and amplifier circuit i.e. whose (normalised) transfer function H(ω) is a constant (i.e. H(ω)=1) over the signal bandwidth.

In summary, with accepting all the assumptions, the relationship between charge density and PEA raw output in the time domain is

$$V(t) = H(t) * G_a(t,r) * (C_P \cdot C_A \cdot K_g(\mathrm{r}) \cdot K_e(\mathrm{r}) \cdot \rho(r)) \qquad (3.6)$$

3.12.2 Signal processing

To reconstruct the charge density ρ(r) from the raw PEA output, V(t), it is necessary to solve Equation (3.6) by employing signal processing techniques such as deconvolution. Moreover, for the cylindrical insulation of mini-cables, the correction for the geometry related influences, K_g and K_e, have also to be taken into account.

In addition to the processes for recovering the space charge profile, signal processing should also include the preconditioning of the raw PEA output. That includes de-noising by signal averaging (and/or numerical filters) and baseline correction.

3.12.2.1 H(t)

The response of sensor–amplifier system which incurs the impedance mismatch has been discussed in Section 3.11.1. Buffer circuits have been developed to minimise the impedance mismatch. To further compensate the attenuation on the low frequency components, deconvolution can be applied with the transfer function H(t) estimated by the known or measured capacitance of the sensor and the input impedance of the buffer amplifier.

3.12.2.2 K_e

The applied pulsed electric field in a cylindrical system is dependent on radius, r, and follows equation (2.1). The pulsed electric field decreases along the radial direction, r, from the inner (radius a) to outer semicon interface (radius b) in proportion to 1/r. The enhancement term K_e on the pressure wave due to the divergent pulse field with respect to the outer interface is:

$$K_e(r) = \frac{E_p(r)}{E_p(b)} = \frac{b}{r} \qquad (3.7)$$

where $E_p(r)$ and $E_p(b)$ are the applied pulse electric field magnitudes at radial positions r and b respectively.

3.12.2.3 K_g

As discussed in Section 2.6.5, the magnitude of the cylindrical acoustic wave reduces with the square root of the radius when travelling in the radial direction. Therefore the reduction factor applied on the generated signal is [27]:

$$K_g(r) = \sqrt{\frac{r}{b}} \tag{3.8}$$

3.12.2.4 $G_a(t,r)$

The effect of the acoustic attenuation and dispersion on the PEA signal has been shown in Section 2.6.3. The signal recovery process for the plane-plane PEA geometry can be referred to reference [18]. Whereas for processing the signal of mini-cables, the geometry effects (as introduced in above two subsections) need also to be considered.

Specifically, the system transfer function G_a related to the acoustic attenuation and dispersion of wave propagation is derived from the calibration measurement in which only the capacitive electrode charges are assumed to be detected as two interfacial peaks P_1 and P_2. Since the signal generated at interfaces can be treated as delta functions, P_1 and P_2 should have the same wave shape but differ in magnitude due to the cylindrical geometry and the applied DC and pulsed Laplacian electrical field, E, at the two interfaces, a and b and the wave radiation in the cylindrical wave path domain. The acoustic transfer function G_a for traveling the entire thickness (b-a) can therefore be estimated from the pulses P_1 and P_2 as:

$$G_a(t, b-a) = \frac{P_2(t)}{\frac{E_a}{E_b} K_e(a)\, K_g(a)\, P_1(t)} \tag{3.9}$$

Then the full matrix of the transfer function $G_a(t,z)$ can be constructed using the same method with that in [18] where z is defined as the distance into the cable insulation from the inner interface, i.e. $z = r-a$.

3.12.3 Calibration

When applying a calibration procedure it is usually assumed that the cable insulation is free of any space charge and hence the magnitudes of the interface charges when a DC voltage is applied is determined by the geometry of the cylindrical system and the magnitude of the applied DC voltage. A calibration signal is therefore recorded prior to any space charge measurements in order to obtain the calibration constant for the PEA instrument. This constant enables the corrected PEA raw output signal to be expressed directly in C/m^3 such that it is electrostatically consistent with the magnitude of the applied electric field. The method involves consideration of the area enclosed by the first interface peak from position b in the cable. The PEA calibration signal is normally obtained by taking measurements under a low DC applied voltage and within a sufficiently short time to ensure no charge has accumulated inside the sample insulation during the calibration measurements. In this case, the PEA output would only contain two peak signals responding to the capacitive electrode charges, at positions a and b. Since these interfacial charges are located in very thin layers, they can be treated as delta functions. The interfacial charge density, σ, can be calculated by:

$$\sigma = \varepsilon_0 \varepsilon_r E \tag{3.10}$$

where ε_0 is the permittivity of free space, ε_r is the relative permittivity of sample and E is the electric field at the interface and can be calculated based on Equation (2.1). Considering the outer interface signal peak, P_1, is not affected by the geometry and propagation effects, the calibration constant is determined [11, 16] by space integration of the signal under the first peak i.e. $\int_{P1} V(r)dr$, then dividing σ_b representing the surface charge density at interface position b.

3.12.4 Example of signal processing applied to raw PEA output data

In this section the traditional approach to reconstruct the space charge profile from raw data obtained using the PEA technique is described in detail. The step by step processing on typical raw PEA output data to reconstruct the space charge profile in cylindrical geometry cables is illustrated using a PEA measurement on an 'as-received' D807D mini-cable under 20 °C isothermal condition.

Step 1. Baseline correction

The first step is to remove any signal acquisition artefacts by establishing a true baseline for the PEA signal. The measured signal contains the system DC drift and low frequency components in the PEA raw signal due to coupling of the pulse generator signal with the PEA output signal, if any, and the pulse voltage induced high frequency signals. The baseline signal is acquired with zero applied DC voltage to the cable such that the charges at the interfaces are only due to the applied pulse voltage, as shown in Figure 3-18. In this figure, the baseline signal is compared with a PEA measurement taken when the DC voltage applied to the cable is increased to +14 kV in order to make clear the position of the interfaces and the relative signal magnitudes. In this case the electrode peak charges become clearly visible. Normally, to decrease the noise level to a minimum in the baseline measurement, the baseline signal is acquired using data averaging. Repeated PEA acquisitions are made typically 10,000 times to reduce the white noise component in the signal by data averaging in the oscilloscope. The resultant PEA baseline signal with zero DC voltage applied to the cable is then subtracted from all subsequent PEA measurements of the space charge.

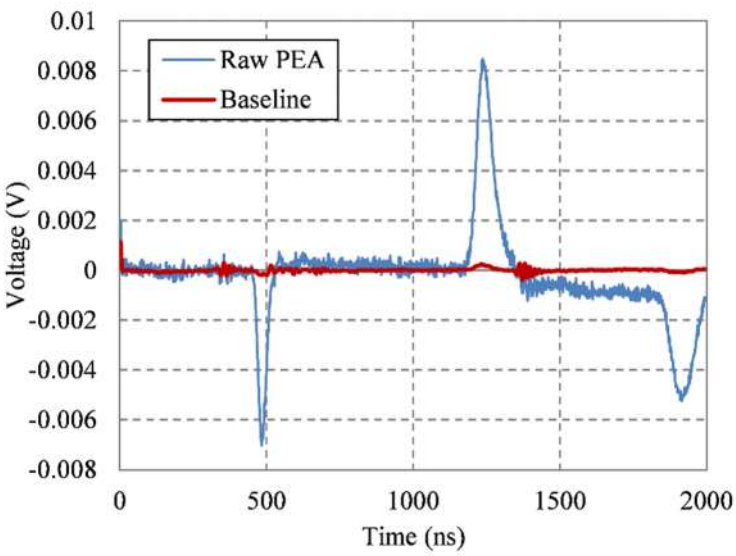

Figure 3-18. Raw PEA outputs under +14 kV calibration bias voltage and the averaging increased V_{off} measurement (with pulse voltage only) which gives the baseline.

Step 2. De-noising

The procedure adopted for raw PEA measurements of the space charge is to average 1000 acquisitions of the PEA raw output and averaging using the oscilloscope to reduce noise in the signal. The measurement and function of the oscilloscope is controlled in Labview. However in some cases, as shown in Figure 3-18 for the data obtained at +14 kV applied voltage, significant white noise may still be present in the data after averaging. Therefore a numerical 80 MHz Gaussian high pass filter (implemented in MATLAB) was used to reduce the high frequency noise in the baseline subtracted raw

PEA output. An example of the de-noised signal compared with the averaged signal is compared in Figure 3-19.

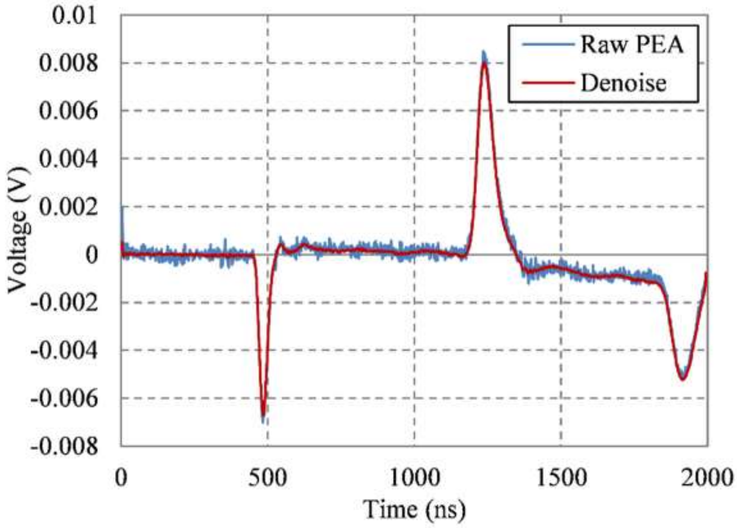

Figure 3-19. De-noising using the numerical Gaussian high pass filter.

Step 3. Correction for electrical mismatch

The buffer circuit of 3.2 kΩ input impedance was used for this test. As discussed in Section 3.10, the low frequency signal components would be attenuated by the high-pass sensor-buffer circuit. To recover the signal, the output signal was convoluted with the inverse transfer function of the RC (C = 170 pF, R = 3.2 kΩ) sensor-buffer circuit as implemented in MATLAB. As shown in Figure 3-20, the recovered signal shows less overshoot in the electrode peaks P_1 and P_2 and a flat signal between the two peaks.

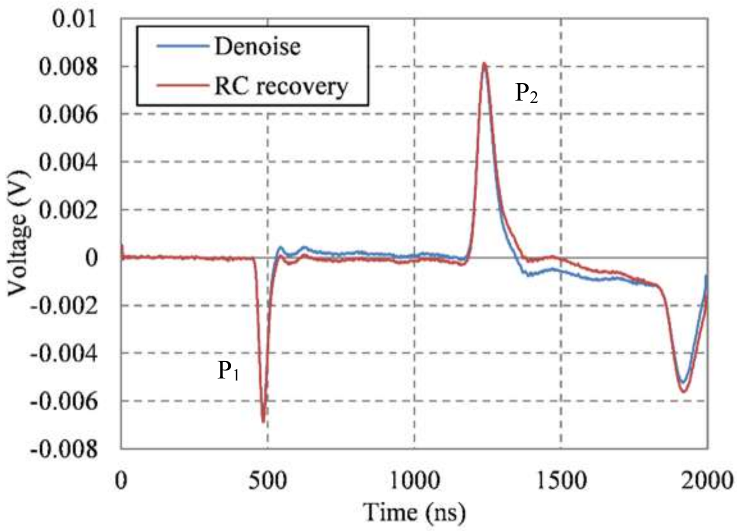

Figure 3-20. Signal recovered (RC recovery) from the electrical mismatching between the sensor (200 nF) and 3.2 kΩ buffer.

Step 4. Acoustic propagation and geometry compensation

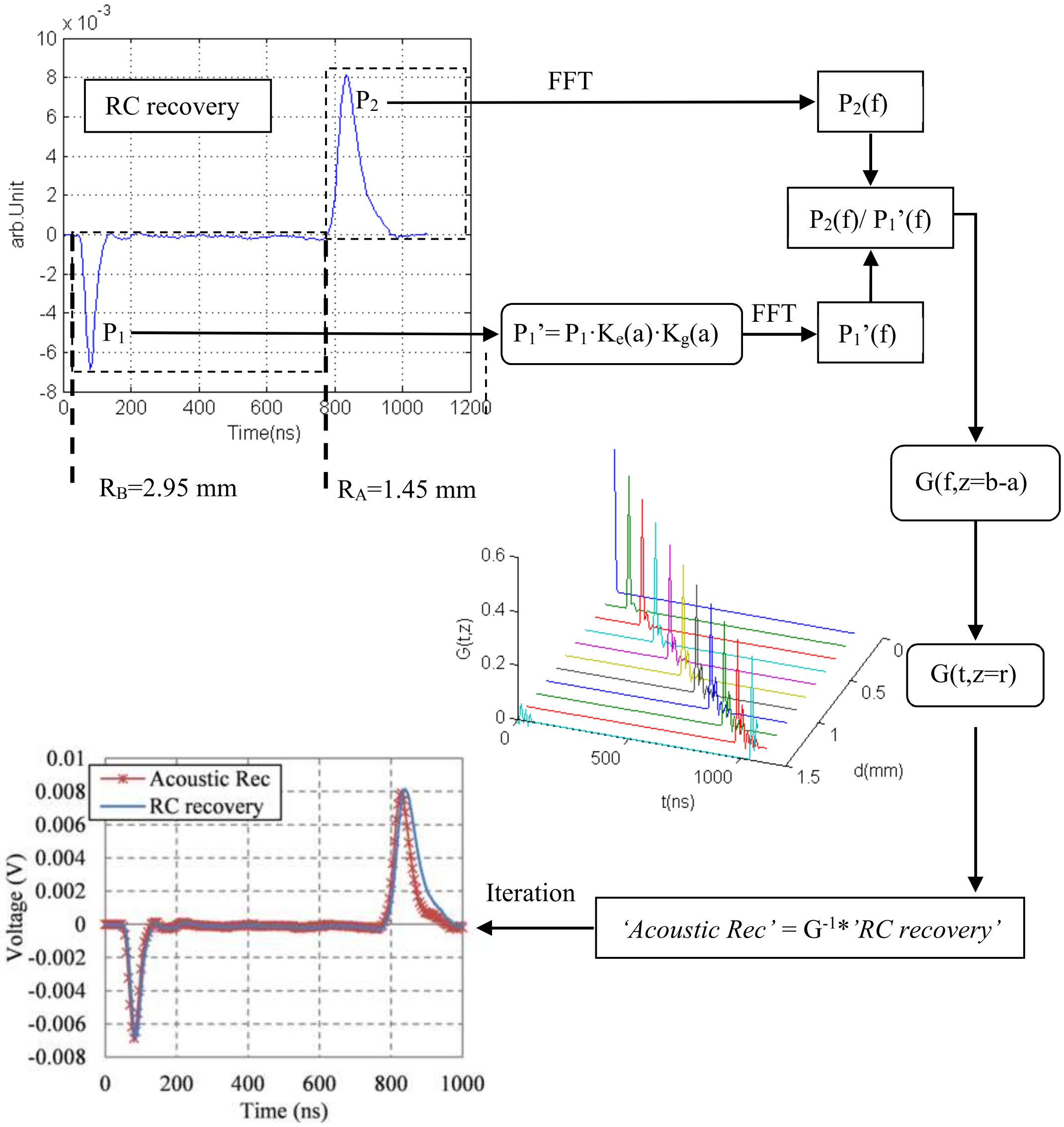

Figure 3-21. Signal recovery from the acoustic and geometry distortion during wave propagation within the insulation.

The procedure of the signal recovery correcting for the acoustic propagation and geometry effects are shown diagrammatically in Figure 3-21. Firstly, the integrated transfer function G(t,z) is constructed following the work in [81] while assuming a Laplacian DC field. Then the corrected voltage signal V'(t) is obtained from the PEA output V(t) by solving

$$V(t) = G(t,z) \cdot V'(t) \tag{3.11}$$

To solve this equation, it is necessary to find the inverse of the transfer matrix, G(t,z). In order to avoid unnecessary high frequency components present in the inverse matrix, it is useful to reduce the sampling frequency of the raw data. Typically the sampling frequency is reduced by a factor of 4 from the maximum of the oscilloscope of 2 GS/s. This is sufficient to reduce the condition number of the otherwise 'ill-conditioned' transfer matrix G(t,z). The procedure was implemented in MATLAB.

The corrected signal and the original RC corrected signal are shown in the lower part of Figure 3-21. The acoustic propagation and geometry correction produces a narrower peak P_2, while P_1 maintains the same, as expected. The area ratio of the two peaks is 2 which is the same as the ratio of Laplacian interfacial field at a = 1.5mm and b = 3 mm.

Step 5. Calibration of the corrected PEA signal

Using the known sound velocity of the cable insulation material at the experimental temperature, the recovered voltage signal, 'Acoustic Rec', as a function of time can be plotted against the radius position with respect to the known mini-cable dimensions (Section 2.5) as shown in Figure 3-22. As described in Section 3.12.3, the calibration coefficient, the product of C_p and C_A, is achieved by determining the ratio of the area of P_1 (shaded area under P_1 in Figure 3-22) and the calculated surface charge density:

$$C_p \cdot C_A = \frac{\int_{P_1} V(r)}{\varepsilon_0 \varepsilon_r E_b} \tag{3.12}$$

This implies that the accuracy of calibration depends on the knowledge of the electrical field at the outer semicon – insulation interface.

With the calculated calibration coefficient, the space charge density profile along the radius can be derived from the corrected PEA voltage signal as shown in Figure 3-22.

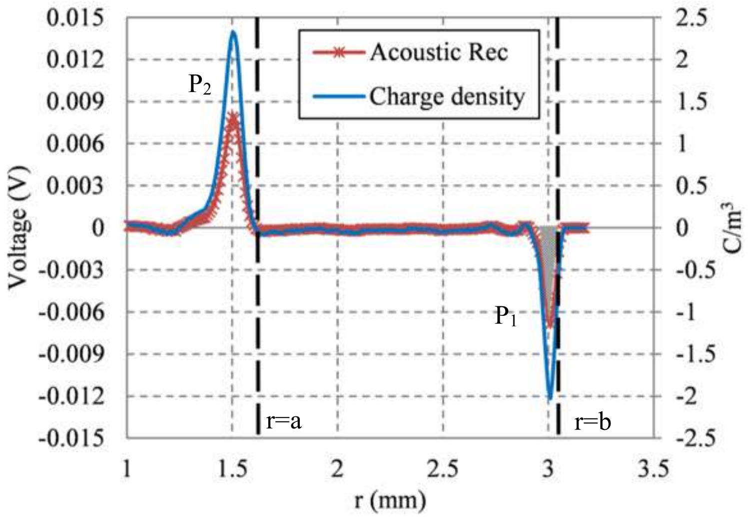

Figure 3-22. Converting the time delay dependent signal 'Acoustic Rec' to the radius position. For convenience of signal processing, the two interfacial peaks are located at the radius of interfaces (i.e. a = 1.5 mm and b = 3 mm), while the true interfaces for the measured signal are indicated by the dash lines. Dash area highlights the area of the P_1 for the voltage signal. Calibrated space charge density as a function of radius is plotted in the second axis.

Step 6. Internal electric field distribution E(r) and electric potential V(r)

Finally, the accuracy and electrostatic consistency of the signal processing and calibration steps can be verified by calculating the electrical field (by applying Poisson's equation to the calculated space charge density) [27] and voltage (by integrating the electrical field across the radius of the cable insulation thickness). These can then be compared to the theoretical field and electric potential (either assuming no space charge or once steady state charging of the cable had occurred) and the applied voltage. As shown in Figure 3-23, the reconstructed electrical field fits the Laplacian distribution with some minor deviations due to the noise presented in the charge density profile. The calculated voltage at the conductor side is consistent with the voltage applied to the cable, +14 kV DC. This example illustrates the importance of a space charge free cable in the PEA calibration. It would be difficult to justify that the cable is free of space charge when the calibration signal is obtained at the beginning of the experiment.

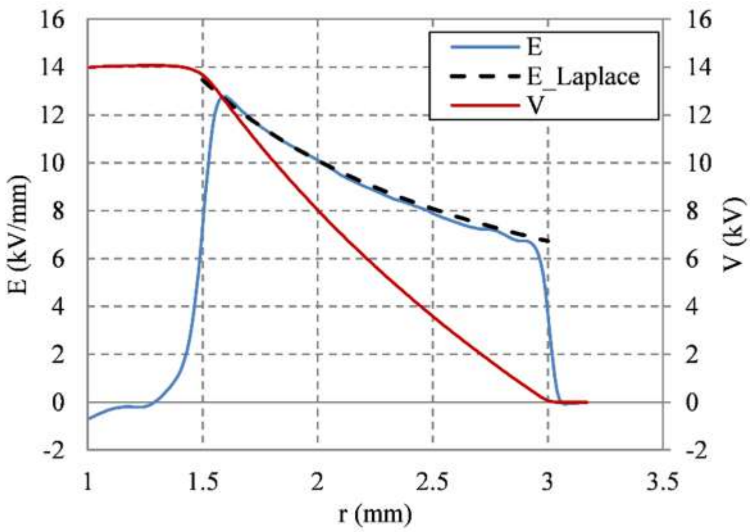

Figure 3-23. Calculated electric field and voltage distribution.

3.13 Summary

The high temperature mini-cable PEA system hardware was developed for measuring the space charge in mini-cables cable under applied maximum DC fields of 0 kV/mm – 30 kV/mm at the inner semicon interface consistent with the service conditions of commercial cables and under controlled isothermal conditions (20 °C – 70 °C). The pulse generator was designed for this system with the coaxial pulse delay line whose length was carefully examined and optimised to provide a noise free measurement window. The design specifications were met on realizing the high temperature requirement.

In addition the design of the PEA cell features the ability of performing verification and comparison tests by employing the cable clamping unit which is able to provide controlled clamping force. This will enable the effect of cable deformation on PEA measurements to be evaluated. Interchangeable base electrodes of two shapes, flat and curved to match the outer diameter of the mini-cables were constructed to enable a comparison on the PEA performance of using the flat or curved base electrode to be made.

The limitations on the size of the sensor film were discussed which leads to the common issue for the PEA apparatus on the importance of impedance matching between the sensor and amplifier to prevent information loss due to the filtering of the low frequency components of the PEA raw output signals. To overcome this problem, two buffer amplifiers of 3.2 kΩ and 75 kΩ input impedance were developed. For most measurements, the 3.2 kΩ buffer amplifier was found to be suitable as it produce less noise although signal correction for the impedance mismatch has to be used.

The assumptions and techniques for the traditional approach to the interpretation of the PEA raw output and performing the necessary signal processing and calibration were reviewed. The traditional signal calibration method was illustrated using real PEA measurement data taken on a manufacturer supplied mini-cable. In order to provide a more robust interpretation of the PEA raw output signals a new approach to the analysis will be presented in Chapter 4.

4 DEVELOPMENT OF SOFTWARE TOOLS FOR INTERPRETATION OF PEA DATA

4.1 Introduction

For a robust understanding and interpretation of the PEA raw data obtained from space charge measurements using cable geometry samples and in assisting the PEA system design, various simulation tools were developed as detailed in this chapter.

A one-dimensional unipolar charge transport model was developed for investigating the space charge accumulation as a consequence of field and temperature dependent conductivity in cylindrical cable insulation. To directly compare the simulated charge profile with experimental results, a 1-D PEA acoustic simulation model was also developed and coupled to the output of the charge transport model. In addition, a Pspice based sensor model focuses on examining the sensor response and hence the overall system response of the PEA apparatus. Bridging these simulation models together will enable the simulated PEA raw output (to be generated from space charge distribution predictions from the charge transport model) to be directly compared to experimentally derived space charge data from mini-cables. This new approach encapsulates the non-ideal characteristics of the PEA system and overcomes the problems associated with the traditional approach of applying signal processing to the raw data to recover the original space charge profile (for example the issues of attenuation and dispersion correction as discussed in [21]).

The one-dimensional simulation approach was further extended to two dimensions in order to examine the influence of the PEA design parameters, i.e. the use of a flat or curved base electrode and the effect of mechanical deformation of the cable under high clamping force.

At the end of the chapter, the application of the new integrated 1D simulation models to interpret PEA data are illustrated step by step.

4.2 1D unipolar charge transport model for cylindrical geometry

4.2.1 Development of charge transport models

The first simulation model for bipolar charge transport in polyethylene (PE) was derived from concepts utilized in semiconductor physics [97] by Alison and Hill [6]. This model utilizes a system of convection (drift of charge carriers in an applied field) and reaction (trapping, recombination of charge carries) equations combined with Poisson's equation to simulate the behaviour of bipolar charge (electrons and holes) transport for degassed cross-linked polyethylene under DC stress in steady state conditions. Charge trapping was assumed to be at a single deep trapping level with a constant trapping cross section and recombination specific to each electron-hole pair. Thereafter, the model has been further developed by many experts [98-101] who bring the process of de-trapping into consideration and use the Schottky injection mechanism as the source of charge carriers at the electrodes instead of a constant charge source as used in Alison and Hill's model. Moreover, a model with exponential distribution of trap depths was developed in [100].

Although the bipolar charge models may be the most advanced in terms of describing the physics of charge transport in PE, it requires a variety of parameters and advanced simulation techniques to solve the set of convection equations. Moreover the calculation would become more complicated when the carrier's mobility is a function of the electrical field.

In this project, the charge formation due to the field and temperature dependent conductivity at relative low applied DC fields (< 30 kV/mm), which will be discussed in Chapter 6, is of interest. To avoid the difficulty of the parameterization of the bipolar charge transport model, a simplified unipolar model that considers the field and temperature dependent conductivity and Ohmic contact at the electrode – insulation interfaces has been developed instead.

4.2.2 Model description

4.2.2.1 Space charge

The fundamental set of coupled equations for the time-dependent space charge simulation is the same as that used for the bipolar charge models: Poisson's equation provides the electrical field distribution as a consequence of space charge formation, while, with respect to the conductivity, the local field determines the current flow which in turn impacts the net charge density. Due to the axial symmetry of the space charge distribution in cable insulation, the model is developed in one dimension. In cylindrical coordinates, the equations are:

Electrical field
$$E(r) = \frac{1}{\varepsilon r}\int_a^b r \cdot \rho(r)\ dr + \frac{K}{r} \tag{4.1}$$

Continuity
$$\frac{\partial \rho}{\partial t} = -\nabla \cdot J \tag{4.2}$$

Ohm's law
$$J = \sigma(E, T) \cdot E \tag{4.3}$$

where E is the electric field; ε is the permittivity of polyethylene and is assumed to be a constant independent of the electric and thermal conditions in this work; ρ is the free charge density distributed in the radius r within the insulation domain from the inner radius, a, and outer radius, b, of the insulation; K is a constant of integration; J is the current density (flux); T is temperature and σ(E,T) is the field and temperature dependent conductivity as described in Section 2.4.

Combining equation (4.2) and (4.3), yields the following equation that describes the growth of the space charge in both time and space:

$$\rho + \frac{\epsilon}{\sigma}\frac{\partial \rho}{\partial t} = J \cdot \nabla(\frac{\varepsilon}{\sigma}) \tag{4.4}$$

The (cylindrical) insulation domain is discretized by m nodes with equal spatial intervals of distance dr as shown in Figure 4-1. The two extra nodes at each end of the insulation domain represent the two electrodes (semicon/insulator interfaces).

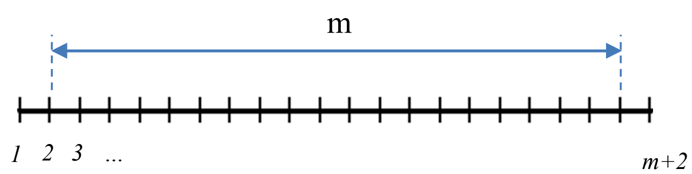

Figure 4-1. Simulation domain comprises m nodes for the insulation and two nodes at terminals representing the electrodes.

In the Finite Difference Method, equation (4.4) can be written as:

$$\rho_i^{n+1} = \sigma_i^n J_i^n \cdot \frac{\Delta t}{2\Delta r}\left(\frac{1}{\sigma_{i+1}^n} - \frac{1}{\sigma_{i-1}^n}\right) - \left(\frac{\sigma_i^n}{\epsilon}\Delta t - 1\right)\rho_i^n \tag{4.5}$$

where Δt and Δr are the time and spatial steps, i = 3,4,…m in the insulation domain and n is the iteration number.

4.2.2.2 Electrode charge

To determine the electrical field across the insulation, the electrode charge which is the combination of capacitive charge and induced charge due to the bulk space charge needs to be determined first.

The capacitive charge density, Q_{DC}, in the simulation domain can be calculated from the capacitive surface charge density which is determined by the Laplacian field E_L (at radial positions, r = a and r = b) and the permittivity, ε, of the insulation as:

$$Q_{DC} = \varepsilon E_L/(\Delta r/2) \tag{4.6}$$

Substituting Equation 2.6 for the Laplacian field E_L at the inner interface r = a, results in:

$$Q_{DC}(r=a) = \frac{\varepsilon U_0}{a ln\left(\frac{b}{a}\right)\left(\frac{\Delta \mathrm{r}}{2}\right)} \tag{4.7}$$

The charge density induced by the accumulated bulk space charge on the inner electrode (i=1) is then calculated from [65]:

$$q_e^n = -\left(\int_a^b \left(1 - \frac{\ln\left(\frac{r}{a}\right)}{\ln\left(\frac{b}{a}\right)}\right) \cdot \rho(r)^n \cdot 2\pi r\, dr\right)/(\Delta \mathrm{r}/2) \tag{4.8}$$

To calculate the electrical field based on Equation (4.1), it is only necessary for one of the electrode charge densities to be known.

4.2.2.3 Electrical field and Voltage

The electric field, based on Equation (4.1), at iteration step n is given by

$$E(r)^n = \frac{1}{\varepsilon r}\int_a^b r \cdot (\rho_i^n + Q_{DC} + q_e^n)\, dr \tag{4.9}$$

and the corresponding voltage distribution is [102]:

$$V(r)^n = \int_a^b E(r)^n\, dr \tag{4.10}$$

4.2.3 Simulation methodology

The simulation program developed in Matlab that implements the charge transport and accumulation due to the field and temperature dependent conductivity is briefly demonstrated in Figure 4-2.

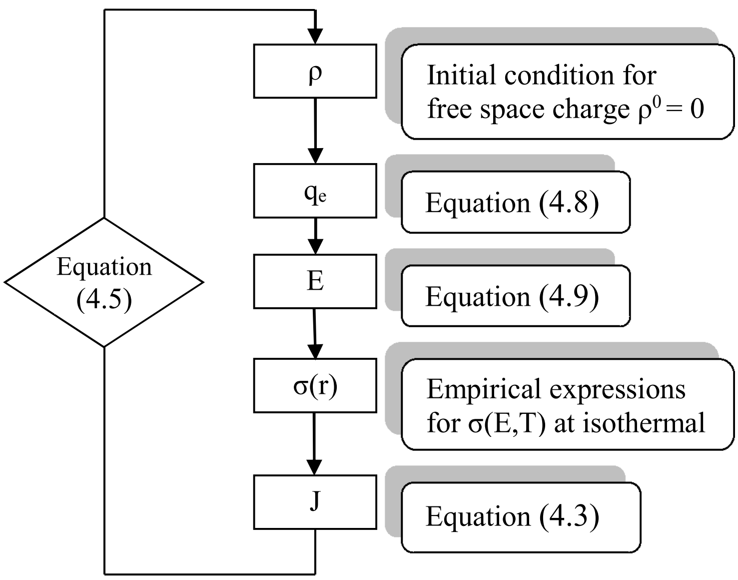

Figure 4-2. Flowchart of the simulation iteration procedure.

The initial condition is that no space charge has accumulated in a (electrically) fresh cable and hence only the capacitive charge in Equation (4.7) due to the applied DC voltage U_0 appears on the electrodes. With this initial condition, the DC electric field is the Laplacian field. The electrical conductivity inside the insulation domain is then calculated based on the expression introduced in Section 2.4 (Equations (2.3) to (2.2)) subject to a specific isothermal temperature. The current flow, J, is then determined using Equation (4.3). With the above initial conditions, the iteration of charge transport starts obeying Equation (4.5).

Based on the procedure given in Figure 4-2, a Matlab simulation program was written that calculates the space charge density, electrical field and voltage distribution as a function of time from voltage application. As an example, the space charge density, electric field and electric potential within the insulator domain, of relative permittivity 2.3, are shown in Figure 4-3 (a), (b) and (c) respectively after a time of 236 minutes. In addition, in Figure 4-3 (d) the ratios of two interfacial stresses E_a/E_b are recorded throughout the simulation time.

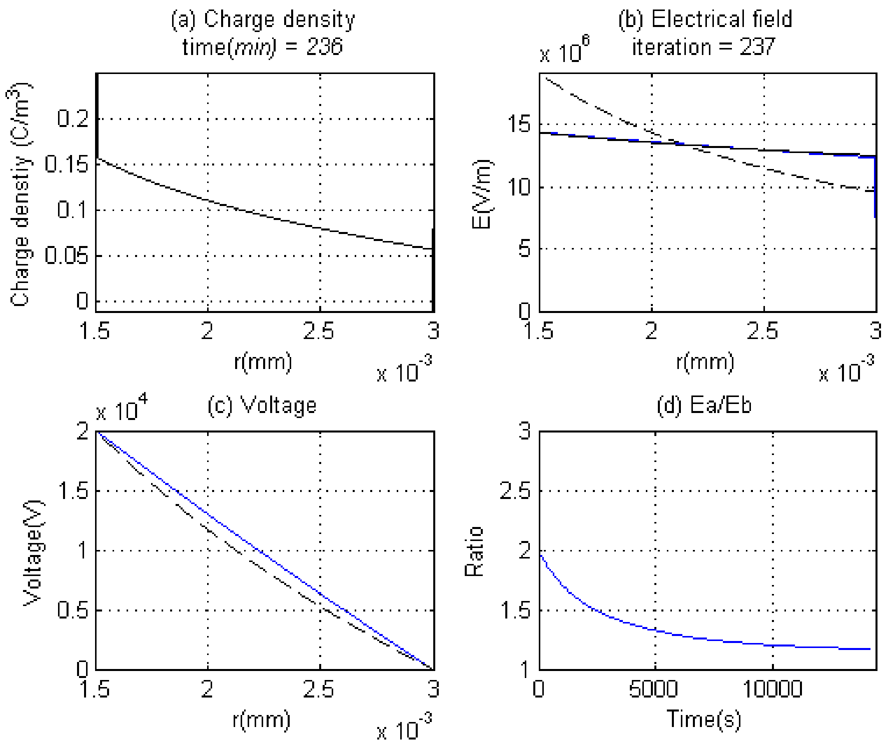

Figure 4-3. Matlab simulation tool for the unipolar charge transport model. The software interface displays the real-time space charge density, electrical field and voltage distribution in (a), (b) and (c) respectively. The black dash lines correspond to the initial conditions and the blue solid lines indicate the iteration results at 236 minutes. (d) displays the historical ratios of two interfacial stresses E_a/E_b during the iteration. The simulation parameters refer to Table 6-1. In specific, σ model 1 was used with 20 kV DC voltage at 50 °C.

The results demonstrate that space charge accumulation occurs within the bulk of the insulation and therefore modifies the electric field distribution within the cable insulation becoming much more uniform compared with the initial Laplacian field. The voltage across the insulation remains the same after the accumulation of space charge and therefore the model is electrostatically consistent. The time evolution of the space charge accumulation is shown as the ratio of the electrode electric fields (E_a/E_b). Space charge accumulation reaches a steady state after about 14000 seconds for the parameters used in this simulation.

4.2.3.1 Heterocharge and homocharge

The unipolar charge simulation model as introduced so far does not include the formation mechanisms of charge injection or ionization of impurities. To be able to mimic the experimental results with homocharge or heterocharge formation, an artificial modification term for the insulation conductivity is introduced. This modification term originates from [103] where an exponential dependence on conductivity close to the electrode interface is described as a consequence of the impurity diffusion into the insulation at the semicon layers. The modified conductivity is expressed as:

$$\sigma_M(r) = \sigma(E,T)(1 + (n_a - 1) \cdot e^{\frac{a-r}{d_a}})(1 + (n_b - 1) \cdot e^{\frac{r-b}{d_b}}) \qquad (4.11)$$

where n_a and n_b are the magnification ($n_{a,b} > 1$) or reduction ($n_{a,b} < 1$) term for the conductivity in the homocharge/heterocharge formation region adjacent to the inner semicon interface at radial position a and outer semicon interface at radius b, d_a and d_b are the distance constants that characterize the thicknesses of the homocharge/heterocharge regions at the inner interface a and outer interface b respectively.

The following example shows the effect of the modification term on the formation of homocharge and heterocharge compared with the original non-modified charge distribution (σ_E). On the inner interface, magnification terms of n_a = 10 (σ_1) and n_a = 100 (σ_2) were applied while reduction term of n_b = 1/10 (σ_1) and n = 1/100 (σ_2) were used for the outer interface as shown in Figure 4-4. With a +12 kV DC voltage applied on conductor, positive charges accumulated, shown in Figure 4-5, adjacent to the inner interface as homocharge and outer interface as heterocharge. The corresponding steady state electrical fields are shown in Figure 4-6.

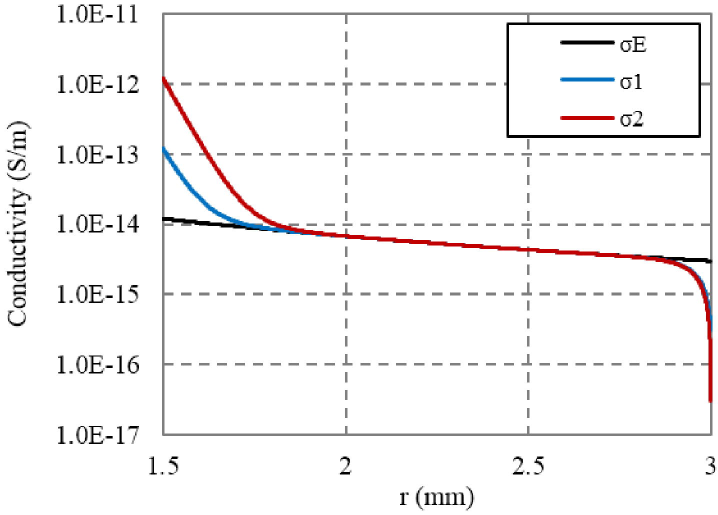

Figure 4-4. Conductivity distributions along the radius. σE: field dependent with na = 1, nb = 1. σ1: na = 10, nb = 1/10, da = db = 0.05 mm. σ2: na = 100, nb = 1/100, da = db = 0.05 mm.

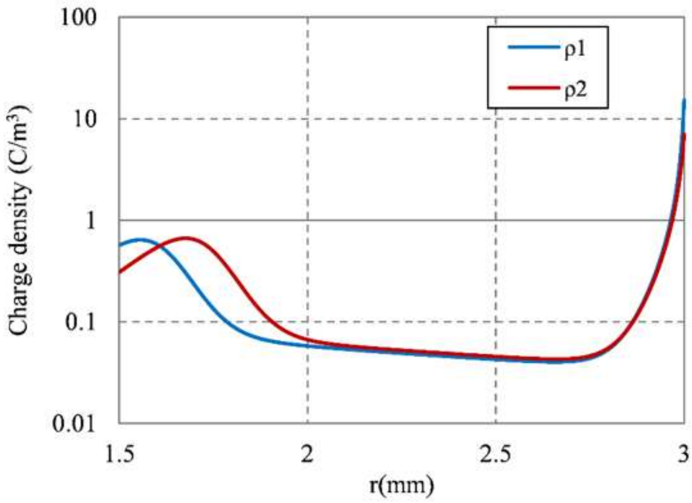

Figure 4-5. Space charge profiles, ρ_1 and ρ_2, at steady state with respect to the initial conductivity distribution of σ_1 and σ_2 respectively.

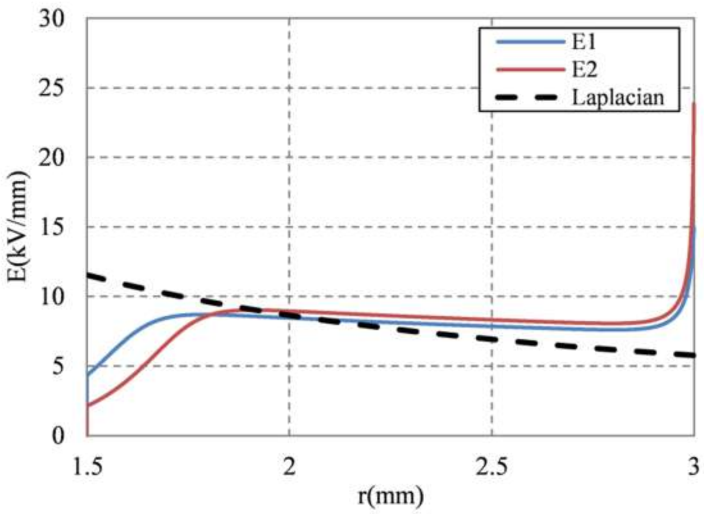

Figure 4-6. Electrical field distributions responding to the charge distributions in Figure 4-5 compared with the Laplacian field.

4.3 1D simulation of PEA acoustic signal

4.3.1 Introduction

To be able to directly compare the charge transport simulation results obtained using the simulation model as described in Section 4.2 with experimental PEA results, an additional simulation model realizing the formation of acoustic waves and their propagation through the PEA apparatus is required. In this section, a 1D model will be introduced with the assumption of ideal coaxial geometry of the cable (i.e. non-deformed cable) and a cylindrical acoustic path (curved electrode) and sensor.

4.3.2 Generation of PEA acoustic signal

The excitation source for the PEA acoustic signal is the pulsed electric field ΔE. Recalling the electrostatic force in a dielectric containing space charge is given by Equation (2.7) and ignoring the electrostriction term, the force vector can be written as:

$$\vec{f} = \rho\vec{E} - \frac{1}{2} E^2 \nabla\varepsilon \tag{4.12}$$

To avoid the complication of the calculation of the charge density at the interfaces, the force density can be expressed as the divergence of Maxwell's tensor M_{ij}. The advantage of using this formulation is first introduced into PEA theory by Holé [71] that the force vector can be written in terms of the electric field vector without the need to calculate the interfacial surface charge densities. Eliminating ρ using Poisson's equation [104] the force vector can be written:

$$f_i = \frac{\partial M_{ij}}{\partial x_j} = \frac{\partial(\varepsilon E_i E_j)}{\partial x_j} - \frac{1}{2}\frac{\partial(\varepsilon E^2)}{\partial x_i} \tag{4.13}$$

where the indexes, i and j refer to the components of the 3-D vector. [71]

Then assuming the permittivity is a constant, the Maxwell tensor becomes:

$$M_{ij} = \varepsilon E_i E_j - \frac{1}{2}\varepsilon E^2 \delta_{ij} \tag{4.14}$$

The application of pulse field, ΔE, results in a transient term in the tensor as:

$$M_{ij} + \Delta M_{ij} = \varepsilon(E_i + \Delta E_i)(E_j + \Delta E_j) - \frac{1}{2}\varepsilon(E + \Delta E)^2 \delta_{ij} \tag{4.15}$$

which can be re-expressed as:

$$\Delta M_{ij} = \varepsilon(E_i \Delta E_j + E_j \Delta E_i + \Delta E_i \Delta E_j) - \frac{1}{2}\varepsilon \Delta E^2 \delta_{ij} - \varepsilon E_k \Delta E_k \delta_{ij} \tag{4.16}$$

In one dimension, Maxwell's tensor becomes a scalar, M, as:

$$\Delta M = \varepsilon E \Delta E + \frac{1}{2}\varepsilon \Delta E^2 \tag{4.17}$$

To define the shape of the applied voltage pulses, a normalised time dependent coefficient V_p was introduced to represent the time dependent applied voltage having a Gaussian wave shape and is given by

$$V_p(t) = e^{\frac{-4\ln(2)}{t_w{}^2}\cdot(t-t_{p})^2} \tag{4.18}$$

where t_p defines the pulse delay time and t_w is the pulse width.

An example of the applied Gaussian pulse of unit magnitude is shown in Figure 4-7.

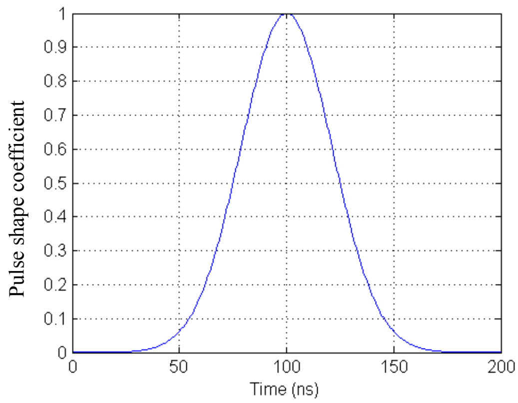

Figure 4-7. The shape of a Gaussian voltage pulse with a width (at half maximum) of 50 ns.

Then the time and radially dependent pulse electric field can be expressed as

$$\Delta E(r,t) = E_p(r) \cdot V_p(t) \tag{4.19}$$

where $E_p(r)$ is the radial dependent field for applied pulse voltage. It is normally assumed that the applied pulse duration is too small in magnitude and duration to cause any space charge accumulation [20] and so $E_p(r)$ can be calculated using Laplace's equation. After substitution into Equation (4.17) followed by the above pulsed field, Maxwell's scalar becomes:

$$\Delta M = \varepsilon E_{DC} E_p V_p(t) + \frac{1}{2}\varepsilon \Delta E^2 V_p(t)^2 \tag{4.20}$$

4.3.3 Wave propagation in 1D cylindrical coordinates

In one dimension and using cylindrical coordinates, the governing equations for acoustic wave propagation in isotropic lossless media are [105]:

$$\frac{\partial P}{\partial t} = -C\frac{1}{r}\frac{\partial(v \cdot r)}{\partial r} \tag{4.21}$$

$$\frac{\partial v}{\partial t} = -\frac{1}{\rho}\frac{\partial P}{\partial r} \tag{4.22}$$

where the coordinate, r, corresponds to the radius. P is the scalar pressure field, *v* is the vector velocity in the radial direction, C represents the bulk modulus (reciprocal of the compressibility) which is approximated to the product of density (ρ) and the square of sound velocity (c), i.e.

$$C = \rho c^2 \tag{4.23}$$

Including the source term which is the Maxwell scalar as given in Equation (4.13), Equation (4.21) becomes:

$$\frac{\partial P}{\partial t} = -C\frac{1}{r}\frac{\partial(v \cdot r)}{\partial r} + \frac{M}{dt} \tag{4.24}$$

The acoustic simulation is based on the Finite-Difference Time-Domain (FDTD) method which was first proposed for solving the time-dependent Maxwell's equations [106]. The FDTD method can be applied to simulate the acoustic wave propagation and scattering as the governing equations for acoustic wave propagation as one field is related to the spatial derivative of the other field.

4.3.4 Simulation domain

The finite difference simulation domains are shown in Figure 4-8. The dimension of the cable is consistent with the mini-cable used for experiments (dimensions see Section 2.5). The centre of the mini-cable is at the origin of the cylindrical coordinate system (i.e. r = 0). Only the wave propagation in the r-direction, i.e. towards the sensor, is of interest, as the oppositely propagated signal would be separated by the time delay of the additional acoustic path in the cable domain. Acoustic absorption and dispersion are not considered in either the cable or the electrode domains. However, this could be implemented by augmenting the acoustic wave equations to express an acoustically absorbing and dispersive media. Alternatively, the acoustic attenuation and dispersion can be applied directly on the simulated signal by convoluting with the propagation transfer function G_a (Section 3.12.1). Therefore the length of the electrode only needs to satisfy Equation (3.2) to avoid space charge signals being overlapped by their reflections. The PMMA block is of sufficient thickness to avoid any reflected acoustic waves at the air-PMMA boundary appearing in the space charge measurement window. As the influence of the coupling between the sensor and acoustic absorber will be extensively discussed with a Pspice simulation model in Section 4.5, the PMMA is defined here as identical to the acoustic properties as the PVDF-TrFE sensor to enable a perfectly matched boundary condition. Two outputs signals were generated by this simulation model: 1. the pressure at the surface (lower r) of the sensor is recorded as the PEA acoustic signal; 2. the integral of the pressure wave over the sensor domain is regarded as proportional to the PEA voltage output signal assuming that the piezoelectric constant d_{33} is a constant for all frequency components making up the PEA output signal. In addition, a RC high pass filter is built into the MATLAB model to simulate the PEA raw output with the effect of the sensor – amplifier (buffer) circuit included in the system response.

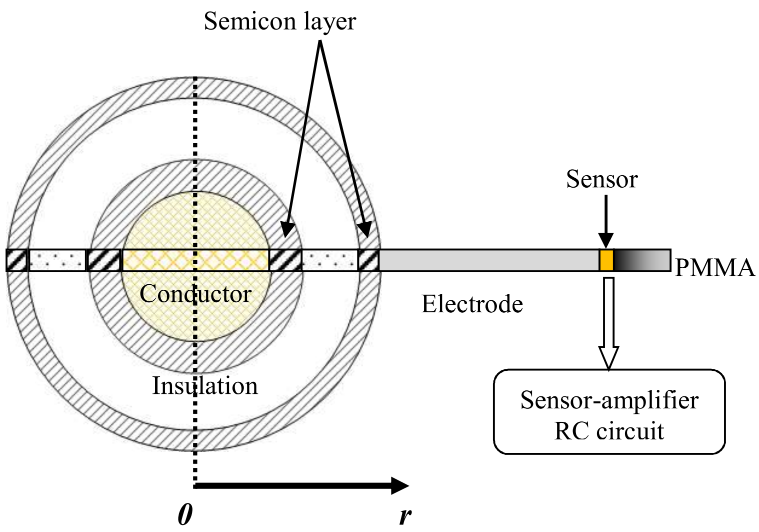

Figure 4-8. Schematic representation of the simulation domains: mini-cable, electrode, sensor and PML layers.

4.3.5 Example application of the 1D simulation model

Combining the 1D PEA acoustic model with the unipolar charge transport model as described on section 4.2, enables the raw PEA output signal to be simulated. This will enable space charge distributions to be directly compared with experimental PEA measurements. The electric field distribution obtained from the simulated space charge data shown previously in Figure 4-6, was used as the input to the PEA 1-D simulation model described above. The simulated PEA voltage signal (as introduced in the last subsection) from the PEA acoustic simulation model (using a 30 ns Gaussian voltage pulse, 52 μm thickness, PVDF-TrFE sensor of 170 pF capacitance and 3.2 kΩ input impedance buffer amplifier) are shown in Figure 4-9. Comparing with the outputs of charge transport model shown in Figure 4-5, the outputs of the acoustic model now includes the signal related to the electrode charges along with the homocharge and heterocharge regions in the insulation next to the semicon layers. The presence of heterocharge has the effect of boosting the charge on the adjacent electrode whilst the region of homocharge has the opposite effect.

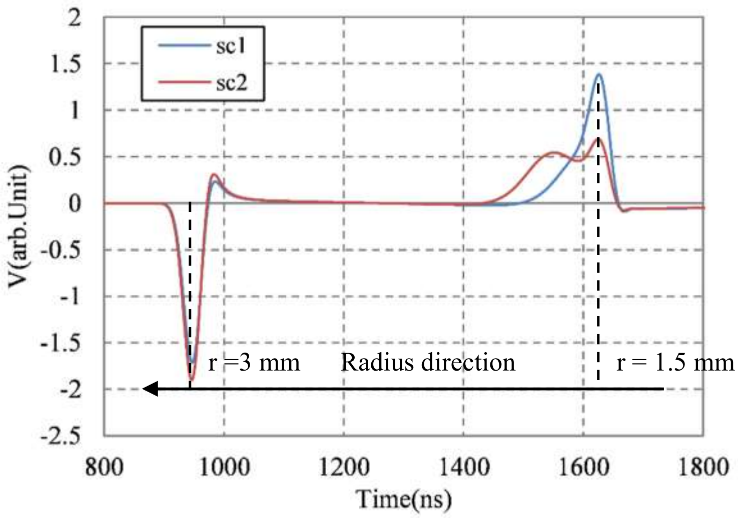

Figure 4-9. Simulated PEA raw output for the space charge distribution predicted in Figure 4-5. 30 ns Gaussian voltage pulse, 52 µm 170 pF PVDF-TrFE sensor and 3.2 kΩ buffer were used in the simulation model.

4.4 Bulk polarization charge in cylindrical geometry

It has been widely accepted for interpreting the PEA measurement results that a zero (flat) baseline represents the condition of no space charge within the bulk of the sample. This is true for measuring homogenous plane-plane samples. Based on this assumption, the deconvolution procedure [68] for removing the system responses (which normally includes signal overshoots) using an artificial Gaussian signal becomes possible. However when applying the PEA measurement technique to the cylindrical geometry cable samples, the PEA method should also respond to the bulk polarisation charge that is induced due to the non-uniform applied electric field. In this case a non-zero baseline would be expected even in the absence of free space charge as shown in Figure 4-10.

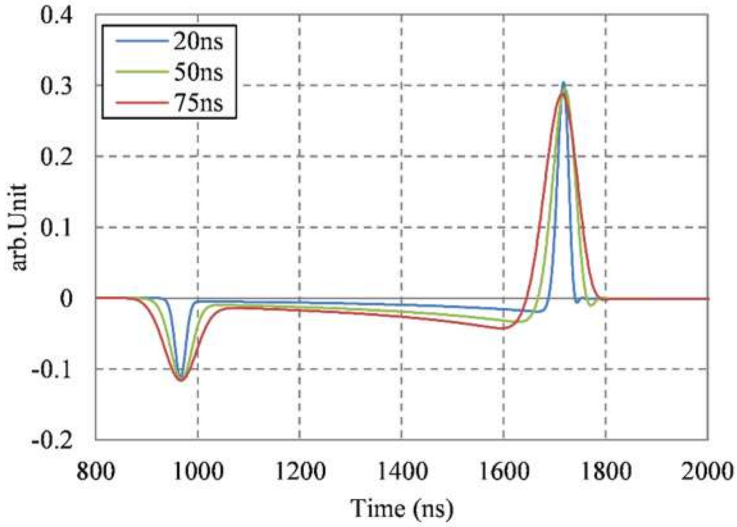

Figure 4-10. The PEA acoustic signals (or output with ideal thin sensor) generated from the 1-D PEA acoustic model for measuring the mini-cable with Laplacian DC field and three different pulse widths: 20 ns, 50 ns and 75 ns.

Based on Poisson's equation, in a homogenous material (where $\nabla\varepsilon = 0$) the relationship between electric field and net space charge density ρ follows [107]:

$$\nabla \cdot \vec{E} = \rho/\varepsilon \tag{4.25}$$

This equation implies that where the space-derivatives of E are not zero, there must be space charge formation. The electrical field in the cable insulation is primarily geometry determined. Consequently, the divergent electrical field leads to local polarization of the insulation material in the radial direction. The PEA output should therefore respond to the polarization charge and should therefore generate an output signal with a sloped baseline between two electrode signals when there is no free charge (net charge) as shown by the simulation result in Figure 4-10. The example profiles with different pulse width also indicates that the relative magnitude of the slope is proportional to the pulse width or, to be more specific, the spatial resolution of the measurement system.

So far, the slope in the PEA output due to the non-uniform polarization of the insulation material under divergent electric field has never been recorded in the experimental PEA data, even though much effort had been made to verify the ability of the system for measuring such a low frequency signal. Further work is therefore required to be done to understand the reason for the absence of the slope in the experimental PEA output signal under divergent electric fields focusing on examining the assumptions made in simulation for the origin of the PEA signal (i.e. the electrostatic force term) and the wave propagation in the dielectric.

4.5 Simulation of piezoelectric sensor

4.5.1 Introduction

The 1D PEA acoustic simulation tool in Section 4.3 provided a simple model for the sensor response (the integral of the pressure wave within the sensor domain). However the FDTD based simulation model is less effective in terms of investigating, for example, the effect of the sensor thickness and the acoustic matching with the backing acoustic absorber.

The piezoelectric sensor is used to convert the PEA acoustic signals (pressure waves) to voltage signals. An essential requirement for the correct interpretation of PEA output signals is that in the conversion, the signal does not suffer distortion and the voltage output remains an accurate representation of the profile of the acoustic pressure wave. In reality, a perfect matched backing material for the sensor film is almost impossible and hence distortion due to the reflection of acoustic waves at the two surfaces of the sensor material is inevitable. Therefore it is necessary to identify the optimized thickness of the sensor with respect to the width of acoustic signal while considering the practical imperfections of acoustic reflections.

For these purposes, a Pspice simulation model of the piezoelectric sensor was built based on existing published works [108-114]. The model was used to determine an optimum thickness from the commercially available dimensions for the PVDF-TrFE film that minimises signal distortion given that, for the experimental PEA apparatus, the acoustic waves have a duration determined by the width of the applied voltage pulse (20 ns).

4.5.2 Literature review of piezoelectric sensor modelling

Using the electromechanical analogy, Mason's electrical equivalent circuit for modelling a electromechanical piezo transducer was first published in 1942 [108], which features a negative capacitance and an ideal transformer for the electromechanical coupling. Afterwards, Redwood [109] incorporated a section of transmission line into Mason's model (substituting the T-network in Mason's circuit) to account for mechanical waves propagating inside the transducer. In 1970, Krimholtz, Leedom and Matthaei [110] introduced an alternative equivalent circuit, the KLM model, which features a frequency dependant electrical network to provide a better electrical representation of the piezoelectric sensor [111]. To avoid the presence of discrete components with negative capacitance, frequency dependent transformer ratio and reactance, Leach [110] developed a controlled-source analogous circuit model for elementary piezoelectric transducers. Based on Leach's model, Puttmer, et al. [112] took the acoustic losses of transducers with a low mechanical Q factor into account by adding resistance in the acoustic transmission line

For materials like PVDF and PVDF-TrFE, due to their frequency dependent dielectric, elastic and piezoelectric properties as well as high dielectric and mechanical losses, special consideration is required when applying classical electromechanical circuit modelling [113]. To realise the mechanical/viscoelastic, dielectric/electrical and piezoelectric/electromechanical losses, Dahiya, et al. [114] developed a SPICE model using complex elastic, dielectric and electromechanical constants.

4.5.3 Pspice model

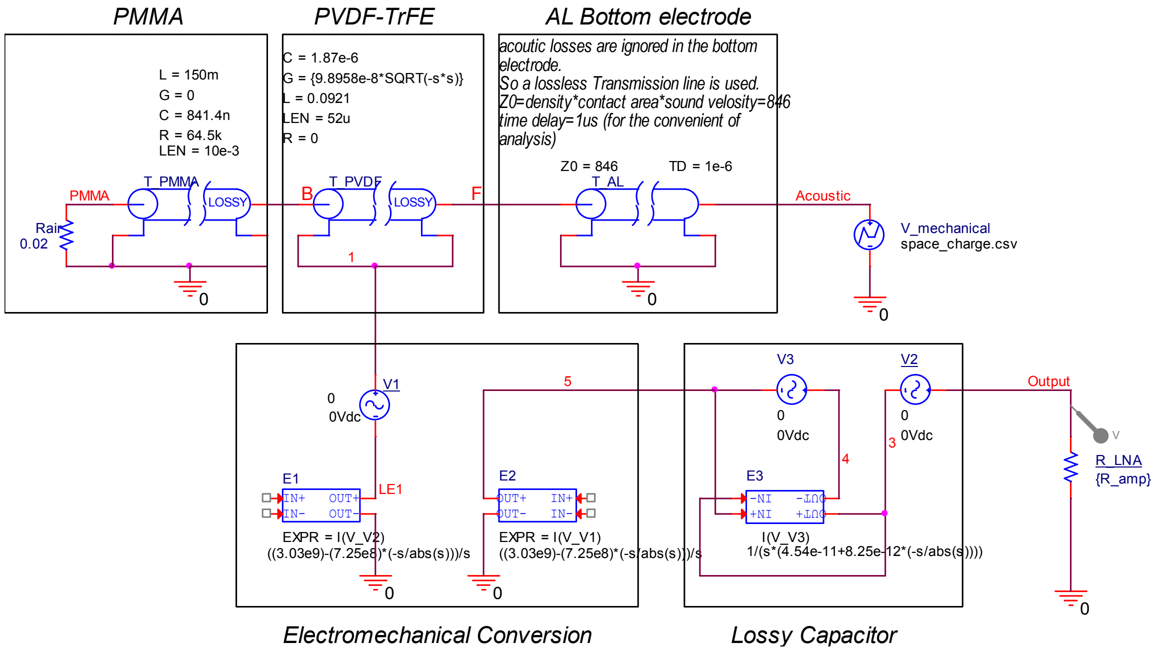

Figure 4-11. Schematic of the Pspice equivalent model of a piezoelectric sensor.

The Pspice simulation model shown in Figure 4-11 was adapted from the lossy piezoelectric polymers model in [114]. This model is comprised of five blocks representing the main components of the PEA apparatus: aluminium bottom electrode, PVDF-TrFE and PMMA blocks implementing the acoustic transmission from sample to sensor; electro-mechanical conversion block realised by a voltage controlled voltage source and a lossy capacitor accounting for dielectric losses in the sensor material. Acoustic losses are neglected in the aluminium bottom electrode to simplify the simulations. The piezo sensor is assumed to be connected to an amplifier/buffer having an input impedance of value, R_LNA, or operating at open circuit with no load connected when the value of R_LNA equal to infinity. Values of parameters used in the model are summarised in Table 4-1.

Table 4-1. Values of parameters for the Pspice simulation model.

	Parameter	Value
PVDF-TrFE	Area(m)	4.90E-05
	C(F)	1.87E-06
	G	9.8958e-8*SQRT(-s*s)
	L(H)	0.0921
	LEN(m)=thickness	5.20E-05
	R	0
PMMA	C(F)	8.41E-07
	G	0
	L(H)	1.50E-01
	LEN(m)	1.00E-02
	R	6.45E+04
AL bottom electrode	Acoustic impedance(Ω)	8.46E+02
	TD(time delay in second)	1.00E-06
Air	Acoustic impedance(Ω)	2.00E-02
Gain terms	E1 and E2	((3.03e9)-(7.25e8)*(-s/abs(s)))/s
	E3	1/(s*(4.54e-11+8.25e-12*(-s/abs(s))))

4.5.4 Acoustic mismatch

In the PEA apparatus, a PMMA block acts as an acoustic absorber and provides mechanical support for the piezoelectric PVDF-TrFE film. To demonstrate the importance of acoustic matching, three matching conditions were simulated: where the acoustic impedance of the acoustic terminal was much lower, the same and much higher than that of PVDF-TrFE. Specifically, the acoustic parameters for air, PVDF and aluminium (values see Table 4-1) are utilised respectively as backing materials. The simulation results for the above three conditions are shown in Figure 4-12.

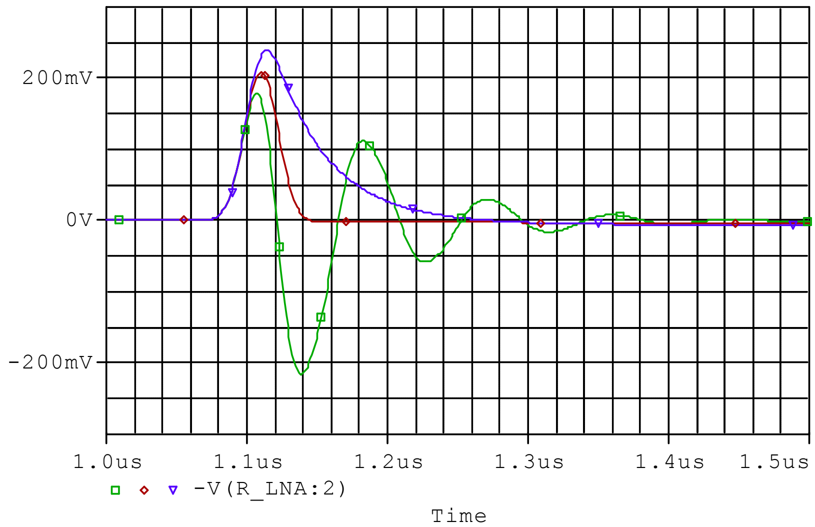

Figure 4-12. Simulated piezo voltage signals generated by a 52 µm PVDF-TrFE film subjected to a 23 ns Gaussian acoustic wave with a perfectly matched boundary (red), air soft boundary (green) and aluminium hard boundary (blue).

The non-disturbed signal, shown in Figure 4-12, was obtained when PVDF is the backing material. In this case no acoustic reflection occurs to disturb the acoustic signal being measured. Air can be considered as a soft boundary for PVDF-TrFE sensor. Reflected waves from the sensor-air interface have 180˚ phase shift to the incident wave, which leads to severe ringing of the PVDF sensor output voltage, both positive and negative. The damping of the signal oscillation depends on the acoustic reflection coefficients at the boundaries of the sensor and the acoustic losses within PVDF-TrFE. On the other hand, aluminium can be treated as a hard boundary for the PVDF-TrFE sensor. Reflected waves from the sensor-Aluminium interface would maintain the same polarity (no phase shift). For aluminium-sensor-aluminium system, the reflected waves from two ‘hard’ boundaries maintain the same polarity leading to broadening of the detected pulse and a slight magnitude enhancement. In practice a PMMA block is employed in the PEA system design as the backing material. PMMA is chosen to minimise acoustic reflections due to that its acoustic impedance is similar to that of the PVDF-TrFE. Therefore, acoustic mismatch would still be present at the sensor/PMMA interface to some extent especially considering a temperature range of 20 °C – 70 °C and therefore the reflected acoustic wave may disturb slightly the space charge signal. This is examined in the next section.

4.5.5 Optimized thickness of sensor film

As discussed above, the acoustic impedance mismatch between sensor and backing material would lead to signal distortion affecting both the pulse shape and magnitude. Moreover in practice, the mismatch is almost inevitable. This section discusses how to minimise the influence of the backing material by optimising the thickness of the sensor film.

A sequence of acoustic pulses with a variety of widths (8 ns, 24 ns and 46 ns) as shown in Figure 4-13 was applied to the PVDF-TrFE film in the simulation model. Voltages generated across the PVDF-TrFE film (under open circuit condition) with various combinations of pulse width and sensor thicknesses are shown in Figure 4-14. In addition, for the convenience of analysis, the signal distortion conditions are classified in Table 4-2.

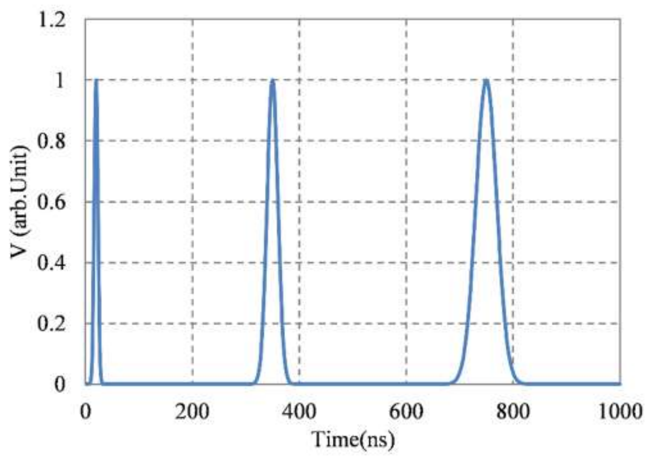

Figure 4-13. Input signal for the Pspice simulation model comprising three Gaussian pulses with the width of 8 ns, 24 ns and 46 ns.

As shown Figure 4-14, when the acoustic pulse width in the PVDF sensor is much less than the sensor thickness, the output voltage amplitude saturates with the 28 μm and 52 μm films giving nearly the same peak amplitudes. This is because the voltage induced across the sensor is due to the integral of the pressure wave over the thickness of the sensor. Therefore sensor thicknesses much greater than the acoustic pressure pulse wavelength are undesirable.

According to simulation results, only when the wave propagation time through the sensor film is less than half of the pulse width, the generated piezoelectric voltage across the sensor film would be less affected by the acoustic mismatch of the backing material in terms of both pulse shape and pulse magnitude. This is particularly the case when the 9 µm sensor film is used. The magnitude would still differ from that when a perfect matched boundary is used. However as long as there is no frequency dependent acoustic reflections, the acoustic wave inside the sensor with different width would be attenuated or strengthened in proportion according to the corresponding acoustic reflection coefficient.

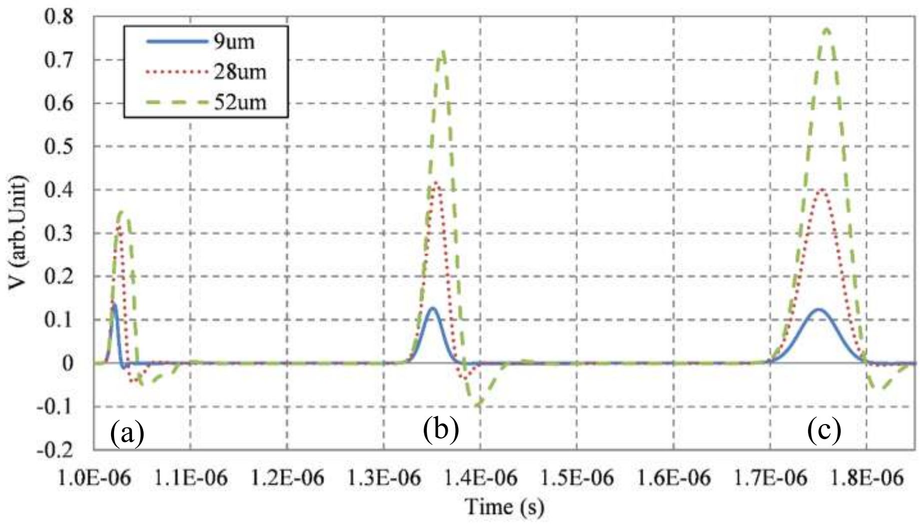

Figure 4-14. Simulation results of the piezoelectric outputs with sensor films of 3 three different thicknesses (9 µm, 28 µm and 52 µm) when a non-perfect acoustic matching present; three different width of Gaussian pulses are used as the source of acoustic wave: (a) 8 ns, (b) 24 ns and (c) 46 ns.

Table 4-2. Evaluation of pulse distortion conditions with different combinations of pulse widths and sensor thicknesses when acoustic mismatch is present at the sensor-backing interface. The colours indicate the degree of signal distortion from serious (red) to modest (yellow) and no distortion (green).

Thickness (um)	Time of Propagation (ns)	8 ns Pulse	24 ns Pulse	46 ns Pulse
9	4	modest	no	no
28	12	serious	modest	no
52	23	serious	serious	modest

4.6 Cable deformation

4.6.1 Introduction

The fundamental assumption for the 1D simulation and also the interpretation of experimental PEA results is that the cable is of an ideal cylindrical geometry. This assumption is feasible if ignoring defects of the cable itself and using a curved electrode matching the cable outer surface. However if a flat electrode was used, the cable deformation against electrode surface might occur. Consequently, it is necessary to determine the degree of distortion of the mini-cable sample and thus the influence of this deformation upon the PEA outputs. In order to introduce cable imperfections and deformation it is necessary to extend the 1-D simulation models introduced earlier in this chapter to 2-dimensions along with the development of a mechanical simulation model to determine the cable deformation for a range of PEA electrode base plate geometries (flat and curved) under a defined clamping force.

In this section, a two-dimensional mechanical simulation model is developed in COMSOL Multiphysics to mimic the deformed (cross-sectional) geometry of the mini-cable subjected to the cable clamp force as used in the real PEA measurement system. The simulation results could be then used to calculate the electric field distribution in the distorted cable and applied to a 2-D PEA acoustic simulation model (Section 4.7) to evaluate the effect of cable clamping pressure on the PEA output. At this stage, due to the high computational overhead in solving the acoustic propagation in 2-D, the simulations will be restricted to space charge free situations where the only charges are the electrode charges plus bulk polarisation charge. In addition, useful information would be generated by the simulation, for example to determine the contact area of the cable and the flat base plate (contact width in 2D model), and the von Mises stress distribution.

4.6.2 Mechanical Model description

The 2D Solid Mechanics interface from the Structural Mechanics Module in COMSOL is appropriate for this simulation.

The geometry of the model is shown in Figure 4-15. A mini-cable sample is clamped to the bottom electrode using a 3-point contact. The length of the cable clamp is 30 mm along the cable axial direction. The mini-cable model has the same dimensions with the mini-cables used in the experiments, comprising the aluminium conductor, polyethylene insulation layer and the two semicon layers which are assumed as polyethylene in this mechanical simulation.

	Radius (mm)
Conductor	0.75
Inner semicon	1.45
Insulation	2.95
Outer semi	3.12

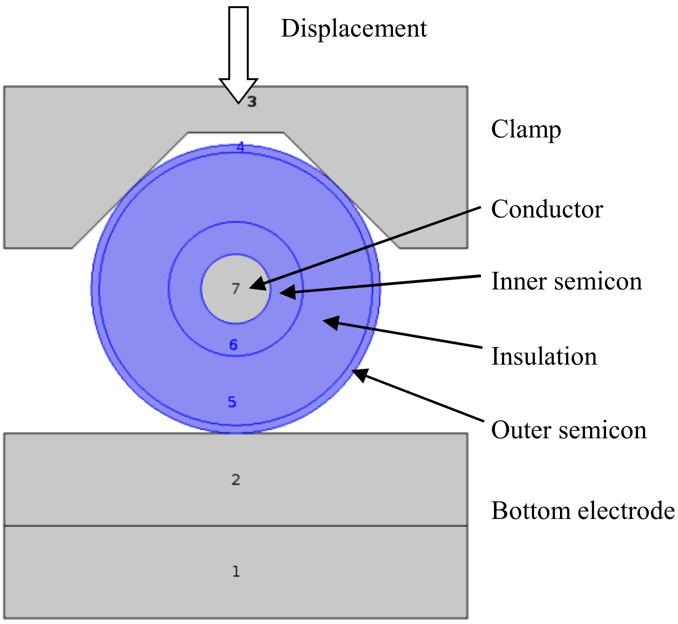

Figure 4-15. Geometry of the model built in COMSOL. Domain 1, 2 are aluminum bottom electrode; Domain 3 is the aluminum cable clamp; Domain 4 and 6 are polyethylene based semicon layers; Domain 5 is the polyethylene insulation layer. Domain 7 is the aluminum conductor.

Contact pairs are defined on the contact boundaries between: mini-cable and clamp, mini-cable and electrode, cable conductor and inner semicon layer. The bottom of the electrode is a fixed constraint. The clamping is realised by applying a prescribed displacement (downwards) on the top boundary of the clamp. Clamping force is calculated from the contact pressure applied to the top surface of the electrode by the cable.

4.6.3 Simulation results

An example of the simulation results (material properties see Table 5-1) are shown in Figure 4-16 and Figure 4-17. Figure 4-16 demonstrates the von Mises force distribution when a force of 380 N was applied onto the cable clamp. The contact width, *d*, was found to be approximately 1.4 mm. The high clamping force also results in high compressional stress in the vicinity of the inner and outer semicon layers. The maximum Von Mises stress in the cable insulation is around 8 MPa. Figure 4-17 highlights the deformation of the geometry. The original non-deformed boundaries are shown as black solid lines while the deformed domains under 770 N clamping force are represented with different colours. Under such a high clamping force, the inner semicon layer was found to be detached from the conductor at two regions.

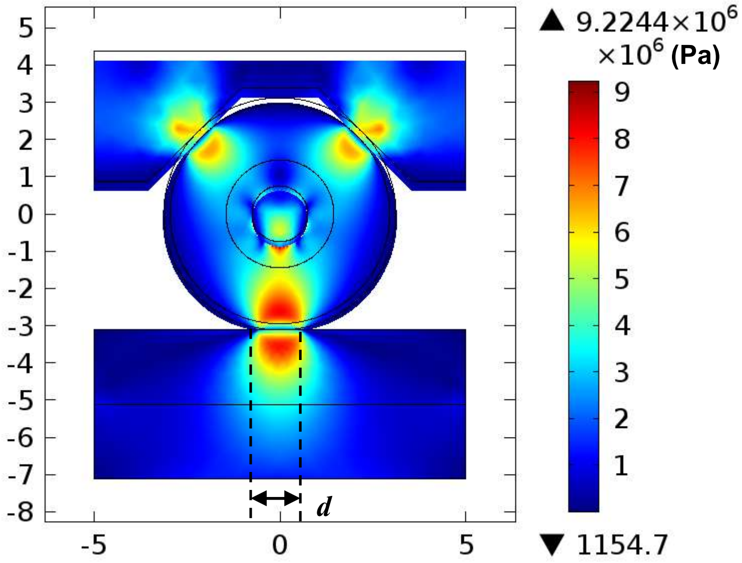

Figure 4-16. Cross-section view of the mechanical stress in the mini-cable sample when the cable clamp has a downward movement of 0.25 mm by applying about 380 N onto the mini-cable. 'd' is the width of contact between the cable and bottom electrode due to mechanical distortion.

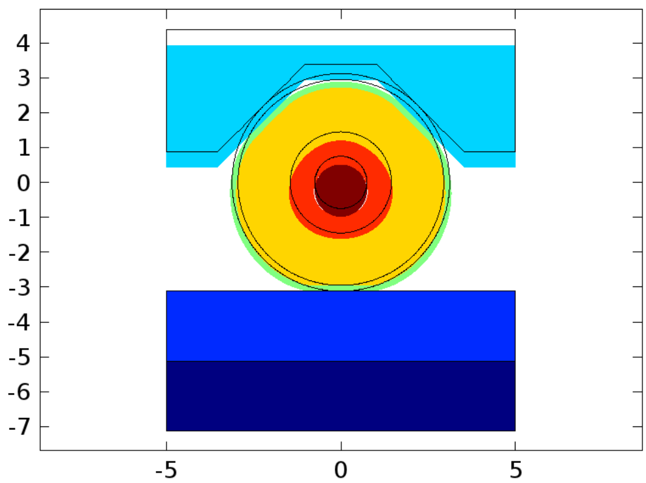

Figure 4-17. Deformed geometry when the clamping force is about 770 N. Original non-deformed boundaries are in black solid lines. Deformed Domains are in different colours.

4.6.4 Maximum clamping force

The simulation also assists in determining the maximum applied clamping force without incurring plastic deformation on the mini-cable insulation. The maximum von Mises forces in the insulation domain under different clamping force are shown in Figure 4-18. Taking a conservative value of the yield stress for polyethylene based insulation as 10 MPa [115], the clamping force applied on the 30mm clamp should be below 550 N.

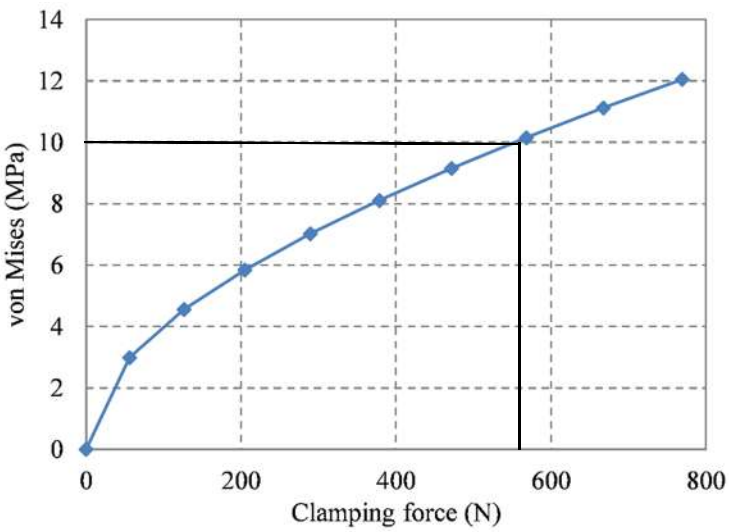

Figure 4-18. Maximum von Mises force in the insulation domain with different clamping force.

4.6.5 Electrical field in deformed cable

The deformed geometry obtained from the mechanical simulation model can be exported to the Electrostatics simulation interface in COMSOL. The required boundary conditions are that an electric potential equal to the applied voltage is specified at the inner semicon – insulation interface and a ground boundary (zero volts) is specified at the outer semicon – insulation interface. The solution of the Laplace electrical field (in the absence of bulk space charge can be obtained based on Poisson's equation in the COMSOL stationary study where the space charge density is set to zero.

The example shown in Figure 4-19 is the surface plot of electrical field magnitude distribution in the insulation domain. As indicated by the contour lines, the field distribution in the space charge measurement region (between cable/electrode contact area and the conductor) is disturbed from the ideal Laplacian case. A line plot of the electrical field along the y-axis in the centre of x-axis (the white dash line in Figure 4-19) is shown in Figure 4-20. Comparing with the dashed line which indicates the Laplace field in the non-deformed insulation, the electrical field in the compressed insulation is significantly different.

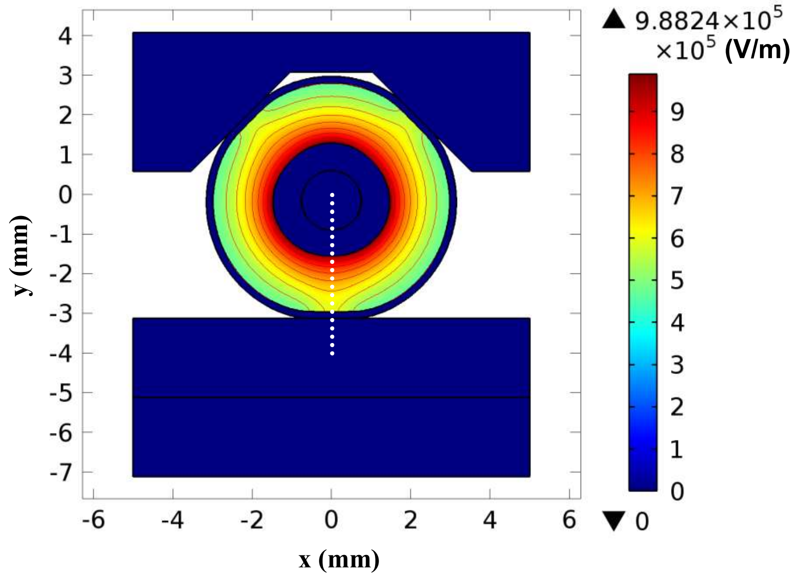

Figure 4-19. Electrical field distribution with contour lines inside the insulation layer with 1 kV DC bias voltage and 470 N clamping force. The unit of colour bar is V/m.

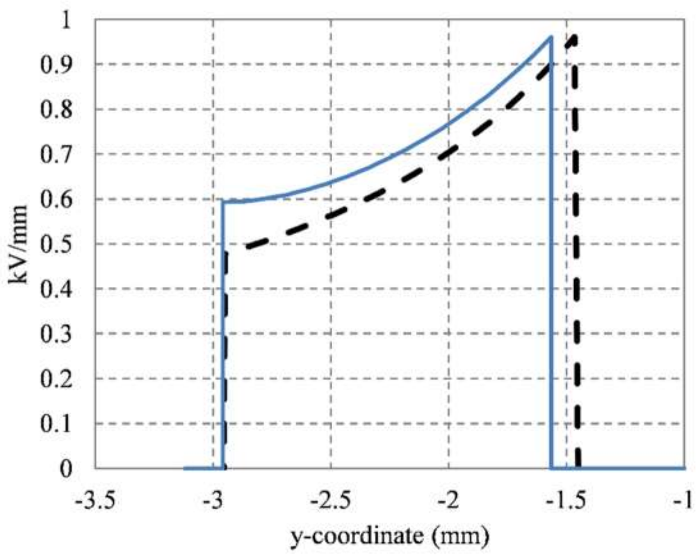

Figure 4-20. Electrical field distribution along the thickness of the insulation with 470 N clamping force. Black dash line is Laplacian field in the non-deformed insulation.

4.7 2D simulation of PEA acoustic signal

4.7.1 Introduction

To evaluate the effect of cable deformation on space charge measurement, the 1D PEA acoustic simulation model (Section 4.3) was extended to two dimensions with the assumption that the cable deformation is consistent along the cable axial direction within the space charge measurement region.

For simplifying the 2D model, only longitudinal waves (and hence the relevant longitudinal components of wave velocity) are considered. As the transverse waves have velocity approximately one-half of the longitudinal velocity they will be separated (in time) by the PEA base electrode acting as an acoustic waveguide (Section 3.9.3.1).

Then the governing acoustic equations for a linearly elastic and isotropic lossless medium in a two dimensional Cartesian coordinate system are:

$$\frac{\partial p}{\partial t} = -C\left(\frac{\partial v_x}{\partial x} + \frac{\partial v_y}{\partial y}\right) \tag{4.26}$$

$$\frac{\partial v_x}{\partial t} = -\frac{1}{\rho}\frac{\partial p}{\partial x} \tag{4.27}$$

$$\frac{\partial v_y}{\partial t} = -\frac{1}{\rho}\frac{\partial p}{\partial y} \tag{4.28}$$

where v_x and v_y are the vector velocity in the x and y coordinate directions respectively, p represents the pressure (scalar), ρ is the mass density of the medium, for longitudinal waves only C_{11} in the elastic stiffness tensor is taken into account i.e. $C = C_{11}$.

4.7.2 Perfectly-matched layer (PML)

Although the simulation of PEA acoustic signal propagation does not involve open-region problems as the air surrounding Polyethylene mini-cable and aluminium electrode will act as a soft boundary condition, it is still reasonable to use absorbing boundary conditions (ABC's) in order to reduce the spatial extent of the computational domain.

The perfectly-matched-layer (PML) absorbing boundary condition [116] is a material-based absorbing boundary condition. The PML introduces a region of high attenuation and produces no acoustic reflections for waves traveling into it.

For associating the attenuation coefficients of the PMLs, α_x and α_y with the vector velocities in the x and y directions, v_x and v_y, the pressure scalar p is artificially split into p_x and p_y [117]:

$$p = p_x + p_y \tag{4.29}$$

Then the acoustic wave equation in the PML region can be constructed as [117]:

$$\rho \frac{\partial v_x}{\partial t} + C\alpha_x \rho v_x = -\frac{\partial p}{\partial x} \tag{4.30}$$

$$\rho \frac{\partial v_y}{\partial t} + C\alpha_y \rho v_y = -\frac{\partial p}{\partial y} \tag{4.31}$$

$$\frac{1}{C}\frac{\partial p_x}{\partial t} + \alpha_x p_x = -\frac{\partial v_x}{\partial x} \tag{4.32}$$

$$\frac{1}{C}\frac{\partial p_y}{\partial t} + \alpha_y p_y = -\frac{\partial v_y}{\partial y} \tag{4.33}$$

The wave equations in the remaining lossless parts of the computational domain have the same form as the equations above but with the attenuation coefficients set to zero.

4.7.3 Computational domain

4.7.3.1 Acoustic path

The actual geometry of the PEA cell containing the acoustic path for PEA acoustic pressure waves is shown in Figure 4-21. Under applied voltage pulses to the cable, the pulsed electric field within the cable insulation causes the space charge to generate pressure waves. These will travel through the cable insulation, outer semicon layer, aluminium bottom electrode and finally act on the piezoelectric sensor. As the extruded semicon layers are made from carbon loaded insulation, they will have similar acoustic properties to the insulation material. In this case, there is no significant acoustic reflection at the outer semicon layer/insulation interface. Air surrounding the mini-cable sample acts as a soft boundary for the acoustic wave (acoustic impedance for air and polymer are about 415 rayls and 1.8 Mrayls respectively), so nearly all acoustic energy would be reflected back into the cable at the cable/air surface. Only the 'window' of contact between the outer semicon layer and the plane electrode will allow acoustic waves to propagate from the cable into the plane electrode and onwards towards the piezoelectric sensor.

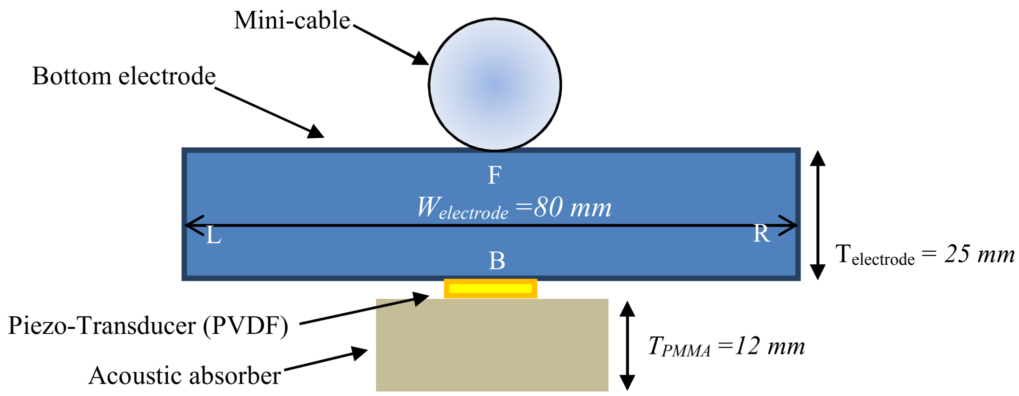

Figure 4-21. Schematic diagram of the PEA cell.

4.7.3.2 Acoustic absorber

An acoustic absorber, made of PMMA, provides additional acoustic path to avoid the signal overlap by the reflected acoustic waves from the rear surface of the piezo-electric sensor, it also provides mechanical support to clamp the transducer onto the surface of the PEA base electrode. The acoustic absorber (PMMA) is chosen as it has similar acoustic impedance with the transducer to minimise the reflection at the transducer – absorber interface.

In the simulation, the transducer is taken as a line (or point) probe, so material properties of the transducer film are ignored. As a consequence, the absorber should have the same acoustic impedance as the bottom electrode instead of the transducer. A simple solution is to extend the bottom electrode to realise the extra time delay introduced by an acoustic absorber. However the drawback of this solution is that increased computational domain aggravates the memory requirements of the computer used for the simulations.

Another (and better) solution is to use an absorbing boundary condition (ABC) at the bottom boundary of the electrode. With a properly defined PML, reflections from the bottom boundary are eliminated.

4.7.4 Simulation procedure

To solve the acoustic wave equations in the PEA domain Matlab software was used.

4.7.4.1 Comsol to Matlab

The simulation results, from the mechanical cable deformation under clamping force, as well as the electrical field distribution, also calculated in Comsol Multiphysics as described in section 4.6, can be exported to and post-processed in Matlab through the Livelink for Matlab toolbox. Alternatively, results can be exported and saved as datasheets (.txt files) and then be loaded into Matlab.

To simulate the PEA signal, two data files are required from Comsol: the deformed geometry of the cable and the electric field distribution within the deformed insulation, as shown in Figure 4-22. The different geometric regions of the cable can be distinguished by different material properties like density, permittivity, etc. For the convenience of loading into Matlab, the data can be exported in terms of a matrix through the COMSOL data Export function. Specifically, points can be selected either in Grid or Regular grid. If the option of Grid is selected, the range of grid (start and end point) and step of increment need to be defined. Only the total number of points needs to be defined for a regular grid (which selects the whole domain as default). Care was taken when defining the number of points to maintain the same spatial step in both dimensions (i.e. $dx = dy$) when the domain is not square. Figure 4-23 shows the grid of points (red dots) representing data that would be exported. In the exported matrix, points responding to the location outside all defined domains are set to NaN (not a number). To reduce the memory usage, the grid only covers the cable and a small part of the electrodes.

The exported files were read into Matlab. The matrix contains the material property (permittivity in this example) but can be reassigned to density (rho) and elastic stiffness (C) as shown in Figure 4-24. Each grid in Figure 4-24 corresponds to each dot in Figure 4-23.

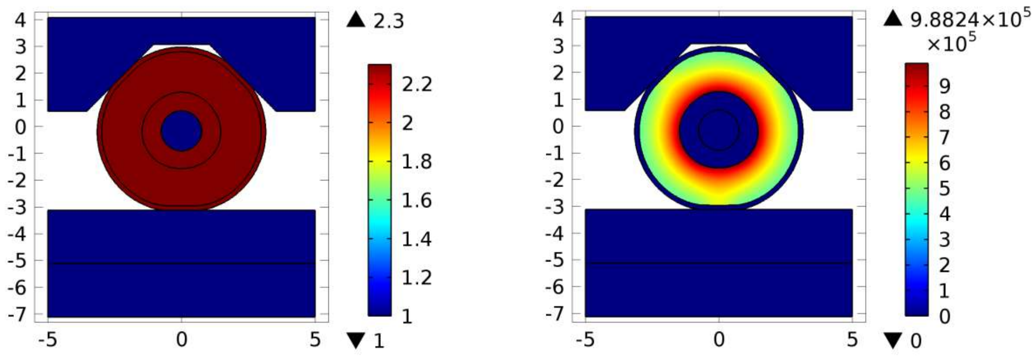

(a) (b)

Figure 4-22. Surface plot of the relative permittivity (a) and Electric field (b); For the electric field, 10 kV DC voltage was applied to the conductor, the outer surface was defined as ground boundarys. A relative permitivity of 2.3 was used for the insualtion.

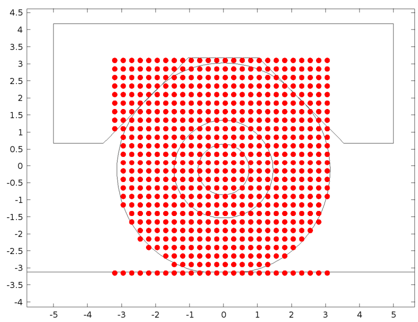

Figure 4-23. Data output in term of grid. (points are from -3.5 mm to 3.5 mm with a increment of 0.2 mm for both coordinate directions)

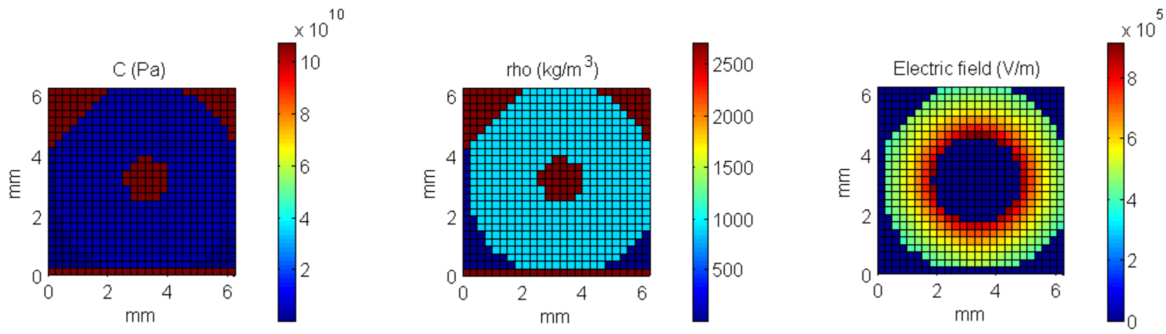

Figure 4-24. Matrix built form the COMSOL exported files in Matlab. (Poor mesh is used here only for the sake of demonstrating the procedure used. A much finer mesh is employed in the actual simulation.)

4.7.4.2 Domains

The COMSOL exported matrices need to be reconstructed to take the bottom electrode and the PML layers into account. Regarding to the discussion in Section 4.7.3, the computational domains are shown in Figure 4-25. For the sake of convenience, the bottom electrode keeps the same width of the cable domain imported from Comsol. PML boundaries are attached at the left, right and bottom of the domain to reduce the computer memory load.

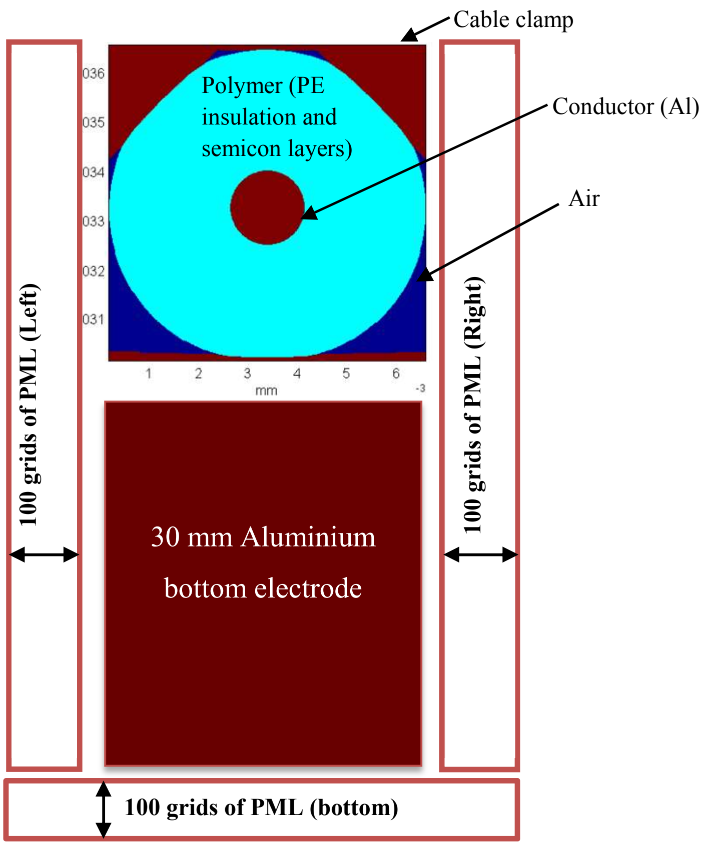

Figure 4-25. Computational domains. (an extral 5 mm was added to the thickness of the 25 mm bottom electrode)

4.7.4.3 FDTD equations

To facilitate the calculation with the split pressure p_x and p_y, the source term M is equality divided into two components along the x and y directions as [117]:

$$M = M_x + M_y \tag{4.34}$$

where $M_x = M_y = 0.5M$.

The 2D FDTD algorithm with PML boundary conditions are developed from equations in section 4.7.2. Taking the source term into account, the governing equations are:

$$p_x^{n+1}(i,j) = A_x\, p_x^n(i,j) - B_x\left(v_x^n(i,j) - v_x^n(i-1,j)\right) + (M_x^{n+1} - M_x^n) \tag{4.35}$$

$$A_x = e^{-C(i,j)\,\alpha_x(i,j)\Delta t} \tag{4.36}$$

$$B_x = \frac{1 - A_x}{dz\,\alpha_x(i,j)} \tag{4.37}$$

$$p_y^{n+1}(i,j) = A_y\, p_y^n(i,j) - B_y\,(v_y^n(i,j) - v_y^n(i-1,j)) + (M_y^{n+1} - M_y^n) \tag{4.38}$$

$$A_y = e^{-C(i,j)\,\alpha_y(i,j)\Delta t} \tag{4.39}$$

$$B_y = \frac{1 - A_y}{dz\,\alpha_y(i,j)} \tag{4.40}$$

$$v_x^{n+1}(i,j) = M_x\, v_x^{n+1}(i,j) - N_x\,(p_x^n(i+1,j) - p_x^n(i,j) + p_y^n(i+1,j) - p_y^n(i,j)) \tag{4.41}$$

$$M_x = e^{-\gamma_x(i,j)\,\Delta t} \tag{4.42}$$

$$N_x = \frac{1 - M_x}{dz\,\rho_x(i,j)\,\gamma_x(i,j)} \tag{4.43}$$

$$v_y^{n+1}(i,j) = M_y\, v_y^{n+1}(i,j) - N_y\,(p_x^n(i,j+1) - p_x^n(i,j) + p_y^n(i,j+1) - p_y^n(i,j)) \tag{4.44}$$

$$M_y = e^{-\gamma_y(i,j)\,\Delta t} \tag{4.45}$$

$$N_y = \frac{1 - M_y}{dz\,\rho_y(i,j)\,\gamma_y(i,j)} \tag{4.46}$$

where the superscript n is the iteration index, dz and Δt are the spatial and time steps respectively. i and j refer to the sample coordinates in x and y directions respectively. The attenuation coefficients α and γ are non-zero only in the PML regions.

In the PML regions, the corresponding attenuation coefficient increases from zero to a maximum in a quadratic form from the inner to outer surfaces. For example, if the PML contains m layers (spatial steps of dz), in the right PML boundary region:

$$a_x(i,j) = \alpha_{max}\left(\frac{i}{m}\right)^2, \quad i = 1, \dots, m-1, \tag{4.47}$$

$$\gamma_x(i,j) = C \cdot \alpha_{max}\left(\frac{i+1/2}{m}\right)^2, \qquad i = 0, \dots m-1, \tag{4.48}$$

A similar procedure was used to set the attenuation coefficients for the other PML layers.

4.7.5 Simulation results for flat PEA base electrode

Table 4-3. Material properties used in simulation

Material	Density (kg/m^3)	Wave velocity (m/s)	Relative dielectric constant
Air	1.8	343	1
Aluminium	2700	6295	\
Polyethylene	900	2200	2.3

Parameters used for this simulation are listed in Table 4-3. In this example, it is assumed that no space charge exists in the cable insulation and therefore both the DC field E_{DC} and pulsed field ΔE are Laplacian fields. The propagation of acoustic waves corresponding to the electrode charges at six different times as they travel through the cable and PEA apparatus are shown in Figure 4-26.

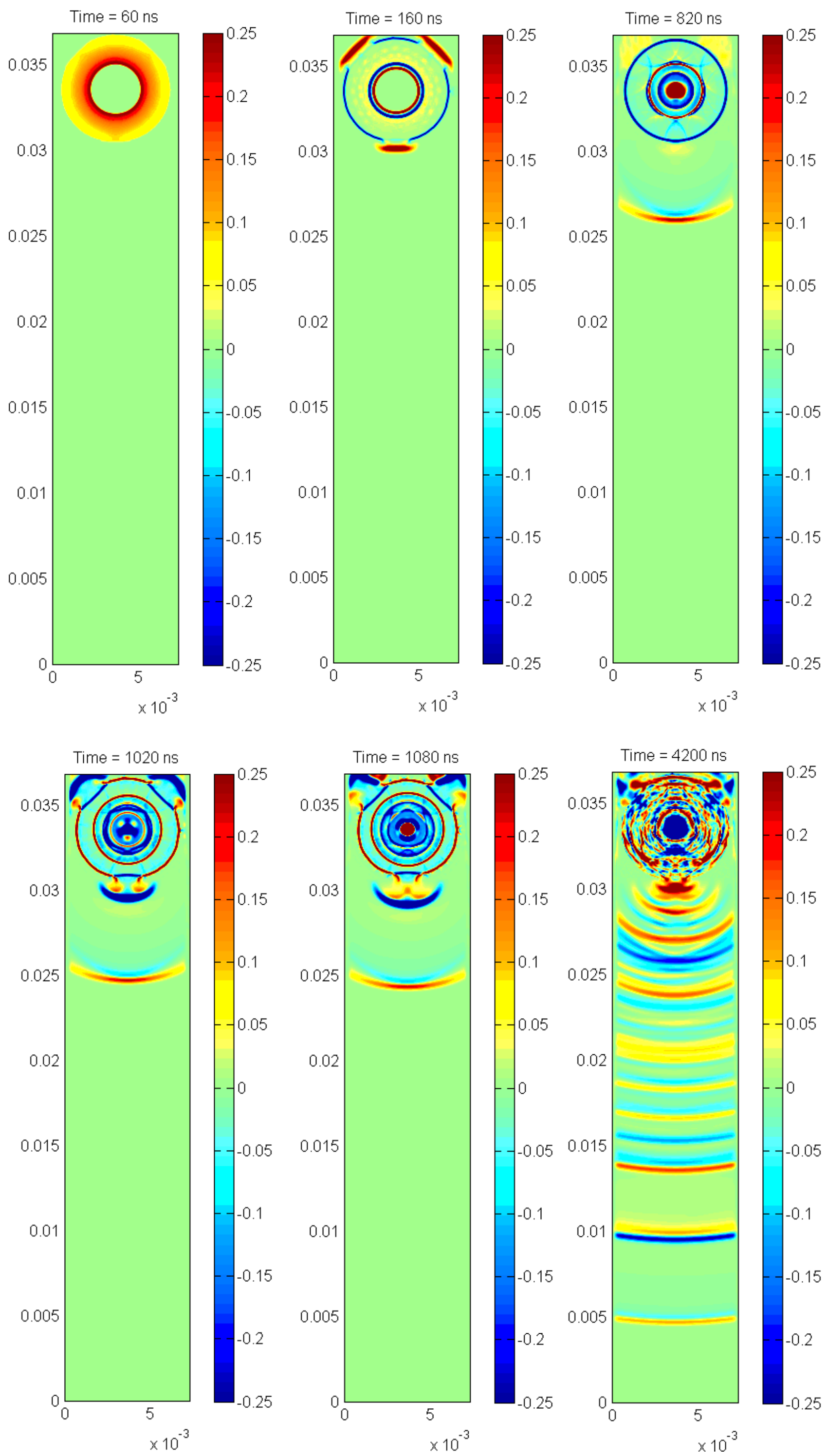

Figure 4-26. Simulation of the PEA acoustic signal propagation from the mini-cable to the flat base electrode at different times (from time t = 0).

The recorded pressure waves correspond to the time points:

- During the application of the pulsed voltage at Time = 60 ns.

- When the pressure wave generated at the outer semicon – insulation interface enters the aluminium electrode at Time = 160 ns.
- The acoustic wave originating at the inner semicon – insulation interface propagating to the cable surface at Time = 820 ns.
- Both waves propagating in the aluminium base electrode at Time = 1020 ns and 1080 ns. Reflections occurred at the edges of contact between the cable and electrode
- When the first wave reaches the acoustic detector at Time = 4200 ns.

Three different point probes are located at the horizontal centre of the bottom electrode with different distances of 0 mm, 12 mm and 25 mm to the cable/insulation interface as shown in Figure 4-27. The simulation outputs which are proportional to the pressure waves at each probe as a function of time are also shown in Figure 4-27. These waveforms consist of an initial delay representing the time taken for the first pulse (origins the outer semicon/insulator interface) to reach the probe followed by the second pulse (from the inner semicon/insulator interface) and subsequent reflection signals.

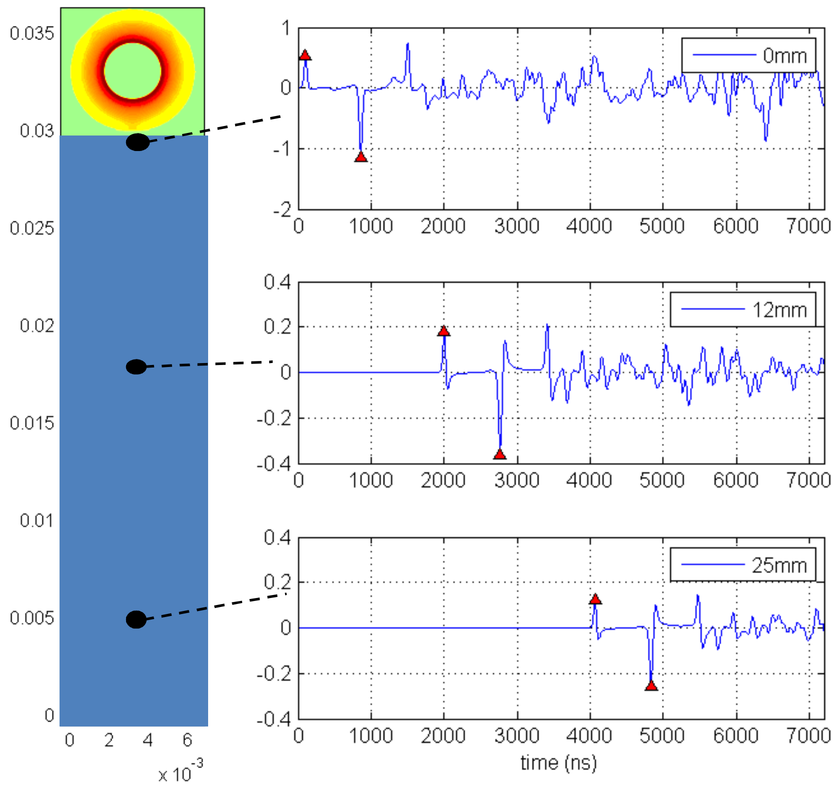

Figure 4-27. PEA acoustic signal obtained by probes with different distance to the cable – base electrode interface: 0 mm, 12 mm and 25 mm. The red triangle markers identify the detected pulses from the outer and inner semicon – insulation interfaces.

An important characteristic of the simulation output is the presence of signal overshoots. The overshoots were observed for the probes which were located at 12 mm and 25 mm away from the cable – electrode interface. However, signal overshoots were not found when the acoustic wave just entered the electrode as detected by the '0mm' probe. Comparing the wave propagation graphs shown in Figure 4-26 at Time = 1020 ns and 1080 ns, it can be noticed that the pressure wave which would eventually lead to the overshoot in the simulation output originates from the acoustic reflections occurring at the edges of the cable – electrode contact interface.

Eliminating the signal overshoot is essential for correctly interpreting the PEA measurement output. Normally, the signal overshoots are regarded as a system response due to the impedance mismatch between the high impedance piezoelectric film and the 50 Ω Low Noise Amplifier (LNA) or due to the acoustic reflection at the PVDF sensor – PMMA backing interface and is usually solved using the signal processing using deconvolution. However, according to above simulation results, reflections at edges of the cable – electrode interface can also be the source of signal overshoots. However unlike for example the system response of the sensor – amplifier circuit, the reflections from edges may not be consistent over experiments as the contact area may change with the clamping force and temperature variations. As a consequence, systematic errors may be incurred during the deconvolution if using the same system response function.

4.7.6 Simulation with curved PEA base electrode

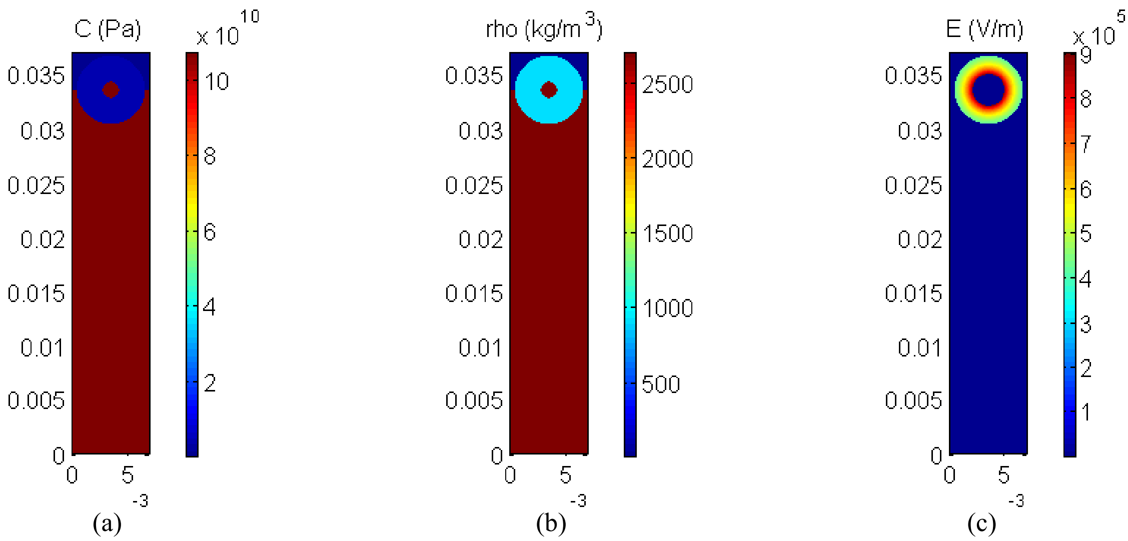

Figure 4-28. Surface plots of the material modulus C (a), density rho (b) and electric field E (c).

As a contrast, the simulation of acoustic wave generation and propagation with a curved electrode has also been performed using the same simulation model and parameters. The geometry, material properties and electric field distributions are shown in Figure 4-28. Corresponding to Figure 4-26, the propagation of PEA acoustic waves with the curved base electrode are demonstrated in Figure 4-29.

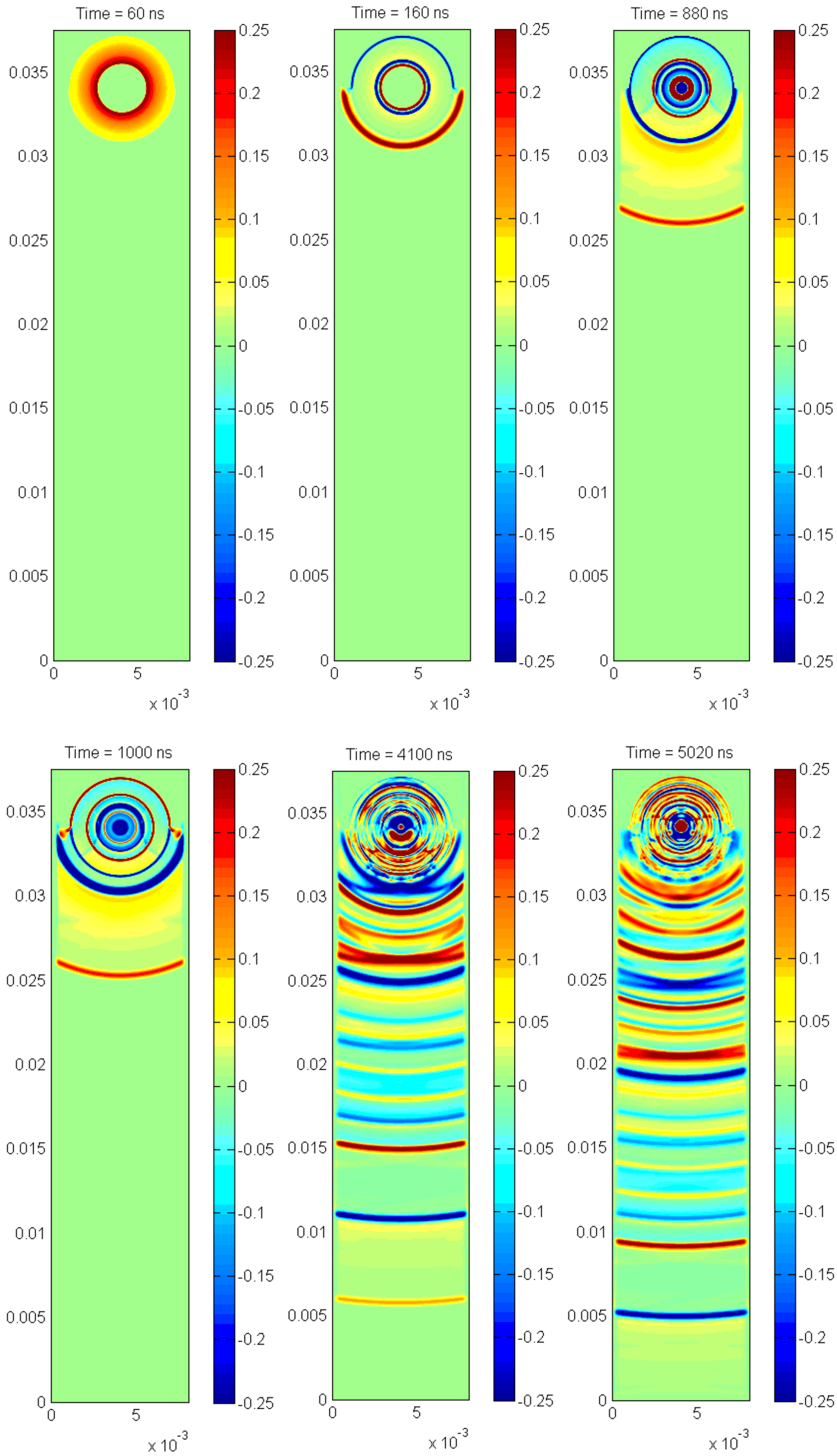

Figure 4-29. Propagation of the PEA acoustic signal from mini-cable to matched curved electrode.

The time dependent simulation output representing the detected acoustic signal by the three point probes positioned at 0 mm, 12 mm and 25 mm from the cable – electrode interface are shown in Figure 4-30. The simulated signals with the curved electrode do not show the signal overshoot as the electrode matches the outer surface of the mini-cable and therefore maintains the cylindrical wavefront of the PEA acoustic signal. The signal deviated from a zero baseline between the first two peaks (representing the electrode charges) are the consequence of bulk polarisation induced by the non-uniform electric field within the cylindrical cable insulation.

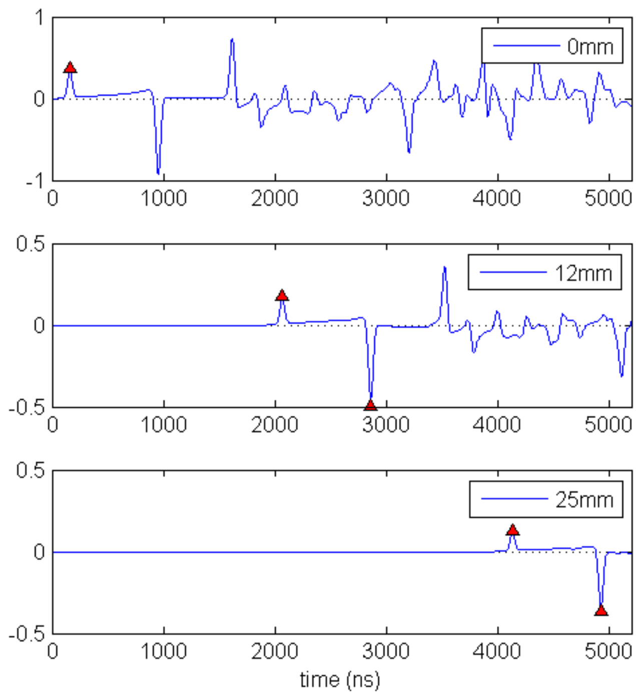

Figure 4-30. PEA acoustic signal recorded by three point probes at 0 mm, 12 mm and 25 mm from the cable – base electrode interface. The markers identify the detected pulses from the outer and inner semicon – insulation interfaces.

4.7.7 Effect of acoustic sensor width

Subject to the shape of base electrode, there is a geometry mismatch between the cylindrical wave and the flat sensor. The influence of this mismatch has been briefly discussed in Section 3.10.2 where it was explained that the extra time delays of the cylindrical pressure wave would be incurred and thus reduces the spatial resolution.

Now with the 2-D PEA acoustic model, it is able to assess the actual effect of sensor width on the space charge measurement results.

The simulation domain with the curved base electrode was adapted to employ the sensor and acoustic absorber (PMMA) domains as shown in Figure 4-31. The thickness of the bottom electrode was made thin to reduce the memory load and to exaggerate the effect of sensor width compared to the previous simulations. The width of the sensor was expressed as the normalised values to the distance to the cable centre as W/D. The material properties of the sensor and the PMMA are listed in Table 4-4. With these parameters, there would be the acoustic mismatch between the sensor and PMMA due to the smaller acoustic impedance for the PMMA.

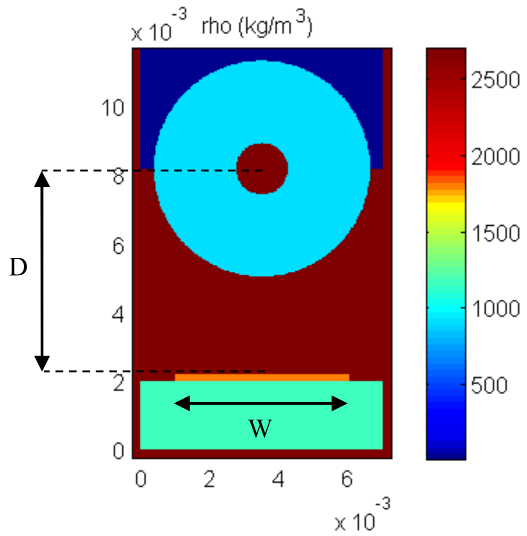

Figure 4-31. Simulation domains distinguished by the density.

Table 4-4. Material properties used in the simulation [118] (the wave velocity of PMMA is adapted to incur reflections).

Material	Density (kg/m^3)	Wave velocity (m/s)	Thickness
Sensor	1780	2140	52 μm
PMMA	1180	2190	2 mm

The simulation compared the signal outputs with three different sensor widths, for W/D = 0.5/6, 1/6 and 5/6, and the results are shown in Figure 4-32. Signal overshoots presented in the data of narrow sensors (W = 0.5 mm and 1 mm) demonstrate the reflected acoustic signal from the mismatched PMMA absorber (of smaller acoustic impedance). However, due to the reduced spatial resolution, the signal overshoots were not observed in the profile with a wide sensor.

In the real PEA system, the PVDF-TrFE film has a width of 5 mm and distance of 30 mm to the cable sensor. This is equivalent of W/D = 1/6. As confirmed by the simulation, for the 52 µm thick sensor film, the actual width of 5 mm for the sensor employed in the PEA system would therefore not affect the spatial resolution from the ideal response.

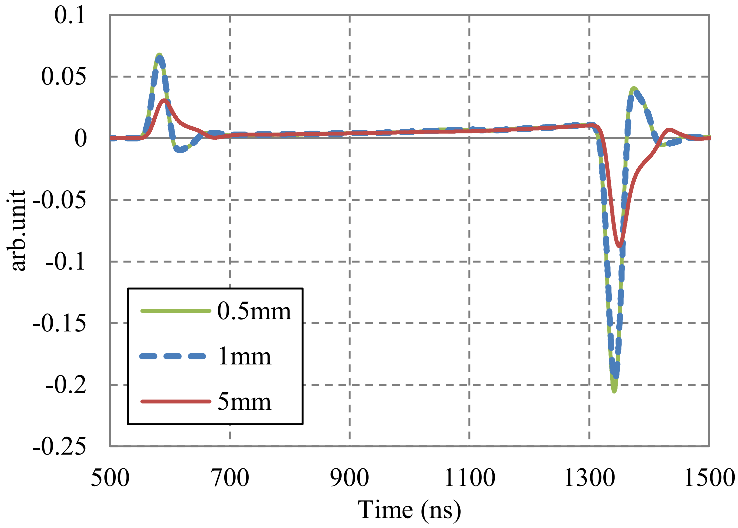

Figure 4-32. 2-D acoustic simulation results with different sensor widths: W = 0.5 mm, 1mm and 5 mm.

4.8 Application of integrated simulation model

The developed simulation models described in this chapter provide an alternative methodology for the interpretation of PEA space charge measurements. The 1-D models provide a complete linkage between charge transport and charge accumulation models and simulated PEA output data. The 2-D models enable the imperfections of the PEA technique to be explored. In this section, the approach taken for the simulation of PEA raw data using the 1-D models will be discussed.

4.8.1 1D PEA system simulation model

Calibration is required for initialising the 1-D PEA system model to adjust the parameters representing the material properties (for example sound velocity, acoustic attenuation and dispersion coefficient) and system features (for example buffer and acoustic absorbers). This can be achieved by matching simulation results with the calibration measurements obtained from the experimental PEA hardware (with low applied DC voltage to reduce the possibility of space charge accumulation in the cable insulation). The process is illustrated by the flowchart in Figure 4-33 and described in detail in the following sections.

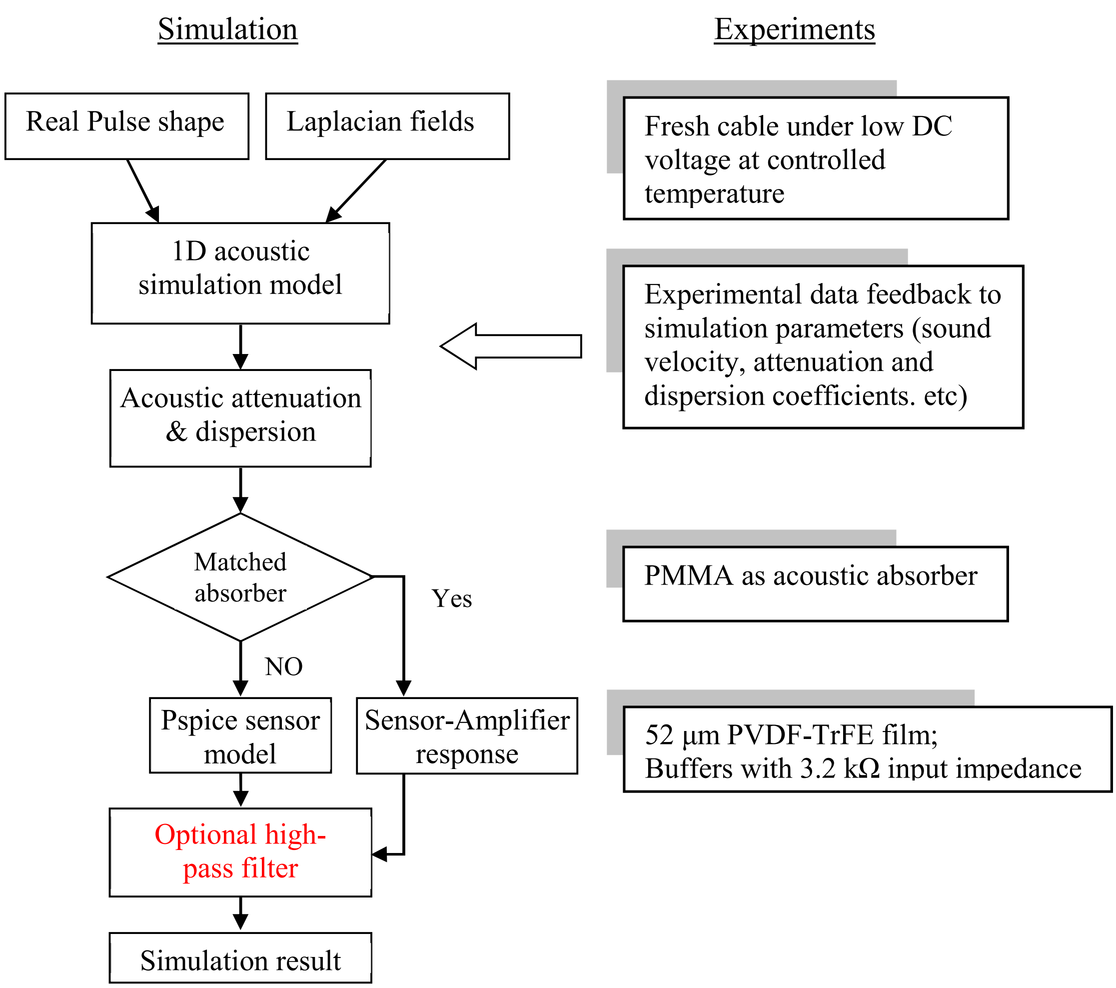

Figure 4-33. Simulation procedure corresponding to the experimental conditions.

4.8.1.1 Calibration measurement

The calibration measurements were performed on a fresh mini-cable at 20 °C initially with zero DC voltage but just the pulse voltage applied (called the V_{off} measurement) for baseline correction and after a voltage of +14 kV DC was applied to the mini-cable (called the V_{on} measurement). The PEA outputs are shown in Figure 4-34. The V_{off} measurement gives the baseline (contains low frequency noise and pulse noise) and pulse response of the PEA system. Then the calibration profile representing the DC capacitive charges was obtained by subtracting the V_{off} measurement from the V_{on} measurement. In addition, from the V_{on} measurement, the sound velocity in the insulation at the measurement temperature is estimated by the time delay between two peaks and the given dimension of the mini-cable.

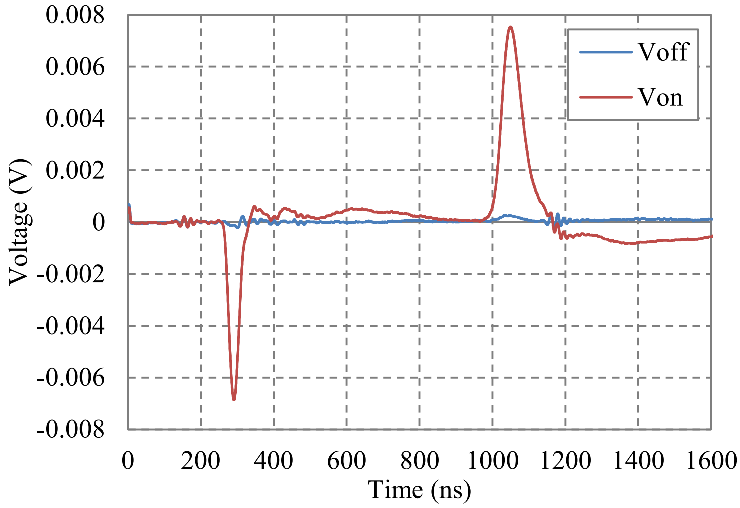

Figure 4-34. PEA outputs (3000 sweeps averaged) of the V_{on} (+14 kV DC) and V_{off} measurement. 3.2 kΩ buffer was used.

4.8.1.2 Acoustic simulation of experimental data

For the 1-D PEA acoustic simulation model, the applied DC electric field and the applied pulsed electric field are required. Since it is assumed that no space charge had accumulated during the calibration measurement, the applied electric field distribution in the cable insulation was assumed to be Laplacian. Instead of assuming a Gaussian wave shape, the shape of the applied pulse voltage was assumed to be the same as that of the attenuated pulse voltage of the hardware pulse generator that is used as the trigger signal for the oscilloscope. The measured waveshape of the attenuated pulse measured using an oscilloscope is shown in Figure 4-35 which is a -52 dB attenuated version of the pulse voltage applied to the cable. The voltage waveform consists of the initial peak followed by smaller amplitude oscillations.

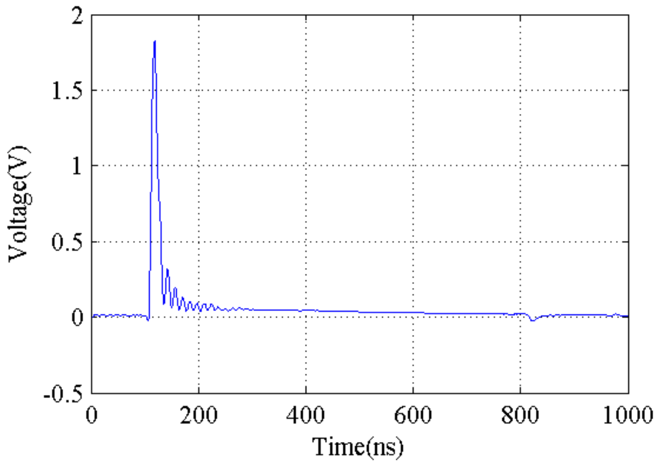

Figure 4-35. Trigger signal which is an attenuated version of the pulse voltage applied to the cable during the PEA space charge measurements

The 1D acoustic model is able to generate two profiles. One is the pressure presented on the sensor surface (as 'PEA acoustic' in Figure 4-36) and another is the integral of the pressure within the 52 µm sensor domain being regarded as the voltage output of the ideal sensor (as '1D acoustic' in Figure 4-36). The difference between these two profiles demonstrates the effect of the thickness of the sensor on the simulated PEA output. The sensor of 52 µm thickness broadens the peak and 'filters out' the pressure waves formed by the subsequent oscillations. The baseline remains the same and the areas of the peaks are preserved.

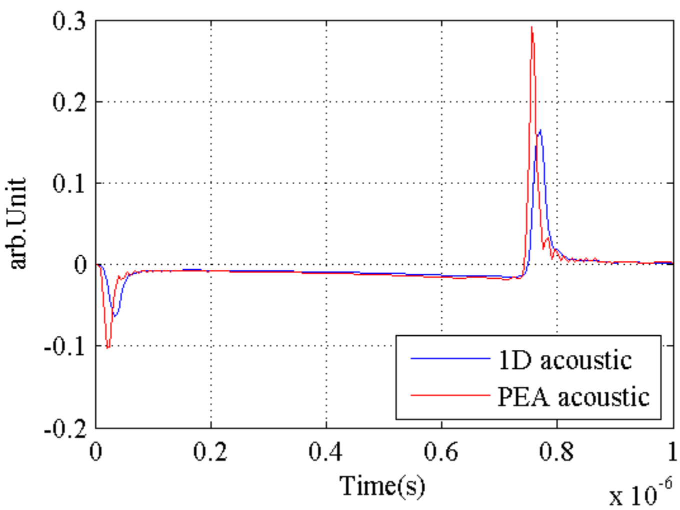

Figure 4-36. Simulation results of the 1D acoustic model. 1D acoustic: output of the ideal 52 µm sensor. PEA acoustic: pressure of the acoustic wave arrived at the sensor surface.

In the 1D model the acoustic absorber for the sensor is assumed to be perfectly matched, having the same acoustic properties as the sensor. If this assumption is also valid in reality (in the real PEA system hardware), the sensor voltage output (1D acoustic) can be directly used for the following data processing otherwise the 1D Pspice model would have to be employed to mimic the effect of an imperfectly matched absorber.

4.8.1.3 Acoustic attenuation and dispersion

To improve the efficiency of the 1-D simulation, the medium (insulation, semicon, aluminium electrode and sensor) were assumed to be acoustically lossless for the propagating pressure waves. The effects of the acoustic attenuation and dispersion within the cable insulation domain were performed independently on the output of the acoustic model by convolution using MATLAB. The system transfer functions and the geometry factors as introduced in Section 3.12 needs to be determined by comparison with the base-line corrected experimental calibration profile. The 1D acoustic model output pressure waves arriving at the sensor and its convolution with the acoustic transfer function, G_a (Section 3.12.2.4), generating the dispersed signal are shown in Figure 4-37. The effect of acoustic loss and dispersion causes the wave shape of the second pulse to be severely distorted compared to the case when attenuation and dispersion are neglected.

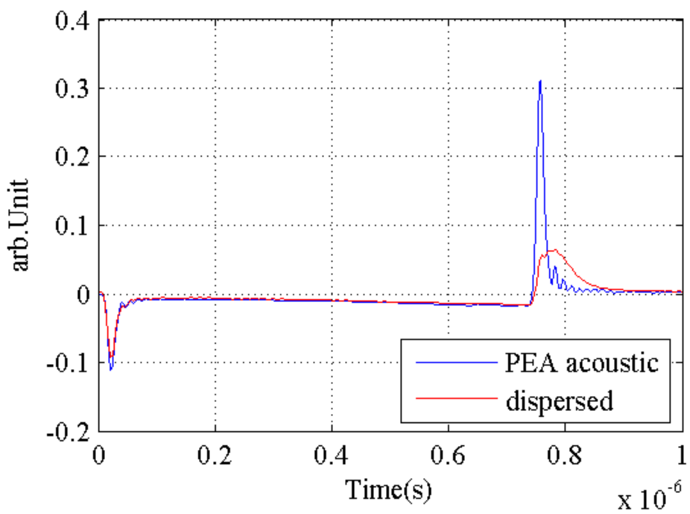

Figure 4-37. Performing the acoustic attenuation and dispersion on the acoustic model output.

4.8.1.4 Pspice sensor model

The dispersed pressure wave profile is then used as the input for the Pspice sensor model. Here, the sensor – buffer (3.2 kΩ) response is also built in the Pspice equivalent circuit of the sensor. In order to fit with the experimental result, the acoustic impedance of the absorber was estimated to be 127 % of the PVDF-TrFE. The output of the Pspice model is shown as the blue line in Figure 4-38. It can be seen that there is a small discrepancy in the level of the baselines of the simulation and experimental results as the bulk signals (between two peaks) shows a DC offset due to the bulk polarization of the PEA while the two peaks are about the same. To fit with the experiments, a first order high pass filter was applied to the simulated data producing the red trace in Figure 4-38. The baseline now compares more favourably with the experimental data. However, the underlying reason for the absence of the bulk polarization response in the experimental data and for the necessity in applying the high pass filter to the simulated data has not been located in the scope of this work. One possibility is that the experimental calibration data has been subject to cable charging due to a non-linear dependence of electrical conductivity with applied electric field. The wave shape for the second pulse clearly shows the effect of dispersion as the pressure waves propagate through the insulation material. Dispersion is caused by a frequency dependence of the pressure wave velocity.

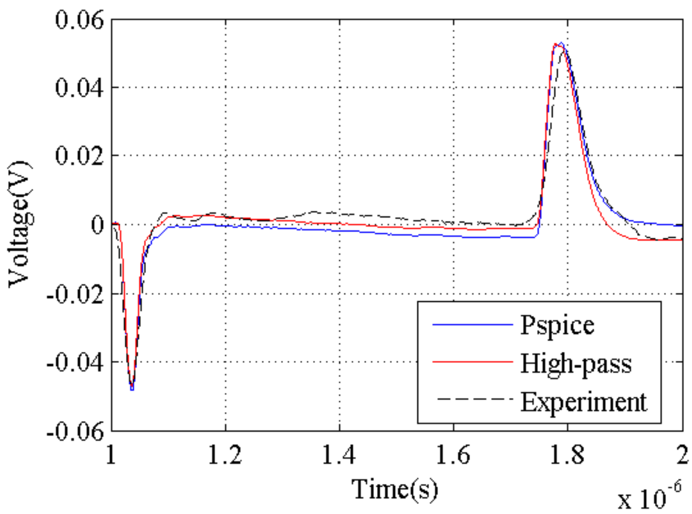

Figure 4-38. The result of the PEA simulation model (High-pass) compared with the output of the Pspice model (Pspice) and the experimental data. The acoustic impedance of the absorber is 127 % of sensor.

4.8.1.5 No acoustic mismatch

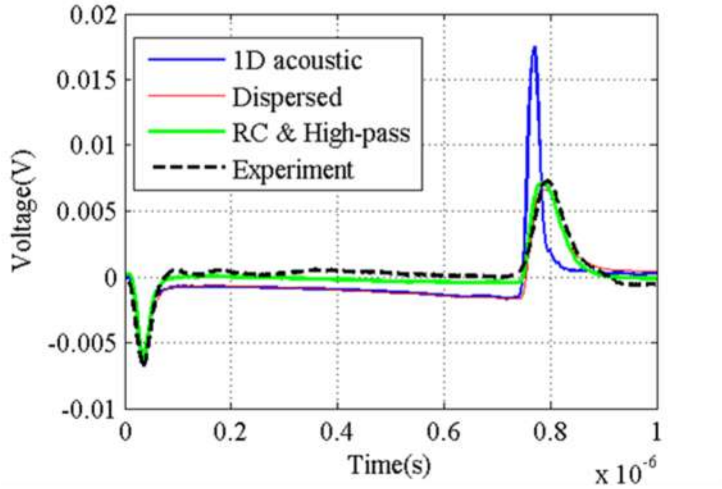

Figure 4-39. Simulation of the raw PEA experimental data. Blue trace is the output from the 1-D acoustic simulation, red trace is the correction for attenuation and dispersion, green trace is the corrected buffer amplifier output signal and after an additional high pass filter. The dashed line is typical experimental data obtained using the experimental apparatus.

If the effect of the acoustic mismatch between sensor and absorber is not significant, the sensor output of the 1-D acoustic model may be used directly. Then a sensor output profile needs to be processed to take into account the impedance mismatch of the sensor capacitance, C, and buffer input resistance, R. This is achieved by convolution using the calculated transfer function of the RC circuit using MATLAB on the simulated data after applying the attenuation/dispersion correction. The simulation results are shown in Figure 4-39. Similar comments can be made regarding the comparison with experimental data.

4.9 Conclusions

In this chapter a number of simulation models have been introduced. The aim of these models is to provide a software toolkit enabling the output from PEA experiments to be critically assessed with the basic underlying principles of charge accumulation in cable insulation and current understanding concerning the operation of a PEA based space charge measurement system applied to cable insulation. The simulation models introduced in previous subsections can be divided into two categories dependent on their purpose. The 1-D charge transport model (Section 4.2) and the 1-D PEA system model which is the amalgamation of the 1-D PEA acoustic pressure wave propagation model, attenuation and dispersion model and piezo-electric sensor model incorporating the buffer amplifier response (Section 4.5) provides a suite of tools that form the basis for an alternative approach to the interpretation. Instead of employing the traditional approach of working backwards from the PEA raw output data to ascertain the space charge profile, models of the electrical conduction processes in insulating materials can be used as the input to PEA simulation models providing an output that can be compared directly with the experimental raw data. The second category of models introduced in this chapter, the mechanical deformation model (Section 4.6), the 1-D and 2-D PEA acoustic pressure wave propagation models (Section 4.3 and 4.7), attenuation and dispersion model and the sensor model (Section 4.5) can be used to investigate the non-ideal characteristics of the measurement technique.

5 COMPARISON OF SPACE CHARGE MEASUREMENTS USING PEA WITH FLAT VS CURVED BASE ELECTRODE

5.1 Introduction

The PEA method was originally designed for flat specimens but has recently been adapted for measuring the space charge in cylindrical geometry samples. Work published in the literature relating to cylindrical cables has used different shapes for the base electrode including flat, ‘double-curved’ (with curved sensor) and ‘hybrid-curved’ (quoted as ‘curved’ in this work as introduced in Section 3.9.2). The authors of the work refer to different advantages/disadvantages associated with the various shapes. However, to the author’s knowledge, little attention has been paid to the validity of the various approaches for the robust determination of space charge or to justify the particular approach of using a particular base plate geometry by direct comparison with the other proposed geometries. The simulations in 2-D of the PEA system measurements suggest that differences in the space charge data obtained using the techniques will likely occur. It is often assumed that the various techniques will all provide the same representative measurement of the space charge inside a cable insulation. In particular, when using the flat electrode for high temperature measurements, there exists no data in literature that explore the impact of the cable clamping force on the experiments. Therefore it is imperative to provide a detailed analysis and comparison on the performance of different shapes of base electrodes.

In this chapter a comparative set of experiments using the PEA technique with flat and curved electrodes will be described in section 5.2. In section 5.3, the influence of cable clamping force on PEA measurements obtained using the PEA apparatus with a flat base electrode will be investigated and the conditions for experimental reproducibility will be explored through experiments and simulation. The feasibility of using a flat base electrode PEA system for high temperature measurements will be explored in section 5.4. Section 5.5 examines the performance of the PEA system using a curved electrode in terms of the sensitivity to the clamping force and contact quality as well as the high temperature measurements.

5.2 Electrode geometry induced overshoots in the flat electrode PEA

The simulations of a flat electrode PEA as described in Figure 4-26 indicate that signal overshoots occurred due to acoustic reflections at the edges of the cable – electrode contact area. To confirm this, space charge measurements were performed on a mini-cable using the flat base electrode and the curved electrode. To minimise potential cable related differences between measurements, different axial positions of the same mini-cable under identical experimental conditions (DC voltage, pulse magnitude, clamping force and temperature) were used for direct comparison between the two configurations.

5.2.1 Experimental results

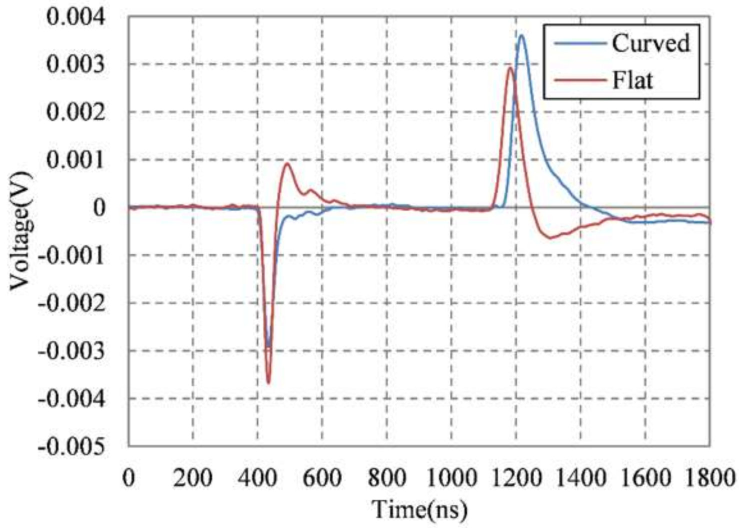

Figure 5-1. PEA voltage outputs (10000 sweeps averaging) with a curved and flat base electrode. The experimental conditions for both measurements are identical: 10 kV DC bias voltage, 24 °C, and 3.2 kΩ buffer. The difference in the length of profiles suggests the more serious deformation of the mini-cable with the flat electrode than with a curved electrode under the same force for clamping.

As shown in Figure 5-1, the experimental results are consistent with the simulation results in that the overshoots only exist when using a flat electrode. The undershoots presented in the PEA raw data when using curved electrode are likely to be the consequence of other system responses which are due, for example, to the mismatching between the sensor and the backing acoustic absorber. In addition, it is obvious that, when the flat electrode is used, the profile length is shorter than when the curved electrode is used, though the clamping forces were the same for both measurements. This is the consequence of the greater mechanical deformation of the cable due to the force being concentrated over a small contact area of the cable on the flat electrode.

5.2.2 Feasibility of signal recovery

It is necessary to determine whether the geometry related response is a linear time-invariant (LTI) system, in other words, whether the geometry induced overshoots can be restored by the technique of deconvolution.

To do so, the flat base plate PEA signals for the mini-cable were simulated using the 2D acoustic model (Section 4.7) with zero bulk space charge using a deformed cable geometry generated by the mechanical model (Section 4.6). The benefits of using the simulation rather than experimental data are that:

- The simulation can focus on a specific system response by assuming a homogenous and acoustic lossless insulation, the ideal sensor and the buffer amplifier of infinite input impedance. Therefore, the overshoots found in the simulation are only related to the geometry of the base plate.
- With the simulation, the PEA signal without overshoots i.e. before being overlapped by the reflected acoustic wave can be accessed. Therefore if there is a LTI system response, the recovered signal by deconvolution should be the same as the un-overlapped signal.

The PEA signals at the entrance (0 mm) and 25 mm from the surface of the flat electrode are shown in Figure 5-2. At the entrance of the electrode, the signal has not been seriously affected by the acoustic reflection while the PEA signal measured at 25 mm depth into the base plate shows clear overshoots. After applying deconvolution on the 25 mm signal, the recorded profile, quoted as ‘decon’ in Figure 5-3, is similar to the 0 mm signal. This demonstrates that the geometry induced overshoots are able to be recovered.

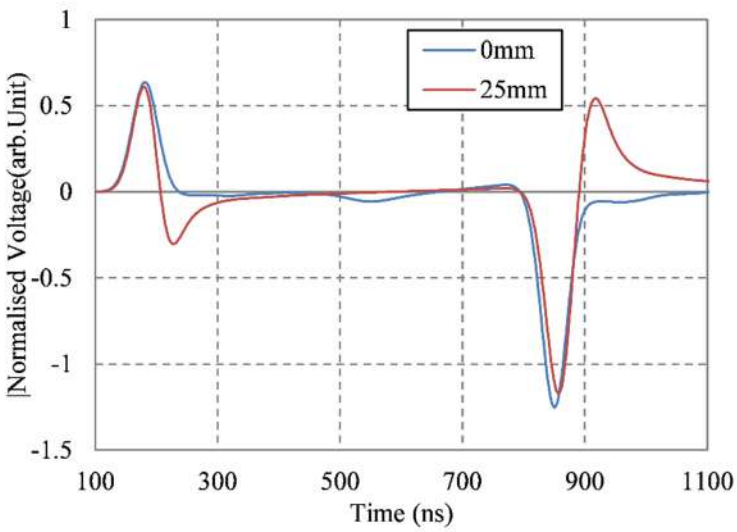

Figure 5-2. Simulated PEA signal at the entrance (0 mm) and 25 mm depth of the flat base electrode.

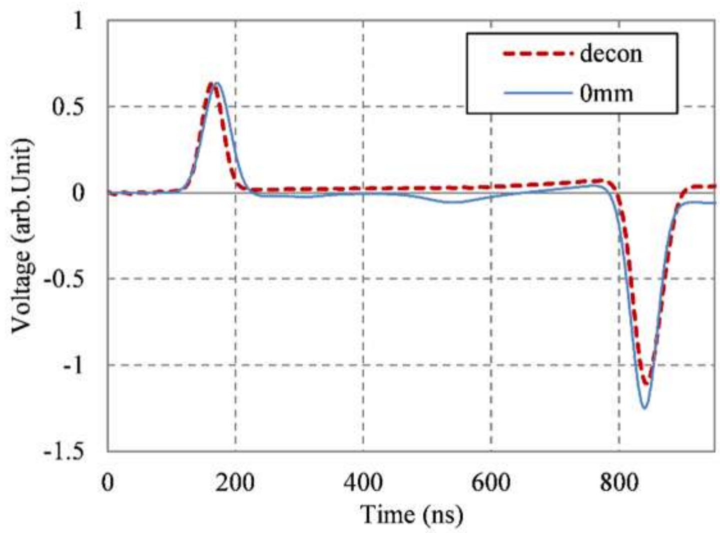

Figure 5-3. After removing the overshoots on the simulated 25 mm PEA signal by deconvolution, the recovered profile 'decon' is about the same as the 0 mm signal.

However, even if the geometry induced overshoots could be solved by deconvolution, it does not mean that the output of the system with different electrodes is equivalent. After applying deconvolution on the two experimental results of Figure 5-1, the processed signals are still dissimilar as shown in Figure 5-4. Specifically, the fall time of P_2 is longer when the flat electrode is used than when the curved electrode is used but the area of P_2 seems bigger when the curved electrode is used than when the flat electrode is used. This means the PEA signals are already different when entering the electrode. The discussion about this difference will be given in the next section.

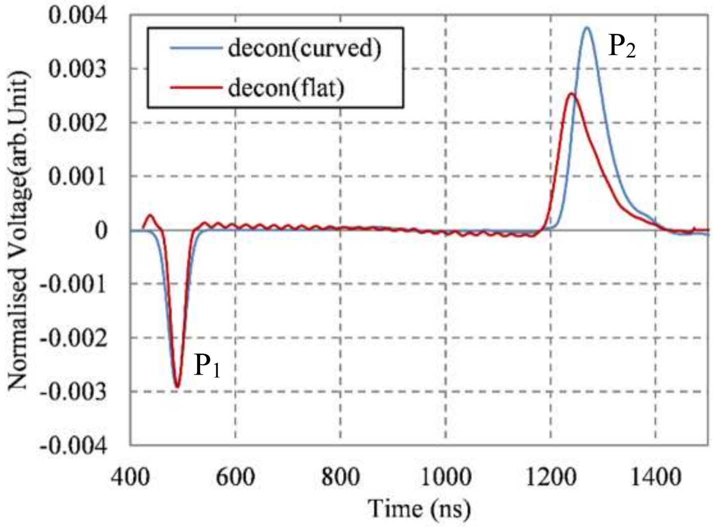

Figure 5-4. Deconvolution over the PEA outputs with flat and curved electrode.

5.3 Influence of cable clamping force on measurement reproducibility

At the end of the last section, it was shown that even after removing the system responses (which are responsible for the overshoots and undershoots) the PEA outputs with the curved and flat electrodes are still not the same. This section focuses on how the clamping forces influence the output signal and hence control the experimental reproducibility in a flat electrode PEA system.

5.3.1 Experimental

A series of experimental PEA measurements with various clamping forces was performed. The cable deformation on the space charge measurement region is characterised by the insulation thickness changes which are quantized by the length variation of the space charge profiles. The experimental results are illustrated in Figure 5-5. Since only the profile length changes are of interest, the PEA raw outputs (without signal processing and calibration) were used. The force applied for each test is estimated by the deformation of the pressure spring that loads the 30 mm cable clamp.

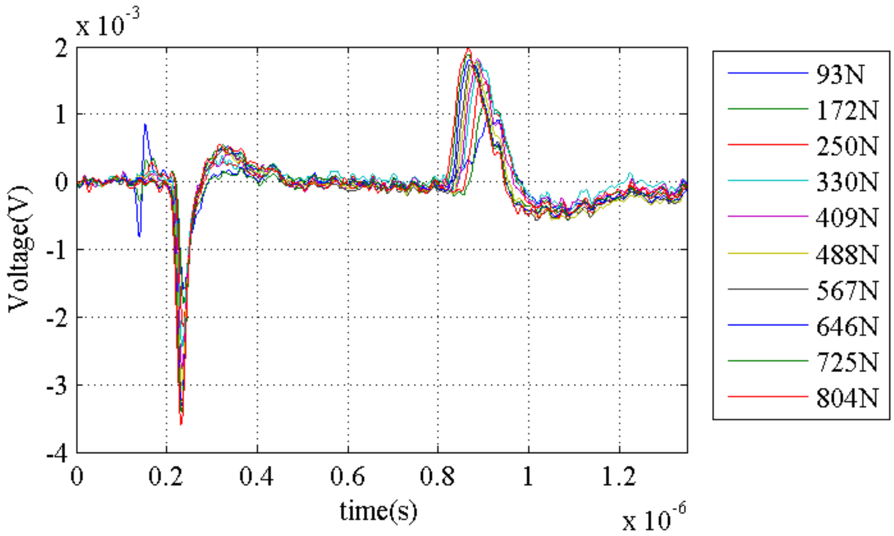

Figure 5-5. PEA output data (using the 3.2 kΩ buffer amplifier and 1000 sweeps averaged) of the mini-cable PEA system. A range of clamping forces was applied on a mini-cable through a 30 mm length clamp, with 10 kV HVDC, 800 V (amplitude) 20 ns (duration) pulse. The pulse at about 0.16 μs at the lowest clamping force (93 N) is due to poor electrical contact between the cable outer semicon and the flat aluminium base electrode.

Since the PEA measurement with 0 N clamping force cannot be performed, an assumption was made that the profile length with 93 N clamping force is 97 % of that with 0 N (based on the theoretical and calculated thickness of mini-cable insulation under 0 N and 93 N clamping force). As the profile length variation under different clamping forces was known, the polyethylene material properties in simulation were adapted to fit with the experiments as plotted in Figure 5–6. The resultant material properties are then listed in Table 5-1, in which the aluminium properties are taken from the COMSOL material library.

The experimental results are also valid for analysing the effect of the clamping force on the PEA outputs, especially in terms of the reproducibility. However, the system response of a real PEA apparatus is complicated. Changing the clamping force may not only modify the degree of cable deformation and the contact area, but other effects like the acoustic transfer coefficient between the cable and the electrode may also be altered as well as the density distribution of the insulation in the cable due to mechanical compression. To confirm the understanding and conclusion of the effect of cable clamping, simulation tools developed in Chapter 4 have also been used. Subsequently, experimental data can be analysed in parallel and compared with the simulated PEA outputs under a range of clamping forces.

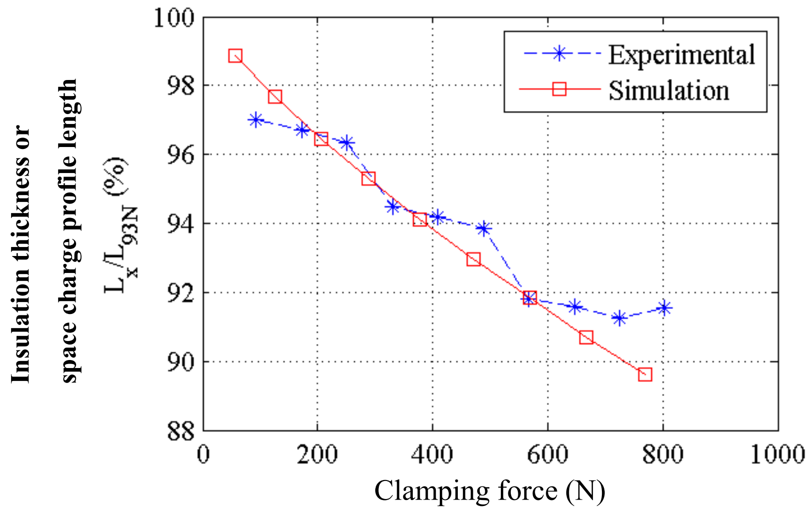

Figure 5–6. Simulated insulation thickness changes and the length variation of the space charge measurement profiles under different clamping forces. An assumption is made that the space charge profile length at 93 N is 97 % of that at 0 N.

Table 5-1. Material properties for mechanical simulation

	Polyethylene	Aluminium
Density [kg/m^3]	920	2700
Young's modulus [Pa]	0.13e9	70e9
Poisson's ratio	0.4	0.33

5.3.2 Simulated PEA signals under different clamping forces.

The COMOL simulation model for cable deformation has been introduced in Section 4.6. The deformed cable geometries under different clamping forces were imported into the 2D Matlab PEA acoustic simulation model as presented in Section 4.7. The Pspice sensor model was not used for this purpose as the clamping force of the cable would not affect the sensor. Consequently the acoustic pressure signals were used directly as it was assumed that the sensor output was proportional to the pressure wave. As has already been shown in Section 4.7.5, the overshoot would be present in the PEA output when using a flat electrode. Therefore both the PEA output with the geometry induced overshoot and the non-disturbed acoustic signal at the entrance of electrode as recorded by the 0 mm probe (see Figure 4-27) were used.

The simulated PEA signals recorded by the transducer and 0 mm probe are shown in Figure 5-7 and Figure 5-8 respectively.

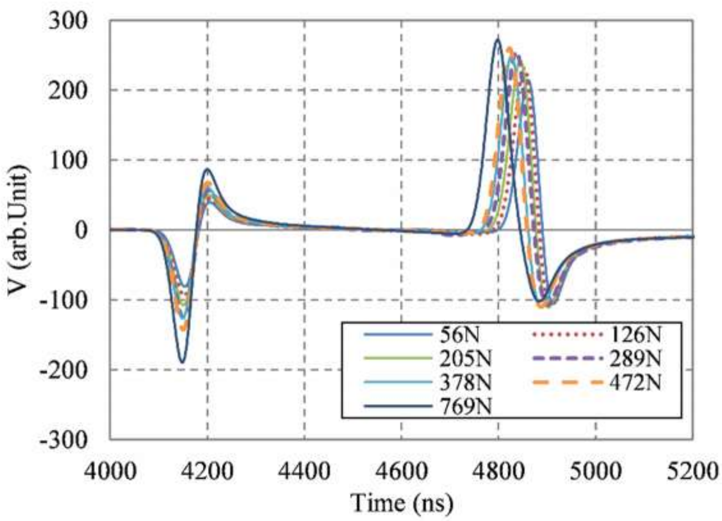

Figure 5-7. Simulated PEA acoustic signals with different clamping forces recorded by the line transducer at 25 mm distance from the cable – electrode interface.

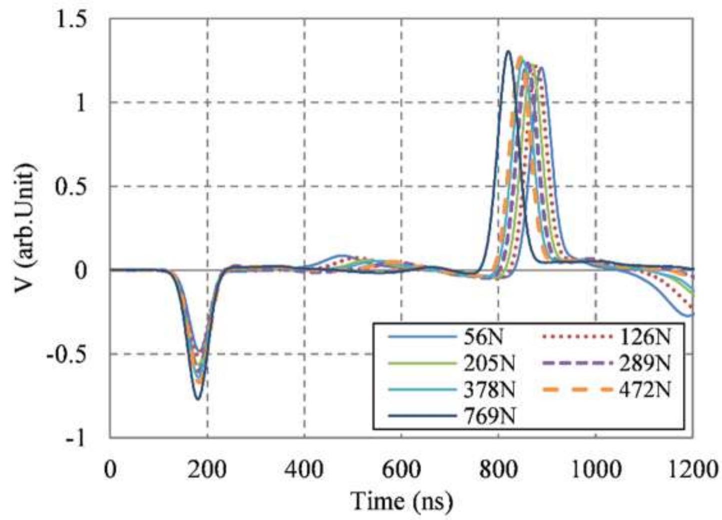

Figure 5-8. Simulated PEA acoustic signals with different clamping forces recorded by the point probe at the cable – electrode interface.

5.3.3 Contact width

Along with changes to the insulation thickness, the contact width of the cable with the flat electrode will also change with cable clamping force. It is not possible from the experimental set-up to measure the contact width directly and an indirect method was used that is based on the amount of cable distortion that occurs under a given cable clamping force. The distortion can be measured directly as the relative change in the inter-electrode peaks in the simulated data and simultaneously, the contact width may also be determined directly from the simulation results as a function of the cable distortion as shown in Figure 5-9. The contact width of a mini-cable in the experiment can then be related to the applied clamping force by measurement of the relative change in peak position in the measured data. A plot of estimated cable contact width as a function of the applied clamping force for the experimental data is shown in Figure 5-10. This demonstrates a significant change in the contact width and therefore the contact area when the cable is clamped with force up to 800 N.

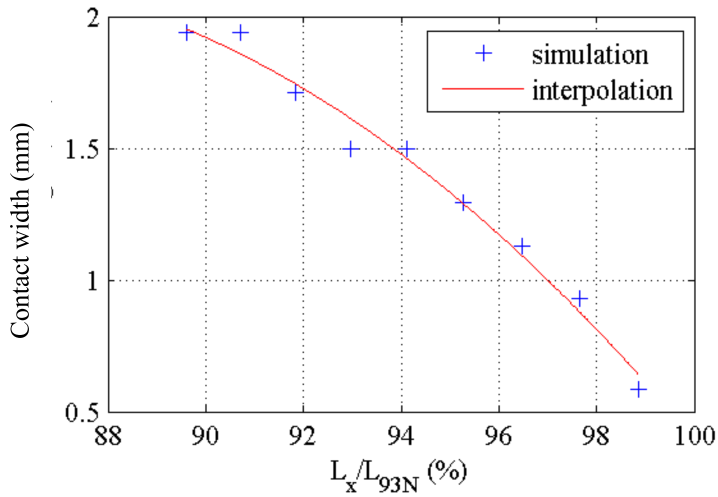

Figure 5-9. Contact width (in the cross-section) of the cable – electrode contact interface as a function of the PEA signal profile length where it is assumed that L would decrease by 3 % with the clamping force of 93 N.

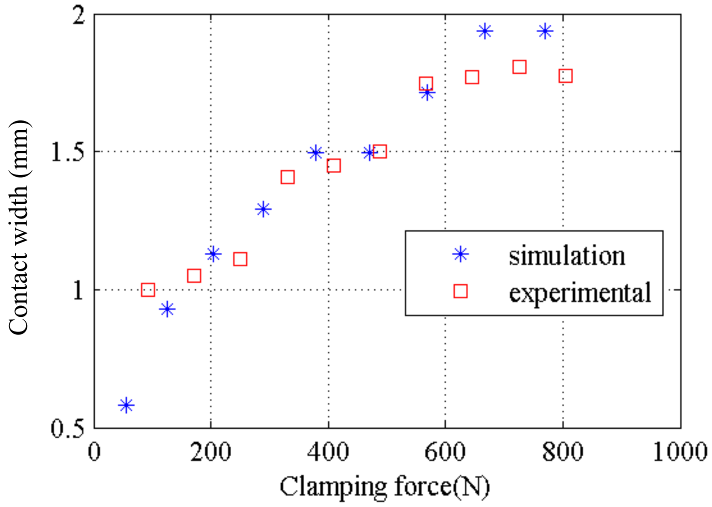

Figure 5-10. Contact width between the cable and base electrode as a function of clamping force.

5.3.4 Discussion

5.3.4.1 Response with clamping force

According to the experimental data (Figure 5-5) and simulation results (Figure 5-7 and Figure 5-8), the voltage signal becomes greater with a higher clamping force. Moreover P_2 shifts to the left and broadens slightly with increasing clamping force. This is likely because the compressive deformation of the mini-cable reduces the thickness of its insulation and therefore the mini-cable loses its cylindrical symmetry.

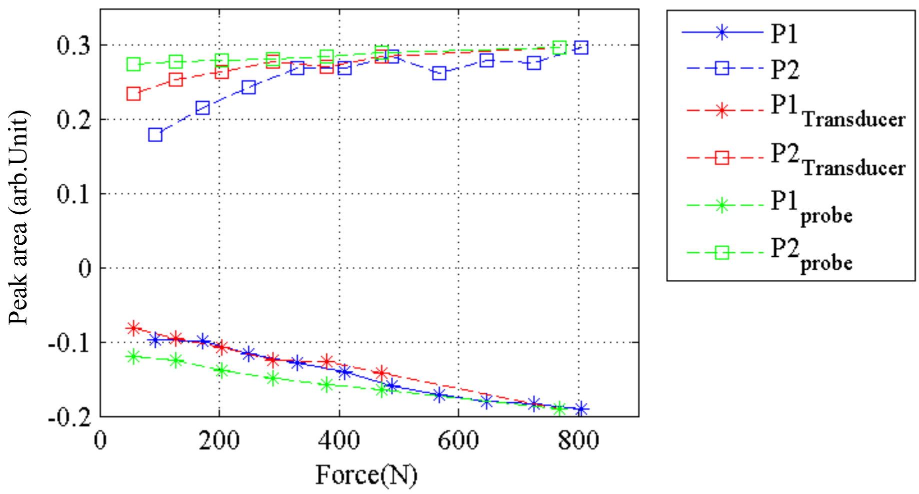

Figure 5-11. Variation of the peak areas as a function of the clamping force. All simulation data normalised to the experimental data (blue) at the maximum force. P_1 and P_2 are peak areas for experimental data. Transducer and probe refer to the data shown in Figure 5-7 and Figure 5-8.

The variations in the peak areas of all experimental and simulation data are plotted in Figure 5-11. It can be seen that the simulation data of both the probe (without overshoots) and transducer (with overshoots) recorded are consistent with experimental results in that both peak areas increase with increasing clamping force.

5.3.4.2 Consequences for calibration and measurement reproducibility

The relative values of the signal peak areas for P_1 and P_2 are related to the interfacial electric fields inside the cable. In the absence of space charge, these areas are determined by the Laplacian electric field as well as the acoustic propagation parameters in the cylindrical geometry including attenuation and dispersion. Correction of attenuation and dispersion is usually achieved by comparison of the pulse shapes of P_1 and P_2 in the frequency domain [11] to obtain the attenuation and dispersion propagation parameters for the cable insulation material. However, due to the non-uniform deformation of the insulation profile, the ratio of the two areas of the two peaks, as shown in Figure 5-12, decrease as a function of increasing clamping force. As a consequence, for room temperature tests, the clamping force has to be held constant throughout all measurements, otherwise systematic errors would occur when reconstructing the space charge profile from the raw experimental data.

It can be noticed that the ratio with the lowest clamping force for the experimental data deviates from the simulation results. This may be due to the relatively large experimental errors with a poor electrical and acoustic contact between cable and electrode.

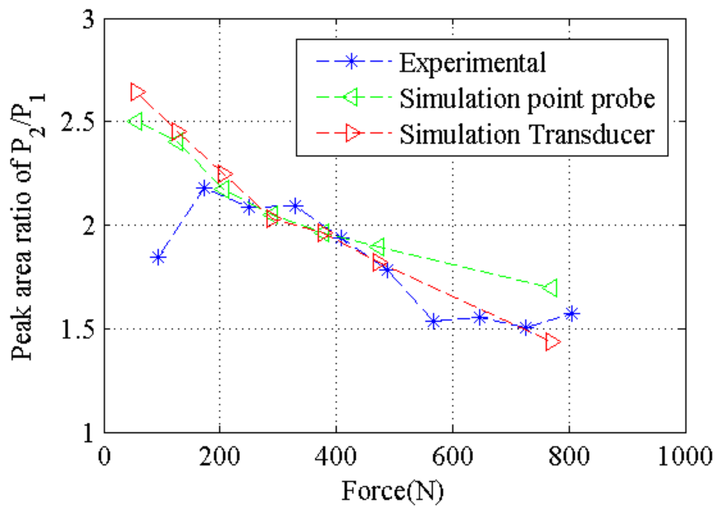

Figure 5-12. Ratios of peak areas as a function of clamping force.

5.3.4.3 *Acoustic signal coupling to the base plate*

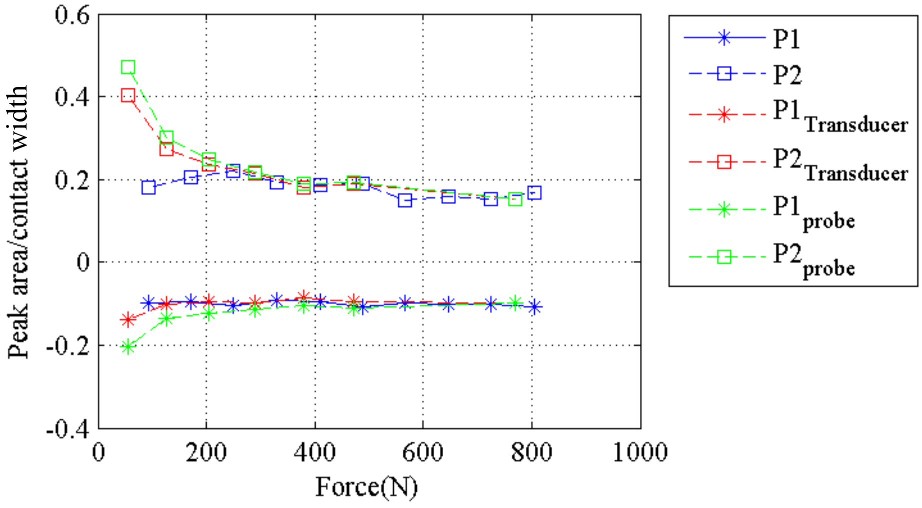

Figure 5-13. The ratio of the area of signal peaks to the contact width at different clamping forces.

Figure 5-13 illustrates how the ratio of peak area to contact width, d, changes with clamping force. It shows that the ratios of P_1/d and P_2/d are independent of the contact force (within experimental uncertainties) for a clamping force greater than 200 N. This confirms that the acoustic energy transferred from the cable to the plane electrode is proportional to the contact area between the cable and the flat base electrode of the PEA apparatus. At clamping forces less than 200 N, the ratios, particularly P_2/d (probe and transducer), show a clear downward trend with the increase of clamping force. It can be inferred that the mechanism of signal enhancement under increased force may not be the same through the thickness of the insulation.

5.3.4.4 *Electrical field in deformed insulation*

Due to the augmented cable deformation with increasing clamping force, the PEA peak area ratio P_2/P_1 change is also partly due to the change in the Laplacian electrical field in the compressed deformed insulation layer. In particular, the ratio of the electric field at the inner and outer semicon interfaces, E_2/E_1 also plays a role in determining the peak area ratio P_2/P_1. The electrical field distribution along the y-coordinate (see Figure 4-19) under different clamping forces is shown in Figure 5-14. The deformation of the thin outer semicon layer is very limited. Therefore the location of the insulation – outer semicon interface, B_1, has little change.

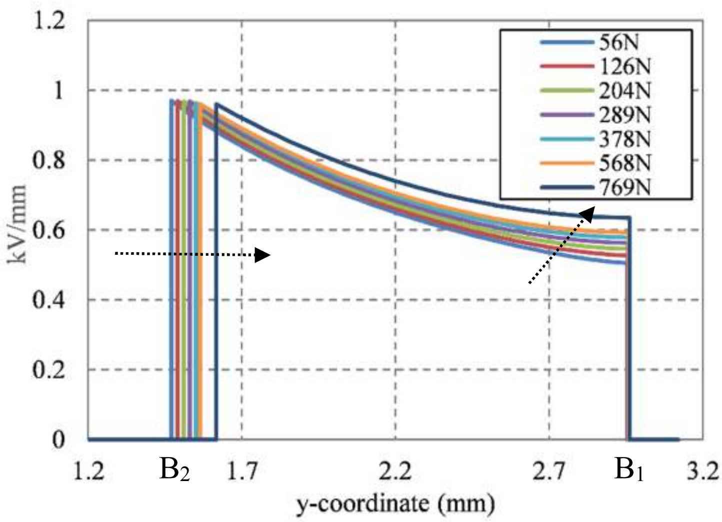

Figure 5-14. Electrical field distribution in deformed insulation layer. Detailed geometry see Figure 4-19.

To estimate the contribution of electrical field enhancement on the boosting of the PEA output signal, the increments of the electrical field at the two interfaces are shown in Figure 5-15. The interfacial electrical field E_2 at B_2 remains almost unchanged. And the increase of E_1 is much lower than the peak area change in Figure 5-11. This indicates that the electrical field increase is not a dominating factor for the enhancement of PEA output.

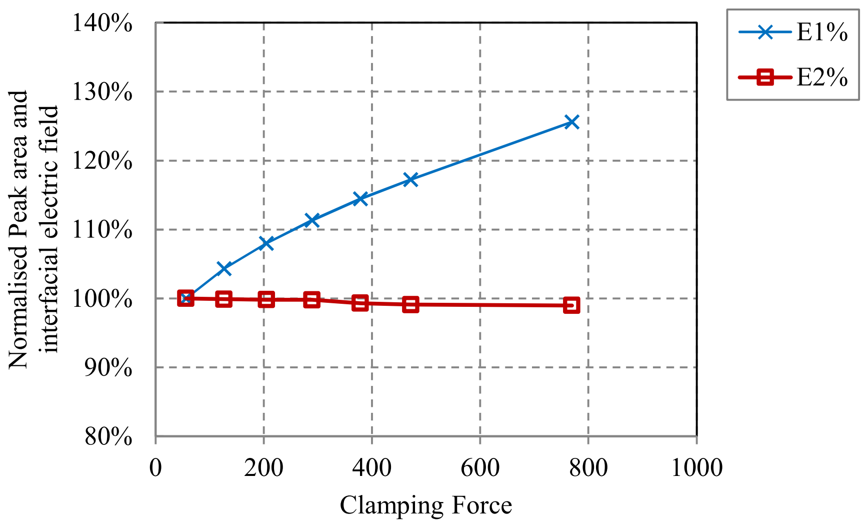

Figure 5-15. Enhancement of interfacial electrical field normalised to the lowest clamping force.

5.4 Feasibility of high temperature measurements with flat electrode

As discussed in the last sections, the clamping force has to be held constant through a room temperature test to preserve an identical PEA system response. However, for measurements at high temperatures or under cyclic thermal conditions, the corresponding variation in material properties, such as the bulk modulus and material thermal expansion, would result in further cable deformation even when the clamping force remains constant. This section discusses the feasibility of using a flat electrode PEA system for space charge measurements on mini-cables during thermal cycles between 25 °C and 70 °C.

A fully degassed mini-cable sample was utilised for this test. A low DC voltage of 8 kV was applied during the test to avoid space charge accumulation inside the mini-cable insulation. Therefore only interfacial charges at two semiconductor – insulation interfaces were generated and measured to evaluate the change of system response over the temperature cycle shown in Figure 5-16.

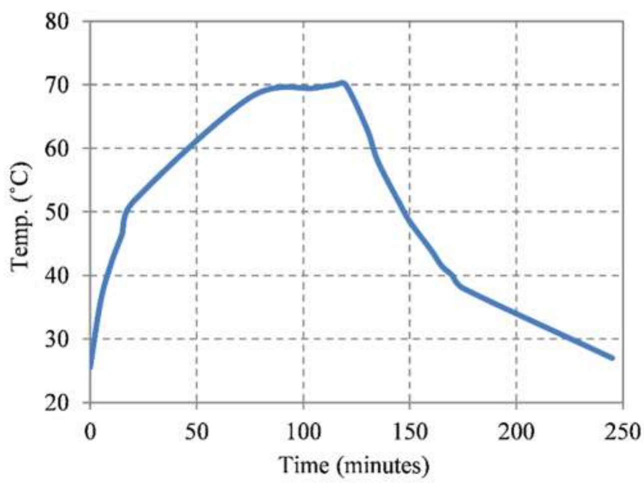

Figure 5-16. Temperature of the PEA cell during heating and cooling processes of the thermal cycle.

The amplified raw signal from the piezo sensor was averaged over 1000 cycles to reduce the incoherent electrical noise produced by the amplifier. Typical averaged signals recorded for a cable clamp force of 250 N at temperatures of 25 °C (before the thermal cycle), 70 °C (during the peaks of thermal cycle) and 25 °C (after the thermal cycle) are shown in Figure 5-17. P_1 and P_2 are due to the acoustic waves generated at the outer semicon-insulation and inner semicon-insulation interfaces respectively. The time delay between these two peaks is related to the temperature dependent acoustic wave velocity in the cable insulation material and the thickness of the insulation material. The time shifts, Δt, between the peaks of P_1 recorded at each temperature are due to the expansion and change in acoustic velocity of the aluminium base plate as well as the outer semicon layer of the mini-cable. Although the position of peak P_1 returns to the same time position following the temperature cycle, the position of P_2 becomes earlier in time after the thermal cycle compared to its original position i.e. before the thermal cycle. This demonstrates that additional distortion of the cable profile had occurred at 70 °C and had frozen-in return to room temperature. The positive voltage overshoot after P_1 in all cases may be due to the IRF (instrument response function) of the system rather than due to the accumulation of space charge.

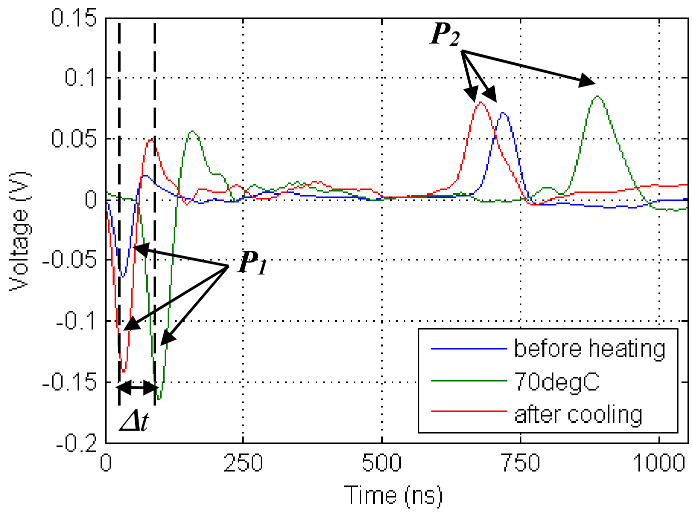

Figure 5-17. Averaged raw PEA outputs of the flat electrode PEA system for a fully degassed mini-cable with +8 kV DC bias voltage and a clamping force of 250 N (applied on a 30 mm cable clamp) before the heating, after being heated to 70 °C and after cooling back to 25 °C.

To compare the waveforms of Figure 5-17, it is useful to normalise the time axis for the 70 °C data to take into account the different acoustic velocities of the aluminium base plate and the cable insulation at 25 °C and 70 °C. According to [119], the acoustic wave velocity in XLPE decreases by 25 % on increasing the temperature from 25 °C to 70 °C. Applying this correction and shifting the time axes of the three data sets to compensate for the change in acoustic velocity in the flat aluminium electrode, the averaged raw data, after converting the time axis to distance using the acoustic velocity at 25 °C, can be re-drawn as shown in Figure 5-18.

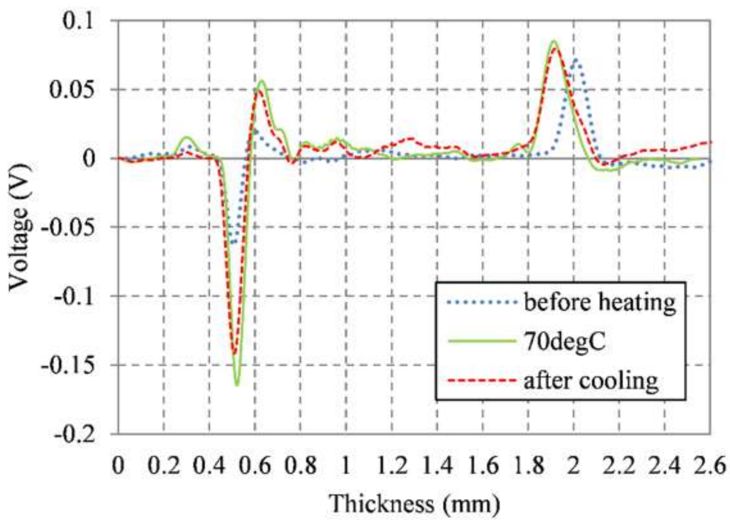

Figure 5-18. Averaged raw data rescaled to correct for acoustic velocity difference at 25 °C and 70 °C and with time axis converted to distance.

In Figure 5-18, the initial PEA measurement taken at 25 °C before the thermal cycle differs significantly to that of the subsequent measurements taken at the elevated temperature of 70 °C and after the temperature was then returned back to 25 °C (after the thermal cycle). First, the amplitude of the peak P_1 measured at the beginning of the experiment is significantly less than that measured at 70 °C and following its return to 25 °C. The second peak, P_2, retains a similar amplitude for all three measurements but the initial measurement appears to have a reduced duration. The second difference between the original measurement at 25 °C and subsequent measurements is that the measured distance between the peaks decreased on heating to 70 °C but that no further change occurred when cooling back to 25 °C.

This observation therefore demonstrates that as the temperature is increased to 70 °C, the softening of the cable insulation causes the cable insulation to deform further under the same applied mechanical clamping force. The deformed surface of the mini-cable has an increased contact area which contributes a ‘flat’ wavefront to acoustic waves generated at the outer semicon-insulation interface. Nevertheless, the deformation is less for the inner part of the mini-cable, which means the cylindrical wavefront of the acoustic waves that originate at the inner semicon-insulation interface is less disturbed.

The cylindrical waves disperse during propagation through the cable insulation while the plane wave originating at the outer interface maintains the same amplitude. As a consequence, P_1 was enhanced more than P_2, and shape change (broadening) only occurs for P_2. On cooling, this deformation appears to be 'frozen in' with only a slight decrease in the amplitude of the space charge profile.

According to the above experiments, mini-cable samples are likely to experience deformation at high temperatures under a reasonable (250 N) clamping force. Subsequent changes in the measured PEA output signals would then indicate different mechanisms for signal variation.

5.5 Verification of the curved electrode for cable PEA system

With a flat bottom electrode, the PEA system response is affected by cable deformation. This brings difficulty for signal processing and calibration. The non-uniform strain within the space charge measurement region may also have a secondary influence on space charge accumulation and pressure wave generation as the strained insulation may have different electrical properties e.g. conductivity and permittivity. The main reason for using a flat electrode is that it has the flexibility of accommodating different dimensions of cable samples. Since issues of cable deformation have arisen when using a flat electrode, it is necessary to try another type of electrode; a curved electrode where deformation of the mini-cable can be minimised.

5.5.1 Clamping force

There is a practical concern regarding the usage of the curved electrode. For the PEA method, the output signal would be affected by the contact quality between the sample and the base electrode. To improve the contact quality, normal approaches are either to reduce the surface roughness of the base electrode, use of inert silicone oil or to increase the clamping force on the sample. For the flat electrode, the mirror finish process is recommended. However, due to manufacturing constraints, the surface quality of the cylindrical groove in a curved electrode may not be easily produced. Therefore, it is necessary to verify whether the contact quality of a given curved electrode would affect the PEA system responses.

According to a quasi-static spring model [120], the transmission coefficient at a two ideally elastic media (acoustic wave transport from media 1 to 2) interface is given by

$$B = \frac{2Z_2}{Z_1 + Z_2 + i\omega Z_1 Z_2 / K} \tag{5.1}$$

where Z_1 and Z_2 are the respective characteristic acoustic impedance of two media; ω is the frequency of the incident acoustic wave, K is a constant representing the coupling quality of two media. For infinite rigid contact, $K = \infty$; for infinite slack contact, $K = 0$. The induced acoustic signal in the PEA method normally contains a wide frequency range, and a poor contact between the mini-cable sample and bottom electrode could result in signal distortion as high frequency components would be attenuated more than low frequency components as shown in Figure 5-19.

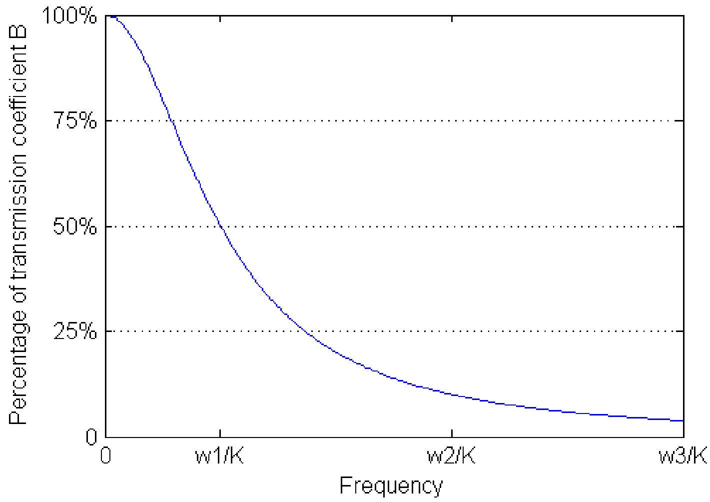

Figure 5-19 Frequency and contact quality dependent transmission coefficient ($w_3 > w_2 > w_1 > 0$ Hz, K is a positive constant)

Experiments were performed to verify whether the contact quality of the cylindrical groove would have a noticeable influence on PEA measurements. Specifically, a low DC voltage of 10 kV was applied to the cable centre conductor to generate only surface charges on semicon-insulation interfaces at room temperature. A range of clamping forces was applied to vary the quality of contact. The processed output signal (integral of PEA output piezoelectric current signal from the 50 Ω input impedance amplifier and de-noised using numerical filter and averaging) is shown in Figure 5-20.

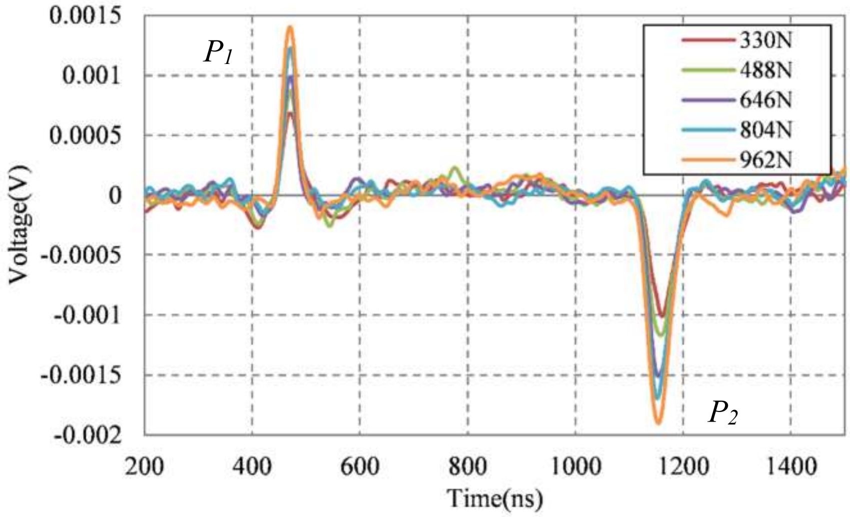

Figure 5-20 Processed PEA outputs under a range of clamping forces (50 Ω amplifier used and detected piezo current integrated to recover voltage).

The peak P_1 represents the acoustic wave generated at the outer semicon-insulation interface. It will contain the highest frequency components of the space charge signal as it has the shortest acoustic path and therefore is the least dispersed. On the contrary, peak P_2 that travels through the whole insulation thickness will contain lower frequency components. The absolute area ratios of P_2/P_1 with estimated error bar under different clamping forces are plotted in Figure 5-21.

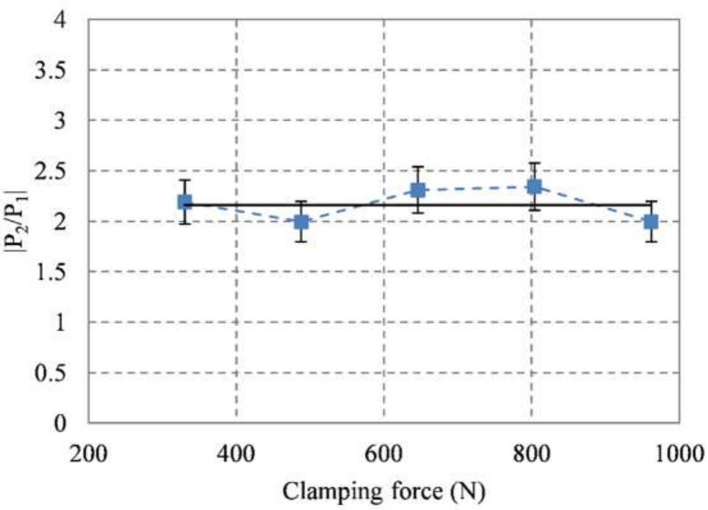

Figure 5-21 Area ratios of P_2/P_1 against the clamping force. Back solid line indicates the mean value.

Considering inherent experimental errors, the peak area ratio $|P_2/P_1|$ shown in Figure 5-21 does not change significantly with the clamping force. Therefore it can be concluded that during the frequency bandwidth of the space charge signal, the clamping force would not have such an effect on the contact quality resulting in a frequency dependent acoustic transmission coefficient at the cable-electrode interface. Additionally, unlike the flat electrode PEA system, the clamping force is not critical for a curved electrode PEA system. However, there is a factor of about 2 for the peak amplitude of P_1 and P_2 when the clamping force is increased from 330 N to 962 N. This observation suggests that a high clamping force does increase the quality of physical contact between the cable and the curved base plate of the PEA cell.

5.5.2 Acoustic coupling

Besides reducing the surface roughness and increasing the contact pressure, another approach to improving the contact quality is to add an acoustic coupler, for example high viscosity silicon oil, between the sample and the base electrode surface. With a mirror finished electrode, the layer of silicon oil may be thin enough to have a negligible influence on the PEA response. For a not so well-controlled electrode surface though, like the curved electrode, it is necessary to determine whether the layer of silicon oil would affect the PEA signal.

The comparative experiment is produced by space charge measurements on the same mini-cable with low DC voltage (+14 kV) at room temperature (about 20 °C) with direct contact (quoted as dry) and sufficient high density silicon oil added (quoted as silicon) between the mini-cable and the cylindrical groove of the electrode. Relatively low clamping pressure was used to maximise the amount of silicon oil and therefore its effect on the PEA output.

The raw PEA outputs (with excessive averaging to minimise noise) under these two conditions are shown in Figure 5-22. It is obvious that adding the silicon oil improves the acoustic coupling between the mini-cable and the base electrode, resulting in the stronger raw output signal than that with dry contact.

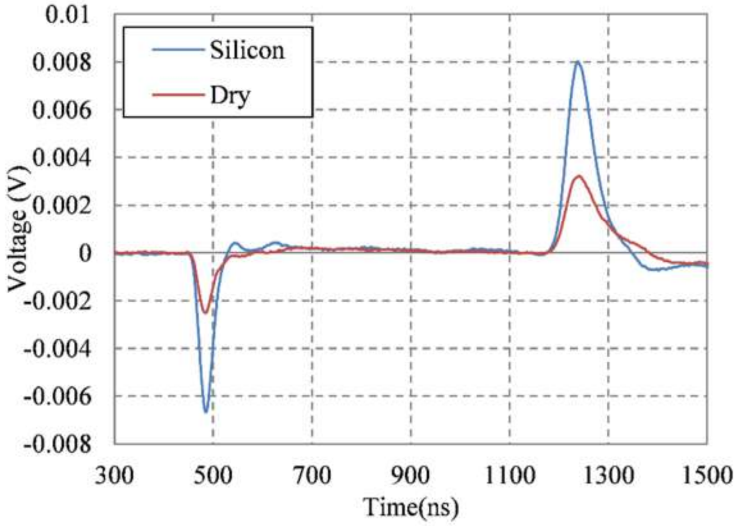

Figure 5-22. Raw PEA outputs (20000 sweeps averaged, with 3.2 kΩ buffer) with the dry and silicon oil improved contact.

After normalising the two signals to the first peak (P_1) as shown in Figure 5-23, it can be seen that the undershoot appears after P_1 and P_2 broaden with dry contact. However, after applying deconvolution (with assuming ideal Gaussian pulse shape) on the signal with dry contact to remove undershoots, the processed signal is the same as when silicon oil is used.

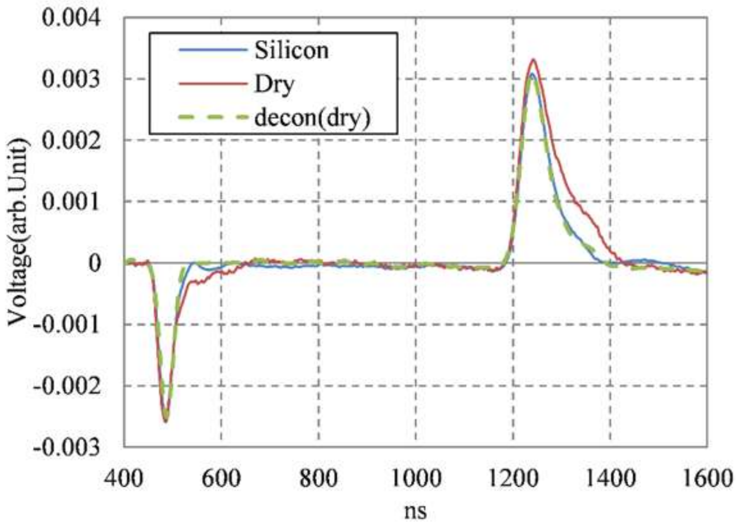

Figure 5-23. Normalised PEA voltage signal after recovery from the sensor-amplifier response. Deconvolution was performed on the PEA signal with dry contact.

The above experimental results suggest that using silicon oil as acoustic couplant could effectively enhance the PEA output signal and may improve the shape of the output signal in terms of avoiding undershoots. However, the usage of silicon oil is still not recommended considering the possible un-determined influence on the material properties of the mini-cable (outer semicon layer and adjacent insulation), especially for high temperature measurements.

5.5.3 High temperature performance

The PEA system response with a curved electrode under a thermal cycle between 20 °C and 70 °C is tested under the same experimental procedures that were described in Section 5.4 for the flat electrode system. The experimental results for 20 °C at the beginning of the thermal cycle, at 70 °C, and after return to 20 °C are shown in Figure 5-24.

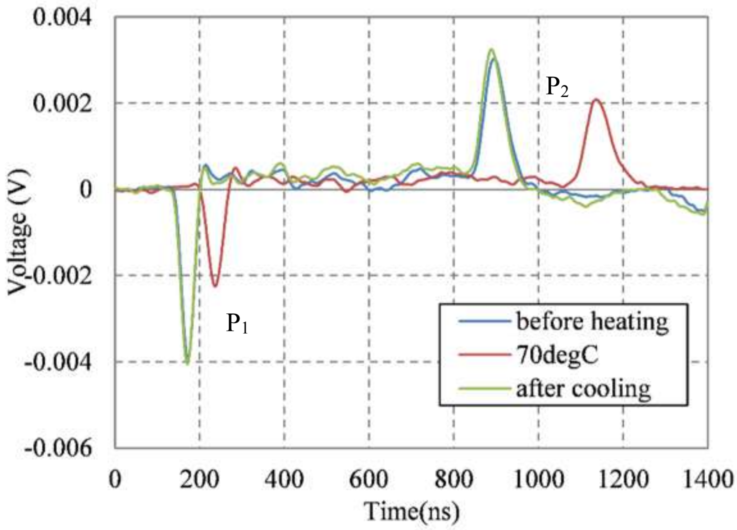

Figure 5-24 Raw PEA outputs of the curved electrode PEA system with +8kV DC bias voltage during a thermal cycle between 20 °C and 70 °C.

Unlike the results obtained using a flat base electrode (Figure 5-17), the lengths of space charge profile remain almost the same before and after the thermal cycle with the curved electrode PEA system. Therefore no significant permanent cable deformation occurred during the thermal cycle. At elevated temperatures, the time delay increases mainly as a consequence of wave velocity reductions in the aluminium PEA base electrode, cable insulation and the outer semicon layer.

Figure 5-24 shows signal reduction at 70 °C compared to the 20 °C measurements. The peak area variation and their ratios during the thermal cycle are plotted in Figure 5-25 (a) and (b) respectively.

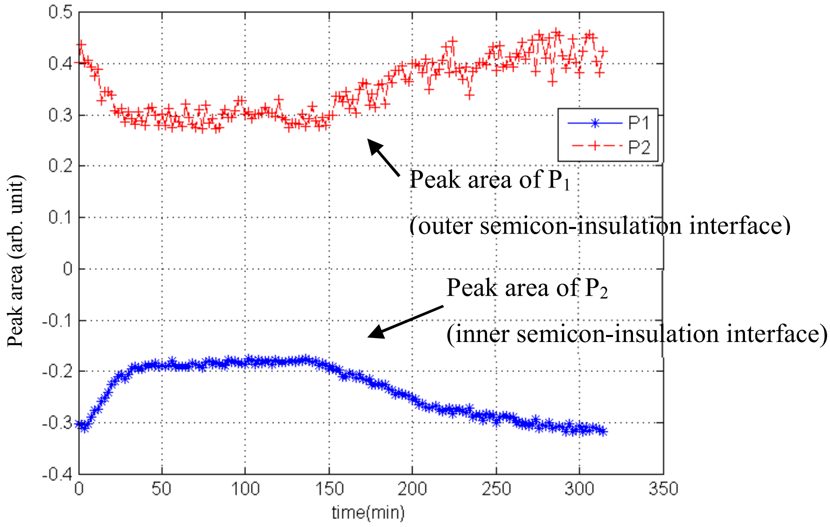

(a)

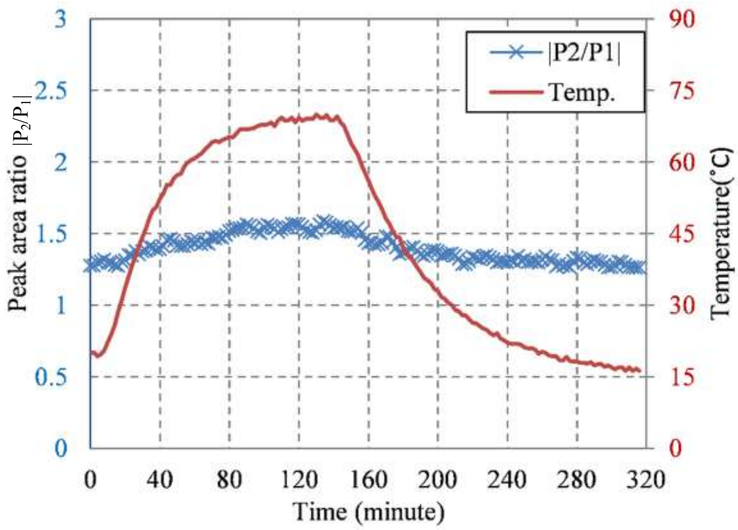

(b)

Figure 5-25 Interfacial peak areas (a) and their ratio P_2/P_1 (b) recorded during the first 3 hours after the clamping force was applied at 60 °C.

It can be seen that the two peak areas change synchronously with the temperature, while their ratio increased slightly at the peak temperature and returns to the same value after cooling back to room temperature. Since the peak area ratio remains relatively constant, the signal reduction during heating and recovery during the cooling at the end of the thermal cycle may be a consequence of many factors. These include:

- The temperature dependent gain of the amplifier.
- The negative temperature coefficient of the pulse coupling capacitor.
- Reduced sensitivity of the PVDF sensor at high temperature.

With respect to the above discussion, the normalised space charge profiles shown in Figure 5-26 confirm the relative stable performance of the mini-cable PEA system with a curved base electrode during the thermal cycle between 20 °C – 70 °C.

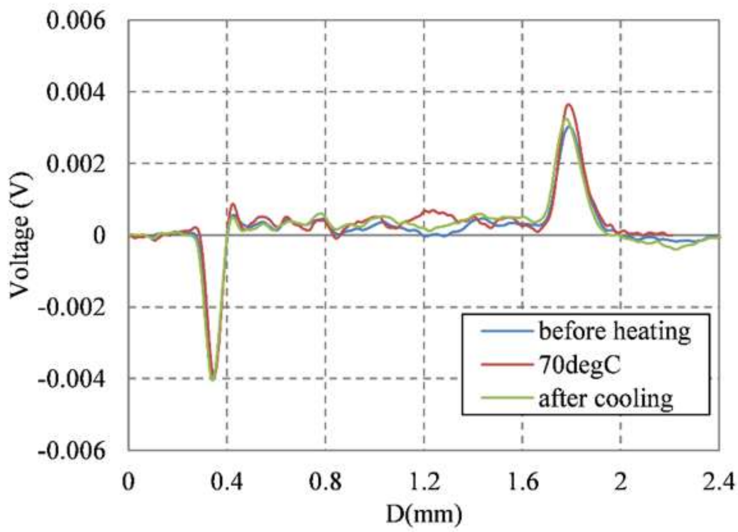

Figure 5-26. Raw data rescaled to correct for acoustic velocity difference at 25 °C and 70 °C and with time axis converted to distance. Profile of '70degC' is normalised to match the magnitude of P_1 of the other two profiles.

5.5.4 High temperature stability

The thermal stability of the PEA system was tested through a set of cyclic temperature tests and high temperature endurance tests over a long time. Specifically, space charge measurements (with low DC voltage of -8 kV to avoid significant space charge accumulation) were taken during four thermal cycles (25 °C - 70 °C). Each thermal cycle took about 4 hours. The time interval between 1st and 2nd, 2nd and 3rd, 3rd and 4th cycle are 3, 11 and 10 hours respectively. The measured space charge profiles at 70 °C of each cycle are plotted in Figure 5-27. Taking the random noise into account, the outputs of the PEA system remain constant over the four thermal cycles without a noticeable systematic change.

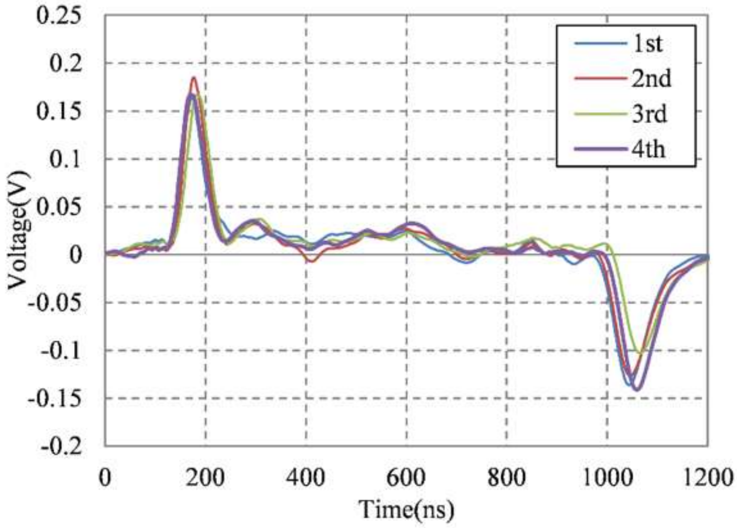

Figure 5-27 Space charge measurements at 70 °C of each thermal cycle (50 Ω amplifier used and detected piezo current integrated to recover voltage).

The long-time stability of the PEA system at 70 °C was tested following the four thermal cycles. Figure 5-28 shows the outputs of the PEA operating at the 70 °C isothermal condition over 20 hours. No significant degradation of the output signal could be found.

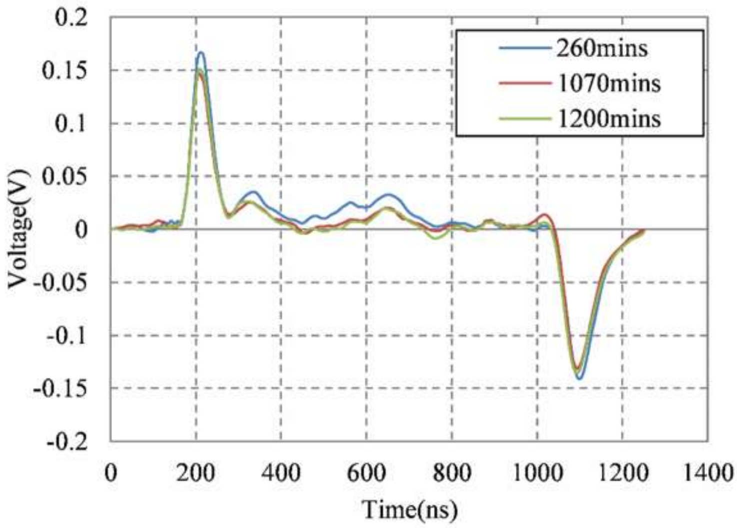

Figure 5-28 Space charge measurements at 70 °C over 1200 minutes (50 Ω amplifier used and detected piezo current integrated to recover voltage).

Combining the temperature cycles and high temperature tests over a long time, the performance of the PEA system can be regarded as stable for space charge measurements under high temperatures up to 70 °C.

5.6 Conclusion: a comparison between flat and curved electrodes

The performances of PEA system with two shapes of base electrode, flat and curved, were assessed in this chapter.

The main potential issue of using the flat electrode for mini-cable PEA system is that the assumption of a line contact (between the cylindrical cable and the flat electrode surface) may be unlikely. In circumstances of high clamping force, noticeable distortion of the mini-cable occurs at the line of contact leading to an increase in the contact area between the cable and flat base electrode. The consequences of the increased contact area on the PEA output are the change in signal overshoot due to reflected acoustic waves from the contact boundaries as observed in the simulations and experiments and the non-linear (radius dependent) signal enhancement which were also verified by both experiments and simulations in Section 5.3. This highlights the significance of maintaining the same clamping force during the experiments for reproducibility and therefore the signal calibration. However, when temperatures become a variable in experimental conditions, it becomes hard to preserve the reproducibility as the cable deformation may vary due to the temperature dependent mechanical properties of the cable insulation even when the clamping force is kept constant. Significant changes to the flat base electrode PEA outputs during the thermal cycle of 25 °C – 70 °C have been demonstrated in Section 5.4. In conclusion, the mini-cable PEA system with a flat electrode is likely to be sensitive to the clamping force and temperature change. Moreover, extra contribution to the signal overshoots would be formed due to the increased contact area. It is recommended when using a flat base plate PEA system with mini-cables to perform a complete thermal cycle under zero voltage conditions to ensure that the majority of the cable deformation takes place before each cable electrical tested under applied voltage.

On the contrary, by matching the PEA base plate to the outer surface of the mini-cable, the curved electrode prevents cable deformation and thus contributes to the experimental reproducibility. Concerning the practical difficulty in producing the low surface roughness for the curved electrode, experiments were taken to examine the effect of contact quality to the PEA outputs regarding different clamping forces and acoustic coupling agency (silicon oil).

Nevertheless, it would be arbitrary to say that the curved electrode is better than the flat electrode as it should be remembered that the development of using the flat electrode was for the purpose of facilitating the measurement of space charge in cables of different dimensions.

6 CABLE CHARGING

6.1 Introduction

As discussed in Section 2.4, the conductivity of polymeric DC insulation material is normally dependent in a non-linear way on the electric field magnitude and temperature. The non-uniform electric conductivity that results when a voltage is applied to the cable causes the formation of space charge which in turn modifies the electric stress in the insulation. Also, during normal in-service operation, a temperature gradient is likely to exist in the cable insulation due to the Joule heating on the conductor whilst the outside temperature of the cable is determined by ambient conditions. Should a temperature gradient (typically greater than 20 °C) exist, this would significantly disturb the electric conductivity of the insulation material and result in raised electric stress at the outer radius of the insulation [8]. Even under isothermal conditions, initially in the absence of space charge, the conductivity is graded on the axial direction due to its dependency on the (geometry determined) Laplacian electric field. The continuity equation states that the time dependence of space charge density at a region of space must be equal to the net current density flowing into that space. Mathematically, we can write this as (in 1D):

$$\frac{d\rho}{dt} = -\frac{\partial J}{\partial x} \tag{6.1}$$

where, ρ is the charge density, J is the current density, x is spatial position and t is time. Initially in the absence of space charge, J is dependent on the conductivity and the local electric field applied. As the field and therefore J are higher in the insulation near to the conductor, dJ/dx, is not zero and from the continuity equation space charge density must build up in the cable. A steady state is achieved when the space charge builds up sufficient field to cause J to become uniform, i.e. dJ/dx = 0 in the insulation. As a consequence, space charge accumulation is therefore an inherent phenomenon, for the HVDC cable insulation when the insulation electrical conductivity has a non-linear dependence on the electric field. For this reason, the process described above is called ‘cable charging’ in this work.

The cable charging transient as discussed above has practical significance for the reliable operation of DC cables. For example, assuming isothermal conditions, the application of voltage of a particular polarity will cause the accumulation of space charge (cable charging) to take place. The space charge field created will oppose and therefore balance the applied Laplace field in the cable insulation, giving rise to a much more uniform field in the insulation material. This is a positive effect; as the high electric field that would exist at the inner conductor/insulator interface would be reduced during cable charging and therefore reduces the likelihood of breakdown in the cable. However, should the applied voltage to the cable be suddenly reversed, as could happen in a Current Commutated DC converter technology HVDC link, the accumulated space charge will produce the opposite effect; increasing significantly the electrical stress in the insulation close to the inner conductor/insulator interface above the initial Laplacian value. This is a negative situation as it would increase the likelihood of electrical failure of the cable insulator during the time before the cable discharges and then re-charges with the reverse polarity space charge. Therefore, it is necessary to know the 'speed' of the charging process such that field intensification is avoided during polarity reversal pausing for sufficient time for the cable to discharge.

Knowledge of the charging transient is also essential when performing accurate PEA measurements particularly with regard to the initial calibration of the PEA apparatus. As mentioned in Section 3.12, the calibration procedure for the PEA normally requires zero space charge in the cable insulation to ensure that the electrode/insulator surface charge densities in Equation (3.10) at the two electrode/insulator interfaces are only dependent on the applied voltage and geometry of the cable. For samples that have no electrical history, the electrical field is normally calculated using Equation (2.1) which is based on the Laplace equation. However, as suggested in reference [27], the formula for steady-state electric field after cable charging (Equation (2.5)) should be used instead; as the bulk charge in the cable will induce charge at the electrode interfaces changing the ratio of the peak areas P_2/P_1. However in practice, the time taken for the charging of a cable is unknown and it may not be clear at the outset if the charging has taken place quickly with respect to the time taken to perform the calibration or that the opposite is true. In some cases, especially for calibration at high temperatures, the cable sample may charge quickly in which case Equation (2.5) will apply, whereas at low temperature, when little charge accumulation occurs through cable charging over the time of the experiment, Equation (2.1) will then apply. Correct calibration of the PEA therefore requires knowledge of the charging transient at applied electric field.

In this chapter the phenomena of cable charging due to the non-linear dependence on conductivity with the applied electric field will be studied. In particular, the transients of space charge formation under isothermal conditions under both charging (poling) and polarity reversal will be studied through both simulation and experiments. Moreover this work has the potential to present a novel method to evaluate the parameters controlling the charging transient on cylindrical cable insulation by means of PEA space charge measurements. By matching the simulation (Section 4.2) with the experiments, the influence upon the electrical field of parameters which determines the conductivity can be identified and the model could be up-scaled to predict cable charging effects in full size commercial cables.

6.2 Simulations of cable charging and polarity reversal

Firstly, it is necessary to confirm that the ‘cable charging’ phenomenon described in this work refers to the process of non-linear conductivity dependence on the non-uniform electric field that exists in the insulator. Secondly, that cable charging can take place under the relatively low DC applied electric field that the cable experiences during normal service conditions over a range isothermal temperature conditions. In addition, the charging dynamics on reversal of the applied DC voltage will also be investigated and is cited in this work as ‘polarity reversal’.

Based on the analytical expressions for the DC steady state electric field in the case of non-charged and when fully charged, Equation (2.1) and Equation (2.5) in Chapter 2, the electric field as a function of radius r for a mini-cable insulator is plotted in Figure 6-1. The accumulated charge due to the power-law field dependent conductivity has the effect of reducing the electric field at the inner conductor and increasing the electric field at the outer conductor from the values given by the Laplace equation. This demonstrates the positive nature of the cable charging process in that it makes the field more uniform inside the cable insulator.

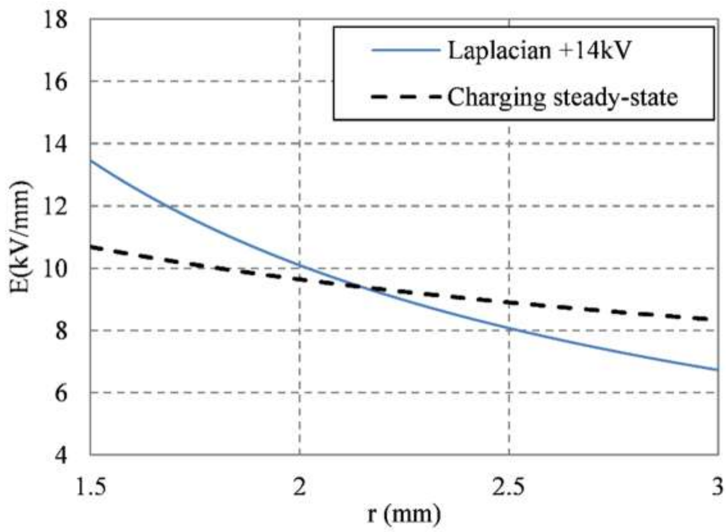

Figure 6-1. Laplacian field and space charge modified electrical field at steady-state with +14 kV DC and assuming a power index of 2 for the calculation of the material conductivity using Equation (2.5).

The variation of space charge density during the polarity reversal under -14 kV DC and 70 °C was simulated using the model introduced in Section 4.2. As shown in Figure 6-2, at beginning of the polarity reversal, the previous (positive) accumulated charge remains. Then on polarity reversal, the positive charge close to the inner electrode decays, being replaced by negative charge. Negative charges generally dominate the insulation after 36 minutes and after approximately 3 hours, a steady-state charge distribution is reached where the negative charges have the same radial distribution as the original positive charge distribution formed during the previous charging.

The steady state electric field distributions just before polarity reversal and after polarity reversal are shown in Figure 6-3, along with the Laplacian field for comparison. Immediately on polarity reversal, the residual positive space charge causes the magnitude of the electric field to increases at the inner electrode interface and decreases at the outer electrode compared with the steady state values after the initial charging. The electric field is now significantly higher than the Laplacian field at the inner electrode. However, as with the initial charging the electric field in the insulator becomes more uniform as negative charge accumulates in the insulation. The length of time in which the electric field at the inner electrode is higher than the Laplacian field value depends on the time constant for the charging process. Finally the steady state electric field distribution under polarity reversal is equal in magnitude but has opposite sign to the original steady state field distribution before polarity reversal.

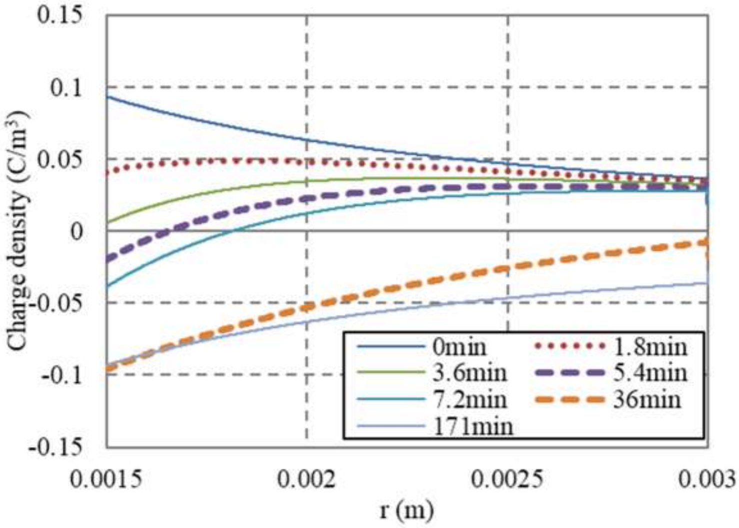

Figure 6-2. Simulation of the space charge accumulation due to the field dependent conductivity, model 1 (parameters see Table 6.1), during polarity reversal (at -14 kV DC and 70 °C).

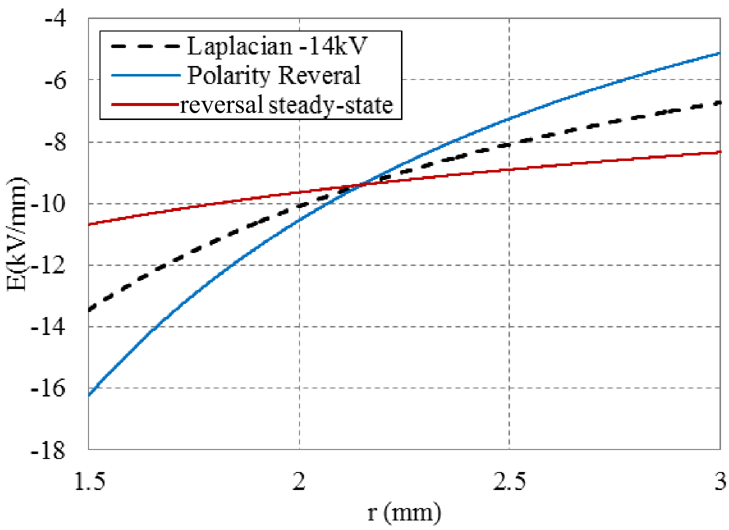

Figure 6-3. Laplacian field and space charge modified electrical fields at the start and after the steady-state field had been achieved following polarity reversal of -14 kV DC.

The overall effect of cable charging on the PEA output signal can be deduced by employing the 1D simulation model that was introduced in Section 4.3 to generate the raw PEA output using the data of Figure 6-1. The simulated PEA outputs for the

Laplacian field distribution (zero accumulated charge) and for the steady-state charged case are shown in Figure 6-4.

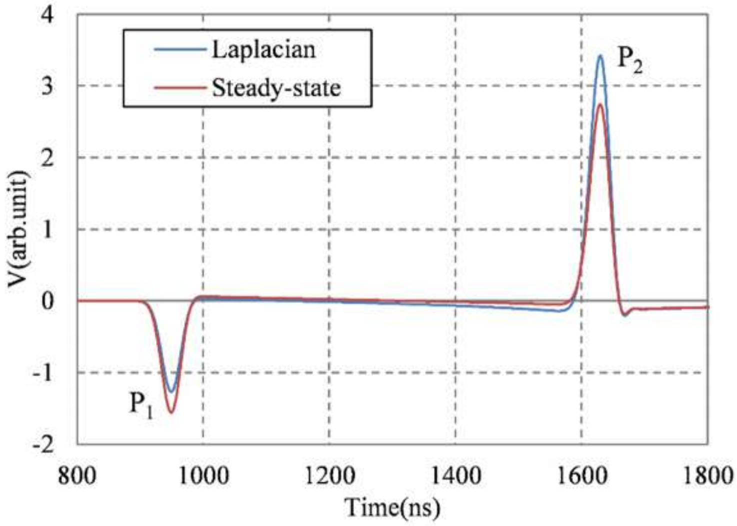

Figure 6-4. Simulated PEA outputs with analytical Laplacian field (zero bulk space charge) and steady-state charge distribution following cable charging. In the simulation, pulse width is 30 ns; the input impedance of the amplifier is assumed to be 2.5 kΩ; the capacitance of the piezoelectric sensor film is assumed to be 170 pF, the insulation is assumed to be acoustic lossless.

As shown in the simulated profiles of Figure 6-4, the changes within the insulation domain (between the two peaks) are small compared to the amplitudes of the interface charges. Moreover, the cable charging negates the contribution of bulk polarisation in the insulation. These factors pose a number of difficulties in measurement of the charging effect within the bulk of the insulation. It can be imagined that with electrical noise, baseline drift and acoustic attenuation all present in the experimental data, the bulk charge signal would become difficult to measure. However, it can be noticed that most obvious changes that exist in the data are the areas of the two interfacial peaks, P_1 and P_2. This observation leads to a new method to follow the cable charging process, which involves monitoring the peak areas as will be introduced in the next sub-section.

6.2.1 Peak area ratio

The areas of the two interfacial peak signals, P_1 and P_2, represent the total electrode charge at the two interfaces of the insulation and are proportional to the electric fields at each interface. Without space charge accumulation, only capacitive charges due to the applied DC and that induced by bulk polarization charge voltage will be formed. Typically, for the cable dimensions of the mini cables, the electric field ratio and therefore the peak area ratio, P_2/P_1 will be approximately 2 for the case when no space charge has accumulated in the bulk. However, on cable charging, the accumulation of the space charge will cause additional induced charges to appear at the electrode interfaces and would generally modify the quantity of electrode charges measured in the PEA outputs. In Figure 6-1, the steady state peak area ratio drops from 2 to approximately 1.3 when the cable has achieved steady state charging. Therefore the variation of the ratios between two interfacial peak areas reflects the total amount of the accumulated space charge in the bulk.

The advantage of measuring the peak area ratio over the total charge quantity are that: The space charge signal is of low frequency and is therefore may easily be attenuated by the sensor/amplifier circuit or other system response of the PEA apparatus; On the contrary, the peak signals are of high frequency and would be less attenuated and more clearly discerned from the background noise.

6.2.2 Charging dynamics

In order to establish the dynamics of the cable charging phenomena and how this relates to the changes in peak areas, time dependent 1-D PEA simulations using the cable charging model of Section 4.2 were used with the conductivity model 1 in Table 6-1 (Section 6.4.3) under 14 kV DC and isothermal condition of 70 °C.

6.2.2.1 Space charge during initial cable charging

A simulation of the peak area ratio (P_2/P_1) change during the cable charging process is shown in Figure 6-5. As predicted in Section 6.2.1, the ratio between the inner and outer interfacial peak signal areas, as well as the interfacial electric fields, changes from about 2 (with respect to the inner radius a ≈ 1.5mm and outer radius b ≈ 3mm) for a Laplacian field (no space charge) to approximately 1.26 after 60 minutes.

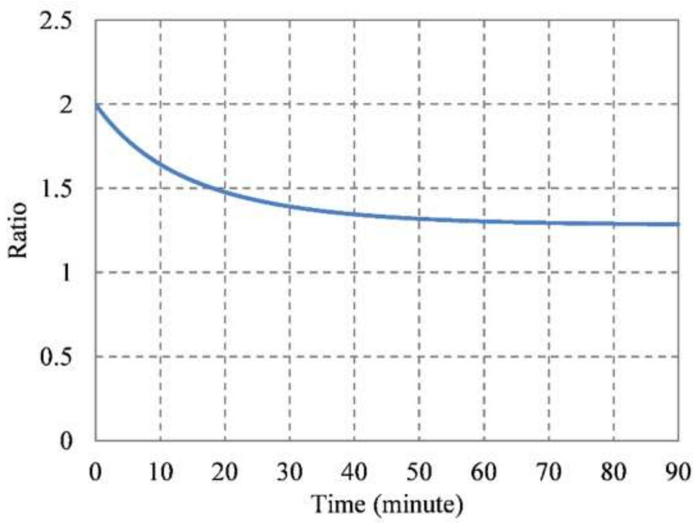

Figure 6-5. Ratios of two interfacial electrical stress E_a/E_b during charging.

Beside the values of the peak area ratio, the more important information contained in Figure 6-5 is the 'speed' of the ratio change. By subtracting the steady state P_2/P_1 ratio from the data in Figure 6-5, the functional shape of the decay, ΔRatio = Ratio - Steady State ratio, can be verified by plotting on a suitable axis. When plotted on a linear axis as in Figure 6-6 (a), the ΔRatio variation seems to follow an exponential decay. However when plotted as Log-linear against time in Figure 6-6 (b), the ratio variation is observed to depart from a strict exponential shape after 40 minutes. This is due to the fact that the conductivity is both time and spatial dependent during the charging transient as the conductivity determines the space charge and therefore the electrical field distribution which in turn modifies the (field dependent) conductivity itself.

Although the peak ratio change may not follow a standard exponential decay, for the convenience of analysis, the concept of 'time constant' will be used to describe the time for charging transient. The term time constant is the time taken for the peak area ratio change to be 36.8 % of its initial value. In addition, the best fit of the experimental data, as shown in Figure 6-6, is obtained by using a Matlab toolbox (Curve Fitting Toolbox) which also gives the time constant of the fitted curve. Then the time constant used would be the mean value of the time to reach 36.8 % of its initial value and the time constant of the fitted curve. In this example, the mean time constant is about 15 minutes.

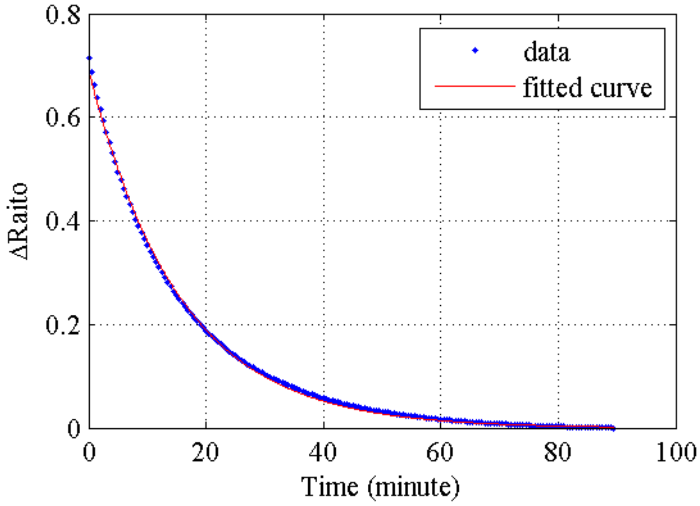

(a)

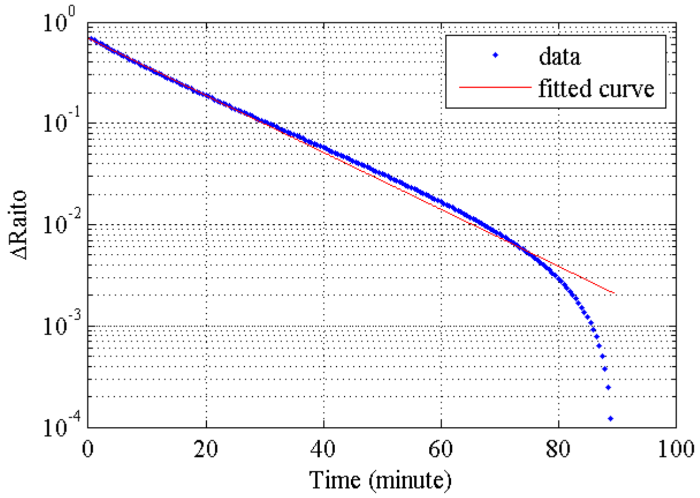

(b)

Figure 6-6. Variation of the peak area ratios compared with the standard exponential decay in linear-linear (a) and log-linear (b) plots. ΔRatio = Ratio – Ratio value of steady-state.

6.2.2.2 Space charge on polarity reversal

For the parameters given in Table 6-1 model 1, Figure 6-7 compares the time dependence of the peak area ratio P_2/P_1 following the polarity reversal with the initial space charge distribution equal to that obtained from the previous charging simulation. Due to the initial accumulated charge within the insulator, effectively acting as heterocharge for inner peak and homocharge for outer peak, the peak ratio at the beginning of the polarity reverse is increased above the Laplacian value with an initial ratio of 3.2. Afterwards the peak area ratio follows the exponential decay to the same steady-state value with the charging process ($P_2/P_1 = 1.3$).

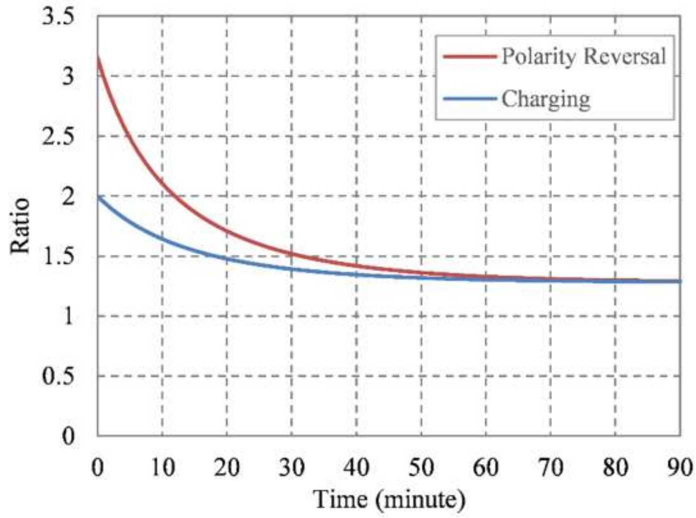

Figure 6-7. Peak ratio variation during charging and polarity reversal.

By subtracting the steady state ratios of the peak area ratios from the data shown in Figure 6-7, and plotting on a log(P_2/P_1) verses linear time it gives two straight lines with the same slope in Figure 6-8 as is the case for the initial charging simulation. The time constant characterising the dynamics of polarity reversal is therefore the same as the previous charging behaviour.

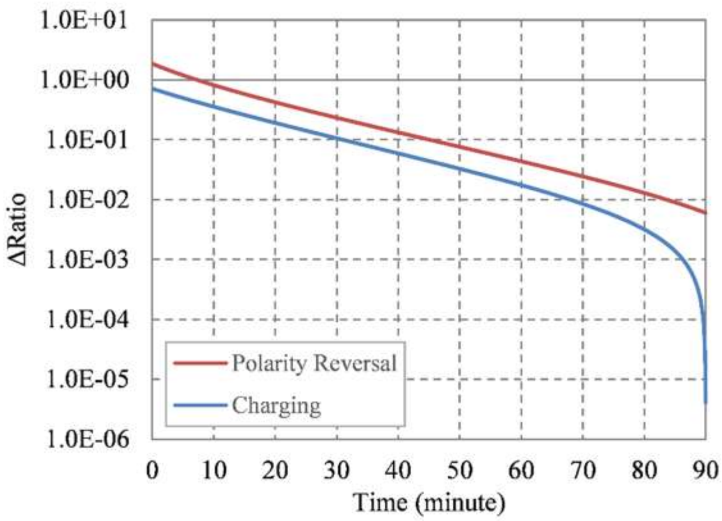

Figure 6-8. The same time constants can be found for charging and polarity reversal.

6.3 Experimental measurements of cable charging

Before being able to measure the space charge accumulation due to the cable charging process, it is necessary to take into account the following:

- To observe the cable charging phenomena, the applied DC voltage should be relatively low to preserve the Ohmic contact of the electrode – insulation interfaces. Under moderate to high DC applied voltages, the electric field may become sufficiently high for the accumulation of homocharge or heterocharge to take place due to charge injection or ionisation of impurities. If care is not taken then these may become the dominating phenomenon rather than the cable charging phenomena investigated here. This places limits on the DC bias voltage applied to the cable and raises the requirements of the system on sensitivity and noise immunity.
- The simulation results shown in Figure 6-2 have shown that the accumulated charge due to cable charging is relatively evenly distributed within the insulation. The magnitude of the accumulated bulk charge is also relatively low compared to the interface charge response of the cable. The bulk charges therefore give rise to PEA signals of low frequency compared with the frequency components of the interface charges. As was mentioned in Section 3.11, PEA systems suffer an electrical impedance mismatch between the piezoelectric sensor and the amplifier giving rise to a high pass filter in which low frequency signals may be attenuated. Care must therefore be taken to ensure that the impedance of the buffer amplifier of the PEA apparatus has sufficiently high input impedance.
- Even if the low frequency charge signals were successfully recorded in the raw PEA outputs, it may be wrongly treated as a part of the overall system response and thus be removed by using deconvolution techniques.

These reasons may also explain why it is quite common to observe bulk charges (interfacial charges, heterocharge or homocharge) in the space charge profiles published in the literature while it is relatively rare to see data presented on space charge due to cable charging using the PEA method for cylindrical geometry samples for example in the literature [8, 12, 15, 22, 121].

6.3.1 Experimental methodology

In order to verify the above observations obtained through simulation, a number of preliminary experimental measurements of the charging and subsequent polarity reversal were carried out using the curved base plate PEA space charge measurement system on a mini-cable (type D807D). The PEA and cable were contained within the temperature controlled oven to give an isothermal temperature inside the cable of 55 °C. A moderately high voltage of 20 kV was applied to the cable for charging experiment to attempt to detect space charge due to bulk polarization in the insulator bulk which as discussed above is difficult to detect. A voltage of -20 kV was then applied to the cable for the subsequent polarity reversal test.

The space charge profiles obtained 3 minutes, 49 minutes and 203 minutes after polarity reversal are shown in Figure 6-9 reveals that the space charge in the cable insulation accumulates to a greater extent within the region close to the inner electrode. The areas under the electrodes peaks also change in response to the change in bulk space charge.

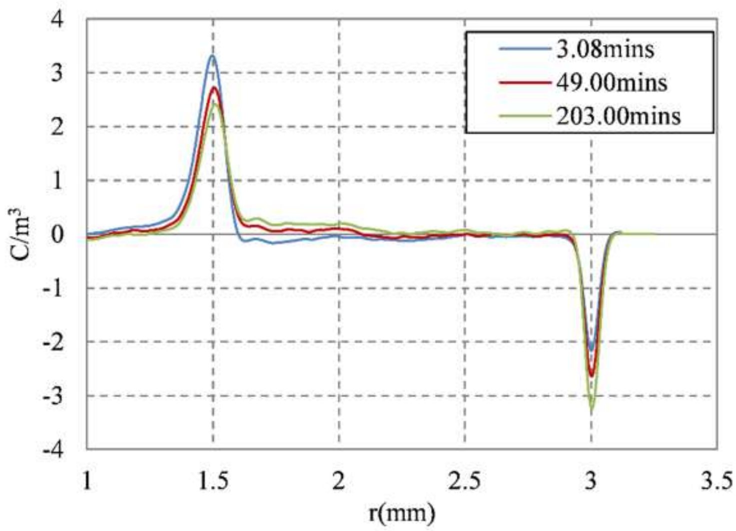

Figure 6-9. Space charge measurements during polarity reversal at 55 °C with 20 kV DC.

PEA space charge measurements taken with the applied voltage set to zero just before the polarity reversal and after steady state charging of the cable under polarity reversal are shown in Figure 6-10. The former space charge profile was multiplied by -1 to aid comparison between the two profiles. The graph shows that the space charge density increases to approximately 0.15 C/m^3 in the insulation close to the inner electrode interface of the cable and decreases with increasing radius. The similar space charge profiles obtained under the two different polarities show that the cable charging is not dependent on the polarity of the applied voltage to the cable and that the net charge accumulated within the cable insulation induce opposite charges on the cable electrode interfaces.

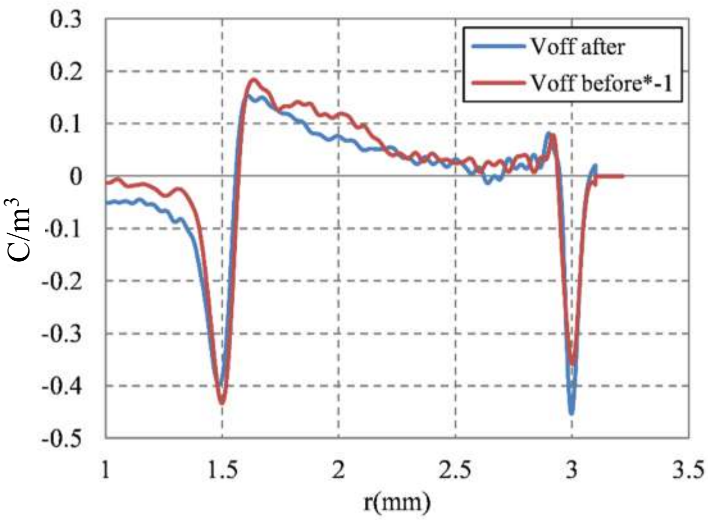

Figure 6-10. V_{off} measurements before and after polarity reversal.

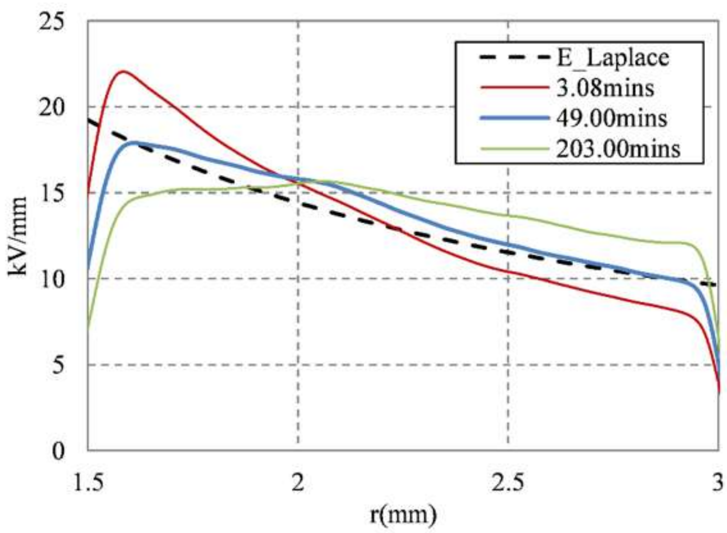

Figure 6-11. Electrical field distribution during polarity reversal calculated from the space charge measurements in Figure 6-9.

The electric field distribution calculated from the space charge distribution of Figure 6-9 is shown in Figure 6-11. Again the measured field profiles compare favourably with those simulated in Figure 6-3.

A second preliminary experiment was undertaken to determine the peak area ratios at 1 minute intervals during charging of the cable and under polarity reversal. The PEA and cable were contained within the temperature controlled oven to give an isothermal temperature inside the cable of 60 °C. This time a voltage of 10 kV was applied to the cable for charging and then -10kV was applied for the following polarity reversal. The tests were therefore carried out with an applied field of 10 kV/mm maximum; similar to the design stresses of commercial cables. The cable was previously degassed prior to the experiment in order to remove any volatile impurities that could contribute to ionic conduction.

The peak area ratio values obtained from the raw experimental data are shown as a function of time in Figure 6-12. The experimental peak area ratios are consistent with the simulation results shown in Figure 6-7. On first application of the applied voltage the peak area ratio was approximately 2 which then subsequently decreased to approximately 1.3. Moreover, the same time constants of about 47 minutes are found and also can be visually confirmed by the two parallel lines in Figure 6-12 (b). This approves that the time constant obtained from polarity reversal is the same with that of charging a space charge free cable.

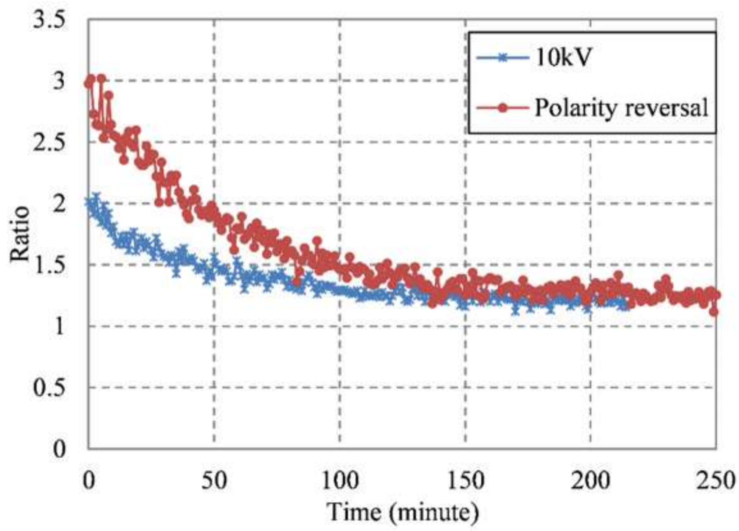

(a)

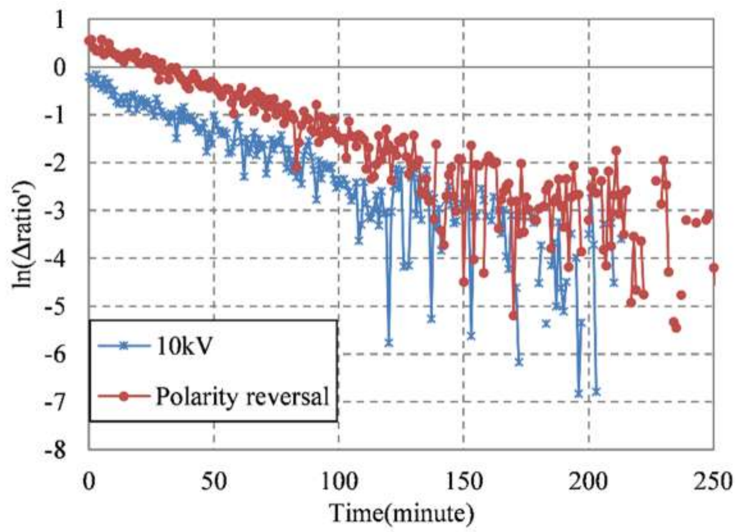

(b)

Figure 6-12. Variation of the peak area ratios obtained through the PEA measurements on a mini-cable at 60 °C with 10 kV for charging and -10kVfor the following polarity reversal plotted in linear-linear (a) and log-linear (b).

6.4 Application of the technique to verify charge transport models

With the methodology proposed in the above section, the charging transient can be assessed by the time constant of the peak area ratio change during either charging or polarity reversal. Since the cable charging phenomena is only determined by the conductivity of the insulation material (with the permittivity assumed to be a constant) experimental space charge charging data could be used to test the various conductivity models introduced in Section 2.4. Space charge measurements were taken as a function of applied voltage and isothermal temperature for comparison with simulations in which the various unipolar charge transport models are assumed to hold.

6.4.1 Experimental method

A group of PEA space charge measurements with combined electric stresses and isothermal conditions are required to obtain the dependency of the conductivity on field and temperature. However, the feasible experimental conditions are limited as shown in Figure 6-13. For the electrical field, the minimum field (E_{min}) is determined by the sensitivity of the PEA system and the maximum field (E_{max}) should be lower than the threshold for significant homo/heterocharge formation. As demonstrated in Figure 6-13, the field threshold for charge injection (schottky injection) is temperature dependent.

The temperature range is naturally within the ability of the measurement system which is 20 °C – 70°C. Nevertheless, the time scope of the experiments may be too extreme at low temperatures. Therefore the lower triangular part in the matrix of experimental conditions may not be feasible. Consequently, only the white range of a trapezoidal shape in the condition matrix should be applied. It should be pointed out that in fact the lowest temperature (dotted blue line) may not be a linear function with the applied field and the field threshold may not linearly reduce with temperature.

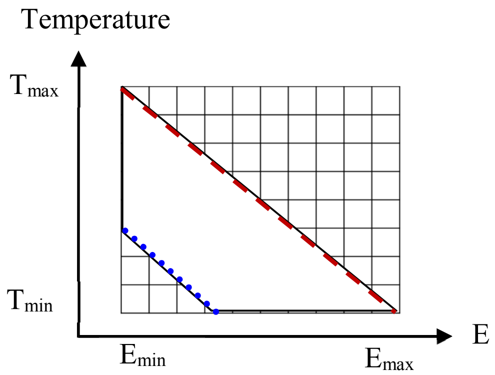

Figure 6-13. Feasible range of experimental conditions on the electric field and temperature.

Ideally, each measurement should be performed on a new (space charge free) mini-cable sample. However it is difficult to ensure or examine the consistency of samples utilised. To avoid any experimental error due to the change of samples, the same mini-cable should be used for all tests. The feasibility of this proposition is benefited by the previously verified (in Section 6.3.1) fact that the time constants for charging and polarity reversal are the same. So, instead of measuring the charging for each new mini-cable, the time constant τ(E,T) can be measured by a series of polarity reversals changing the temperature or voltage at each polarity reversal.

A degassed mini-cable (D806D) was used for this experiments. The PEA measurements were performed at two isothermal temperatures, 50 °C and 70 °C. At 70 °C, the time constants for cable charging were obtained under absolute DC bias voltages of 6 kV, 8 kV, 10 kV, 12 kV and 14kV. At 50 °C, only two levels of DC voltage, 12 kV and 20 kV, were applied due to time constraints.

6.4.2 Experimental results

The time constants calculated from the peak area ratio changes are presented in Figure 6-14. The graph shows that the time constants obtained are dependent on both voltage and temperature and range between 14 minutes at 15 kV and 70 °C and 300 minutes at 12 kV and 50 °C for this particular cable. Extrapolating to room temperature would yield time constants of the order of 1000 minutes and hence the phenomena of cable charging would not necessarily be discernable in short term space charge measurements.

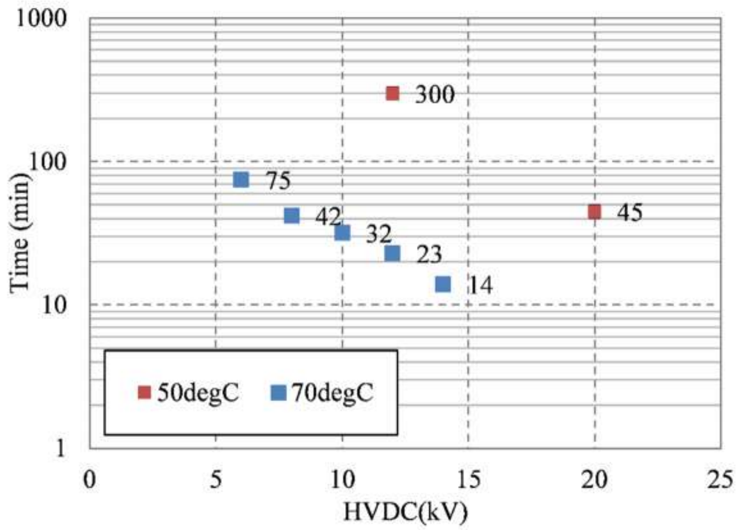

Figure 6-14. Charging time constants obtained from the PEA measurements on a mini-cable during a sequence of polarity reversals at 50 °C and 70 °C. The 10% error bar (not clearly shown in this figure) was applied due to the variation of the time constants obtained from different methods (see Section 6.2.2.1).

In the log-linear plot of Figure 6-14, the time constant at 70 °C seems to fall on a straight line indicating an exponential dependence of the conductivity with the DC voltage. However, as shown in Figure 6-15, where the data is re-plotted on a linear axis and where an exponential and additionally a power law best fit to the data is also plotted, within the scope of experimental DC voltages it is unclear which function, power law or exponential, of the time constant follows the DC field.

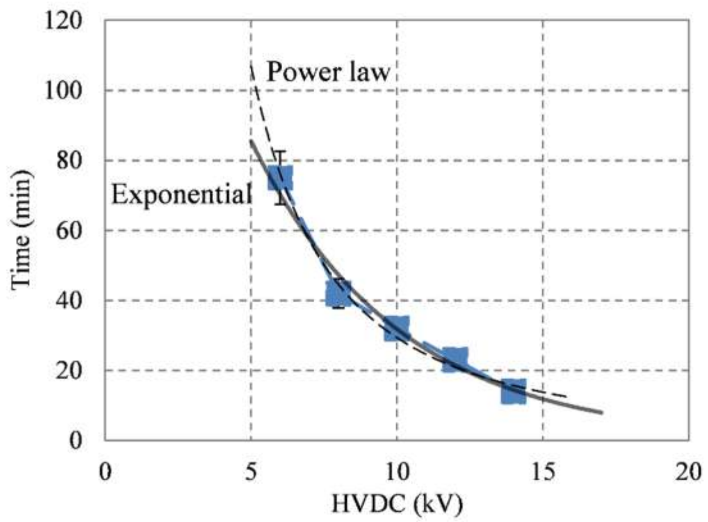

Figure 6-15. Comparison of the power law and exponential trend lines to the time constant at 70 °C.

6.4.3 Simulation

With the experimental charging time constants obtained from above experiments, the 1D Matlab simulation model for cable charging (developed in Section 4.2) was then utilised to identify the values of the model parameters in the three empirical conductivity expressions regarding to the field and temperatures dependency.

All three empirical conductivity models (introduced in Section 2.5) were attempted to fit the charging transient (time constant) with the experimental results. The parameters found for the models are summarised in Table 6-1.

Table 6-1. Parameters for the conductivity functions

σ model		Constants	Temperature coefficient	E coefficient (°C)	
				50 °C	70 °C
1	$\sigma(E,T) = \sigma_0 e^{\alpha T} \left(\frac{E}{E_0}\right)^{\nu}$	σ_0= 1.36e-19 ($\Omega^{-1}m^{-1}$); E_0=10kV/mm	α= 0.156 (1/°C)	ν = 4	ν = 1.8
2	$\sigma(E,T) = \sigma_0 e^{\alpha T + \beta E}$	σ_0= 5e-21 ($\Omega^{-1}m^{-1}$)	α= 0.175 (1/ °C)	β = 0.26 (kV/mm)	β = 0.2 (kV/mm)
3	$\sigma(E,T) = Ae^{-\frac{\varphi \cdot q}{k_B T}} \frac{sinh(B\|E\|)}{\|E\|}$	A= 9.98e10 ($\Omega^{-1}m^{-1}$)	φ = 1.3 eV	B = 3e-7	

6.4.3.1 Model 1:

The time constants obtained from simulations using the ‘power law’ conductivity model 1 are shown in Figure 6-16. Subject to the power law dependency of the electrical field in the equation, the time constant shows the same dependency on the applied DC voltages as indicated by the straight dash line in log-log plot. Moreover, to fit with the experimental data, the field power index, ν, needs to be temperature dependent. With the parameters in Table 6-1, the model 1 provides a good fit with the experiments.

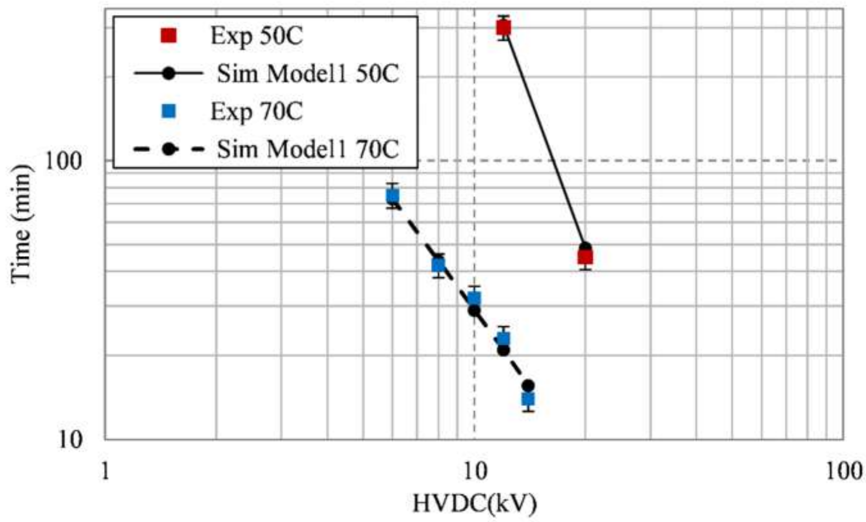

Figure 6-16. Time constants calculated from the conductivity model 1.

6.4.3.2 Model 2:

Similarly, Figure 6-17 shows the simulated time constants with respect to the exponential field dependent conductivity, model 2. The exponential term in the model results in the straight dash line on the log-linear plot which represents that the time constant for cable charging reduces exponentially with increasing DC voltage. The value of the β coefficient is however less dependent on temperature than for the power exponent of model 1.

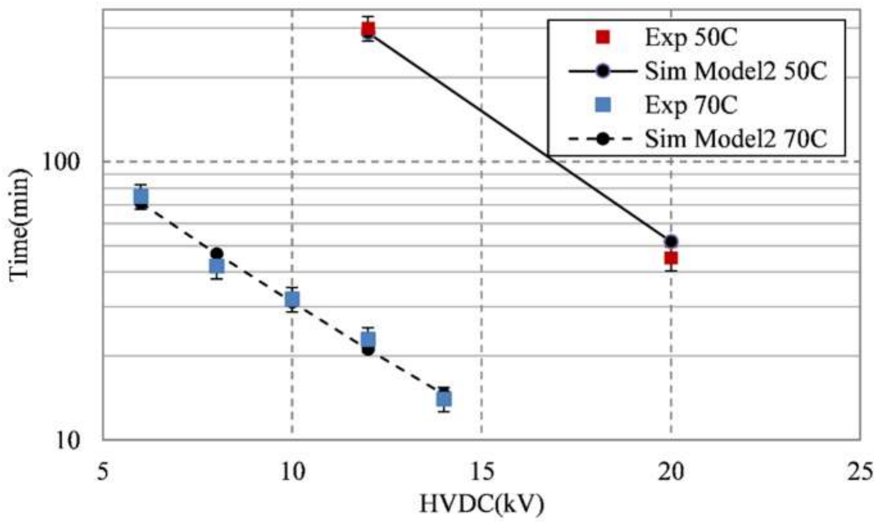

Figure 6-17. Time constants calculated from the conductivity model 2.

6.4.3.3 Model 3:

The parameters for conductivity model 3 are more difficult to be identified than the other two models due to the hyperbolic functional dependence of the E term. With the parameters listed in Table 6-1, the simulation results could match with the experimental results with 10 % error bars as shown in Figure 6-18

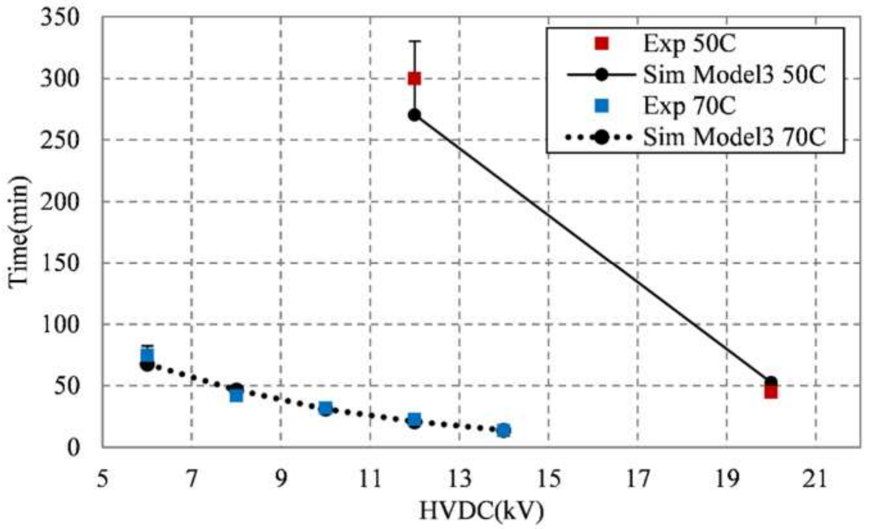

Figure 6-18. Time constants calculated from the conductivity model 3.

6.5 Concluding remarks

In this chapter, space charge accumulation in mini-cables was investigated due to the phenomena of cable charging. Cable charging is the result of the insulator material's electrical conductivity being a non-linear function of the applied electric field which is non-uniform in the cylindrical cable geometry. PEA measurements have shown the existence of this phenomenon in XLPE based mini-cables. The time constants involved in the accumulation of the bulk space charge within the insulation was dependent on the applied voltage and on temperature. The time constants ranged from 14 minutes to 300 minutes dependent on the actual experimental conditions of applied voltage and isothermal temperature applied to the cable. Although, the cable charging effect has been proposed in the literature before, extrapolation to room temperature predicts time constants typically of 1000s of minutes and it is therefore not surprising that this effect has not been demonstrated experimentally in the literature before. Simulations of charge accumulation using a unipolar model for field dependent charge transport based on three empirical formula has shown that the models can successfully simulate the charging process and that the three models provide an adequate description of the field dependent charge transport that is responsible for the observed charge accumulation. Further experiments to fill in the condition matrix will allow better comparisons to be made between the experimental data and the simulations based on the three empirical formulae used.

Charge accumulation through the phenomena of cable charging must therefore be taken into account when performing PEA calibration, otherwise an incorrect assumption could be made regarding the ratio of the charge peak areas that is often employed as the basis for the signal processing to recover the space charge distribution using traditional approaches. The approach taken here of starting with a model for charge transport and then applying PEA simulations to determine the PEA raw output data does not suffer from this problem.

7 APPLICATION OF TECHNIQUE TO PRACTICAL MINI-CABLE INSULATION SYSTEMS

In the chapters so far, the software analysis tools developed in Chapter 4 have been applied to cables assuming ideal conditions of material homogeneity, cable concentricity etc. However practical mini-cable systems, as well as their full-size commercial counterparts, are rarely ideal. In practice the cable insulation and semicon layers are not exactly concentric as this is difficult to control during the extrusion process used during manufacture. In addition a degassing stage is required to remove chemical impurities from the insulation material that form due to the chemical cross-linking. This may result in non-uniform electrical properties in the cable insulation and give rise to the conditions necessary for space charge accumulation. It has also been assumed that the acoustic properties of the insulation and the inner and outer semicon layers are the same and that no reflection of the acoustic waves occurs at these interfaces. In this chapter the 2-D PEA simulation models will be applied to assess the effect of cable non-concentricity on the PEA raw output signal in section 7.1. The use of the 1-D simulation tools to examine the effect of acoustic mismatch between the insulation and semicon layers is described in section 7.2. In section 7.3 within the context of temperature and voltage ramp tests, the 1-D software tools will be used to examine the temperature dependence of cable charging and space charge accumulation within the insulation of non-degassed mini-cables. These cables were deliberately used as they were found to have two distinct morphological different regions inside the cable insulation.

7.1 Application of the 2-D PEA simulation to non-concentric cables

7.1.1 Sample non-concentricity

Figure 7-1 shows a typical cross-section photographic image of a non-degassed mini-cable. Referring to the best-fit (dashed) circles, noticeable deviation of the insulation and semicon layer thicknesses can be observed.

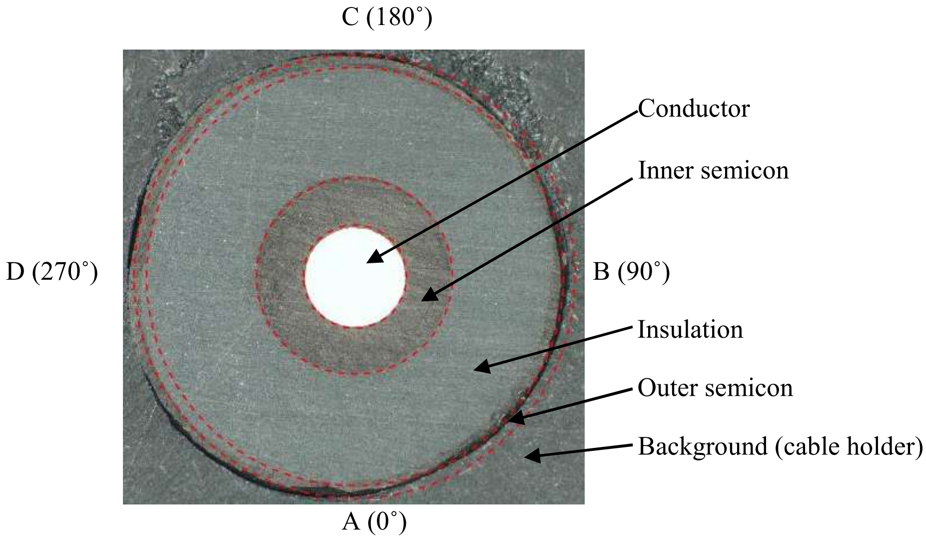

Figure 7–1. Cross-section of a mini-cable. Red dash circles are best-fit boundaries for the conductor, the inner semicon/insulator interface, the outer semicon/insulator interface and the outer profile of the cable.

In addition, the deviation of the insulation thickness was estimated from the length variation of the space charge profiles. The mini-cable PEA system with the flat base electrode is appropriate for this purpose as only the slice of insulation perpendicular to the electrode surface would be measured. The section of mini-cable under test was rotated by 90˚ for each test. Therefore, as illustrated in Figure 7–1, four angular positions (A, B, C and D) representing the insulation thickness on four angles could be measured. A low and fixed clamping force was applied for each test to minimize or at least maintain the same deformation of the mini-cable. The lengths of space charge profiles were obtained by measuring the time delay for the two interface peaks, P_1 and P_2 and converted to distance from the acoustic velocity of the insulation. The profile lengths are recorded as shown in Figure 7–2 with the assumption that the mean value is the ideal thickness of 1.5 mm. The standard deviation in the measurements was found to be 52.6 μm.

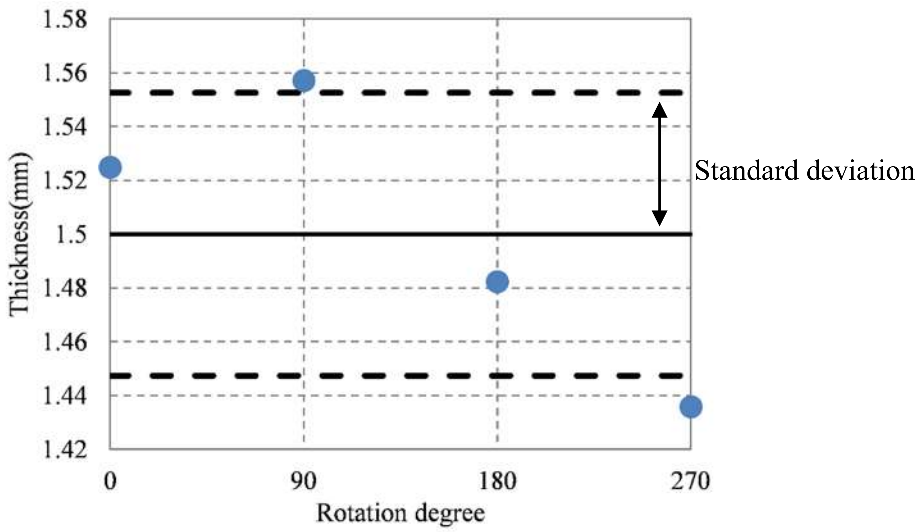

Figure 7–2. Insulation thicknesses obtained from the PEA measurements at 4 angles of the same section of the mini-cable. The mean value of the four data is assumed to be the ideal thickness of 1.5 mm. Dash lines indicate the ± standard deviations.

Likewise the thickness deviation was measured along the axial direction of the mini-cable at the same angle. Measurements were taken on five random positions along a 1 m mini-cable. The measurement results shown in Figure 7–3 indicate that there is less deviation for the insulation thickness on the axial direction.

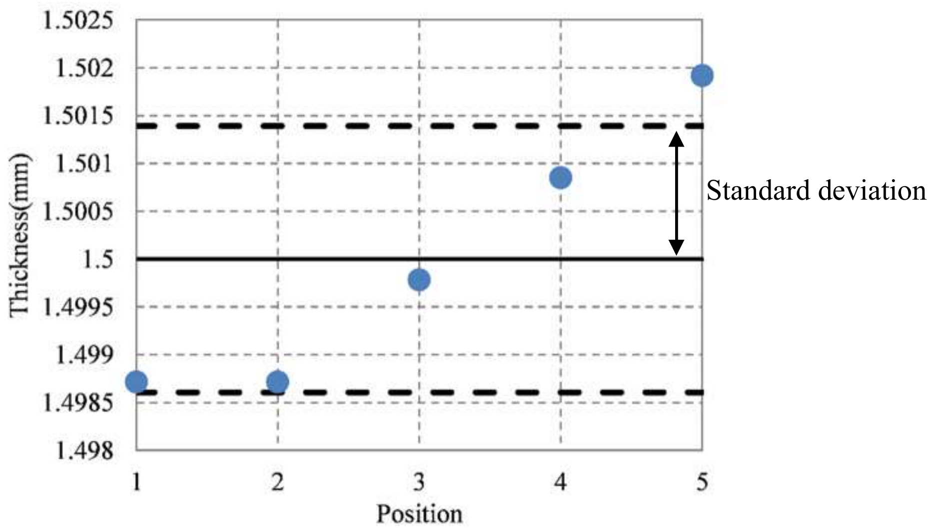

Figure 7–3. Insulation thickness obtained from PEA results at 5 random positions. Dash lines indicate the ± standard deviations.

7.1.2 Simulation

To examine how the non-concentricity of a mini-cable would affect PEA outputs, the 2D acoustic simulation tool developed in Section 4.7 was used. Referring to the statistics illustrated in the above subsection (Section 7.1.1), a deviation of 0.2 mm in the horizontal direction from the coaxial centre was applied to the conductor and inner semicon layer to simulate the worst case scenario where the simulation domain (developed in COMSOL) is shown in Figure 7–4. The simulated PEA outputs with the concentric and non-concentric cable geometries are compared in Figure 7–5. The second peak (P_2) for the non-concentric cable is slightly smaller and earlier in time than that for the ideal concentric cable. However, even under serious non-concentric circumstances for the mini-cable, the difference in PEA outputs with the current system characteristics (i.e. thickness of the bottom electrode and width of the sensor film) are small compared with the spatial resolution of the PEA apparatus.

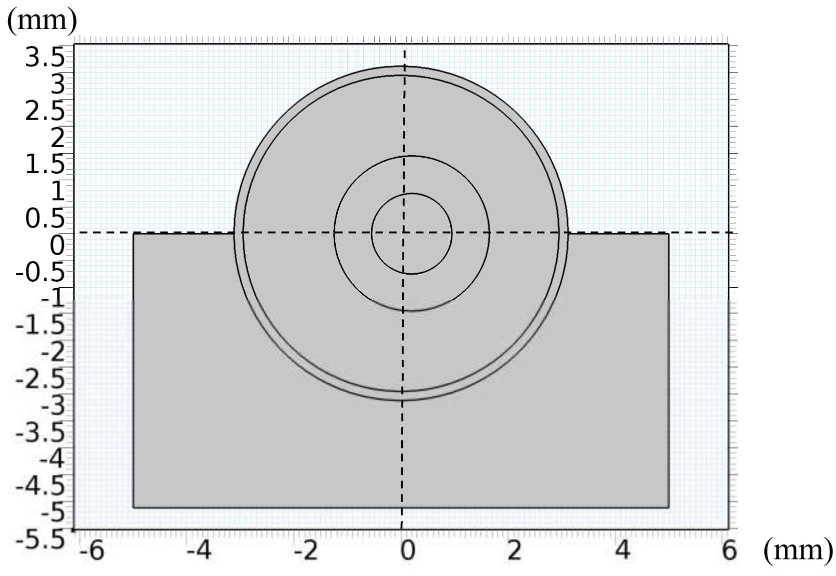

Figure 7–4. Centre of the conductor and inner semicon layer (at position [0.2 mm 0]) is 0.2 mm deviated from the centre of outer semicon layer (at position [0 0]) in the horizontal direction

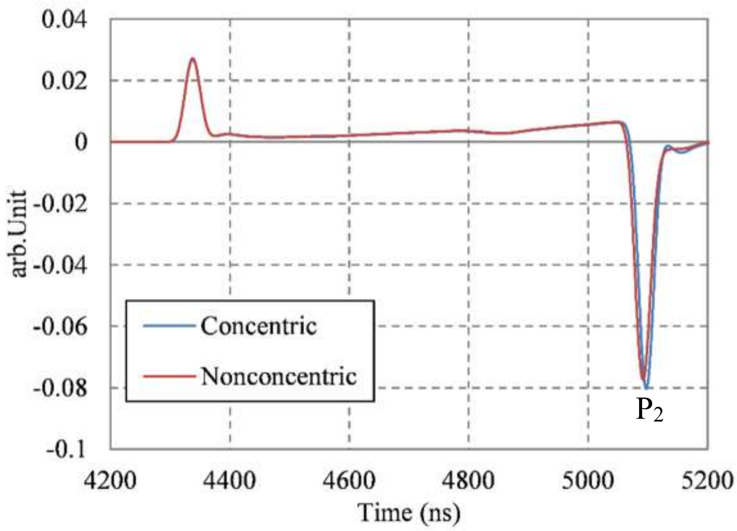

Figure 7–5. Small difference exists in P_2 when the centre of conductor and inner semicon layer is slight (0.2 mm) derived from the centre of insulation and outer semicon layer. The simulation tool has been introduced in Section 4.7. Acoustic attenuation was ignored. A perfected (52 µm thick and 5 mm wide) piezoelectric sensor and matched acoustic absorber were assumed and without considering the effect of sensor – amplifier circuit.

7.2 Influence of the temperature dependence of the acoustic properties of the sample on PEA measurements

The reproducibility for the measurements under various temperatures is not only affected by the thermal stability of the system, but by the temperature dependent characteristics of material properties as these may also alter the system response as the temperature is changed. In this section, the influence of the acoustic matching between the insulation and the semicon layers at different temperatures is investigated through experiments and simulation.

7.2.1 Experiments

The experimental PEA raw output signals obtained from the same mini-cable at two isothermal conditions, 21 °C and 65 °C, are shown in Figure 7–6. For the convenience of analysis, the time delay has been normalised to P_1. The meaning of P_1 and P_2 are consistent in this work, representing the interfacial charge at the outer and inner interfaces. P_3 is the reflected acoustic wave from the central conductor that was generated at the inner semicon – insulator interface but travelling opposite to P_2 towards the central conductor. Therefore P_3 travels twice the thickness of the inner semicon layer.

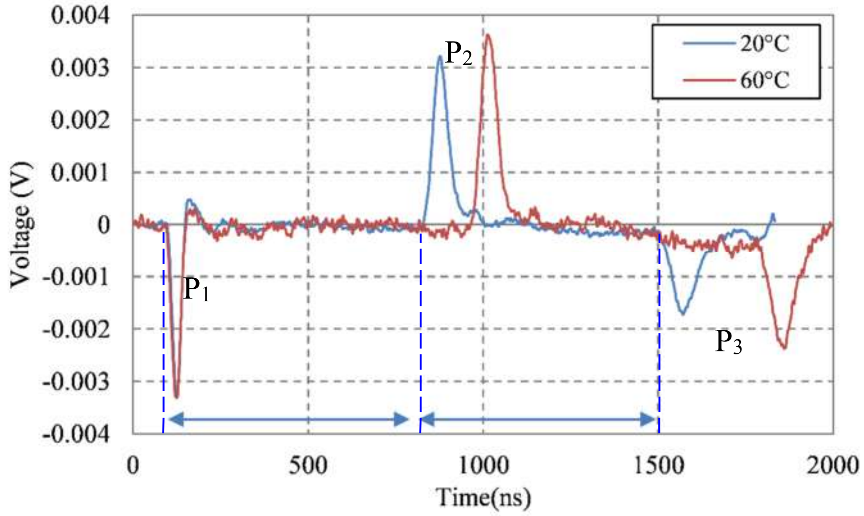

Figure 7–6. Raw PEA outputs at 20 °C and 60 °C. The time delay was normalised to the P_1.

As shown in Figure 7–6, at 65 °C the time delay of both P_2 and P_3 with respect to P_1 are longer than that at 21 °C. This is due to the wave velocity reduction in both the insulation and semicon layers at elevated temperatures. If it is assumed that the thickness of both layers remains the same, then the matching of wave velocities for two materials at the two temperatures can be estimated by the variation in time delays. If the temperature dependencies of the velocities, V_{PE} and V_{semi} are identical, the ratios between the time delays, T_{PE} and T_{semi}, should be the same at the two different temperatures. As illustrated in Table 7-1, T_{semi}/T_{PE} (which equals V_{PE}/V_{semi}) changes from about 95 % at 65 °C to 93.5 % at 21 °C. Although the density variation with temperature was not accessed by experiments, the slight change in the wave velocity ratios indicates that a slight change in the acoustic matching between the insulation and semicon layers may exist during the temperature range of 21 °C to 65 °C.

Table 7-1. The time delays between peaks at two temperatures. V_{PE} and V_{semi} are the wave velocity in the insulation and semicon materials; D_{PE} and D_{semi} are the thickness of insulation and inner semicon layers. Referring to the dimension of the mini-cable (Section 2.5), the thickness of the insulation layer is about twice that of the inner semicon layer i.e. $D_{PE} \approx 2 \times D_{semi}$.

Time delay	between peaks	Equal to	Time delay at 20 °C	Time delay at 60 °C
T_{PE}	P_2 to P_1	D_{PE}/V_{PE}	725 ns	866 ns
T_{semi}	P_3 to P_2	$2\times D_{semi}/V_{semi}$	678 ns	823 ns
T_{semi}/T_{PE}	\	V_{PE}/V_{semi}	93.5 %	95.0 %

7.2.2 Simulation

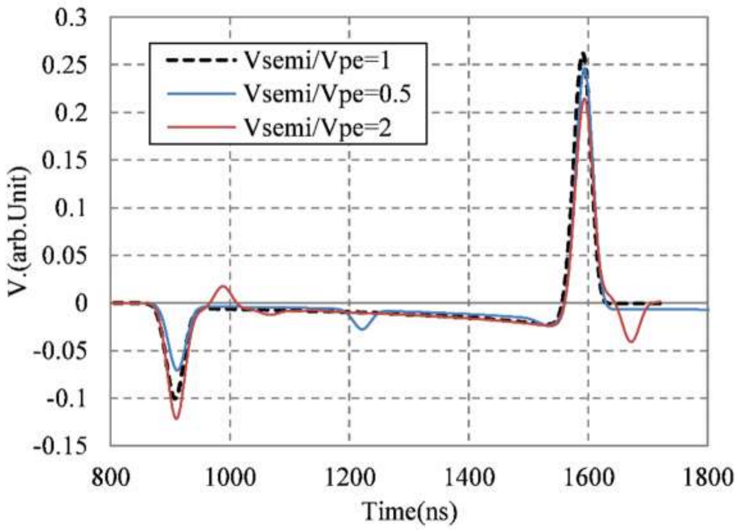

Figure 7–7. 1D simulation of PEA outputs when the wave velocity in semicon material is the same, half and twice that in insulation.

Using the 1D simulation model (Section 4.2), the PEA output signals with significant mismatch between insulation and semicon layers can be assessed. In the simulation, the densities of the two materials are assumed to be the same. Simulations were performed under three conditions: where the wave velocity in semicon material is the same, half and twice that in the insulation. The simulation results are shown in Figure 7–7. The peak magnitude (or area) changes under different matching conditions. Moreover the small bulk signals due to the reflection in the semicon layer can be observed under mismatched conditions.

The variation in the peak area ratio is of major significance, P_2/P_1 as summarised in Table 7-2, as the calibration of the PEA apparatus and the correction for attenuation and dispersion rely on the correct ratio being applied during the signal processing of the raw PEA output data. The change in the area ratio is related to the mechanical force generated at interfaces when the pulsed voltage is applied to the sample. On application of a pulsed electric field, the interfacial charges produce two acoustic waves travelling in opposite directions (as compressive and rarefaction waves). The energies of these two waves and hence their amplitudes will be the same if the acoustic properties of the two materials on either side of the interface are identical. However, when there is a mismatch in the acoustic properties, the relative amplitudes of the compressive and rarefaction waves will change. The P_1 refers to the acoustic wave propagating towards the outer semicon while the P_2 refers to the acoustic wave propagating towards the insulation. Then the change in acoustic matching between insulation and semicon layers would lead to the variation of P_2/P_1.

Table 7-2. Ratios of the interfacial peak areas with different wave velocity in semicon material.

V_{semi}/V_{pe}	2	1	0.5
P_2/P_1	1.766	2.616	3.481

In fact, the semicon layers are normally made from the same insulation material but loaded with carbon particles to give a high electrical conductivity. As a consequence, as has also been approved by the experimental data where similar temperature characteristics for the insulation and semicon material were found, the insulating layer and semicon layers should have similar acoustic properties. The small bulk reflected signals as illustrated in the simulation results can be treated as an indicator for the case of serious acoustic mismatch.

7.3 Voltage sequence test

In order to simulate the service life of full size HVDC cables, voltage ramp space charge measurements under different isothermal temperatures of 30 °C, 50 °C and 70 °C are of interest to the cable manufacturing industry. Here, experiments of the space charge measurements on mini-cables were designed with a sequence of voltages changing every three hours in sequence as shown in Figure 7-8. The voltage sequence comprises 10 kV being applied for three hours, then a voltage off period for three hours, followed by the same plan except the voltage is increased to 20 kV then 30 kV. Following this, a polarity reversal at 30 kV was applied for 3 hours.

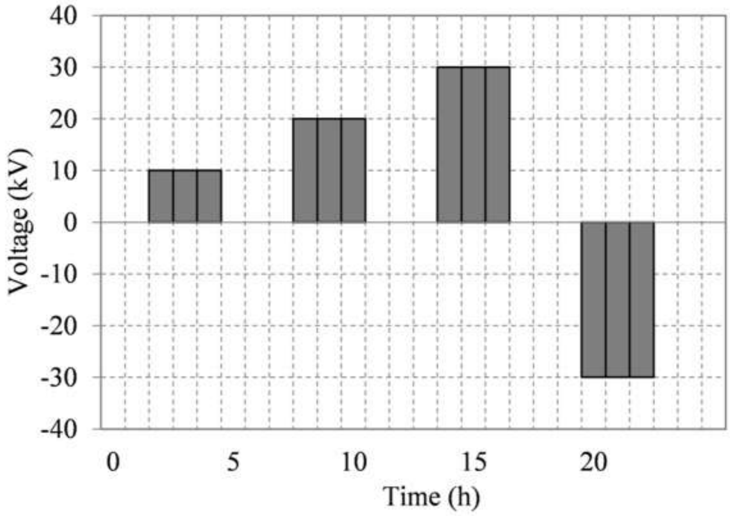

Figure 7-8. Voltage sequence to be applied on the mini-cable. The first two hours is for heating the sample and the PEA cell to the required isothermal condition.

The experiment for each voltage sequence takes at least 26 hours including the first two hours for stabilising the oven temperature and the following 8×3 hours voltage on (V_{on}) and voltage off (V_{off}) measurements. Given the long duration of the experiments, the measurements system was automated. The voltage sequence was programmed in the Labview to control the output voltage of the HVDC power supply. However to produce a polarity change, this needs to be manually changed as the power supplies are unipolar. To minimise any possible effect of the pulsed voltage on space charge formation in the cable, the pulses were applied 20s before and 5s after the space charge measurement. Individual PEA space charge measurements were taken with a time interval of one minute using the oscilloscope (1000 sweeps averaged) controlled by a computer running the Labview data acquisition software. Raw PEA voltage signals were stored in the computer synchronously during the measurement and were processed afterwards in Matlab.

7.3.1 Non-Degassed Sample

As- received D806D mini-cables were used for the voltage sequence tests. Preliminary observations of the non-degassed cable insulation, by cutting the cable with a knife to produce thin sections, showed a visual contrast difference in the insulation layer as illustrated by the photograph in Figure 7-9.

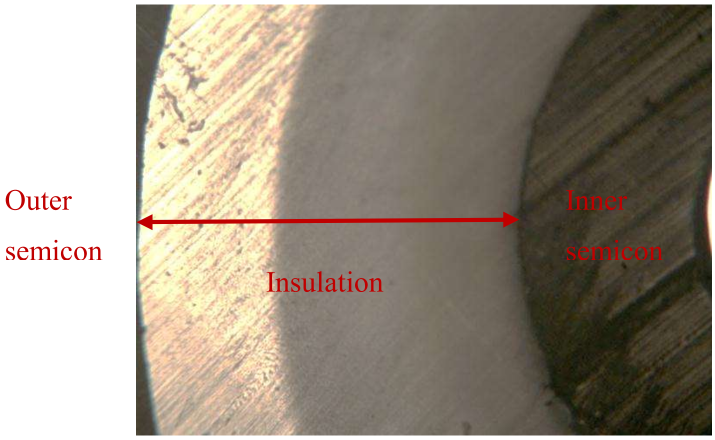

Figure 7-9. Cross-section photo of an as-received D806D mini-cable

Under transmitted light, the cable insulation shows two radial regions. The inner region absorbs the transmitted light through the cable section more than the outer region. Hence the inner region appears dark while the outer region appears light. There also appears to be a sharp interface between these two different regions. The radial position of the transition between the two regions was found to vary within a single cable sample and also found to depend on the storage time of the cable sample from manufacture.

7.3.2 PEA measurements at 30 °C

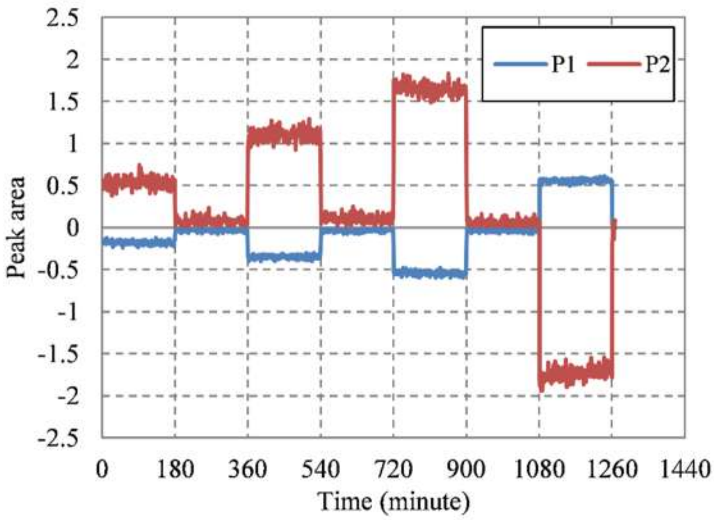

Figure 7-10. Peak areas of the two interfacial charge signals during the voltage sequence at 30 °C.

PEA space charge measurements over the full voltage cycle were carried out and the two interfacial peak areas, P_1 and P_2, were calculated from the space charge data. The peak areas of P_1 and P_2 as a function of time over the full voltage sequence test are shown in Figure 7-10. No noticeable variations in either peak areas can be observed during the test except at +/- 30 kV where a slight reduction in the area of P_2 can just be observed, indicating that the phenomena of cable charging is starting to occur.

The accumulation of a small amount of homocharge near the inner interface was identified by the V_{off} measurements following voltage application at +/- 30 kV as shown in Figure 7-11.

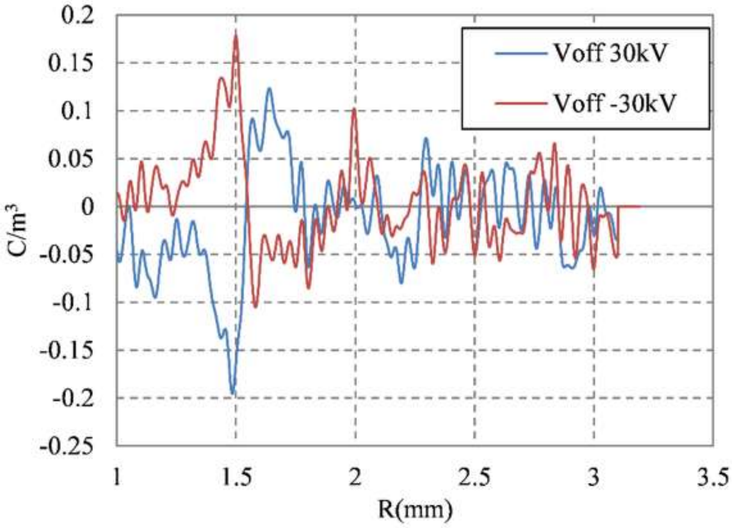

Figure 7-11. V_{off} measurements shortly after removing +30 kV and -30 kV DC bias voltages.

7.3.3 PEA measurements at 50°C

Unlike the test at 30 °C, obvious peak area changes can be noticed during +20 kV, +30 kV poling and -30 kV polarity reversal at 50 °C as illustrated in Figure 7-12. The peak area P_2 decreases and peak area P_1 increases during voltage application which is consistent with the cable charging phenomena discussed in Chapter 6. During the voltage off measurements the peak areas did not return to zero but showed a decay in time as the cable charge dissipates. The peak area ratios of P_2/P_1 during V_{on} measurements plotted in Figure 7-13 also confirm the variation of interfacial charge signals and the boost in the amplitude of P_2 on polarity reversal due to the charge already accumulated during the previous voltage application. These results are consistent with the cable charging phenomena due to a field dependent electrical conductivity of the insulator material.

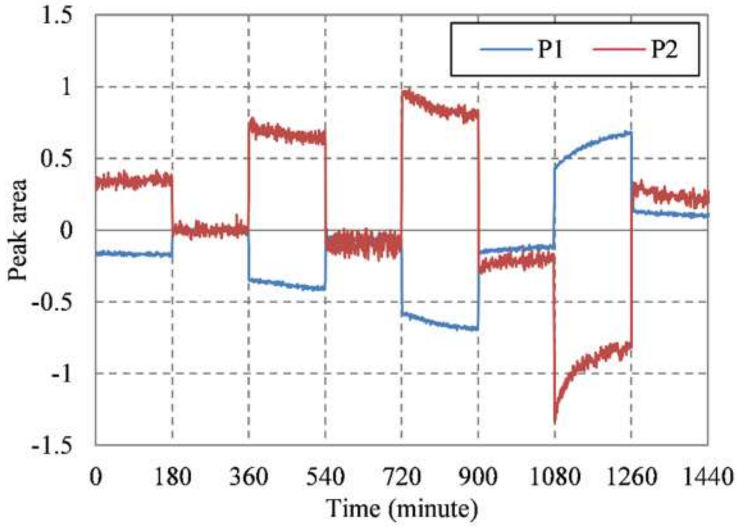

Figure 7-12. Peak areas of two interfacial charge signals during the voltage sequence at 50 °C.

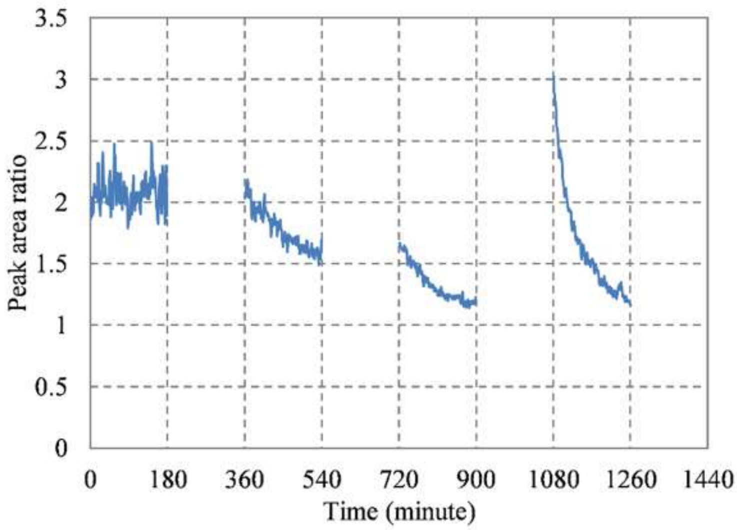

Figure 7-13. Peak area ratios of P_2/P_1 during V_{on} measurements at 50 °C.

Typical space charge profiles obtained during the positive poling stages are shown in Figure 7-14. An important finding is that a bulk space charge signal (as pointed out by the dash circle) was formed during the +20 kV poling and kept increasing during +30 kV poling. However, the bulk signal disappeared (within 10 minutes) when the DC voltage was reduced to zero as indicated by the V_{off} measurements shown in Figure

7-15. The V_{off} measurements also confirm the cable charging phenomena in which positive charge were formed during the +30 kV poling. The distribution of the space charge due to cable charging fits with the theory (Chapter 6) in that the charge density reduces with increasing radius. Comparing the V_{off} data at the beginning (at 910min) and end (at 1072 min) of the 3 hour discharging period, a minute charge density reduction may just be observed from the space charge in the insulation bulk and is more clearly observed in the induced interfacial charge signals.

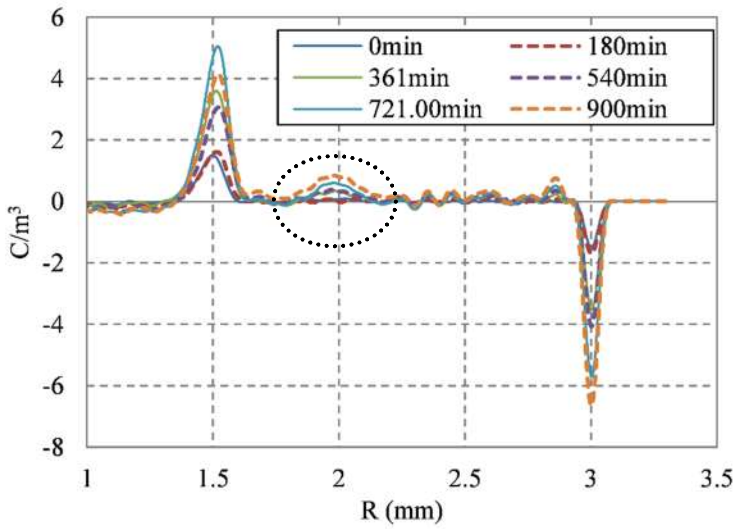

Figure 7-14. (Calibrated) space charge profiles at start (0 min) and end (180 min) of +10 kV, start (361 min) and end (540 min) of +20kV and start (721 min) and end (900 min) of +30 kV poling states.

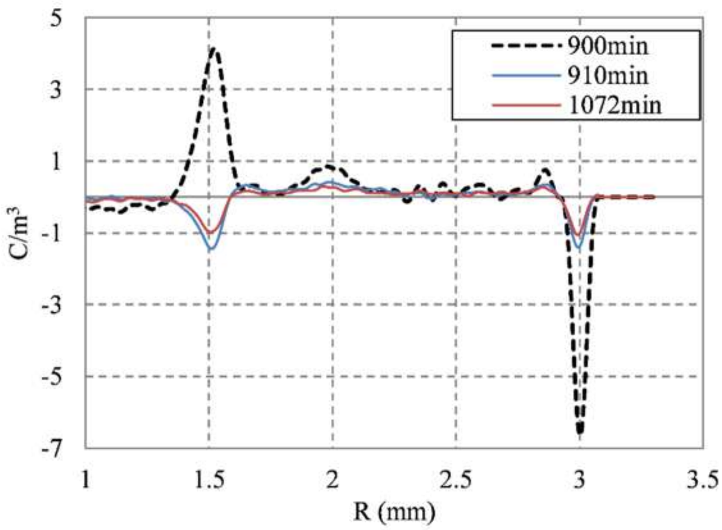

Figure 7-15. Voltage-off measurements after the +30 kV poling whose last measurement (900 min) is shown as a reference.

On polarity reversal, the electrical field generated by the residual charges remaining from the previous poling would be superimposed on the DC field, increasing the area of P_2 and therefore the maximum electric stress at the inner semicon/insulator interface. Specifically, before the -30 kV DC was applied, the electrical field produced by the remaining charge at 1072 minutes (space charge profile shown in Figure 7-15) of the voltage sequence is shown in Figure 7-16 (solid green line). When -30kV DC voltage was then applied, the electrical field across the insulation is the sum of the DC Laplace field (E_L) and the charge induced field (1072 min). As demonstrated in Figure 7-16, the summed field is consistent with the calculated field from the V_{on} space charge measurements at 1084 minutes.

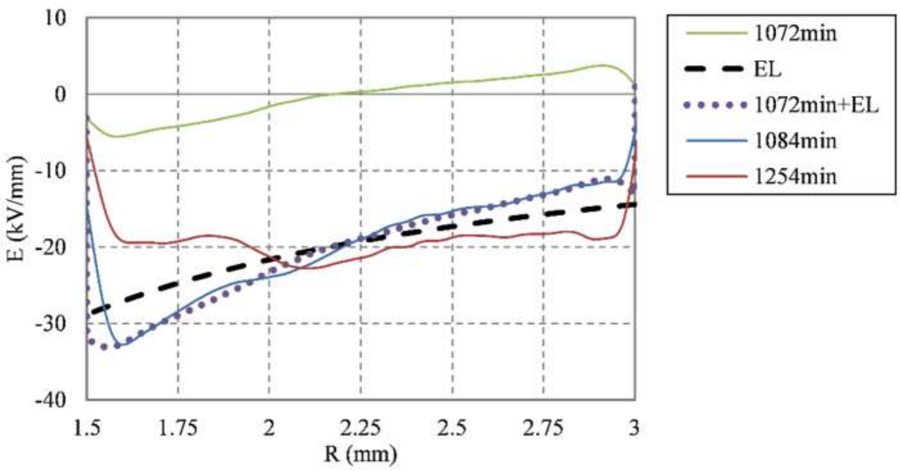

Figure 7-16. Electrical field distributions obtained from the space charge measurements just prior to polarity reversal (1072 minutes) and after polarity reversal (1084 min). The dotted line is the sum of the residual field before polarity reversal (1072 min) and the theoretical Laplace field (EL). The electric field at the end of the polarity reversal is also shown (1254 min).

Due to the phenomena of cable charging, the electric field eventually became more uniform under the reversed polarity poling as shown by the electric field at 1254 minutes in Figure 7-16. In this case, negative charges accumulated within the insulator bulk with positive induced charges on the semicon/insulator interfaces as can be detected by the space charge measurements during the polarity reversal as shown in Figure 7-17.

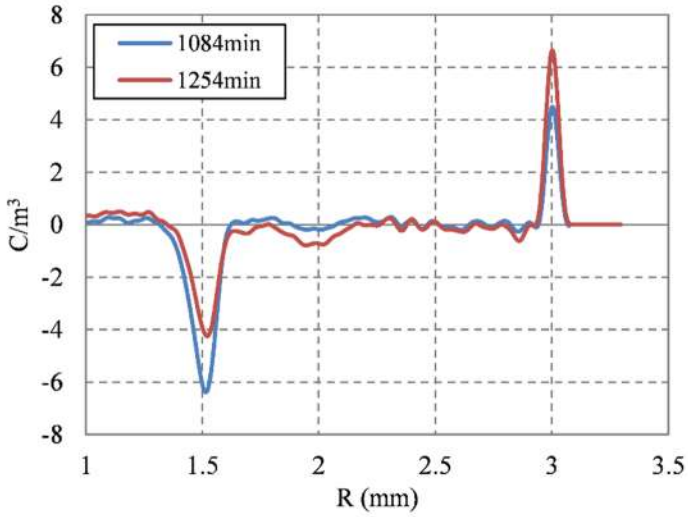

Figure 7-17. Space charge measurements at the beginning (1084 min) and at the end (1254 min) of the -30 kV polarity reversal.

Additional voltage-off measurements were taken following the polarity reversal period to follow the discharging of the cable. After the removal of the -30 kV DC voltage, three space charge profiles are shown in Figure 7-18. The accumulated charges gradually discharged with a corresponding reduction in the induced electrode charges as represented by the two interfacial peak signals in the space charge profiles. After discharging for about 18 hours at 50 °C, a certain amount of charges were still found to be trapped in the insulation.

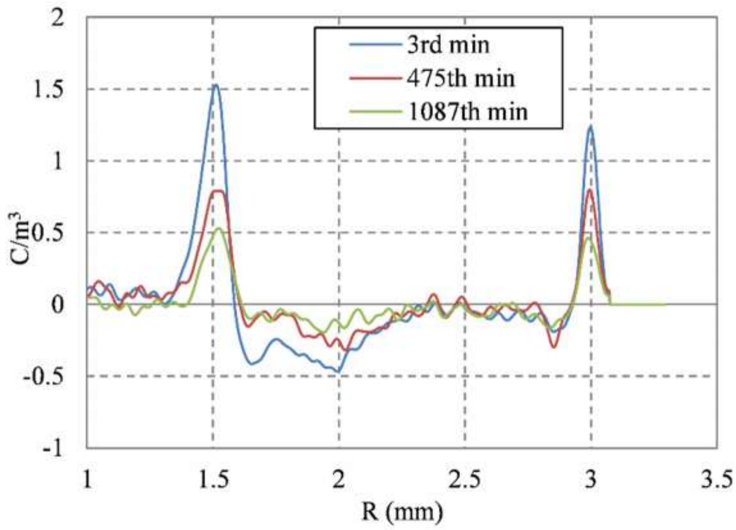

Figure 7-18. V_{off} space charge measurements after -30 kV poling. Profiles are labelled as the time since voltage off rather than the time in the voltage sequence test.

7.3.4 PEA measurements at 70 °C

At 70 °C, space charge accumulation due to cable charging and the bulk signal identified in the 50 °C measurements formed quickly (if not instantaneously) after applying the +10 kV bias voltage as shown in Figure 7-19 (a). The rapidly formed space charge under low DC voltage makes it difficult to perform signal calibration for the PEA signal. Therefore for the space charge data at 70 °C, the calibration coefficient ($C/m^3/V$) was obtained by first integrating the charge distribution to obtain a distribution in proportion to the electric field. A scale factor was then identified to ensure that the integral with respect to the radius of the electric field is equal to the applied DC voltage.

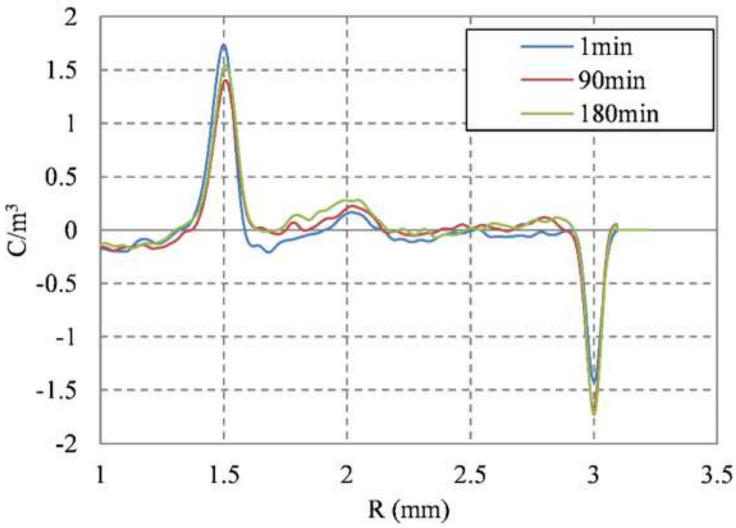

(a)

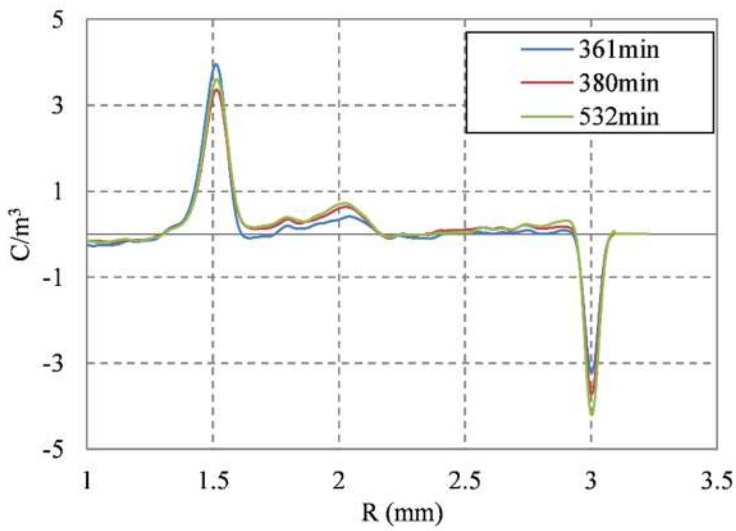

(b)

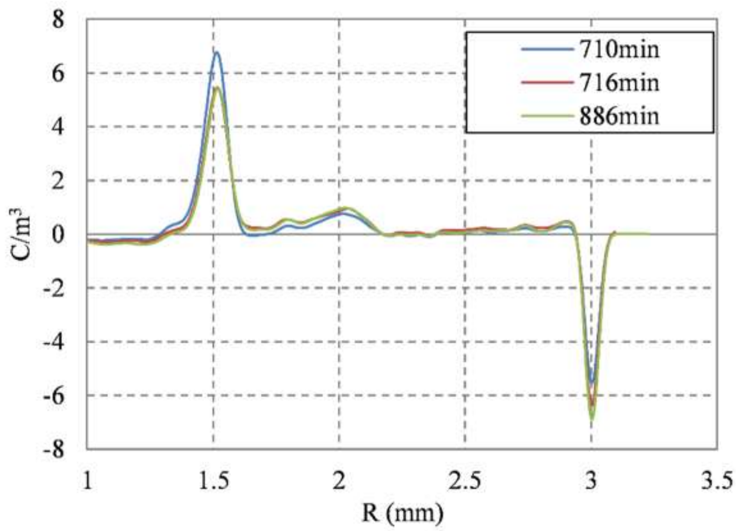

(c)

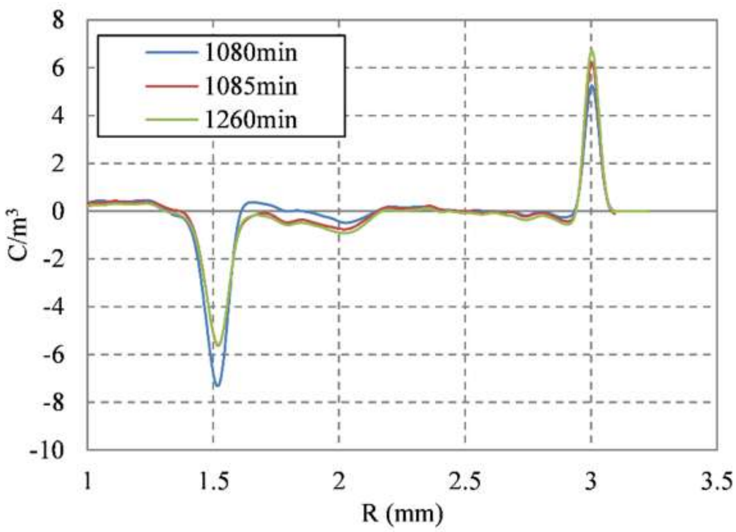

(d)

Figure 7-19. Space charge measurements during (a) +10 kV, (b) +20 kV, (c) +30 kV and (d) -30 kV poling.

At the higher DC voltage of +20 kV, the bulk signal increased accordingly until reaching a quasi-steady state after about 20 minutes as indicated by Figure 7-19 (b). At 30 kV poling voltage, the bulk signal kept increasing and quickly reached the quasi-steady state after about 6 minutes. Under polarity reversal, the previously accumulated positive charge decreased rapidly and the equivalent amount of negative charge formed within 5 minutes as shown in Figure 7-19 (d).

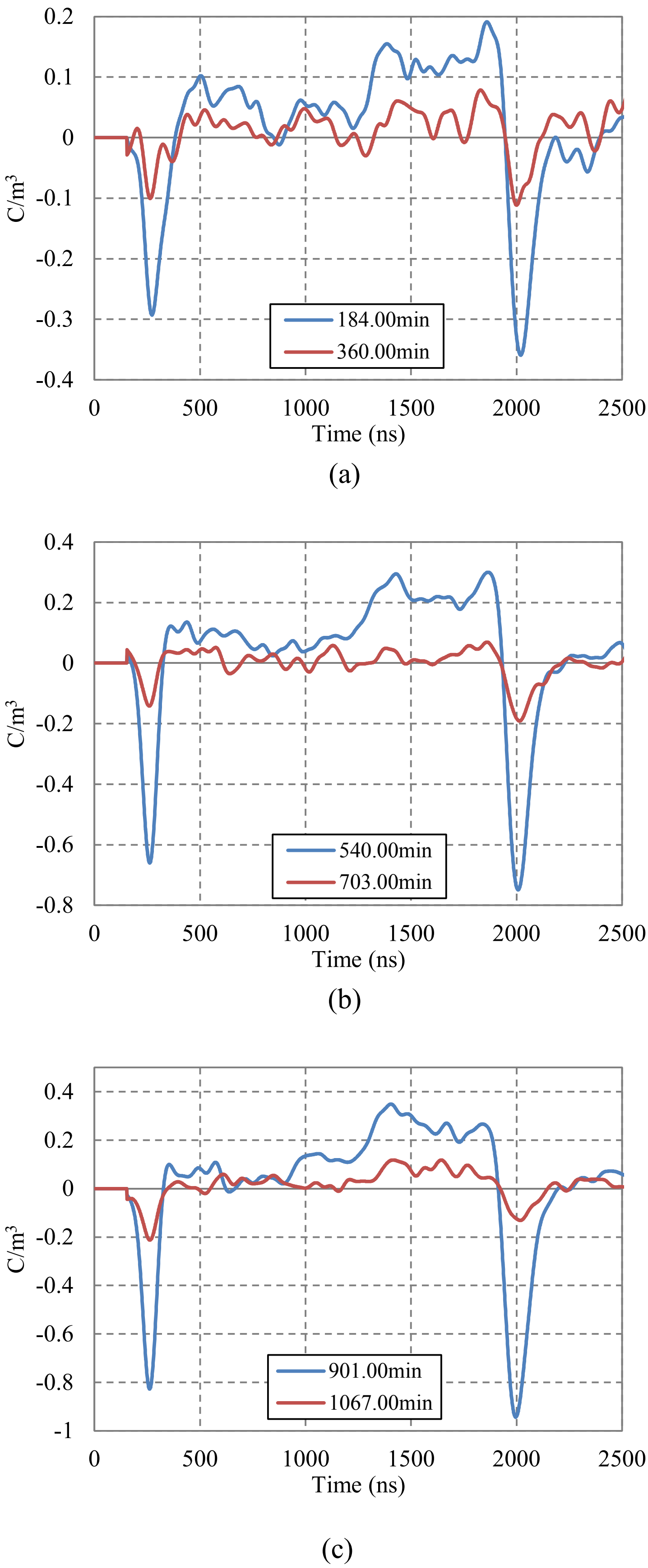

Figure 7-20. Space charge measurements at start and end of dischargings after 10 kV, 20 kV and 30 kV poling.

The voltage-off space charge profiles at the start and end of discharging periods after +10 kV, +20 kV and +30 kV poling states are shown in Figure 7-20. After discharging for about 3 hours for each stage, the remaining space charge density is at the same level of instrumental noise and therefore can only be inferred from the induced interface charges.

To compare the time of charging transient under different poling voltages, the peak areas, P_1 and P_2, and their ratios (P_2/P_1) during the voltage sequence are plotted in Figure 7-21 and Figure 7-22 respectively. It is clear that the charging time transients are much shorter at higher bias voltages and shorter than the equivalent measurements taken at 50 °C. Moreover, the transient time for +30 kV poling and during the polarity reversal of -30 kV are almost the same as shown in Figure 7-22 (b).

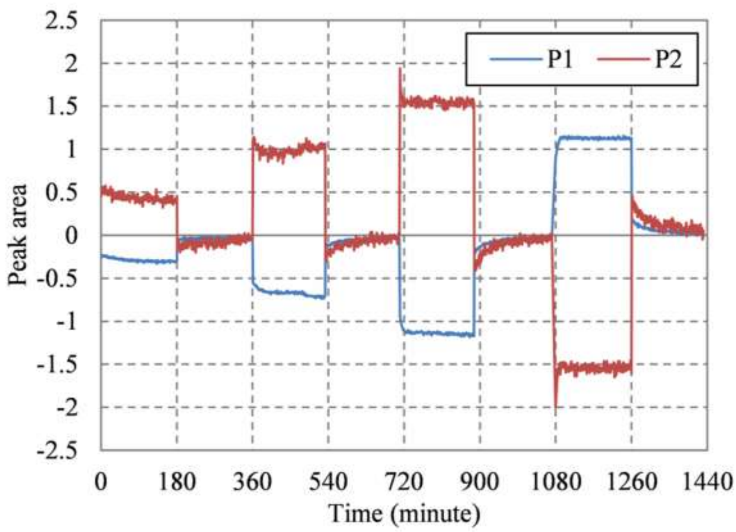

Figure 7-21. Peak areas of two interfacial charge signals during the voltage sequence at 70 °C.

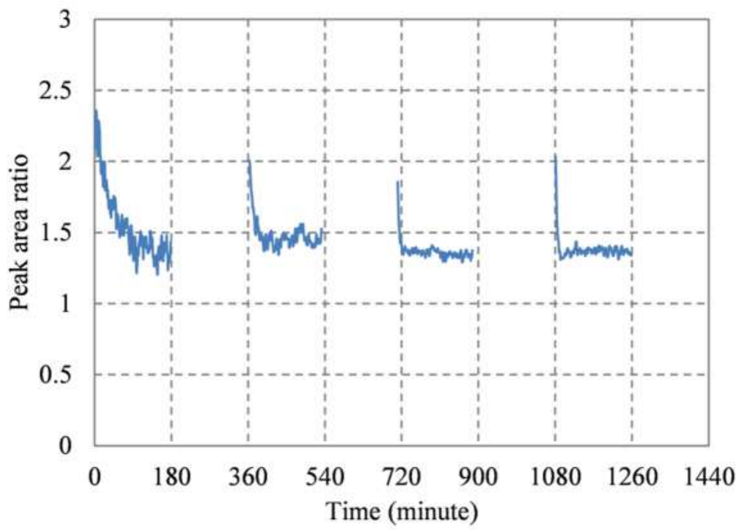

(a)

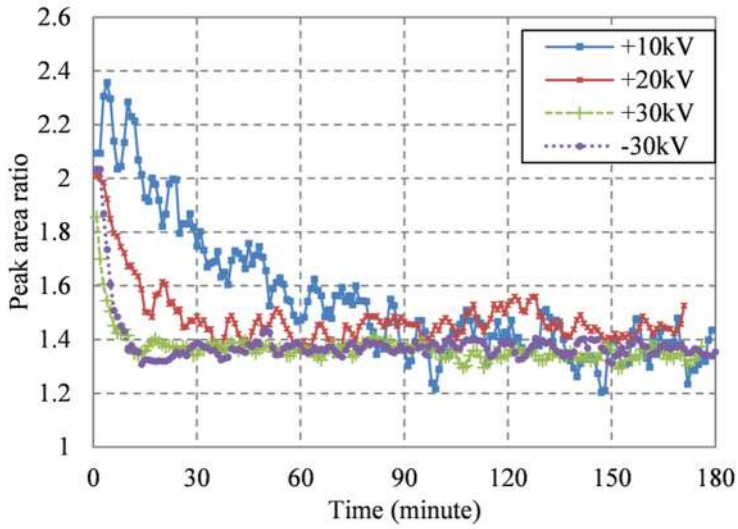

(b)

Figure 7-22, Peak area ratios of P_2/P_1 during each V_{on} measurements at 70 °C. (Ratios are a function of the actual poling time rather than the time of the voltage sequence) (a) over the full sequence and (b) charging transients overlaid for comparison.

7.3.5 Simulation of voltage sequence tests

The most conspicuous feature of the voltage sequence tests is the formation of a bulk signal. As can be observed in Figure 7-9, a contrast different exists in the insulation layer which may indicate the insulation layer has non-homogeneous properties along the radius direction. One possible explanation for the formation of the bulk signal is that the dark region (near the inner semicon layers) may have a higher electrical conductivity compared with the lighter region. To verify this assumption, the simulation tools introduced in Section 4.2 and 4.3 were used for comparison with the experimental data. Among the voltage sequence tests at the three different temperatures, the experimental data at 70 °C demonstrates the cable charging processes for all three applied voltage levels. Therefore the conductivity in the simulation model was adapted to match both the shape of the PEA output and the peak area change of the charging processes at 70 °C.

According to Figure 7-20, a small amount of charge remained after discharging for 3 hours. For the convenience of simulation, this residual space charge was neglected and the simulated charging processes at each voltage were assumed to start from a space charge free condition.

The conductivity of the insulation is assumed to be field and temperature dependent. In addition, the dark region is assumed to have an enhanced conductivity by the factor, Eh(r), shown in Figure 7-23.

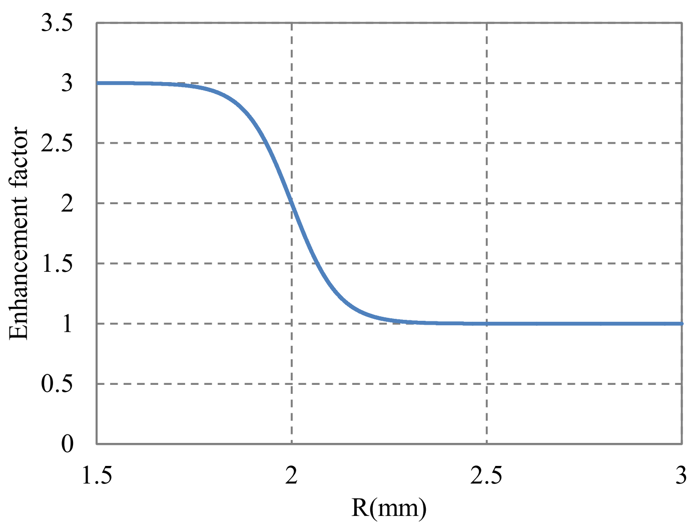

Figure 7-23. Enhancement factor of the conductivity as a function of radius.

The mathematical expression for the conductivity with the parameters that best match the experimental results is:

$$\sigma(E,r) = 3 \times 10^{-17} \cdot e^{0.1\times(70℃-25℃)} \cdot \left(\frac{E(r)}{10kV/mm}\right)^2 \cdot Eh(r) \tag{7.1}$$

Therefore, the initial conductivities as a function of radius at the three DC voltages are plotted in Figure 7-25.

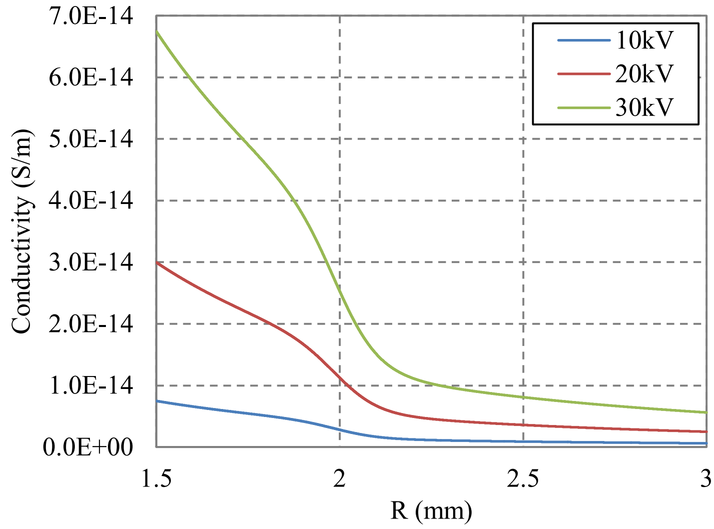

Figure 7-24. Conductivity as a function of radius in the insulation at three voltage levels.

With respect to the conductivity in Equation (7.1), the simulated PEA outputs at each quasi-steady state are shown in Figure 7-25 with the corresponding experimental data at the end of each poling stage. In the 1D simulation, the generated PEA output is of arbitrary voltage unit and was therefore normalised to the charge density of P_1 of the experimental results. As shown in Figure 7-25, simulated PEA raw signals have a good match with the experimental results while the charge near the inner electrode is slightly underestimated by the simulation. This may be due to extra conductivity enhancement factors (maybe the diffusion of impurities from the semicon layer into the insulation) existing near the inner insulation – electrode interface.

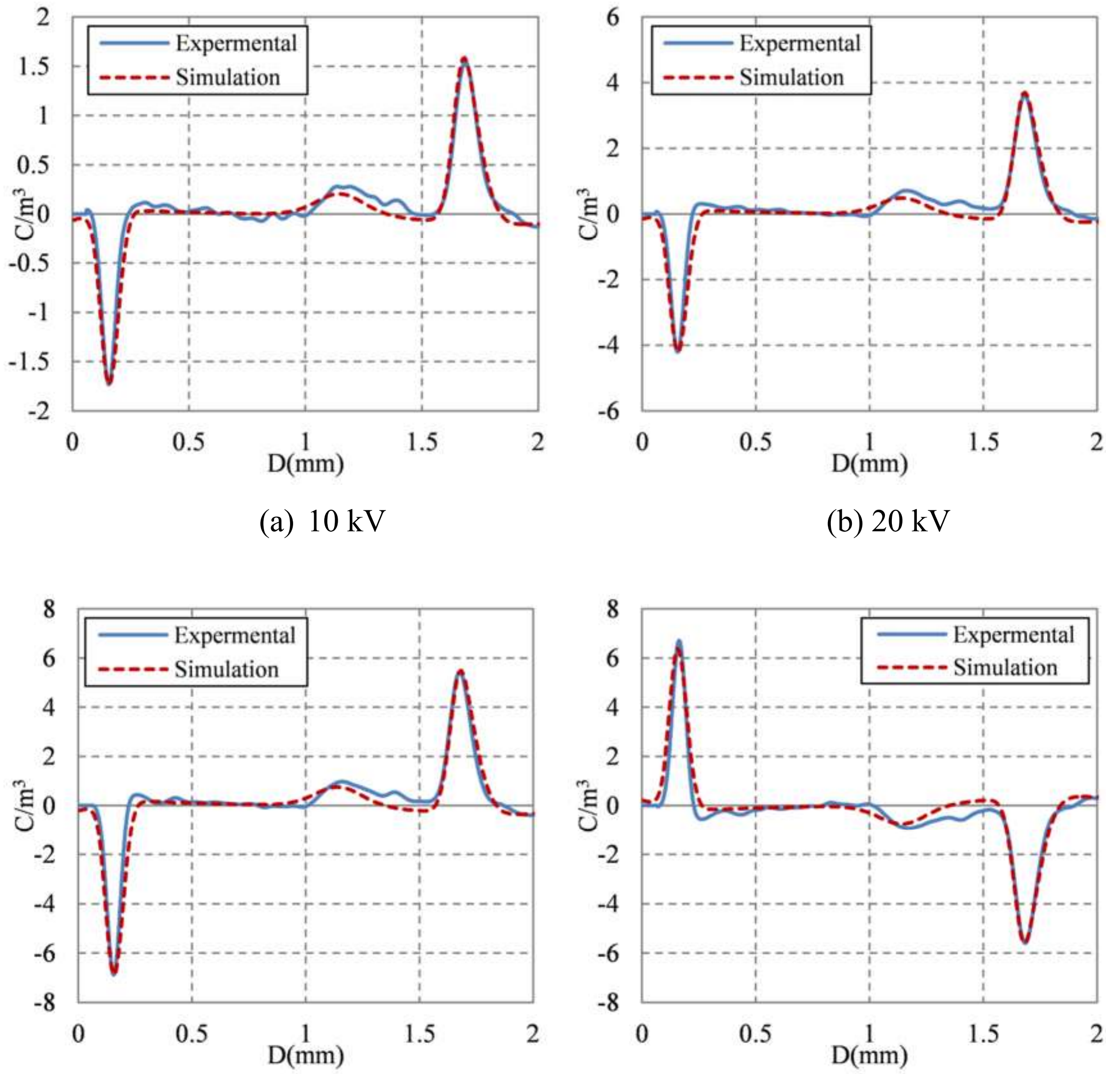

(a) 10 kV

(b) 20 kV

(c) 30 kV

(d) -30 kV

Figure 7-25. Simulated PEA outputs at quasi-steady state of each voltage level, (a) 10 kV, (b) 20 kV, (c) 30 kVand (d) -30 kV, compared with the experimental results. Simulated PEA signals were normalised to the P_1 of the experimental results.

With the parameters in Equation (7.1), the time constants of the peak area ratio changes due to space charge accumulation as generated by simulations match the experimental data calculated from Figure 7-22 (b) as shown in Figure 7-26.

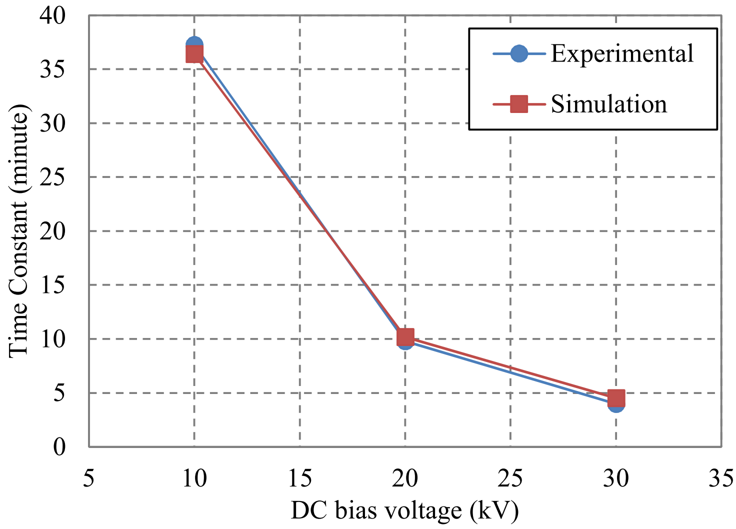

Figure 7-26. Time constants of the peak area ratio change during the charging process. Experimental data were calculated from the data in Figure 7-22.

7.3.6 PEA space charge measurements on Degassed D806D mini-cable

It was suggested that the bulk space charge signal that was observed during the voltage sequence tests for as-received D806D mini-cables at 30 °C, 50 °C and 70 °C was related to the contrast difference observed visually and interpreted in terms of a non-homogeneous electrical conductivity in the insulation (Figure 7-9). To verify this hypothesis, space charge measurements were also performed on the Degassed D806D mini-cable.

The degassing by high temperature vacuum treatment on the fresh samples is expected to produce the isothermal crystallization and remove any residual low molecular weight byproducts [34]. Specifically, the as-received D806D mini-cables were degassed in a vacuum oven at 60 °C for 20 days. After the degassing, the contrast difference in the insulation was found to have disappeared (as confirmed by visual observation on thin slices). The space charge measurements were performed at 70 °C with an applied voltage of 36 kV for three hours followed by a polarity reversal of -36 kV DC bias voltage. The raw PEA voltage output signals (1000 sweeps averaged) were to be used for this test as the bulk signal may form immediately even during a calibration measurement at a low applied voltage of 10 kV DC. Therefore calibration measurements were not taken.

The experimental results at the start and at the end of the 3-hour poling with +36 kV DC and the time taken shortly after the voltage reduction to zero are shown in Figure 7-27 (the time delay variation of P_2 is due to the transient instability of the oven temperature at the beginning of the test). Under these conditions, the bulk charge signal did not appear during the test. However, formation of heterocharge was observed near the outer semicon – insulation interface. Similar results were found in the polarity reverse test (-36 kV voltage applied) as shown in Figure 7-28. These results therefore support the hypothesis that the bulk space charge that had formed in the non-degassed samples was related to the non-homogeneous impurity present in the insulation material.

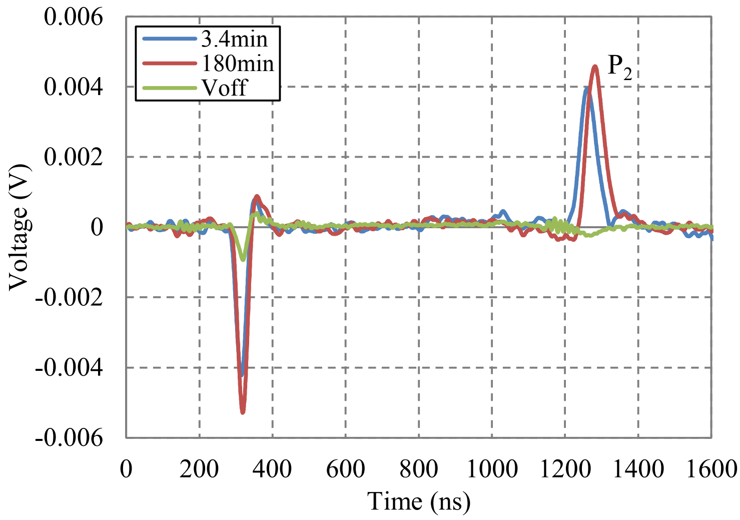

Figure 7-27. Raw PEA outputs of the degassed D806D mini-cable at 70 °C under +36 kV DC bias voltage over 180 minutes and the measurement shortly after voltage off. The shift of P_2 may mainly be due to the temperature variation of the oven at the start of the test.

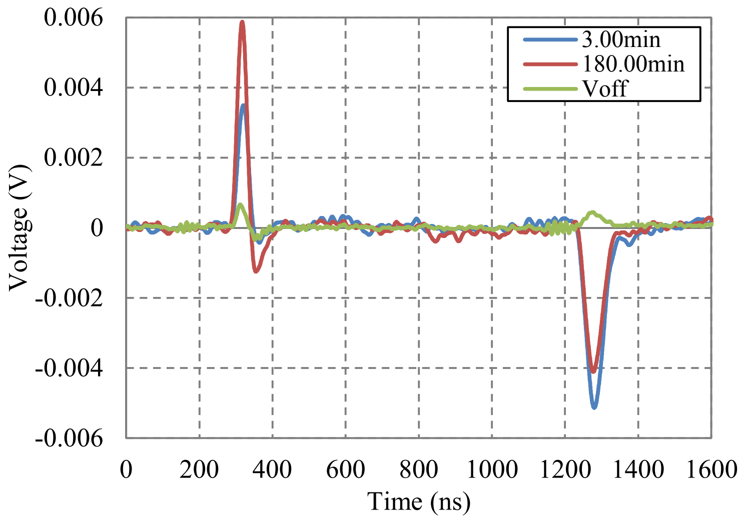

Figure 7-28. Raw PEA outputs of the degassed D806D mini-cable at 70 °C during the polarity reverse of -36 kV for 180 minutes and the measurement shortly after voltage off.

7.4 Conclusions

In this chapter the 2-D PEA simulation model has been used to assess the effect of cable non-concentricity on the PEA raw output signal. The 2-D simulation has shown that the PEA technique is robust against central conductor and inner semicon displacements perpendicular to the space charge measurement direction with very little distortion of the PEA output profile compared to the concentric arrangement. The 2-D model can be used to assess other forms of non-concentricity and distortion of the cable insulation.

The 1-D simulation tools were used to examine the effect of acoustic mismatch between the insulation and semicon layers in the mini-cable. A significant result here is that the ratio of the peak areas (P_2/P_1) depends not only on geometrical considerations but also on the degree of acoustic mismatch between the insulating material and the semicon material. This could lead to large calibration errors or errors introduced during the attenuation and dispersion correction of the PEA raw data as the values of the attenuation/dispersion coefficients are selected based on the expected peak area ratios determined by the geometry of the cylindrical cable alone. However, for the mini-cable tested here, the time delay variation with temperature would imply that the insulation and the semicon layers have similar acoustic properties.

The 1-D models were also employed to determine the parameters for the unipolar charge transport model for space charge accumulation for non-degassed samples in which a radial non-uniform electrical conductivity exists due to incomplete extraction of cross-linking by-products from the cable insulation. This leads to bulk space charge build-up inside the insulation in addition to the normal space charge accumulation due to the non-linear dependence of electrical conductivity with the applied electric field. The charge transport model gave simulated space charge accumulation dynamics consistent over a range of voltage and temperature with experiment. Hence this model could in principle be up-scaled to predict the space charge dynamics in commercial size cables.

8 DISCUSSION

8.1 Introduction

Analysis of PEA raw output signals to reconstruct the space charge profiles in cylindrical geometry insulation systems such as the case for high voltage cables usually employ the signal processing techniques of deconvolution, radial correction and attenuation/dispersion correction as reviewed in Chapter 2. The application of these techniques has their limitations and can potentially lead to erroneous conclusions when incorrectly interpreting raw PEA output data. A number of these assumptions are shown in Figure 3-17, for example the linearity in the acoustic force term with the free space charge density, perfect acoustic matches between different materials in the cable and PEA apparatus and can potentially lead for example to the incorrect calibration of the PEA apparatus. Also, the resultant (post-processed or recovered) space charge profiles may to some extent depend on the assumed values of the parameters used in the signal processing techniques applied. These include parameters such as the acoustic velocity, attenuation and dispersion coefficients. In the process of recovering the space charge profiles from raw PEA data it is often assumed that the material properties remain constant during long term or elevated temperature measurements and that the changes observed relate solely to changes in the space charge profile. However, in material such as polyethylene, the material is not mechanically stable and changes to the PEA raw output data may be due to changes involving the mechanical aspects such as material density that relates to change in electrical permittivity. In this case the PEA response will also include a perturbation due to the non-constant permittivity.

PEA measurements using a cylindrical geometry are also more difficult to interpret than for the case of uniform plane-plane geometry owing to the additional force terms (as introduced in Section 2.6.2 from the work of Holé [71, 72]) that appear when a non-uniform electric field is applied. These additional terms involve electrostriction (changes in the dimension of the insulation on application of an applied field), the formation of bound (polarisation charge in the bulk of the insulator) and the possibility of non-uniform radial dependent permittivity and conductivity owing to the method of manufacture (extrusion) of the mini-cables. The first two force terms have not fully been addressed in the literature particularly with regard to re-construction of the free charge density within the insulation when applied to cylindrical geometry systems. The work of Liu, et al. [11] and others notably Fu [27], Bodega [122] have assumed that the origin of the electrostatic force term is just the free charge density.

8.2 Simulation

The work contained in this thesis provides an alternative and complementary route for the robust interpretation of PEA data through the development of computer based simulation tools that include the complete signal generation, transmission and detection pathway. The simulation models developed here take into account the:

- The formation of space charge through charge transport simulation as the model introduced in Section 4.2.
- The geometrical aspects of the PEA experimental technique, namely the generation of acoustic waves from radial dependent space charge in cylindrical geometry insulation materials. (Section 4.3)
- The transport of the longitudinal waves within the cable insulation, taking into account the attenuation and dispersion of the acoustic waves. (Section 4.8.1.3)
- The transmission of the acoustic waves at the cable contact with the PEA base plate that is determined by the geometry of the PEA base electrode as being simulated in Section 4.7.
- The propagation of the acoustic waves through the PEA base plate into the electro-acoustic sensor and finally the absorber material as the 1D model in Section 4.3 and the 2D model in Section 4.7.
- The conversion of the acoustic waves into an electrical signal that is then subsequently amplified by a non-ideal preamplifier (realized in either the PEA acoustic model in Section 4.3 or the Pspice model in Section 4.5).

To achieve this, this work has developed a number of computer based analysis tools based on the finite difference method for simulating charge accumulation in cable systems using either empirical based non-linear unipolar field and temperature dependent conduction models or unipolar physical charge hopping transport conduction models (as discussed in Section 2.4). This work extends on the work of Bodega [122] who applied the model to charge accumulation in cylindrical samples having a temperature gradient, Boggs [103] who further developed the models for heterocharge and homocharge accumulation through a radial dependent conductivity. In this work the conduction models are used to show the dynamics of cable charging due to the non-linear dependence of electrical conductivity of the insulation material. The impact of cable charging on the calibration and post analysis of PEA raw data has not yet been fully explored in the literature. For example, Bodega [122] uses the assumption of an uncharged cable as the basis for the calibration data while Fu [27] employs the assumption that the cable is fully charged (the steady state equations developed and explored by McAllister et. al. [65] has the basis for their calibration). Often in the literature, for example in references [12, 13, 22, 80, 84], the authors do not state which assumption was used for the calibration of the PEA apparatus.

Pressure wave generation and a propagation model are based on the current physical understanding concerning force developed by charges in dielectrics and the method of coupling the electrostatic force to the source of mechanical wave propagation as suggested by Holé [71]. The modelling of acoustic wave propagation of the longitudinal acoustic waves through the cable insulation and the PEA space charge measurement apparatus was achieved using finite difference methods in 1-D and 2-D to solve the appropriate time dependent differential equations. The modelling of the process of detection by conversion of the propagating acoustic waves to electrical signals using a piezoelectric sensor as achieved using a Pspice equivalent circuit model based on the existing work [108-114]. Finally the Pspice model for the piezoelectric sensor was modified to include the imperfection due to the impedance mismatch with the buffer amplifier.

The simulation models developed here provide a novel means of applying space charge transport models for cable insulating materials to simulate the accumulation of charge and the corresponding raw PEA output signal that can then be compared to actual raw PEA data. In this way, the imperfections in the experimental technique/apparatus can be built into the analysis. In addition, the simulation models developed here can also be usefully employed as design tools to inform the design and optimisation of future PEA experimental apparatus.

8.3 Comparison with Experiments

In general a good correspondence was found between the simulated and experimental data. In chapter 4, 1-D simulations and the 2-D with cylindrical base electrode simulations showed good correspondence with the raw output PEA data obtained experimentally using a cylindrical base electrode.

Although good agreement was obtained for the electrode peaks the expected baseline signal due to bulk polarisation charge was not observed in the experimental data. This could be due either to an incorrect assumption in the physics of the dielectric and space charge force terms in the accepted theory for the PEA method or due to an unidentified shortcoming in the experimental PEA apparatus. Much effort was applied in order to account for the lack of bulk polarisation charge in the experimental PEA data but no reasons could be found to account for the differences in the PEA baseline and that expected from the simulations. This therefore remains an unresolved issue and it is recommended that this be the subject of further investigation.

Good correspondence was found in the 2-D simulations and experiments using a flat PEA base electrode under different clamping force as described in Chapter 5 as well as in the 1-D simulations and experiments on the mini-cable which is believed to have a nonhomogeneous property in the insulation and thus results in a bulk charge signal as discussed in Section 7.3.

8.4 High temperature mini-cable PEA system

As described in Chapter 3, in order to verify the developed simulation models, a bespoke cylindrical space charge measurement system based on the PEA method (as reviewed in Section 2.6) was developed. Although the basic design methods for a PEA measurement system were used, the basic design was extended to enable a controlled mechanical pressure to be exerted by the cable clamp and interchangeable base electrodes to encompass the two different base plate geometries, curved and flat that have been used in the literature [12, 80, 123]. The PEA apparatus was also designed to withstand high environmental temperatures, up to 70 °C to enable isothermal measurements to be taken on cables over a range of temperatures. The PEA system was enclosed in a temperature controlled oven and enabled isothermal test conditions to be set up from 25 °C to 70 °C to mimic the test conditions usually applied to full size manufactured cables. This enables controlled charging and discharging cable tests to be undertaken on the mini-cables to examine the charging and discharging dynamics. In order to operate at temperatures up to 70 °C an alternative piezoelectric sensor material (PVDF-TrFE) had to be identified as the traditional material (PVDF) used is not stable at these high temperatures [91, 92]. A buffer amplifier with high input resistance was found to be necessary to provide good electrical match to the low noise amplifier. The complete system allowed PEA raw data to be generated and processed either by direct comparison with the simulation predictions using the models described above or by the conventional approach of using signal processing techniques on the raw PEA data to reconstruct the space charge distributions.

In Chapter 5, the developed simulation models as described in Chapter 4 have been used in conjunction with the developed hardware to compare the relative performance of PEA systems having flat or curved geometry base plates under the influence of differing clamping pressure. Also, the effect of resultant mechanical distortion of the cable insulation was demonstrated using mechanical deformation simulation in COMSOL and the PEA hardware. Comparison of PEA raw data obtained from a flat and cylindrical PEA base electrode systems have been investigated for the first time. The results of this comparison showed significant differences due to the way in which the acoustic waves are coupled from the cable to the base electrode. In the case of a flat base electrode PEA system, both experimentally and through simulations the signal peaks due to the electrode charges show distortion (overshoot) due to acoustic reflection at the base plate surfaces on either side of the contact area. The baseline signal between the electrodes peak signals show less contribution from the bound polarisation charge that is expected and observed in the 2-D simulations for the cylindrical base electrode case. Secondary changes dependent on the thermal history and the clamping pressure were also observed. The limited area of contact between the cylindrical cable and the flat base electrode depends on the clamping pressure and the degree of softness (which is temperature dependent) of the insulating material of the cable. The raw signal output is proportional to the area of contact of the cable with the flat base electrode. When carrying out temperature cycling measurements using a flat PEA base electrode it is recommended that a complete temperature cycle is first undertaken to allow for the initial high temperature deformation to be frozen in. This would allow the most significant changes to be conditioned out before system calibration and electrical experiments and lead to a significant improvement in the reproducibility of experimental data obtained.

8.5 Cable Charging

In Chapter 6, the effect of cable charging due to non-linear field dependence of insulator conductivity, a process that has found to be identified empirically in previous research on polymeric insulation [26] was determined experimentally. The results were compared with simulations using the various empirical models for the field/temperature dependence on conductivity. Cable charging was found to occur due to a non-linear conductivity-field relationship of the insulator material and this leads to an accumulation of free charge in the bulk. The accumulation of charge leads to induced charges appearing on the electrode surfaces and hence changing the overall peak areas. This cable charging process was best followed by following the evolution of the ratio of the two electrode space charge peak areas. Good correspondence between model and experimental raw data was found. The time taken to achieve the steady state was found experimentally to depend on the actual cable insulation material used (i.e. changes between different cable types supplied) the applied voltage (field) and temperature. For a given cable type, the time required to reach steady state was found to follow that predicted from simulations based on two alternative non-linear empirical relationships of the conductivity with field and temperature as well as a model based on charge carrier hopping transport. However, it was not possible at this stage to identify the best-fit relationship from the limited experimental data available.

8.6 Application of technique to mini-cable insulation systems

The application of the technique to practical cable systems in which the insulation material has an in-built radial dependence of polymeric morphology has been described in Chapter 7. Using the novel approach, it has been shown how local changes to the electrical conductivity in unipolar based conduction models can be used to interpret experimentally derived PEA data in terms of bulk charge formation in cables subject to moderate cycled electrical stress levels similar to their service stress level ~10 kV/mm – 30 kV/mm and after polarity inversion at 30 kV/mm.

In the case of non-homogeneous cable insulation, the difference could be visually observed on cross-section cuttings. The darker inner region would gradually disperse during the degassing process or when left in the laboratory. This suggests either a morphological contrast due to differences in crystallinity or more likely impurity concentration differences within the cable due to incomplete degassing of the cable. Space charge measurements on the D806D mini-cables were performed under three isothermal conditions of 30 °C, 50 °C and 70 °C. On each temperature, the voltage sequence of +10 kV, 0 kV, +20 kV, 0 kV, +30 kV, 0 kV, -30 kV and 0 kV was applied with a time interval of three hours for each voltage level. Experimental results shows that no obvious charge accumulation at 30 °C during the period of measurement. The bulk signal only becomes obvious at 50 °C with a bias voltage of +20 kV. At 70 °C, the bulk signal is observed immediately (within the 1 minute time interval of measurements) and formed even at the lowest voltage level of +10 kV.

Using the simulation tools developed in Chapter 6, the formation of the bulk signal observed experimentally can be inferred as the consequence of a radius dependent enhancement on the conductivity (where the darker region has a significantly higher conductivity, consistent with a higher concentration of impurities in the inner dark region). By employing the unipolar charge transport model and the 1-D acoustic simulation model with considering the acoustic attenuation and dispersion, the simulated space charge profiles could match the experimental data. Not only matched at the steady-state condition for the PEA outputs, the matched transients were proved by comparing the time constants of the variations of peak area ratios between the experiments and the simulation. These results demonstrate the temperature and field dependence of the enhanced electrical conductivity within the insulation again consistent with an enhanced concentration of impurities.

9 CONCLUSIONS AND FUTURE WORK

9.1 Conclusions

9.1.1 Background to the Work

The work contained in this thesis was intended to develop a toolbox of computer simulation software in order to provide a systematic and robust methodology for the interpretation of PEA (pulsed electroacoustic) space charge data. The work was to be supported and verified by the development of PEA hardware for the measurement of space charge accumulation in mini-cables. Mini-cables are small scale cables which are constructed employing the same manufacturing techniques and materials as in commercial scale cables and are useful for development of new cable designs in a traditional laboratory environment without the necessity of an expensive HV test laboratory. The software tools developed here are therefore intended for manufacturers of HV cables to upscale the results on mini-cables to the full scale of commercial HV cable systems in order to reduce development costs.

The traditional approach is to generate PEA data (usually from mini-cables) and then process the raw PEA data to recover the distribution of space charge that had accumulated in the test insulator material at the time of measurement. This involves a number of signal processing steps to provide a calibrated space charge distribution. While these processing steps are relatively straightforward for plane-plane thin film geometry samples owing to the uniform applied electric field, in the case of cylindrical geometry systems like mini-cables, the traditional processing steps have to be modified to take into account the non-uniform applied electric field and the different geometrical aspects of the PEA apparatus on the generation of the acoustic pressure waves and their subsequent transmission to the PEA sensor. In the literature, these modified processing steps have additional assumptions regarding their use to recover the space charge distribution in cylindrical cable systems. Also, in the literature, the adaption of the signal processing techniques used for plane-plane sample geometry to cylindrical geometry samples has largely ignored the different experimental PEA hardware configurations used. For example, in the literature there are many different approaches taken when applying PEA techniques to space charge measurements in which the coupling of the acoustic waves from the cable sample to the PEA apparatus is attempted in different ways. The two most common are the flat base plate PEA system where a 'line' the contact exists between the cylindrical outer surface of the cable and the flat PEA base electrode and the curved base electrode PEA system where the curvature of the base plate is machined to match the curved outer surface of the mini-cable. In the literature, the two schemes are considered identical as far as the signal processing is concerned and the flat electrode system is often considered to be preferred owing to its convenience in the measurement of space charge in different diameter cables.

9.1.2 Significant contributions to the research field.

In this thesis the main overarching contribution to the research field was the development of the necessary software tools to encompass the complete experiment and measurement process of charge accumulation, signal generation and detection using the PEA technique and subsequent signal distortion caused by the signal amplification stage of charge in model cable systems. This is the first time that the complete simulation of PEA measurement process has been applied to cylindrical geometry systems and the simulation outputs show good agreement with experimentally derived PEA raw signal outputs from mini-cables. In this work it is proposed that the simulation tools offer an alternative methodology and approach for the robust interpretation of space charge measurements on mini-cables. In this alternative approach, a model for charge transport and space charge accumulation in cable insulation is coupled with a PEA simulation model for acoustic wave generation and propagation of the generated waves through the cable insulation and PEA apparatus and subsequent detection and amplification to produce simulated raw PEA signals. These simulated signals can then be directly compared with the experimentally derived raw PEA signals. This approach can be used in tandem with traditional methods of recovering the space charge profile from the raw PEA output data using signal processing or replacing them and allows for the effects of instrumental imperfections to be built into the simulation model. This work therefore builds on existing approaches in the literature by providing an alternative processing methodology that allows the assumptions used in the traditional approach to be tested and verified.

In this work, three different unipolar charge transport models, previously identified in the literature, having field and temperature dependent electrical conductivity as considered by [2, 24, 25, 65, 122] or where a non-uniform electrical conductivity is imposed [103] due to impurity diffusion at semicon electrodes were used as the basis for charge accumulation in the simulation technique. It is shown that the dynamics of the natural charging of the cable due to the non-linear field dependent conductivity can be best followed by monitoring the ratio of the peak areas of the electrode charges in the PEA raw output data. This was confirmed by experiments that the charging dynamics cause the peak area ratio to change in time as charge accumulates in the bulk of the cable insulation. The change in the electrode peak areas is due to that induced by the bulk charge. The simulation approach proposed here can successfully reproduce the results of Bodega[122] (for the charging dynamics) and Boggs [103] (for the heterocharge/homocharge accumulation). Parallel experimental results on mini-cables also showed that the time span for the charge dynamics to settle to a steady state from an initial uncharged cable to a fully charged cable depended on the cable insulator material and the experimental conditions, temperature and applied electric field. Time constants of 14 to 300 minutes were found and are well within the range of a typical PEA experiment. This has significant impact on the ability to apply correctly a calibration procedure on the raw PEA output. Often in the literature it is assumed that no space charge accumulation occurs at fields less than 10 kV/mm or that steady state has been achieved at the time of calibration. However the results found here demonstrate that the assumption that the cable is space charge free at these fields cannot necessarily be relied upon, particularly using degassed samples at temperatures of 50 °C to 80 °C. In the literature the precise details of the PEA calibration are often neglected or simply not given. The work in the thesis builds on the work of Bodega and Boggs by building in the PEA system response into the analysis allowing simulation output to be directly compared to raw PEA data rather than by comparing the output of idealised charge transport and accumulation models to be compared with calibrated PEA output signals. The results here confirm the existence of the non-linear electric field – conductivity relationship in cable insulating materials such as cross-linked polyethylene and that charge build-up in the bulk of the insulator material (cable charging) is a real process and that it occurs at all applied fields and in particular at the service fields of commercial cables ~10 kV/mm. The results here also highlight the importance of taking into account the charging dynamics and stating the details of the PEA calibration procedure, for example no space charge or steady state charging when reporting results in the literature.

In this thesis the comparison of flat base electrode and curved electrode PEA systems have been compared by simulation and by experiment. This necessitated the development of 2-D simulation models for the generation, transmission and detection of the acoustic waves in a cylindrical PEA apparatus and the development of PEA hardware with interchangeable base electrodes (curved and flat). The simulation model was developed using FDTD method in MATLAB and was adapted by modification of the material boundaries to simulate either a flat or curved PEA base electrode hardware. This allows the two techniques to be compared using computer based simulation and in hardware for the first time. The acoustic wave generation by space charges in the cable system was calculated from the physics of forces on charges in dielectrics and includes contributions from space charge, non-uniform permittivity, electrostriction and the response due to bound polarisation charge that is induced in the bulk of the insulation material when a non-uniform electric field is applied. These additional force terms are often excluded from consideration in the literature. The model also allows the imperfections of the PEA technique to be built-in (i.e. acoustic mismatches between the various materials used in the cable design and PEA apparatus leading to acoustic reflections). In parallel with the cylindrical PEA simulation models, a hardware based PEA system was also developed that included controlled clamping force, interchangeable flat and curved base plates and temperature control in order to obtain reproducible results. The simulations and the hardware both showed that there were a number of significant differences between the flat and curved base plate PEA systems that need to be taken into consideration when applying the technique to practical mini-cable systems.

The main differences when applying the PEA technique using a flat or curved base electrode are:

The curved base electrode is the preferable option as the mechanical distortion of the cable when working at high temperatures during temperature cycling experiments is minimised. When a flat electrode system was used, the cable suffers mechanical distortion at high temperatures that is then frozen in when the cable is returned to a low temperature. This causes the area of contact of the cable and the base plate to increase on the first elevated temperature cycle which then increases the signal amplitude of the raw PEA output. This distortion is due to the mechanical force acting on the cable using the cable clamp to ensure an acoustic contact between the cable and the base electrode of the PEA system. As this mechanical distortion is unavoidable, it is recommended that when using a flat PEA base electrode to undertake a conditioning thermal cycle with no applied voltage to the cable to ensure that the initial distortion has occurred before applying electrical stress to the cable. This will minimise PEA response differences during subsequent cycles.

While the flat base electrode PEA system is convenient for the measurement of space charge in cables of differing diameter, the flat base electrode PEA response includes an additional pulse overshoot due to acoustic reflections at the base plate – air interface on either side of the region of contact that does not appear when the curved electrode system is employed. In principle this overshoot can be corrected by applying adequate signal processing (deconvolution). However, the additional deconvolution can have the effect of increasing noise and ringing in the de-convolved signal.

The effect of cable clamping pressure was also investigated. It was found that the PEA amplitude response was affected significantly for the case of the flat base electrode system where the raw PEA signal output increased with increasing clamping force. This is due to the increase in contact area with increasing clamping force. This leads to a change in the ratio of the electrode peak areas that could lead to miss-interpretation of the electrode charges and the calculated internal electric field within the cable from the processed raw data from the PEA system. As the cable insulation softens at high temperature, this effect will increase in significance. In the case of the curved base electrode PEA system, while the amplitudes of the PEA raw output data increased with cable clamp pressure, the relative amplitudes of the electrode peaks remained the same. The curved base electrode PEA system is therefore significantly less susceptible to changes in cable pressure and the resultant cable deformation.

Taking the advantage of the 2-D and 1-D PEA simulation tools, the effect of possible non-concentric cable geometry and mismatches between the semicon layer and the insulation during the experimental temperature conditions on the raw PEA output have been analysed. It was found that the PEA technique was robust against lateral changes to the position of the central conductor and surrounding semicon layer. It was also found that acoustic reflections at the semicon – insulation interfaces could cause peaks in the PEA response that could be confused with accumulated charge in the bulk.

However the software tools developed can predict the positions of these reflected signals.

The proposed analysis tools have also been used to interpret the accumulation of bulk charge within the mini-cable insulation. The observed build-up of space charge was found to be consistent with an inhomogeneous distribution of impurities leading to a radial dependence of electrical conductivity possibly due to incomplete degassing of the cable.

9.2 Suggested further work

9.2.1 Improvement on existing work

Currently, there remains one important issue regarding the correspondence between the experimental and simulation results. This is the problem that the bound polarisation signal predicted in the simulations is not present in the experimental data. This may be a consequence of an unknown system response acting as a high pass filter as was demonstrated in section 4.8.1 or due to the assumptions made in the simulation procedure. For the 1D and 2D PEA acoustic simulation models, it was assumed that the insulation material was isotropic and the shear waves were not taken into account. Further work may be needed to verify these assumptions and to consider more closely the coupling of the acoustic waves through the mini-cable and PEA apparatus.

In the PEA acoustic pulse propagation models, the insulation domains are assumed to be acoustically lossless and the effect of acoustic attenuation and dispersion is achieved by numerical processing on the sensor received signals. Simulation of the propagation of the acoustic waves in a lossy and dispersive medium may provide an alternative approach to the simulation at the expense of increasing complexity of the simulation algorithm. In addition, the current acoustic simulation models, especially the 2D model, demands large memory requirements of the computer. Improved modelling techniques may be developed to improve the efficiency of simulation.

9.2.2 Proposed experiments

In this thesis, the space charge due to the field dependent conductivity in the polymeric insulation has been considered under isothermal conditions. However, the temperature gradient may have more significant influence on the conductivity divergence across the insulation thickness and consequently seriously alter the electrical field. To evaluate the space charge accumulation under temperature gradients, the current system needs to be modified to enable the Joule heating on the cable conductor and more accurate temperature control on the PEA cell. With the solid experimental data, the simulation models (unipolar charge transport model and the PEA acoustic models) will be further developed to employ the gradient temperature.

In addition to the temperature, humidity may play an important role in the space charge behaviours [124, 125]. Therefore humidity is recommended to be specified for further work. And the effect of humidity on the space charge accumulation in polymeric cables is of interest.

With the simulation tools introduced in this thesis, it is convenient to analyse the PEA signal measured on a multi-layer insulations. Further work may include the space charge measurement on cable joints.

There is some concern about whether model cable samples can represent the behaviours of the full size cable as some phenomena may be voltage-dependent rather than field-dependent. Therefore it is necessary to have a comparative study of space charge measurement on model cables of different scales as well as full size commercial cables.

REFERENCES

[1] M. Salah Khalil, "International research and development trends and problems of HVDC cables with polymeric insulation," *Electrical Insulation Magazine, IEEE,* vol. 13, pp. 35-47, 1997.

[2] T. Tanaka and A. Greenwood, *Advanced Power Cable Technology: Basic concepts and testing*: CRC Press, 1983.

[3] D. Fabiani, G. C. Montanari, C. Laurent, G. Teyssedre, P. H. F. Morshuis, R. Bodega*, et al.*, "Polymeric HVDC Cable Design and Space Charge Accumulation. Part 1: Insulation/Semicon Interface," *Electrical Insulation Magazine, IEEE,* vol. 23, pp. 11-19, 2007.

[4] Z. Yewen, J. Lewiner, C. Alquie, and N. Hampton, "Evidence of strong correlation between space-charge buildup and breakdown in cable insulation," *Dielectrics and Electrical Insulation, IEEE Transactions on,* vol. 3, pp. 778-783, 1996.

[5] G. C. Montanari and D. Fabiani, "Evaluation of dc insulation performance based on space-charge measurements and accelerated life tests," *Dielectrics and Electrical Insulation, IEEE Transactions on,* vol. 7, pp. 322-328, 2000.

[6] J. M. Alison and R. M. Hill, "A model for bipolar charge transport, trapping and recombination in degassed crosslinked polyethene," *Journal of Physics D: Applied Physics,* vol. 27, p. 1291, 1994.

[7] S. Deipino, D. Fabiani, G. C. Montanari, C. Laurent, G. Teyssedre, P. H. F. Morshuis*, et al.*, "Feature article - Polymeric HVDC cable design and space charge accumulation. Part 2: insulation interfaces," *Electrical Insulation Magazine, IEEE,* vol. 24, pp. 14-24, 2008.

[8] D. Fabiani, G. C. Montanari, C. Laurent, G. Teyssedre, P. H. F. Morshuis, R. Bodega*, et al.*, "Feature article - HVDC Cable Design and Space Charge Accumulation. Part 3: Effect of Temperature Gradient," *Electrical Insulation Magazine, IEEE,* vol. 24, pp. 5-14, 2008.

[9] L. A. Dissado, C. Laurent, G. C. Montanari, and P. H. F. Morshuis, "Demonstrating a threshold for trapped space charge accumulation in solid dielectrics under DC field," *Dielectrics and Electrical Insulation, IEEE Transactions on,* vol. 12, pp. 612-620, 2005.

[10] P. Morshuis and M. Jeroense, "Space charge measurements on impregnated paper: a review of the PEA method and a discussion of results," *Electrical Insulation Magazine, IEEE,* vol. 13, pp. 26-35, 1997.

[11] R. Liu, T. Takada, and N. Takasu, "Pulsed electro-acoustic method for measurement of space charge distribution in power cables under both DC and AC electric fields," *Journal of Physics D: Applied Physics,* vol. 26, p. 986, 1993.

[12] W. Xinsheng, T. Demin, Y. Tanaka, T. Muronaka, T. Takada, C. Shinoda*, et al.*, "Space charge in XLPE power cable under dc electrical stress and heat treatment," *Dielectrics and Electrical Insulation, IEEE Transactions on,* vol. 2, pp. 467-474, 1995.

[13] N. Hozumi, T. Okamoto, and T. Imajo, "Space charge distribution measurement in a long size XLPE cable using the pulsed electroacoustic method," in *Electrical Insulation, Conference Record of the 1992 IEEE International Symposium on*, 1992, pp. 294-297.

[14] M. Marzinotto and G. Mazzanti, "A procedure for space charge measurements in full-size HVDC extruded cables," in *Electrical Insulation and Dielectric Phenomena (CEIDP), 2011 Annual Report Conference on*, 2011, pp. 804-807.
[15] T. Takeda, N. Hozumi, H. Suzuki, K. Fujii, K. Terashima, M. Hara*, et al.*, "Space charge behavior in full-size 250 kV DC XLPE cables," *Power Delivery, IEEE Transactions on,* vol. 13, pp. 28-39, 1998.
[16] K. Nagashima, Q. Xiaokui, Y. Tanaka, and T. Takada, "Calibration of accumulated space charge in power cable using PEA measurement," in *Conduction and Breakdown in Solid Dielectrics, 1998. ICSD '98. Proceedings of the 1998 IEEE 6th International Conference on*, 1998, pp. 60-63.
[17] B. Vissouvanadin, C. Laurent, S. Le Roy, Teysse, x, G. dre*, et al.*, "A deconvolution technique for space charge recovery in lossy and dispersive dielectrics using PEA method," in *Electrical Insulation and Dielectric Phenomena (CEIDP), 2010 Annual Report Conference on*, 2010, pp. 1-4.
[18] Y. Li, M. Aihara, K. Murata, Y. Tanaka, and T. Takada, "Space charge measurement in thick dielectric materials by pulsed electroacoustic method," *Review of Scientific Instruments,* vol. 66, pp. 3909-3916, 1995.
[19] S. Holé, T. Ditchi, and J. Lewiner, "Influence of divergent electric fields on space-charge distribution measurements by elastic methods," *Physical Review B,* vol. 61, pp. 13528-13539, 05/15/ 2000.
[20] S. Holé, "Behind space charge distribution measurements," *Dielectrics and Electrical Insulation, IEEE Transactions on,* vol. 19, pp. 1208-1214, 2012.
[21] Y. Tanaka, K. Hanawa, K. Suzuki, and T. Takada, "Attenuation recovery technique for acoustic wave propagation in PEA method," in *Electrical Insulating Materials, 2001. (ISEIM 2001). Proceedings of 2001 International Symposium on*, 2001, pp. 407-410.
[22] N. Hozumi, H. Suzuki, T. Okamoto, K. Watanabe, and A. Watanabe, "Direct observation of time-dependent space charge profiles in XLPE cable under high electric fields," *Dielectrics and Electrical Insulation, IEEE Transactions on,* vol. 1, pp. 1068-1076, 1994.
[23] P. Carstensen, A. A. Farkas, A. Campus, and U. H. Nilsson, "The effect of the thermal history on the space charge accumulation in HVDC crosslinked polyethylene cables," in *Electrical Insulation and Dielectric Phenomena, 2005. CEIDP '05. 2005 Annual Report Conference on*, 2005, pp. 381-388.
[24] S. Boggs, D. H. Damon, J. Hjerrild, J. T. Holboll, and M. Henriksen, "Effect of insulation properties on the field grading of solid dielectric DC cable," *Power Delivery, IEEE Transactions on,* vol. 16, pp. 456-461, 2001.
[25] L. A. Dissado and J. C. Fothergill, *Electrical Degradation and Breakdown in Polymers*: Institution of Engineering and Technology, 1992.
[26] I. W. McAllister, G. C. Crichton, and A. Pedersen, "Charge accumulation in DC cables: a macroscopic approach," in *Electrical Insulation, 1994., Conference Record of the 1994 IEEE International Symposium on*, 1994, pp. 212-216.
[27] M. Fu, "Space Charge Measurement in Polymer Insulated Power Cables Using the PEA Method," PHD Thesis, Department of Electronics and Computer Science, University of Southampton.
[28] G. Mazzanti and M. Marzinotto, *Extruded Cables for High-Voltage Direct-Current Transmission: Advances in Research and Development*: Wiley, 2013.
[29] E. Peschke and R. von Olshausen, *Cable systems for high and extra-high voltage: development, manufacture, testing, installation and operation of cables and their accessories*: Wiley VCH, 1999.

[30] T. Tanaka and A. Greenwood, *Advanced Power Cable Technology: Present and Future* vol. 2: CRC Press, 1983.
[31] J. C. Fothergill and R. N. Hampton, "Polymer insulated power cable," in *Advances in High Voltage Engineering*, ed: Institution of Engineering and Technology, 2004, pp. 477-510.
[32] K. Matsui, Y. Tanaka, T. Takada, T. Fukao, and T. Maeno, "High-sensitivity PEA system with dual-polarity pulse generator," *Electrical Engineering in Japan,* vol. 166, pp. 1-7, 2009.
[33] T. L. Hanley, R. P. Burford, R. J. Fleming, and K. W. Barber, "A general review of polymeric insulation for use in HVDC cables," *Electrical Insulation Magazine, IEEE,* vol. 19, pp. 13-24, 2003.
[34] R. Arora and W. Mosch, *High Voltage and Electrical Insulation Engineering*: Wiley-IEEE Press, 2011.
[35] P. J. Phillips, "Morphology - Electrical Property Relations in Polymers," *Electrical Insulation, IEEE Transactions on,* vol. EI-13, pp. 69-81, 1978.
[36] K. S. Suh, C. R. Lee, J. S. Noh, J. Tanaka, and D. H. Damon, "Electrical conduction in polyethylene with semiconductive electrodes," *Dielectrics and Electrical Insulation, IEEE Transactions on,* vol. 1, pp. 224-230, 1994.
[37] S. Mitsumoto, M. Nagao, and L. A. Dissado, "The space charge decay of LDPE and HDPE under different temperatures," in *Electrical Insulating Materials (ISEIM), Proceedings of 2011 International Conference on*, 2011, pp. 51-53.
[38] N. L. Dao, P. L. Lewin, I. L. Hosier, and S. G. Swingler, "A comparison between LDPE and HDPE cable insulation properties following lightning impulse ageing," in *Solid Dielectrics (ICSD), 2010 10th IEEE International Conference on*, 2010, pp. 1-4.
[39] R. Nath and M. M. Perlman, "Effect of crystallinity on charge storage in polypropylene and polyethylene," *Electrical Insulation, IEEE Transactions on,* vol. 24, pp. 409-412, 1989.
[40] F. H. Kreuger, *Industrial High DC Voltage*: Delft University Press, 1992.
[41] R. Arrighi, "From Impregnated Paper to Polymeric Insulating Materials in Power Cables," *Electrical Insulation, IEEE Transactions on,* vol. EI-21, pp. 7-18, 1986.
[42] P. J. Caronia, J. S. Furno, K. P. Pang, and S. R. Szaniszlo, "Advances in TR-XLPE insulation," in *Transmission and Distribution Conference, 1999 IEEE*, 1999, pp. 56-61 vol.1.
[43] D. Wald and A. Smedberg, "Evolution of Medium Voltage Cable Technology in Europe," *Electrical Insulation Magazine, IEEE,* vol. 24, pp. 31-35, 2008.
[44] J. M. Oudin, M. Fallou, and H. Thevenon, "Design and Development of DC Cables," *Power Apparatus and Systems, IEEE Transactions on,* vol. PAS-86, pp. 304-311, 1967.
[45] L. A. Dissado, G. Mazzanti, and G. C. Montanari, "The role of trapped space charges in the electrical aging of insulating materials," *Dielectrics and Electrical Insulation, IEEE Transactions on,* vol. 4, pp. 496-506, 1997.
[46] G. C. Montanari, "Bringing an insulation to failure: the role of space charge," *Dielectrics and Electrical Insulation, IEEE Transactions on,* vol. 18, pp. 339-364, 2011.
[47] M. Abou-Dakka, A. Bulinski, and S. S. Bamji, "Effect of additives on the performance of cross-linked polyethylene subjected to long term single and periodically reversed polarity DC voltage," *Dielectrics and Electrical Insulation, IEEE Transactions on,* vol. 20, pp. 654-663, 2013.

[48] B. Aladenize, R. Coelho, F. Guillaumond, and P. Mirebeau, "On the intrinsic space charge in a DC power cable," *Journal of Electrostatics,* vol. 39, pp. 235-251, 1997.

[49] J. C. Fothergill and L. A. Dissado, *Space Charge in Solid Dielectrics*: Dielectrics Society, 1998.

[50] H. J. Wintlet, "Schottky Injection Currents in Insulators: The Effect of Space Charge on the Time Dependence," *Electrical Insulation, IEEE Transactions on,* vol. EI-12, pp. 424-428, 1977.

[51] T. W. Hickmott, "Formation of Ohmic contacts: A breakdown mechanism in metal-insulator-metal structures," *Journal of Applied Physics,* vol. 100, pp. -, 2006.

[52] A. J. Campbell, D. D. C. Bradley, H. Antoniadis, M. Inbasekaran, W. W. Wu, and E. P. Woo, "Transient and steady-state space-charge-limited currents in polyfluorene copolymer diode structures with ohmic hole injecting contacts," *Applied Physics Letters,* vol. 76, pp. 1734-1736, 2000.

[53] P. N. Murgatroyd, "Theory of space-charge-limited current enhanced by Frenkel effect," *Journal of Physics D: Applied Physics,* vol. 3, p. 151, 1970.

[54] M. A. Lampert, "Simplified Theory of Space-Charge-Limited Currents in an Insulator with Traps," *Physical Review,* vol. 103, pp. 1648-1656, 09/15/ 1956.

[55] B. Shklovskii, *Hopping Transport in Solids*: Elsevier Science, 1991.

[56] L. A. Dissado and J. C. Fothergill, *Electrical degradation and breakdown in polymers*: P. Peregrinus, 1992.

[57] G. Teyssedre and C. Laurent, "Charge transport modeling in insulating polymers: from molecular to macroscopic scale," *Dielectrics and Electrical Insulation, IEEE Transactions on,* vol. 12, pp. 857-875, 2005.

[58] H. Kiess and W. Rehwald, "Electric conduction in amorphous polymers," *Colloid and Polymer Science,* vol. 258, pp. 241-251, 1980/03/01 1980.

[59] K. S. Suh, S. J. Hwang, J. S. Noh, and T. Takada, "Effects of constituents of XLPE on the formation of space charge," *Dielectrics and Electrical Insulation, IEEE Transactions on,* vol. 1, pp. 1077-1083, 1994.

[60] Y. Maeno, N. Hirai, Y. Ohki, T. Tanaka, M. Okashita, and T. Maeno, "Effects of crosslinking byproducts on space charge formation in crosslinked polyethylene," *Dielectrics and Electrical Insulation, IEEE Transactions on,* vol. 12, pp. 90-97, 2005.

[61] D. Chu and B. M. Weedy, "HVDC Extruded Cables-Parameters For Determination of Stress," *Power Apparatus and Systems, IEEE Transactions on,* vol. PAS-103, pp. 662-667, 1984.

[62] W. Choo, G. Chen, and S. Swingler, "Electric Field in Polymeric Cable due to Space Charge Accumulation under DC and Temperature Gradient," *IEEE Transactions on Dielectrics and Electrical Insulation,* vol. 18, pp. 596-606, 2011.

[63] D. K. Das-Gupta, "Conduction mechanisms and high-field effects in synthetic insulating polymers," *Dielectrics and Electrical Insulation, IEEE Transactions on,* vol. 4, pp. 149-156, 1997.

[64] A. R. Blythe and D. Bloor, *Electrical Properties of Polymers*: Cambridge University Press, 2005.

[65] I. W. McAllister, G. C. Crichton, and A. Pedersen, "Space charge fields in DC cables," in *Electrical Insulation, 1996., Conference Record of the 1996 IEEE International Symposium on*, 1996, pp. 661-665 vol.2.

[66] F. H. Buller, "Calculation of Electrical Stresses in DC Cable Insulation," *Power Apparatus and Systems, IEEE Transactions on,* vol. PAS-86, pp. 1169-1178, 1967.
[67] R. Bodega, P. H. F. Morshuis, G. C. Montanari, D. Fabiani, and J. J. Smit, "The Use of Cable System Models for the Assessment of Space Charge Behaviour in Full-size DC Cable Systems," in *Electrical Insulation and Dielectric Phenomena, 2006 IEEE Conference on*, 2006, pp. 732-735.
[68] T. Maeno, T. Futami, H. Kushibe, T. Takada, and C. M. Cooke, "Measurement of spatial charge distribution in thick dielectrics using the pulsed electroacoustic method," *Electrical Insulation, IEEE Transactions on,* vol. 23, pp. 433-439, 1988.
[69] J. A. Stratton, *Electromagnetic Theory*: Wiley-IEEE Press, 2007.
[70] W. K. H. Panofsky and M. Phillips, *Classical Electricity And Magnetism*: Dover Publications, Incorporated, 2005.
[71] S. Holé, "PEA Signal Simulation in the case of Plane-Wire-Plan Geometry samples," LeicesterApril 2013.
[72] S. Holé, T. Ditchi, and J. Lewiner, "Non-destructive methods for space charge distribution measurements: what are the differences?," *Dielectrics and Electrical Insulation, IEEE Transactions on,* vol. 10, pp. 670-677, 2003.
[73] G. Chen, Y. L. Chong, and M. Fu, "A Novel Calibration Method in the Presence of Space Charge in Dielectric Materials Using the Pulsed Electroacoustic Technique," presented at the 8th Internaional Conference on Properties and Applications of Dielectric Materials, Bali, Indonesia, 2006.
[74] Y. Li and T. Takada, "Progress in space charge measurement of solid insulating materials in Japan," *Electrical Insulation Magazine, IEEE,* vol. 10, pp. 16-28, 1994.
[75] K. Fukunaga, "Industrial applications of space charge measurement in Japan," *Electrical Insulation Magazine, IEEE,* vol. 15, pp. 6-18, 1999.
[76] R. Liu and et al., "Pulsed electro-acoustic method for measurement of space charge distribution in power cables under both DC and AC electric fields," *Journal of Physics D: Applied Physics,* vol. 26, p. 986, 1993.
[77] R. Coelho, B. Aladenize, and P. Mirebeau, "On the intrinsic space-charge in a d.c. power cable," in *Electrical Insulation and Dielectric Phenomena, 1996., IEEE 1996 Annual Report of the Conference on*, 1996, pp. 278-282 vol.1.
[78] G. Williams, *Fourier Acoustics: Sound Radiation and Nearfield Acoustical Holography*: Academic Press, 1999.
[79] K. Fukunaga, H. Miyata, M. Sugimori, and T. Takada, "Measurement of Charge Distribution in the Insulation of Cables Using Pulsed Electroacoustic Method," *Trans. IEE Japan,* vol. 110-A, pp. 647 -648, 1990
[80] T. Muronaka, Y. Tanaka, T. Takada, S. Maruyama, and H. Mutou, "Measurement of space charge distribution in XLPE cable using PEA system with flat electrode," in *Electrical Insulation and Dielectric Phenomena, 1996. IEEE 1996 Annual Report of the Conference on*, 1996, pp. 266-269 vol.1.
[81] M. Fu and G. Chen, "Space charge measurements in polymer insulated power cables using flat ground electrode PEA system," *IEE Proc.-Sci. Meas. Technol,* vol. 150, pp. 89-96, 2003.
[82] K. Terashima, H. Sukuki, M. Hara, and K. Watanabe, "Research and development of 250 kV DC XLPE cables," *Power Delivery, IEEE Transactions on,* vol. 13, pp. 7-16, 1998.

[83] T. Yamanaka, S. Maruyama, and T. Tanaka, "The development of DC+/-500 kV XLPE cable in consideration of the space charge accumulation," in *Properties and Applications of Dielectric Materials, 2003. Proceedings of the 7th International Conference on*, 2003, pp. 689-694 vol.2.

[84] I. A. Tsekmes, D. van der Born, P. H. F. Morshuis, J. J. Smit, T. J. Person, and S. J. Sutton, "Space charge accumulation in polymeric DC mini-cables," in *Solid Dielectrics (ICSD), 2013 IEEE International Conference on*, 2013, pp. 452-455.

[85] W. Le, D. Fabiani, G. C. Montanari, and U. H. Nilsson, "Study of the space charge measurement results on two kinds of extruded XLPE mini-cables," in *Properties and Applications of Dielectric Materials, 2009. ICPADM 2009. IEEE 9th International Conference on the*, 2009, pp. 918-921.

[86] A. See and et al., "Measurement of space-charge distributions in solid insulators under rapidly varying voltage using the high-voltage, high-speed pulsed electro-acoustic (PEA) apparatus," *Measurement Science and Technology,* vol. 12, p. 1227, 2001.

[87] D. Fabiani, G. C. Montanari, L. A. Dissado, C. Laurent, and G. Teyssedre, "Fast and slow charge packets in polymeric materials under DC stress," *Dielectrics and Electrical Insulation, IEEE Transactions on,* vol. 16, pp. 241-250, 2009.

[88] S. Delpino, D. Fabiani, G. C. Montanari, L. A. Dissado, C. Laurent, and G. Teyssedre, "Fast charge packet dynamics in XLPE insulated cable models," in *Electrical Insulation and Dielectric Phenomena, 2007. CEIDP 2007. Annual Report - Conference on*, 2007, pp. 421-424.

[89] P. H. F. Morshuis, R. Bodega, D. Fabiani, G. C. Montanari, L. A. Dissado, and J. J. Smit, "Dielectric Interfaces in DC Constructions: Space Charge and Polarization Phenomena," in *Solid Dielectrics, 2007. ICSD '07. IEEE International Conference on*, 2007, pp. 450-453.

[90] R. Bodega, G. Perego, P. H. F. Morshuis, U. H. Nilsson, and J. J. Smit, "Space charge and electric field characteristics of polymeric-type MV-size DC cable joint models," in *Electrical Insulation and Dielectric Phenomena, 2005. CEIDP '05. 2005 Annual Report Conference on*, 2005, pp. 507-510.

[91] G. Eberle and W. Eisenmenger, "Thermal depolarization of PVDF: anomaly at 180°C," *Electrical Insulation, IEEE Transactions on,* vol. 27, pp. 768-772, 1992.

[92] H. Kitajima, Y. Tanaka, and T. Takada, "Measurement of space charge distribution at high temperature using the pulsed electro-acoustic (PEA) method," in *Dielectric Materials, Measurements and Applications, Seventh International Conference on (Conf. Publ. No. 430)*, 1996, pp. 8-11.

[93] M. Fukuma and et al., "Space charge and external circuit current measurements in LDPE films during breakdown tests," *Journal of Physics D: Applied Physics,* vol. 35, p. 14, 2002.

[94] T. Maeno, K. Fukunaga, and T. Takada, "High-resolution PEA charge distribution measurement system," in *Conduction and Breakdown in Solid Dielectrics, 1995. ICSD'95., Proceedings of the 1995 IEEE 5th International Conference on*, 1995, pp. 244-248.

[95] TDK. Ultra-high Voltage Ceramic Capacitors Molded Type with Metal Terminals UHV, FHV Series [Online]. Available: http://www.farnell.com/datasheets/84908.pdf

[96] P. S.A.S. PIEZOELECTRIC FILMS TECHNICAL INFORMATION [Online]. Available: http://www.piezotech.fr/image/documents/22-31-32-33-piezotech-piezoelectric-films-leaflet.pdf
[97] A. Many and G. Rakavy, "Theory of Transient Space-Charge-Limited Currents in Solids in the Presence of Trapping," *Physical Review,* vol. 126, pp. 1980-1988, 1962.
[98] E. Belgaroui, I. Boukhris, A. Kallel, G. Teyssedre, and C. Laurent, "A new numerical model applied to bipolar charge transport, trapping and recombination under low and high dc voltages," *Journal of Physics D: Applied Physics,* vol. 40, p. 6760, 2007.
[99] S. L. Roy, P. Segur, G. Teyssedre, and C. Laurent, "Description of bipolar charge transport in polyethylene using a fluid model with a constant mobility: model prediction," *Journal of Physics D: Applied Physics,* vol. 37, p. 298, 2004.
[100] F. Boufayed, G. Teyssedre, C. Laurent, S. L. Roy, L. A. Dissado, P. Segur*, et al.*, "Models of bipolar charge transport in polyethylene," *Journal of Applied Physics,* vol. 100, p. 104105, 2006.
[101] F. Baudoin, S. L. Roy, G. Teyssedre, and C. Laurent, "Bipolar charge transport model with trapping and recombination: an analysis of the current versus applied electric field characteristic in steady state conditions," *Journal of Physics D: Applied Physics,* vol. 41, p. 025306, 2008.
[102] M. Fu, G. Chen, A. E. Davies, and J. G. Head, "Space charge measurements in power cables using a modified PEA system," in *Dielectric Materials, Measurements and Applications, 2000. Eighth International Conference on (IEE Conf. Publ. No. 473)*, 2000, pp. 74-79.
[103] S. Boggs, "A rational consideration of space charge," *Electrical Insulation Magazine, IEEE,* vol. 20, pp. 22-27, 2004.
[104] S. Holé and et al., "Improvement of PEA signal analysis using simulations for complex geometry samples," *Journal of Physics D: Applied Physics,* vol. 35, p. 19, 2002.
[105] P. M. C. Morse and K. U. Ingard, *Theoretical Acoustics*: Princeton University Press, 1968.
[106] Y. Kane, "Numerical solution of initial boundary value problems involving maxwell's equations in isotropic media," *Antennas and Propagation, IEEE Transactions on,* vol. 14, pp. 302-307, 1966.
[107] J. R. Macdonald, "Space Charge Polarisation," in *Electrode Processes in Solid State Ionics*. vol. 25, M. Kleitz and J. Dupuy, Eds., ed: Springer Netherlands, 1976, pp. 149-183.
[108] W. P. Mason, *Electromechanical transducers and wave filters*: D. Van Nostrand Co., 1948.
[109] M. Redwood, "Transient Performance of a Piezoelectric Transducer," *Acoustical Society of America,* vol. 33, pp. 527-536, 1961.
[110] W. M. Leach, Jr., "Controlled-source analogous circuits and SPICE models for piezoelectric transducers," *Ultrasonics, Ferroelectrics and Frequency Control, IEEE Transactions on,* vol. 41, pp. 60-66, 1994.
[111] J. L. San Emeterio and A. Ramos, "Models for Piezoelectric Transducers Used in Broadband Ultrasonic Applications," in *Piezoelectric Transducers and Applications*, A. Vives, Ed., ed: Springer Berlin Heidelberg, 2008, pp. 97-116.
[112] A. Puttmer, P. Hauptmann, R. Lucklum, O. Krause, and B. Henning, "SPICE model for lossy piezoceramic transducers," *Ultrasonics, Ferroelectrics and Frequency Control, IEEE Transactions on,* vol. 44, pp. 60-66, 1997.

[113] L. F. Brown and D. L. Carlson, "Ultrasound transducer models for piezoelectric polymer films," *Ultrasonics, Ferroelectrics and Frequency Control, IEEE Transactions on,* vol. 36, pp. 313-318, 1989.
[114] R. S. Dahiya, M. Valle, and L. Lorenzelli, "SPICE model for lossy piezoelectric polymers," *Ultrasonics, Ferroelectrics and Frequency Control, IEEE Transactions on,* vol. 56, pp. 387-395, 2009.
[115] C. P. Martin, A. S. Vaughan, and S. J. Sutton, "The thermomechanical behaviour of crosslinked polyethylene cable insulation material," in *Electrical Insulation and Dielectric Phenomena, 2003. Annual Report. Conference on*, 2003, pp. 88-91.
[116] Z. Li and A. C. Cangellaris, "GT-PML: generalized theory of perfectly matched layers and its application to the reflectionless truncation of finite-difference time-domain grids," *Microwave Theory and Techniques, IEEE Transactions on,* vol. 44, pp. 2555-2563, 1996.
[117] Y. Xiaojuen, D. Borup, J. W. Wiskin, M. Berggren, R. Eidens, and S. A. Johnson, "Formulation and validation of Berenger's PML absorbing boundary for the FDTD simulation of acoustic scattering," *Ultrasonics, Ferroelectrics and Frequency Control, IEEE Transactions on,* vol. 44, pp. 816-822, 1997.
[118] P. E. Bloomfield, L. Wei-Jung, and P. A. Lewin, "Experimental study of the acoustical properties of polymers utilized to construct PVDF ultrasonic transducers and the acousto-electric properties of PVDF and P(VDF/TrFE) films," *Ultrasonics, Ferroelectrics and Frequency Control, IEEE Transactions on,* vol. 47, pp. 1397-1405, 2000.
[119] U. B. Buchholz, M. Jaunich, W. Stark, W. Habel, and B. A. T. Petersson, "Acoustic data of cross linked polyethylene (XLPE) and cured liquid silicone rubber (LSR) by means of ultrasonic and low frequency DMTA," *Dielectrics and Electrical Insulation, IEEE Transactions on,* vol. 19, pp. 558-566, 2012.
[120] H. G. Tattersall, "The ultrasonic pulse-echo technique as applied to adhesion testing," *Journal of Physics D: Applied Physics,* vol. 6, p. 819, 1973.
[121] W. Choo and G. Chen, "Electric Field Determination in DC Polymeric Power Cable in the Presence of Space Charge and Temperature Gradient under dc Conditions," presented at the 2008 International Conference on Condition Monitoring and Diagnosis, Beijing, China, 2008.
[122] R. Bodega, "Space Charge Accumulation in Polymeric High Voltage DC Cable Systems," PHD, dottore in ingegneria elettrica, Universiteit Delft, Politecnico di Milano, geboren te Lecco (Italië), 2006.
[123] M. Fu, G. Chen, A. E. Davies, and J. Head, "Space charge measurements in cables using the PEA method:--Singal data processing considerations," presented at the 7th Internationa Conference on Solid Dielectrics, Eindhoven, the Netherlands, 2001.
[124] B. Alijagic-Jonuz, P. H. F. Morshuis, and J. J. Smit, "Effect of temperature and humidity on space charge quantities," in *Electrical Insulation and Dielectric Phenomena, 2002 Annual Report Conference on*, 2002, pp. 903-905.
[125] G. C. Montanari and F. Palmieri, "The effect of humidity on space charge accumulation in XLPE," in *Electrical Insulation and Dielectric Phenomena, 2003. Annual Report. Conference on*, 2003, pp. 205-208.

APPENDIX A. MAGNITUDE REDUCTION OF OUTGOING CYLINDRICAL WAVE

Using the Hankel function, the propagation of a 20 ns Gaussian wave generated at radius=1.5 mm of a lossless cylinder was simulated as shown in Figure A-1. The magnitude reduction of the outgoing cylindrical wave fits with the approximation of the Hankel function for the far field that follows the behaviour of $1/\sqrt{r}$. As compared in Figure A-2, the areas of the Gaussian wave at different radius are consistent with that calculated by a reduction factor $\sqrt{(r_{1.5mm}/r)}$.

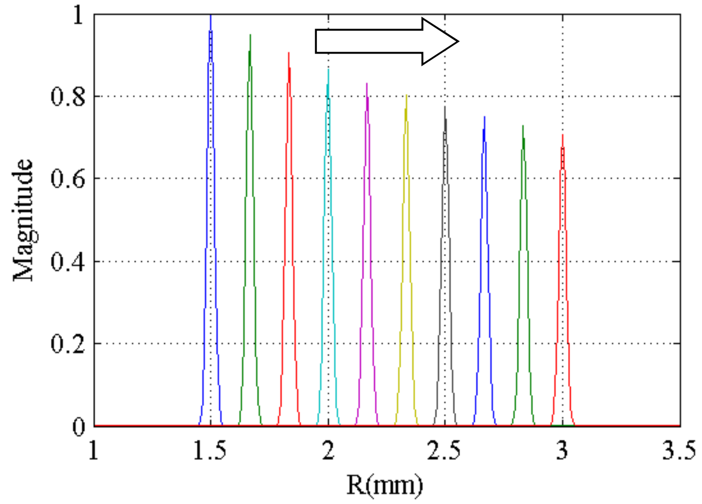

Figure A-1. Simulation of a 20 ns Gaussian wave propagating in a cylindrical homogeneous lossless media from radius a = 1.5 mm to 3 mm.

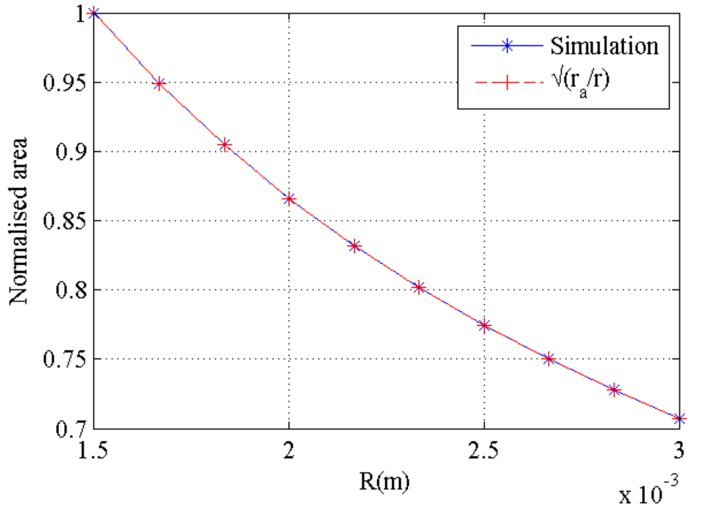

Figure A-2. Area reduction of the cylindrical wave during the outward propagation compared with the reduction term of $\sqrt{(r_{1.5mm}/r)}$.

APPENDIX B. SIMULATION OF PULSE GENERATOR

The pulse generator circuit is simulated using Pspice as shown in Figure B-1(a). The HV MOSFET switch is simulated by a voltage controlled switch circuit element 'Vtrige'. The TTL signal which triggers the switch is generated by a pulse voltage source. In reality, a one-meter coaxial cable is used for connecting the DC power supply to the input of the switch. A 100 mH inductance is assumed at this connection point. The RG 213/U coaxial cable is used as a delay line and deliveries the voltage pulse to the mini-cable. The π type 50 Ω attenuator provides an impedance matching load for the 50 Ω coaxial cable and also provides a small trigger signal for the oscilloscope which is simulated by a 50 Ω resistive load. The 1700 pF high voltage blocking capacitor, 'HVcoupling', is before the mini-cable. The high voltage injection point that provides the DC voltage to the cable is not shown in the simulation circuit as only the pulse response was of interest.

The mini-cable used for this project has a length of 1 meter and is simulated by a distributed model of 10 segments, each of which represents a 0.1m sub-section of the mini-cable, as shown in Figure B-1(b). Each mini-cable segment was modelled as a series resistor, R_{semi}, representing the outer semicon resistance, and R_{cu}, representing the inner conductor resistance and inductor, L_{semi}, representing the outer semicon layer inductance and inductor Lcu, representing the central conductor inductance, and with shunt capacitance, C_C, and conductance, G. The simulation parameters are listed in Table B-1. Among these parameters, the one most affecting the pulse quality is the capacitance C_c. With respect to the diameter of the mini-cable used in this work, the calculated capacitance per unit length is about:

$$C = \frac{2\pi\varepsilon_0\varepsilon_r}{\ln(\frac{b}{a})} \approx 185\ pF/m \tag{B.1}$$

where the relative permittivity of polymer insulation, ε_r, is 2.3, a and b are the inner and outer radius of the insulation layer. In the simulation, a conservative value of 300 pF/m for 1m mini-cable was used. The position of the PEA cell was half way along the mini-cable which had a contact length of 30mm which was simulated simply using a 30 pF capacitor.

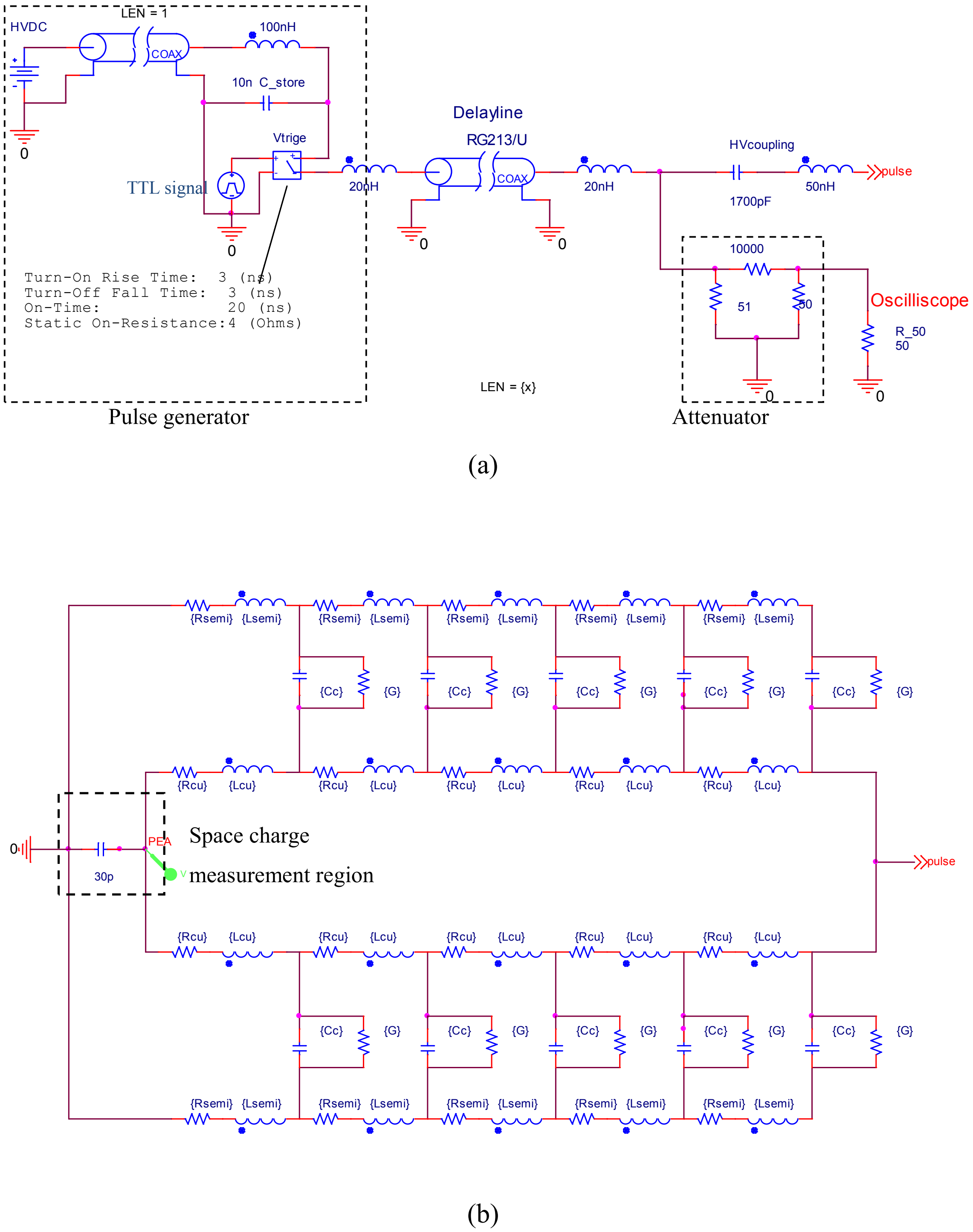

Figure B-1. Pspice simulation models of the (a) pulse generator circuit and (b) mini-cable.

Table B-1. Parameters for the mini-cable modelling.

Component	Value	Description
R_semi	1800 Ω/dm	Resistance of the outer semicon
Lsemi	10 nH/dm	Inductance of the outer semicon
Cc	30 pF/dm	Capacitance of the insulator (conservative)
G	1e-11 s/dm	Conductivity of the insulator
Rcu	1.1 mΩ/dm	Resistance of the conductor
Lcu	5 nH/dm	Inductance of the conductor

The simulation result in Figure B-2 shows the voltage pulse across the space charge measurement region of the mini-cable with a 2 kV DC source and 1m coaxial delay line. The simulation result illustrates that oscillations are produced after the main voltage pulse as a result of the pulse reflections in the short coaxial cable. In reality, the voltage oscillation would be even greater if the input impedance of the attenuator was deviated from the ideal value of 50 Ω or the mini-cable had a larger capacitance than the value used in simulation or had an increased length. The voltage oscillations may disturb the space charge signal. This addresses the importance of using a sufficiently long delay line to guarantee clean pulses.

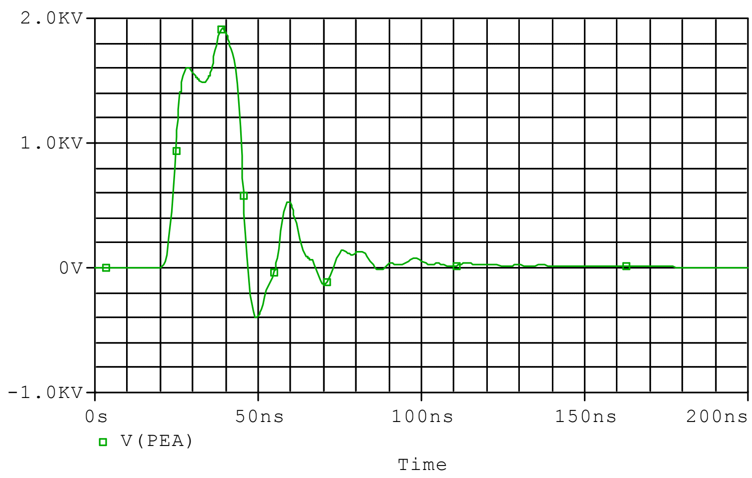

Figure B-2. Simulated voltage pulse across the section of mini-cable that is under PEA measurement. In the simulation model, 1m coaxial cable delay line and 2 kV DC supplier were used.

APPENDIX C. THERMAL DISTRIBUTION OF MINI-CABLE

The feasibility of locating the capacitor and cable terminals outside the oven is studied by the thermal distribution simulation using COMSOL MULTIPYSICS.

The mini-cable is simplified by assuming the semicon layers have the same material properties as the cable insulation. The simulation domain of mini-cable is comprised of a $r = 0.75$ mm copper conductor and a surrounding 2.25 mm thick polyethylene layer to match the physical dimensions of a real mini-cable. Normally the mini-cable used in the project is about 1-1.2 m and the middle of the cable is under the PEA apparatus. In the simulation, it is necessary to include half of the cable, i.e. 50 cm, to study the temperature gradient along the length of the cable.

A 15 cm section of the mini-cable is assumed to project outside the oven and the thickness of the oven door is ignored. The ambient temperature (outside the oven) is assumed to be 20 °C and oven temperature is 90 °C. This generates a worst case temperature gradient along the cable length. The temperature along the centre of the conductor is calculated in the simulation.

Heat flux boundary conditions were applied to the outer surface of the cable. A wide range of convection heat transfer coefficients, H_t, for the section of mini-cable inside the oven was tested in the simulation. The simulation of the temperature profiles are shown in Figure C-1, while the heat transfer coefficient for mini-cable outside the oven was assumed to be $4 \times H_t$. The simulation indicates that the cable temperature can reach the isothermal condition for the PEA measurements when H_t above 10 $W/(m^2 \cdot K)$.

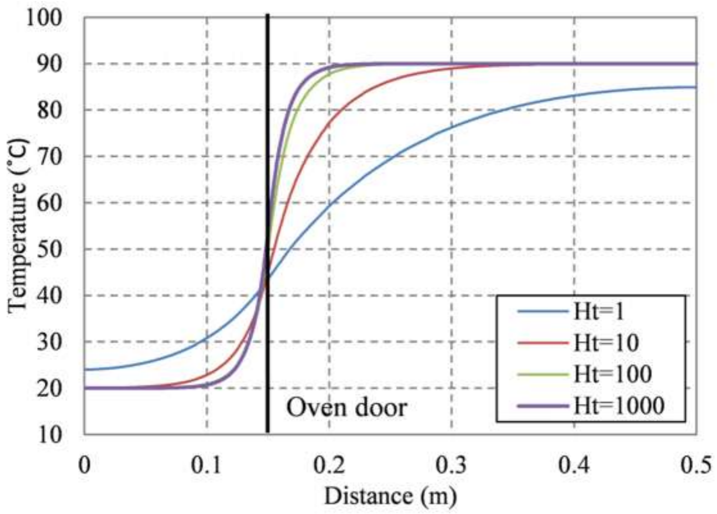

Figure C-1. Temperature distribution on the conductor with a variety of convection heat transfer coefficients H_t (W/(m^2·K)) for the part of mini-cable inside the oven. The heat transfer coefficient for the part of mini-cable outside the oven is assumed to be 4 × H_t.

In addition, considering the ambient condition for mini-cable outside the oven is not well controlled. The heart transfer coefficient may vary due to factors like convection cooling. Therefore a range of enhanced heart transfer coefficient, $1H_t$, $10H_t$, $100H_t$, was applied to the 15cm cable section outside the oven. As the results shown in Figure C-2, the isothermal condition can be achieved in the worst situation.

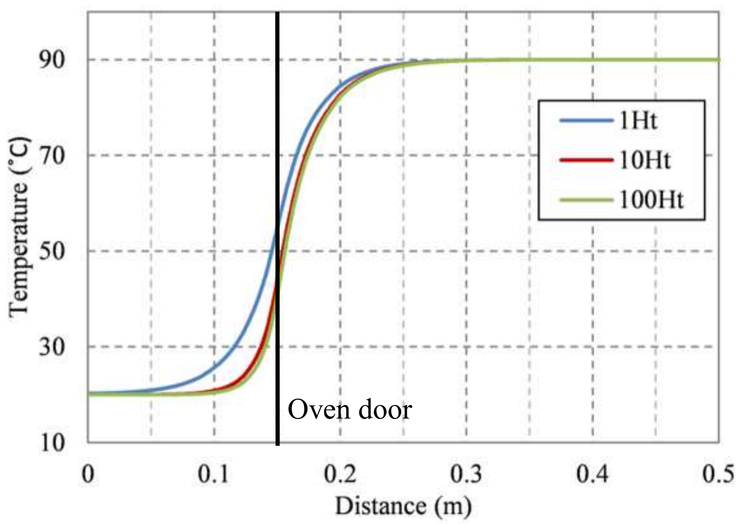

Figure C-2. Temperature distribution on the conductor when the convection heat transfer coefficient for the part of mini-cable outside the oven is 1, 10 and 100 times bigger than that H_t = 25W/(m^2k) inside the oven .

APPENDIX D. MINIMUM WIDTH OF THE WAVEGUIDE (BOTTOM ELECTRODE)

As a waveguide for the PEA acoustic signal, the width of the bottom electrode, $W_{electrode}$ as shown in Figure D-1, has to be wide enough to ensure the reflected acoustic waves from two sides do not overlap the direct transmitted signals and therefore appear in the measured space charge profile. The minimum waveguide width, $W_{electrode}$, follows the relationship:

$$t_{sc} + \frac{T_{electrode}}{V_{AL}} < \frac{2\times\sqrt{(T_{electrode}/2)^2+(W_{electrode}/2)^2}}{V_{AL}}.$$

where t_{SC} is the time interval of the useful space charge profile, $T_{electrode}$ is the thickness of the base electrode of the PEA cell, V_{AL} is the acoustic velocity of the longitudinal pressure waves in aluminium.

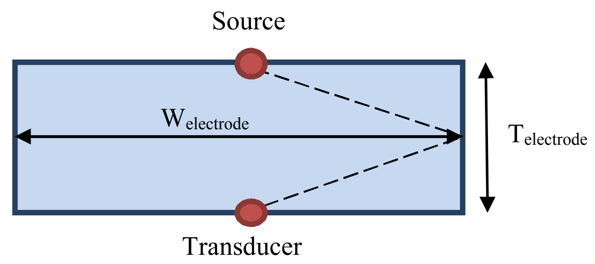

Figure D-1. Schematic diagram of the waveguide. Dashed line indicates the path of the acoustic wave that would reach the transducer after reflection at the side boundary.

Assuming the duration of the space charge signal, t_{sc} is 700 ns, the sound velocity in aluminium, V_{AL}, is 6400 m/s, thickness of the waveguide, $T_{electrode}$ is 25 mm, then according to the equation above, the minimum width of the base electrode is about 16mm. A simulation of acoustic wave propagation based on the method described in section 4.7 with the above parameters has verified this calculation as shown in Figure D-2. A point acoustic source located at the position of the contact of the cable with the bottom electrode generates two Gaussian pulses at times t = 0 ns and t = 700 ns. P_1 and P_2 denote the first positive pulse and the second negative pulse. The first pulse reaches the two sides of the 16 mm wide bottom electrode after 1279 ns. Since the acoustic impedance of air is much smaller than that of aluminium, the acoustic waves reflect back into the bottom electrode with a cylindrical wavefront denoted as P_R. At about 3950 ns, P_1 reached the piezo-senor. And after about 700 ns (at 4660 ns), the second peak P_2 arrives at the sensor. Almost at the same time, the reflected wave P_R (from P_1) also acted on the piezo-sensor. This simulation confirmed that the calculated minimum width of the bottom electrode (16 mm) is just sufficient to separate the reflected waves from the space charge profile (in the time window between P_1 and P_2).

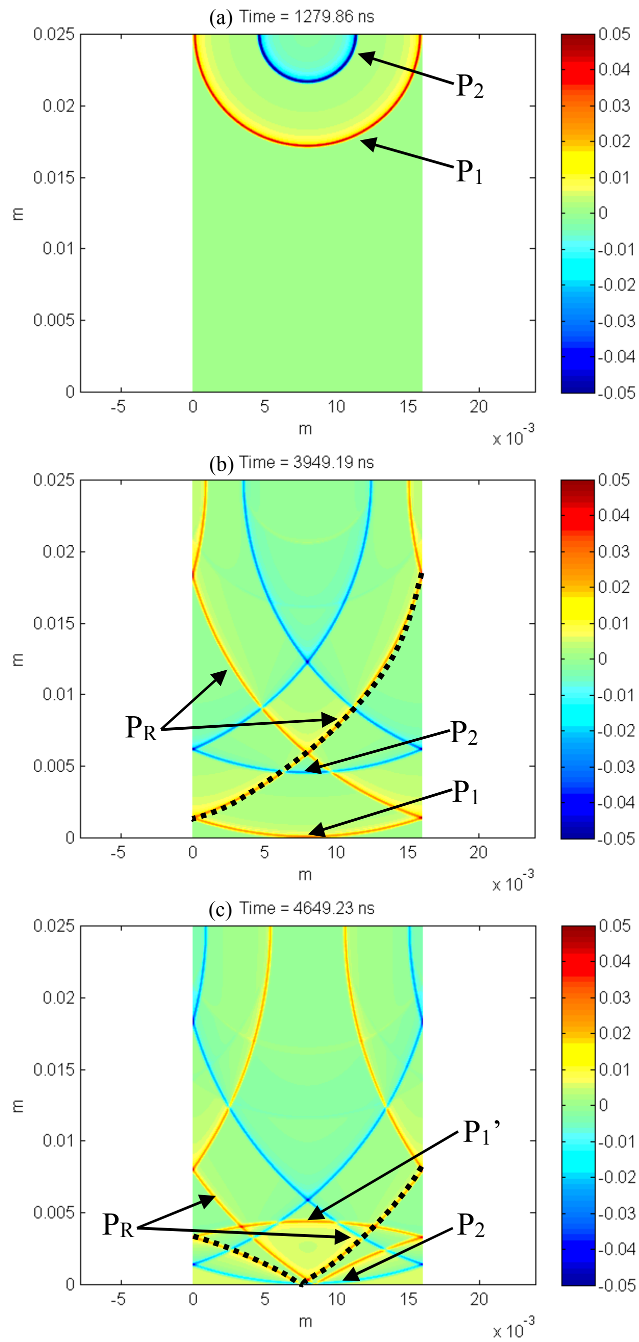

Figure D-2. Wave propagation inside an aluminium wave guide of 16 mm wide and 25 mm thick. The excitation sources are two Gaussian pulses P_1 and P_2 with a time delay of 700 ns. P_R represents the reflected signals form the two sides of the wave guide. P_1' is the reflected signal of P_1 at the bottom of the wave guide. (a) at time = 1279.86 ns, (b) at time = 3949.19 ns, (c) at time = 4649.23 ns.

APPENDIX E. FEASIBILITY OF USING PEA CURRENT SIGNAL

If the RC time constant of the sensor – amplifier circuit is much shorter than the pulse width, then the recorded signal (the voltage across the input resistance) is actually proportional to the sensor current signal. Theoretically, the PEA voltage signal can be recovered by integrating the current signal as the response of the RC circuit is well known. However when considerable noise exists in the raw PEA current signal, there may be some practical difficulties in the numerical integration.

Three methods are proposed here to restore the electrical mismatch:

1. Apply the inverse transfer function of a RC high pass filter using the calculated capacitance of the piezo-electric sensor and the known input impedance of the amplifier.
2. When the capacitance of the piezo-electric sensor is small enough, the RC network works as a differentiator on the piezoelectric signal. Therefore time integration of the measured current signal would then generate the original voltage signal.
3. Deconvolution with an ideal Gaussian pulse.

To examine the above three methods, a simple RC circuit as shown in Figure E-1 was simulated to produce an idealised high pass noisy PEA output signal. The 20 ns Gaussian Pulse, as shown in Figure E-2, was assumed as the generated voltage across the 100 pF piezo film. The voltage across the 50 Ω resistor represents the raw PEA output. In addition, 4 dB (S/N ratio) white Gaussian noise was added to the raw output signal.

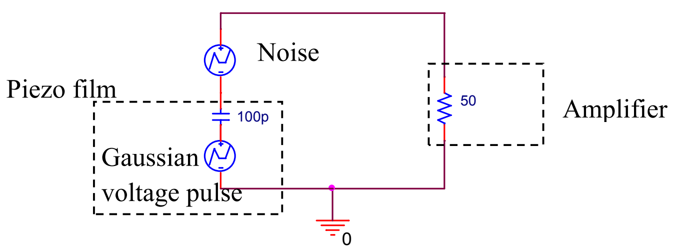

Figure E-1. Equivalent circuit of the piezo film – Amplifier system with a noise source.

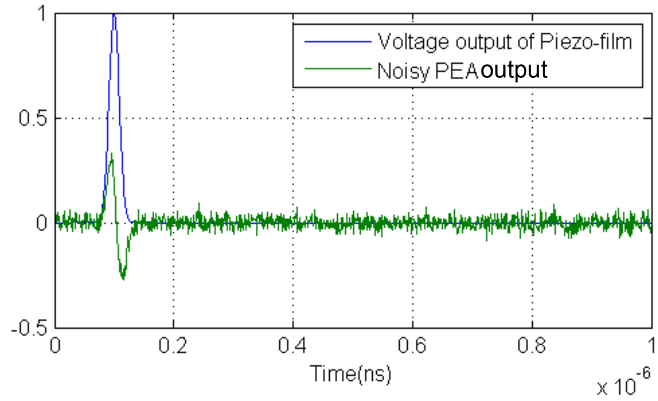

Figure E-2. System response of a 100 pF piezo-sensor and 50 Ω resistor representing the low noise amplifier. The voltage across the piezo-sensor is the assumed to be an ideal Gaussian pulse. 4 dB (S/N) white Gaussian noises are added to the voltage cross the resistor which is regard as the raw PEA output.

Applying the three numerical methods to restore the simulated noisy PEA output, the recovered signals are compared in Figure E-3. It is clear that the presence of noise results in serious baseline drift in all cases. Furthermore, the drift is random and hence hard to be removed. This is due to the fact that to recover the original pulse, it is necessary to integrate the raw data (as it is the differential of the original signal). In fact all three signal processing techniques are attempting to perform the same integral in different ways. Offset errors in the raw data accumulate when performing the time integral exaggerating the baseline drift. A low impedance (50 Ω) amplifier is therefore unsuitable for the application and a much higher input impedance buffer amplifier will be necessary to avoid performing the numerical integration on the raw data.

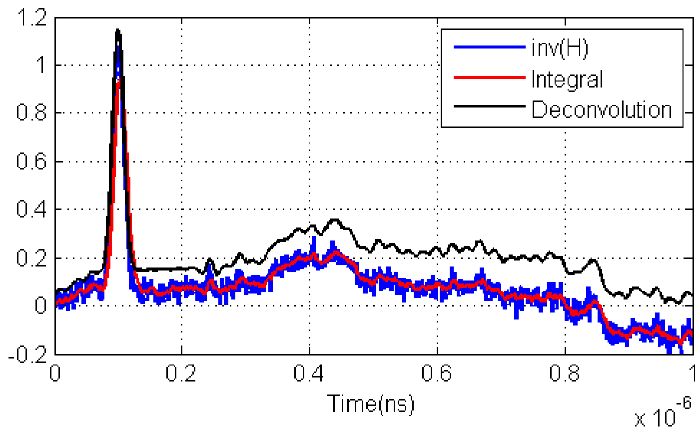

Figure E-3. Signal processing for solving the impedance mismatch between a 100 pF Piezo-sensor and a 50 Ω LNA. Three methods were utilised: applying the inverse transfer function of a RC high pass filter (blue line); integration (red line); and deconvolution with an ideal Gaussian pulse (black line).

APPENDIX F. BUFFER CIRCUIT AND SIMULATION

The greater input impedance of the buffer contributes to recording lower frequency components of the sensor piezo-voltage signal, but with the penalty of higher noise level. Consequently, two buffer amplifiers with 3.2 kΩ and 75 kΩ input impedances were designed to assess their relative performance.

The PSpice simulation circuits of the two buffers are shown in Figure F-1.The electrical equivalent of a PVDF-TrFE film is represented by a voltage generator (*Vs*) in series with a capacitance (C_sensor) which is in parallel with a high resistance resistor. This resistor is required by the pSpice simulator but the resistance is made sufficiently high not to affect the simulation outputs. The voltage across the piezoelectric film is proportional to the mechanical pressure applied on it. Since voltage pulses generated by the pulse generator for the PEA system are of 20 ns duration, the minimum width of pressure waves acting on the sensor film would not below 20 ns. The amplifier is biased for a common emitter configuration and the input impedance of the buffer is determined by the bias resistors R_1, R_2, and the output resistance as seen at the base of the transistor. For the 3.2 kΩ and 75 kΩ buffers, two 6.4 kΩ and 150 kΩ bias resistors are used respectively. A low noise NPN transistor, BC550C, which has a current gain, $\beta = 270$ for the 3.2 kΩ buffer circuit was utilised. Nevertheless for the higher impedance 75 kΩ buffer, two PRF949 transistors of high transition frequency and $\beta = 150$ were connected in the Darlington configuration. The capacitance of the PVDF-TrFE film was assumed to be 170 pF as calculated previously. C_{input} and C_{couple} are coupling capacitors for removing the DC offsets from the input and output terminals. V_{cc} is the DC supply for the buffer, which is normally 10 V – 15 V.

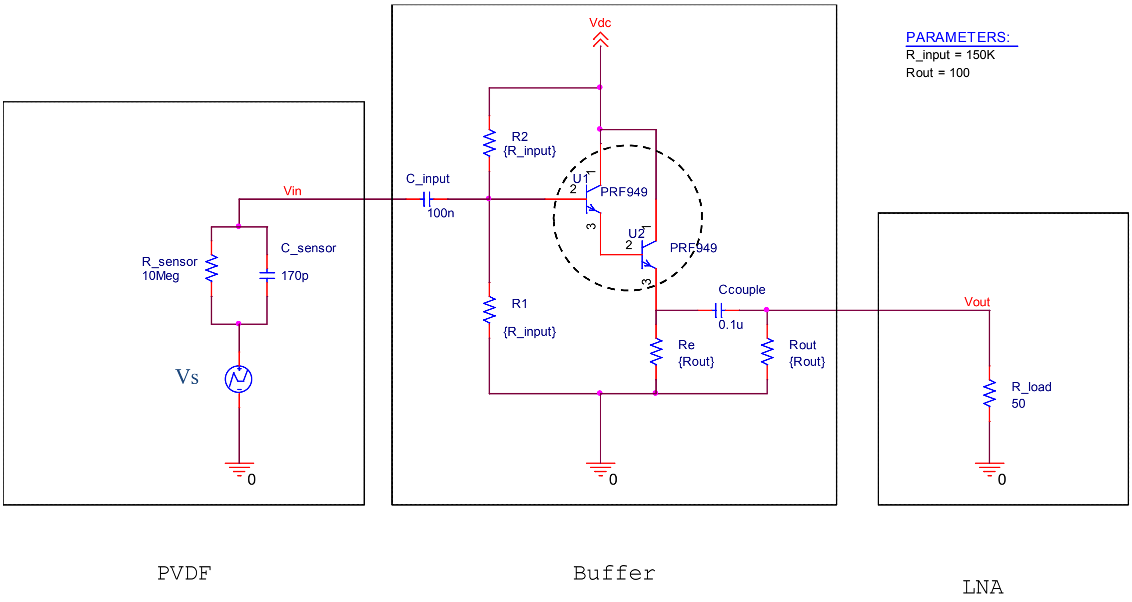

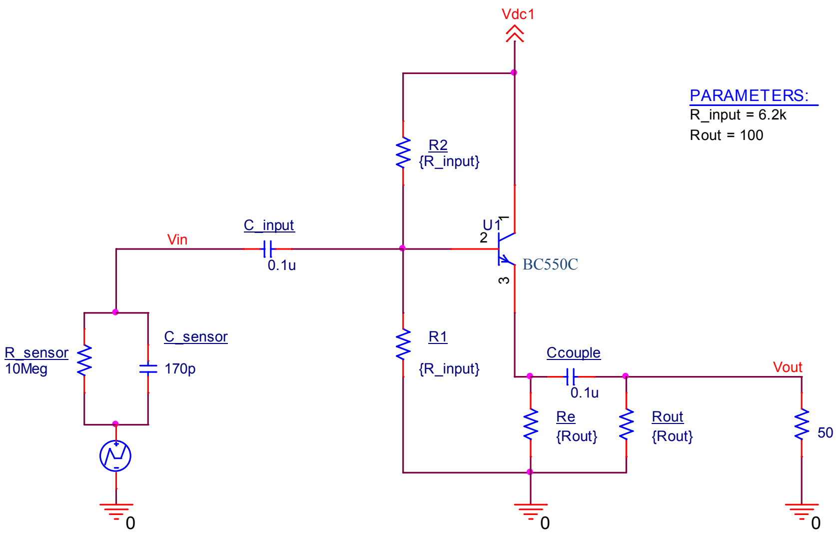

Figure F-1. Pspice simulation circuit of the 75 kΩ buffer amplifier (top). For 3.2 kΩ buffer (lower circuit), the Darlington transistors were replaced by a BC550C transistor.

The simulated frequency response, using PSpice for the two different input impedance buffer amplifiers are shown in Figure F-2. As expected, the 75 kΩ buffer has a lower 3 dB cut-off of less than 100 kHz while the 3.2 kΩ buffer has a 3 dB cut-off frequency of 500 kHz. Both buffers are able to maintain a flat response to 50 MHz, the maximum frequency assuming 20 ns voltage pulses.

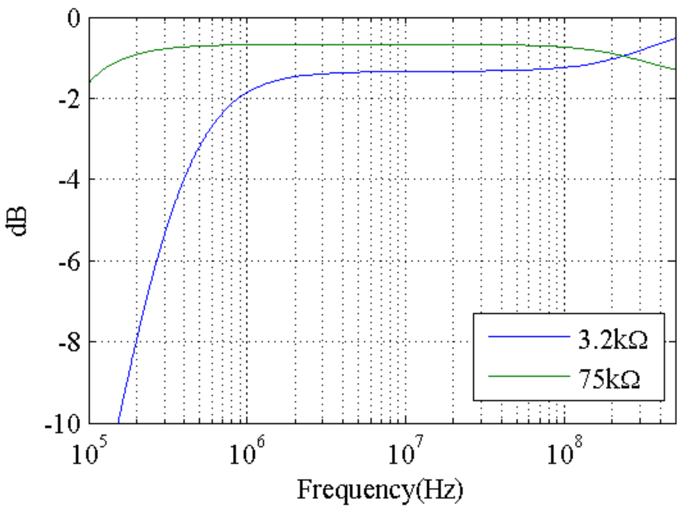

Figure F-2. Frequency responses of buffers with 3.2 kΩ and 75 kΩ input impedance.

Simulations in the time domain were also carried out. An assumed idealised signal consists of two Gaussian pulses, 20 ns for the first pulse and 40 ns for the second pulse after a time delay of 700 ns to mimic the raw output response of the PEA. A linear offset was added to represent the lowest frequency in the PEA response. The simulation results of both buffer circuits are shown in Figure F-3 and compared to the idealised signal. The output of 3.2 kΩ buffer maintains the shape of two pulse signals with small overshoots while the low frequency linear signal is significantly attenuated. On the contrary, the 75 kΩ buffer almost retains the input signal with only small attenuation at the lowest frequency.

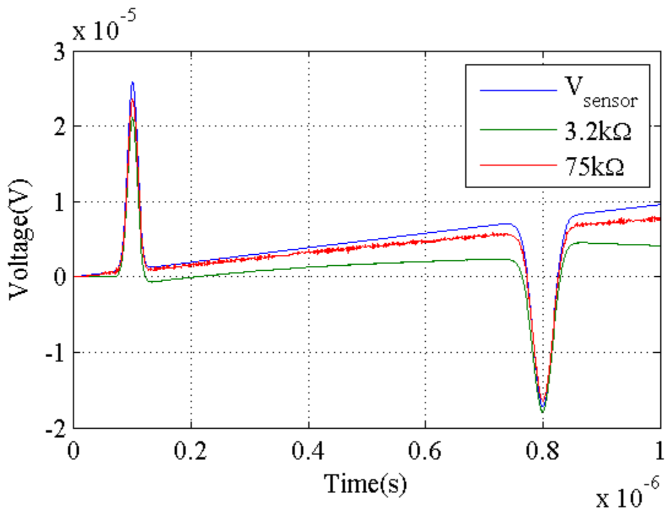

Figure F-3. Time domain simulation for the 3.2 kΩ and 75 kΩ input impedance buffers. The blue line is the artificial piezoelectric voltage signal.